



HAL
open science

Energy coupling mechanisms in pulsed surface discharges for flow control

Philippe Castera

► **To cite this version:**

Philippe Castera. Energy coupling mechanisms in pulsed surface discharges for flow control. Other. Ecole Centrale Paris, 2015. English. NNT : 2015ECAP0041 . tel-01225674

HAL Id: tel-01225674

<https://theses.hal.science/tel-01225674>

Submitted on 6 Nov 2015

HAL is a multi-disciplinary open access archive for the deposit and dissemination of scientific research documents, whether they are published or not. The documents may come from teaching and research institutions in France or abroad, or from public or private research centers.

L'archive ouverte pluridisciplinaire **HAL**, est destinée au dépôt et à la diffusion de documents scientifiques de niveau recherche, publiés ou non, émanant des établissements d'enseignement et de recherche français ou étrangers, des laboratoires publics ou privés.



THÈSE

présentée par

Philippe Castera

pour l'obtention du

GRADE de DOCTEUR

Formation doctorale : Énergétique et Physique

Laboratoire d'accueil : Laboratoire d'Énergétique Moléculaire
et Macroscopique, Combustion (EM2C)
du CNRS et de l'ECP

Energy coupling mechanisms in pulsed surface discharges for flow control

Soutenue le 22 juillet 2015

Jury :	Prof. Emmanuel Odic	Laboratoire GeePs, CentraleSupélec	Président
	Prof. Sergey Macheret	Purdue University	Rapporteur
	Prof. Jean Larour	LPP, Ecole Polytechnique	Rapporteur
	Prof. Dunpin Hong	GREMI, Université d'Orléans	Examinateur
	Dr. Gilles Zalamansky	Dassault Aviation	Examinateur
	Dr. Patrick Gnemmi	Institut Saint-Louis	Examinateur
	Dr. Paul-Quentin Elias	ONERA	Encadrant
	Prof. Christophe Laux	Laboratoire EM2C, CentraleSupélec	Directeur de thèse

École Centrale des Arts et Manufactures
Grand Établissement sous tutelle
du Ministère de l'Éducation Nationale
Grande Voie des Vignes
92295 Châtenay-Malabry Cedex
Tél : 33 (1) 41 13 10 00
Télex : 634 991 F EC PARIS

**Laboratoire d'Énergétique
Moléculaire et Macroscopique,
Combustion (E.M2.C.)**
UPR 288, CNRS et École Centrale Paris
Tél : 33 (1) 41 13 10 31
Fax : 33 (1) 47 02 80 35

2015ECAP0041

À mes grand-pères

*An jenem Tag im blauen Mond September
Still unter einem jungen Pflaumenbaum
Da hielt ich sie, die stille bleiche Liebe
In meinem Arm wie einen holden Traum.
Und über uns im schönen Sommerhimmel
War eine Wolke, die ich lange sah
Sie war sehr weiß und ungeheuer oben
Und als ich auf sah, war sie nimmer da.*

*Seit jenem Tag sind viele, viele Monde
Geschwommen still hinunter und vorbei.
Die Pflaumenbäume sind wohl abgehauen
Und fragst du mich, was mit der Liebe sei.
So sag ich dir: ich kann mich nicht erinnern
Und doch, gewiß, ich weiß schon, was du meinst.
Doch ihr Gesicht, das weiß ich wirklich nimmer
Ich weiß nunmehr: ich küßte es dereinst.*

*Und auch den Kuß, ich hätt ihn längst vergessen
Wenn nicht die Wolke dagewesen wär
Die weiß ich noch und werd ich immer wissen
Sie war sehr weiß und kam von oben her.
Die Pflaumenbäume blühn vielleicht noch immer
Und jene Frau hat jetzt vielleicht das siebte Kind.
Doch jene Wolke blühte nur Minuten
Und als ich auf sah, schwand sie schon im Wind.*

Bertol Brecht, Erinnerung an die Marie A.

Acknow-ciements

HC SVNT DRACONES

The Hunt-Lenox Globe

The dragons of all those I may have forgotten. . .

Les remerciements sont en général la dernière partie que l'on écrit pour mettre un point final à une aventure de plusieurs années. C'est aussi agréable que dangereux, j'ai bien peur d'oublier de citer des gens ici : vous pourrez me maudire jusqu'à la 13^e génération pour vous avoir omis dans ces lignes, même si je sais ce que je vous dois. J'ai rédigé cette thèse en anglais à Paris, il est donc parfaitement logique que les acknow-ciements oscillent entre anglais et français selon les circonstances. . .

First of all, I would like to thank Prof. Jean Larour and Prof. Sergey Macheret for having accepted to review my dissertation. Their comments were very useful to complete this definitive edition and gave us new ideas for future work. I would like to add special thanks to Prof. Macheret for having traveled so far from West Lafayette to attend my viva. Many thanks to the other members of the jury: Prof. Dunpin Hong, Prof. Patrick Gnemmi, Dr. Gilles Zalamansky and Prof. Emmanuel Odic who accepted to preside the jury.

Je tiens à remercier Dr. Philippe Lalande, chef de l'unité Foudre Plasmas et Applications de l'ONERA, pour m'avoir permis de faire cette thèse dans la partie palaisienne de l'unité. Et bien sûr, un grand merci à toute l'équipe de Palaiseau : Dr. Denis Packan, Dr. Julien Jarrige, Dr. Clément Zaepffel, Dr. Laurent Chemartin, Dr. Julien Labaune, ainsi que mes collègues thésards, Rafael Alexandre Sousa Martins et Félix Cannat. Vous aurez bientôt droit à "Dr." vous aussi, hold fast guys! J'ai eu beaucoup de plaisir à travailler avec toute l'équipe et à discuter de tout et de rien. Merci donc à Denis d'avoir ramené un peu de sérieux au moment du café (n'oublie pas, c'est jeudi qu'on a droit au chocolat !) notamment au moment du superball ou encore lorsqu'on se demande que peut-on faire dans un caisson spatial, je ne répéterai pas les idées de certains. . . Je remercie les docteurs Jarrige et Zaepffel de leur extrême considération pour les thésards et de m'avoir toléré à leur table pendant tout ce

temps. Plus sérieusement, merci à Julien J. et Clément pour leurs conseils sur la spectroscopie (et du coup de main pour bouger le spectro, même pas un tour de rein !), et merci particulièrement à Clément pour son aide avec les quelques montages électroniques que j'ai eu à utiliser : si tu veux encore jouer de la musique avec les décharges, tu sais où me trouver pour traduire les partitions ! Merci à Julien L. de m'avoir fait bien rire avec les noms de ses programmes et désolé d'avoir vendu la mèche pour ERIS... Je vous suis reconnaissant à tous les trois d'avoir contribué grandement à enrichir ma culture nanardesque (moi aussi, "je sais où tu te caches"), nos discussions scientifiques ou sur la condition désespérante du thésard exploité par les permanents ont rendu plus supportables nos heures de RER. Merci à Laurent, transfuge de Châtillon qu'on a assez souvent vu à Palaiseau (la faute aux GRIFONS) et qui est venu le jour J me soutenir. Petite pensée enfin pour mes camarades thésards Félix et Rafael, encore que Félix sera docteur dans très peu de temps au moment où j'écris ces lignes. J'ai une pensée émue pour ces marcassins qui ont fait connaissances avec le radiateur de ta voiture, Félix, assassin... Obrigado Rafael pour ta bonne humeur, qui a mis un peu de soleil brésilien dans la grisaille palaisienne (de rien Julien).

Au cours de ces trois ans et plus passés à l'ONERA, j'ai eu l'occasion d'interagir ou de discuter de choses et d'autres avec des collègues d'autres services. Que soient donc ici remerciés Christophe Brossard et Nicolas Fdida (nos voisins "de la travée d'à côté"), Philippe Thobois (avec qui j'ai eu le plaisir de parler de nanotubes et de Bertin pendant son passage à FPA, il faut toujours que j'aille voir la voie de l'aérotrain), Axel Vincent-Randonnier, Alexandre Bresson et l'équipe des atomes froids, Jean-Pierre Faleni, Mikaël Orain (j'espère que les images Schlieren que vous avez prises ont été utiles à Robert !), Nelly Dorval (merci pour la lampe de calibration, et merci d'être venue le jour J pour la soutenance), Michel Lefebvre et Brigitte Attal-Tretout. Un grand merci également à Hélène Meler dont l'aide m'a été très précieuse pour organiser ma participation à la conférence AIAA 2014 et mon détour par Pittsburgh au retour d'Atlanta...

J'ai eu la chance de pouvoir mener de front la thèse et un autre beau projet. Un immense merci à tous les chanteurs des LTV (Les Temperamens Variations, Le Troisième Virage, Lauter tollkühne Vokalisten, Le Troupeau de Vaches ? On se perd dans toutes ces possibilités, l'important c'est de mûgir) qui m'ont permis d'obtenir ma qualification de déménageur de piano (certifié Erard et Grotrian Steinweg) et de "faire autre chose", dans la bonne humeur et en gardant toujours une haute exigence de qualité. La faute au chef/tyran/gourou qui nous pousse dans nos retrachements et nous donne la joie de faire sonner ensemble toute cette belle musique ! Même si j'ai tendance, comme plusieurs autres chanteurs à préférer l'eau végétale à l'eau sucrée. Mention spéciale pour Jeanba, qui m'a permis de me retrouver cité dans une thèse d'histoire de l'art, au côté de noms aussi prestigieux que Cédric Villani... Merci à ceux qui étaient

à Paris ce jour-là et qui ont pu se libérer pour ma soutenance : Antoine et Bénédicte (qui nous reçoivent toujours à bouteilles ouvertes pour les libations de fin de saison), Thibault et Emma, Hervé, Thierry J., Elisabeth, Daniel (merci à tous les deux pour la BD, et merci pour les entrées au Bourget !). Je n'oublie pas tous ceux qui n'ont pas pu venir mais qui m'ont envoyé des petits messages d'Italie (Thierry V., madame Marnier) ou d'ailleurs (Sylvie "die Kirchenmaus", Anne, Luc, Rudolf, Denis, Sandrine, Florence et Philippe...).

Je dois bien sûr remercier aussi tous mes amis d'ici ou d'ailleurs qui m'ont soutenu au cours de cette période pas toujours très drôle. Merci donc à Lego, Morgane, Pierrick et Marie, le gang d'Antony, pour leur hospitalité après les nombreuses soirées passées à refaire le monde jusqu'à trop tard pour le dernier RER, les raclettes du mois de juin au Cahors, la fête du vin et du fromage, les soirées nanar : Kung Fury ou Iron Sky 2 ? Merci à PG et Nat pour les "soirées sous les rosiers", sans oublier Matthieu, Thomas et Xav', le reste de notre équipe pour les virées champenoises. J'en profite pour remercier également Astrid et Alexandre, mes fournisseurs en champagnes et autres nectars qui nous ont permis d'organiser de superbes visites et de grandes dégustations, idéales pour se changer les idées. Merci à Alif, Francis, Thibault et Mael pour les diners bien accompagnés et les soirées whisky (ainsi qu'un petit weekend très agréable en bords de Loire). Merci à Floflo et Mélanie, mes aînés dans le doctorat : Floflo, vive le van der Waals, avec la bonne composition chimique. Et merci d'ailleurs à tes parents pour leur accueil lors de notre séjour à Cannes pour le festival, foi de Sidi van Cetera ! Je n'oublie pas mes autres aînés dans le doctorat : Jess, tovarich Momo, Da et Adrien. By the way, projet N2 is still alive! On va bien finir par comprendre ce qui se passe dans ce tube. Merci à PH Vendetta et Lucie pour les soirées de safari au début de ma thèse : nous avons fait grand œuvre pour la salubrité publique. Merci à mon Romanone Conti, tes retours à Paris ont toujours été l'occasion de promenades nocturnes réjouissantes, à tenter d'éviter les bières trop coupées tout en devisant de choses et d'autres. Merci à Nico et Adeline pour toutes ces soirées notamment en été sur les berges du canal Saint-Martin, et pour m'avoir fait découvrir *Lie to me*. Un grand merci à toute l'équipe de Partout/Ailleurs pour les picnics en bord de Seine, soirées ciné, les verres au Board: Jérémy, Sandrine, Laurine et Nico, Émeric et Amélie, Olivia/Jeanine, Jehanne et Rémy. On a toujours été très mal reçus à Chartrettes (merci Fred et Evelyne), je ne comprends vraiment pas pourquoi on s'obstine à y retourner ! Au fait, pourquoi s'embêter à prendre le train pour aller à Strasbourg quand on peut prendre l'avion pour se retrouver à La Réunion ? Merci à ce propos à Jean et Marie pour leur accueil pendant ces vacances royales à la Réunion : j'étais très heureux de pouvoir passer une grosse semaine avec vous et ma filleule (Eve, ton parrain pense à toi) ! J'ai aussi une pensée pour Evelyne et Marie-Alyette, cette thèse est aussi dédiée à mon grand-père spirituel malgré le peu de mécanique quantique qui y est écrit. Merci à Dougui pour les barbecues avec toute l'équipe du Petit Palais, où

l'on parle français, anglais, espagnol et même quelques mots de russe ! Niels, ma personne remercie grandement le buddyovich pour toutes ces leçons de choses et séances cinématographiques de Große Qualität, avec des films aussi merveilleux que Véloce et Vénère ou la Rando des Étoiles, et autres péripéties de nos amis Paul Le Marcheur (RIP), l'Étalon des Forêts, Arnaud Noirnègre et Vincent Gasoline. . . J'aurais dû venir vous rendre visite pendant votre séjour australien, nous trouverons bien une occasion de retourner dans ces contrées.

Speaking of travels, these three years were marked by several weddings that gave me perfect opportunities to return to Asia. Thanks first of all to François et Jasmine de m'avoir invité et ainsi donné l'occasion de revoir Taipei et votre petit Louis qui n'est plus si petit ! J'en ai profité pour revenir à Singapour, où j'ai retrouvé d'autres futurs mariés. Many thanks to Alex and Susan for their welcoming and comfortable couch in SG, and much more for this wonderful stay in Suzhou (city of gardens, for sure) and Shanghai with their families (la bise à Bob, Bernie et Caro)! My week in London with you after the viva was the perfect vacation to relax. I shall not forget Milord Nikhil, friend and flatmate from our time in SG, who invited me to a magical journey throughout Incredible India! My time in Jaipur was really great thanks to Jagdish who helped organize all my taxi, the light of Rajasthan over the forts of Amer, Jaigarh or Nahargarh is a sight to behold! The private visits of Taj Mahal and Fatehpur Sikri are these kinds of moment that I shall remember for a very long time. . . I am deeply in your debt, Milord! To think it all started with bloody Johnny and hole drilling at 8am on a Saturday morning by Chinese Garden. . . Je n'oublie pas mister Louen (yes, I have done my exposé, and I have been told it was rather successful) et ces petits weekends fort sympathiques passés à Dublin. J'aurais vraiment voulu vous rejoindre pour vous expliquer les différences de style entre Angkor Wat, Bayon et Preah Khan. . . Au moins me consolé-je en pensant que mes notes de voyage en Asie du Sud-Est ont pu vous servir un peu au cours de vos pérégrinations. Parfois, on réalise lors de ces voyages que le monde est vraiment tout petit : ainsi ai-je retrouvé Steven Kleinveld et Gilbert Rogé, mes anciens maîtres de stage chez Dassault Aviation, respectivement à Atlanta (conf' oblige) et à Londres sur le parvis de Saint-Paul (ce qui est déjà plus inattendu). J'en profite pour les remercier de m'avoir formé voici déjà quelques années à la programmation, et pour leurs encouragements faute d'avoir pu venir assister à la soutenance. Enfin un grand merci à Quentin, mon compagnon de thèse de l'autre côté de l'Atlantique (tu m'as battu avec tes papiers¹, my best to T.J. . .), pour cette semaine géniale passée à Pittsburgh au retour de la conf' AIAA à Atlanta, cela m'a rappelé nos tribulations new-yorkaises voici quelques années. Encore toutes my congratulations to Jenny et toi, j'ai bien noté votre invitation and rest assured I will come and visit you in NYC as soon as you get settled! We do have to celebrate, j'apporte le champagne ! On pourra causer encore une fois jusqu'à des heures indues à

¹Hinton et al. (2015); Sun et al. (2015)

propos des œuvres de Philip K. Dick et Frank Herbert tout en planifiant nos activités pour le prochain millénaire : "*Bi-la Kaifa*" ou presque. . .

Je n'ai pas toujours eu besoin d'aller à l'autre bout du monde pour fêter des beaux mariages. Merci à Maxime et Marie-Cécile de m'avoir invité pour leur mariage dans la région lyonnaise, dommage que je n'ai pas eu le temps de venir vous voir au Pays Basque cet été. Je vais pouvoir me rattraper maintenant que vous voilà de retour à Paris avec la petite Émilie ! Hiero et Jenny m'ont permis de découvrir Toulouse, et je suis particulièrement reconnaissant à Hiero d'avoir bien voulu prendre une flûte pour trinquer avec moi ! Ce weekend dans le vrai Sud a été l'occasion de revoir Giuliano, je dois toujours vous rendre visite amico mio pour voir votre petite Selena ! Merci aussi à Clémence et Vincent pour ce mariage sur la côte d'émeraude, qui m'a permis de retrouver les autres Fénéloniens : FX, Typhen (perdue au pays des lamas et bientôt au Panama), Alex (thanks for these nice weekends by your place in Villers, old sport!). I've never heard anything more stupid than 'out of sight, out of mind': my not writing that often does certainly not mean I have forgotten my friends, however far away they may be! This holds obviously for Swadhin, my very mean brother from BNL now in Halifax, and for John and Mary whom I was delighted to see again during my last trip to NYC!

Je dois aussi remercier les gens qui sont venus parfois de très loin pour ma soutenance et que je n'ai pas encore cités: Flavien (venu tout exprès de Toulouse, mais sans lifter), Matthieu (Sama de passage depuis Hanoi, il faut que je vienne vous voir !), Jean-Louis (qui a supporté mon exposé en anglais et que je n'ai même pas vu entrer, honte à moi), Taupa, Antony (qui représentait dignement tous mes camarades kyukyu du CEPESJA, Alexis, Tonio, Hugues, JP, PVD dont le buffet ne m'a pas déçu, Alif et tous les autres, cela fait longtemps que je n'ai pas sorti mon shinai mais je ne désespère pas de revenir). J'étais très content de voir aussi ce jour-là mes professeures de prépa, Madame Yvon et Madame Allano, venues également représenter Mademoiselle Brunet. C'est aussi grâce à vous que j'en suis arrivé là. Merci enfin à mes collègues de bureau à Centrale pour leur accueil ces derniers mois et pour être venus m'écouter causer de plasma: Maxime (qui est depuis retourné dans son cercueil, en attendant de finir son manuscrit), Manuel (l'homme aux costards, d'un calme olympien sauf peut-être en revenant de réunion), Macole (qui les supporte tous depuis plus de trois ans) et Thomas (notre éternel stagiaire, grand adepte de la guerre des NERF, quoi qu'il souffre déjà bien de PhD²).

Il me reste à remercier les deux personnes sans qui cette thèse n'aurait jamais eu lieu : Christophe Laux, mon directeur de thèse à Centrale, et Paul-Quentin Elias, mon encadrant à l'ONERA. Ils n'ont pas ménagé leur peine, notamment dans les derniers jours où nos répétitions de soutenance ont duré jusqu'à fort tard.

²Permanent head Damage

Christophe, merci de m'avoir fait découvrir le monde passionnant des plasmas, d'où l'on peut vraiment toucher à tous les domaines de la physique. Cela fait maintenant 7 ans que nous avons commencé à travailler ensemble depuis ce projet innovation mené avec Air Liquide. Puis il y a eu l'éternel projet N2, que je me retrouve aujourd'hui à encadrer : c'est à ce moment-là que l'idée de poursuivre en thèse a commencé à se préciser. Merci pour tes conseils, ta bonne humeur (notre première réunion à l'ONERA en février 2012 restera marquée d'une pierre blanche comme le seul jour où je t'ai vu t'énerver au point d'être grossier ! Encore que, depuis lors, un certain rapport...) et ton énergie jusqu'à des heures avancées lors des réunions qu'on réussissait à caser entre le deuxième et le troisième agenda. J'en suis toujours ressorti avec de nouvelles pistes à explorer.

Paul-Quentin, cette thèse te doit beaucoup. Merci pour ton énergie et ton enthousiasme qui m'ont plusieurs fois permis de remonter le creux de la vague. Ton expérience m'a été d'une grande aide pour toutes les mesures que nous avons eu à réaliser. Et je ne parle pas de ta maîtrise de *Python*, tu finiras bien par faire comprendre à Denis et Christophe que l'univers est codé en *Python* et tourne sur un Raspberry Pi ! Désolé de t'avoir déçu avec mes courbes de modèle superposées aux données, promis je bricolerais un bouton "ADD BAD DATAPOINT"... Et j'éviterai de faire du Shakespeare dans mes articles: "*Thou sodden-witted lord! thou hast no more brain than I have in mine elbows.*³ *More of your conversation would infect my brain.*⁴". Ces trois ans et un peu plus à partager ton bureau ont été très formateurs, merci pour tes qualités humaines et scientifiques qui ne sont plus à démontrer. Profite bien du soleil de Californie, en espérant que vous ayez trouvé des revendeurs d'Ayala !

Pour mettre un point final à ce roman, je remercie toute ma famille: Bouli et Amatxi venus tout exprès de Bordeaux, Zazie et les jumelles (qui m'ont appelé la veille du jour J), Anne-Charlotte et Sylvain (pour les nombreuses soirées chez eux toujours super sympa), Marie-Amélie qui a réussi à passer, Jean et Marie (qui ont loupé de peu la soutenance), GrandMaman (partie trouver refuge à Saint-Jean de Luz), Sire mon frère qui a bien voulu me faire l'honneur de sa présence ("Zorro est arrivé ! Un peu en retard..."). Et enfin mes parents qui m'ont toujours soutenu et m'ont donné la curiosité et la volonté d'aller au bout de cette aventure.

³Troilus and Cressida (2.1.41)

⁴Coriolanus (2.1.91)

Abstract

In this study, we investigate the mechanical effects generated by pulsed surface discharges and their efficiency as an actuator. Using a specific electrode configuration, it is possible to create a short-lived, pulsed, rectilinear plasma channel and to heat it up rapidly (several Joules in less than a microsecond) through Joule heating. This fast energy deposition causes the formation of shock waves that can then interact with the surrounding flow.

We study the electrical behavior of the pulsed surface discharge to assess the energy deposited in the plasma channel through Joule heating. To do so, we perform a parametric study on the circuit configuration and identify the main parameters driving the discharge dynamics. Several resistance models are implemented in a numerical description of the electrical circuit and their predictions of the current and deposited energy are compared with experimental measurements.

Spectroscopic measurements in different circuit configurations give access to some of the plasma properties such as the electron number density that can reach values up to $2 \times 10^{18} \text{ cm}^{-3}$. Fast imaging also gives insight into the plasma channel radius. The shock waves generated by the pulsed surface discharge in different circuit configurations are visualized through Schlieren imaging. These shock waves generate an impulse that increases linearly with the energy deposited in the discharge. We develop a shock model to describe the shock trajectory and to compute the impulse imparted by the pulsed surface discharge. The model is in good agreement with our measurements and the pulsed surface discharge is found to have a mechanical efficiency of 0.12 mNs/J for our setup configuration. We conclude this study by comparing the proposed pulsed surface discharge actuator with other common designs and offer some directions for future studies.

Keywords: plasma actuator, pulsed surface discharge, non-linear resistance, optical emission spectroscopy, Schlieren imaging, electron number density, shock waves, mechanical efficiency.

Résumé

Un aéronef est généralement conçu pour des conditions de vol spécifiques et peut voir ses performances dégradées en dehors, par exemple lors des phases d'approche au décollage ou à l'atterrissage. Le contrôle d'écoulement tente donc d'améliorer les caractéristiques de vol (portance, traînée . . .) en manipulant l'écoulement autour de l'avion. Ceci peut aussi aider au contrôle d'attitude et au guidage d'engins hypersoniques. En effet, les technologies classiques de guidage ne sont alors plus applicables, notamment du fait de leur long temps de réponse (de l'ordre de quelques dizaines de millisecondes). Il faut donc avoir recours à d'autres moyens pour agir sur l'écoulement.

Le contrôle d'écoulement peut être passif ou actif. Le contrôle passif utilise de petits obstacles (comme les générateurs de vortex ou les riblets) pour modifier localement l'écoulement. Dans le cas du contrôle actif, un actionneur transforme l'énergie qui lui est fournie en une action mécanique ou thermique sur l'écoulement pour obtenir l'effet escompté (retard de transition ou de détachement). Plusieurs types d'actionneurs existent, dont les actionneurs plasma. De tels actionneurs sans pièces mobiles peuvent être installés directement sur les ailes. Un actionneur plasma ionise le gaz dans l'écoulement afin de le manipuler au moyen de champs électromagnétiques. L'ionisation peut être localisée en surface ou dans un petit volume, et peut être déclenchée au moyen de haute tension, de micro-ondes ou de laser focalisé par exemple. Le plasma ainsi créé permet alors d'accélérer ou de chauffer localement l'écoulement. De tels actionneurs plasma peuvent avoir des fréquences d'action plus élevées que leurs équivalents mécaniques ou fluidiques. Différents modèles d'actionneurs plasma ont été développés pour diverses applications. Les actionneurs à décharge barrière diélectrique par exemple, utilisent un courant alternatif pour créer un vent ionique et accélérer l'écoulement: ceci permet un contrôle précis de la couche limite et de ses interactions avec l'écoulement principal et permet par exemple de retarder le décollement (et donc d'augmenter l'angle de décrochage). Toutefois, les actionneurs à décharge barrière diélectrique ne peuvent créer des vents ioniques que de l'ordre de quelques mètres par seconde; de plus hautes tensions sont requises pour atteindre des vitesses plus élevées; au-delà d'une tension seuil, la décharge filamente, ce qui réduit son efficacité en termes de production de vent ionique. Les filaments peuvent même évoluer en étincelles,

au risque d'endommager l'actionneur. Pour les hautes vitesses, un autre exemple d'actionneur plasma est le sparkjet: une étincelle est créée dans une petite cavité (au moyen d'impulsions de courant) et chauffe rapidement le gaz qui s'y trouve. Le gaz chaud crée alors un jet synthétique qui peut interagir avec l'écoulement, même à haute vitesse. Le rechargement de la cavité en gaz (provenant de l'écoulement) limite néanmoins la fréquence d'action du sparkjet à quelques kilohertz; l'étincelle pulsée érode également les électrodes dans la cavité.

La décharge de surface linéaire à laquelle nous nous intéressons dans cette étude représente un nouveau type d'actionneur plasma. Une géométrie particulière d'électrodes permet de créer de manière pulsée un filament rectiligne de plasma et de le chauffer très rapidement par effet Joule (à raison de plusieurs Joules en moins d'une microseconde). Ce chauffage rapide entraîne la formation d'ondes de choc qui peuvent interagir avec l'écoulement ambiant. Nous étudions ici les effets mécaniques de la décharge de surface et son efficacité en tant qu'actionneur. Nous tentons donc de répondre à cette question: disposant d'une certaine quantité d'énergie électrique, quelle impulsion la décharge de surface peut-elle communiquer à l'écoulement ?

Nous avons tout d'abord analysé le comportement électrique de la décharge de surface dans diverses configurations de circuit, en changeant la capacité, la tension de charge, l'inductance ou la longueur de la décharge. Les courbes de courant et de tension présentent deux phases distinctes: une phase de propagation (correspondant à la formation du filament de plasma) et une phase d'arc (au cours de laquelle l'énergie est déposée dans le canal). La phase de propagation est pilotée par les lois de Toepler, avec une vitesse de propagation proportionnelle à la tension de charge. La plus grande partie de l'énergie électrique initialement stockée dans les condensateurs est déposée dans la décharge au cours de la phase d'arc. La durée du dépôt d'énergie dans la décharge dépend de la configuration du circuit et de l'énergie stockée initialement dans les condensateurs. Nous avons développé un modèle électrique du courant mesuré dans la décharge pendant la phase d'arc. Si ce courant présente bien des oscillations, ces dernières ne peuvent être décrites correctement avec la solution classique de l'oscillateur amorti pour le circuit RLC. Sur la base d'études antérieures, nous avons donc décrit le filament de plasma par différents modèles de résistance non-linéaire évoluant au cours du temps. Ces différents modèles (Rompe-Weizel, Vlastós, Toepler et Braginskii) ont été fittés aux données expérimentales. Tous ces modèles (à l'exception de celui de Toepler) sont basés sur des considérations théoriques et sont caractérisés par un paramètre propre que nous comparons à nos fits. Les modèles décrivent tous une résistance qui diminue très rapidement avant d'atteindre une valeur constante. Le modèle de Rompe-Weizel est le plus proche de nos données expérimentales, particulièrement pendant les 300 premières nanosecondes de la phase d'arc.

Le modèle de Rompe-Weizel suppose que la densité électronique augmente pendant la phase d'arc. Nous avons donc étudié la densité électronique dans la décharge par la spectroscopie résolue en temps. Nous avons fitté avec un profil de Voigt la raie H_α dont les élargissements et les décalages ont été abondamment détaillés. Nous avons ainsi obtenu l'évolution au cours du temps de la densité électronique dans le filament de la décharge. Dans un circuit à basse inductance, la densité électronique augmente exponentiellement jusqu'à des valeurs de l'ordre de $2 \times 10^{18} \text{ cm}^{-3}$ pendant le pic de puissance de la phase d'arc. Cette croissance exponentielle est cohérente avec le modèle de Rompe-Weizel, qui fait l'hypothèse que l'énergie déposée dans la décharge sert à ioniser le gaz. Après ce pic de puissance, la densité chute comme le carré inverse du temps. Nous avons également obtenu des profils transverses de la densité électronique qui présentent les mêmes tendances (croissance exponentielle suivie d'une chute en carré inverse). Nous avons d'autre part mesuré le rayon de la décharge par imagerie rapide: le rayon croît linéairement aussi bien au cours du temps pendant le pic de puissance qu'après (quoique plus lentement). A partir de ces mesures, nous avons calculé une résistance pour la décharge qui est cohérente avec nos mesures et avec le modèle de Rompe-Weizel, corroborant ainsi notre choix d'utiliser ce modèle pour décrire le comportement de la décharge de surface dans un circuit électrique. Dans un circuit à haute inductance, nos mesures spectroscopiques montrent que la densité électronique présente des oscillations qui coïncident avec le dépôt d'énergie dans la décharge. Dans un tel circuit oscillant, plusieurs pics successifs chauffent la décharge à tour de rôle. La densité électronique commence par augmenter jusqu'aux environs de $6 \times 10^{17} \text{ cm}^{-3}$ pendant le premier pic de puissance avant de diminuer. Le pic de puissance suivant relance le processus d'ionisation, ce qui entraîne une légère augmentation de la densité électronique. Des oscillations similaires sont également visibles sur l'évolution du rayon de la décharge.

Le chauffage rapide du filament de plasma entraîne la formation d'ondes de choc. Ces ondes de choc génèrent une impulsion mécanique que nous mesurons avec une balance de moment. L'impulsion créée par la décharge de surface est proportionnelle à l'énergie déposée dans la décharge, pour un circuit à basse inductance. Dans un circuit à haute inductance toutefois, l'impulsion est beaucoup plus faible. Pour comprendre cette disparité, nous avons visualisé par imagerie Schlieren les ondes de choc créées par la décharge de surface. Dans un circuit à basse inductance, une seule onde de choc cylindrique est émise, tandis que plusieurs chocs imbriqués sont créés dans des circuits à haute inductance. Nous avons enregistré la trajectoire du choc dans ces différentes configurations de circuit. Aux temps longs, le choc se propage à vitesse constante (faiblement supersonique) quelle que soit l'énergie déposée dans la décharge. L'ajout d'énergie n'affecte que la phase initiale, quand la propagation du choc peut être décrite avec le modèle de Taylor-Sedov pour les chocs forts. Pour décrire cette transition entre choc fort et choc faible, nous avons utilisé un modèle de

piston qui donne la trajectoire du choc en fonction du temps et de l'énergie initialement déposée dans la décharge. Notre modèle prédit bien la trajectoire du choc (dans un circuit à basse inductance) quand nous considérons que 30% de l'énergie déposée dans la décharge sert à lancer le choc. Ce résultat est en accord avec d'autres expériences sur diverses configurations de décharges. Pour calculer l'impulsion créée par la décharge de surface, nous avons pris un profil de type Friedlander pour la pression derrière le choc, et obtenu une formule analytique qui donne l'impulsion en fonction de l'énergie et des caractéristiques du gaz. Les valeurs calculées avec cette formule sont en accord avec nos mesures à 2% près, et nous obtenons une efficacité mécanique pour la décharge de surface de l'ordre de 0.12 mNs/J pour notre configuration d'étude.

Nous souhaitons par ailleurs étudier l'intérêt potentiel de la décharge de surface comme actionneur plasma. Nous la comparons à d'autres type d'actionneurs. La décharge de surface étant par nature pulsée, nous la comparons tout d'abord à un autre actionneur pulsé, le sparkjet. Si celui-ci produit une impulsion proportionnelle (en première approche) à la racine de l'énergie apportée, la décharge de surface produit une impulsion qui est directement proportionnelle à l'énergie apportée. Le sparkjet est par ailleurs limité à quelques kHz en fréquence d'action, du fait du temps nécessaire au rechargement en gaz de la cavité. La décharge de surface se produisant directement à l'air libre, le circuit électrique et l'alimentation peuvent être ajustés afin d'atteindre des fréquences plus élevées. Néanmoins, les chocs imbriqués, tels qu'observés dans les configurations à haute inductance, limitent l'efficacité mécanique de la décharge. Ceci est probablement dû à la présence d'un canal de gaz chaud et peu dense qui reste au dessus de la surface après le dépôt d'énergie, d'où une limite de la fréquence d'action à quelques centaines de Hz (en absence d'écoulement). Si toutefois la décharge est placée dans un écoulement, le canal de gaz chaud est balayé après le dépôt d'énergie, et la décharge pourrait alors être utilisée à des fréquences de plusieurs dizaines de kHz.

Quand la décharge est utilisée de manière répétitive, elle crée une force moyenne qui peut être comparée à la poussée créée par les actionneurs à décharge barrière diélectrique (DBD). Il faut tout d'abord noter que, si la plupart des actionneurs DBD créent une force tangentielle, la décharge de surface crée une force normale à la surface. Nous avons mesuré une efficacité mécanique de 0.12 mNs/J pour la décharge de surface (dans notre configuration d'étude), tandis que les actionneurs DBD ont une efficacité allant de 0.10 mNs/J à 0.60 mNs/J selon la géométrie et le mode de fonctionnement de l'actionneur. Un actionneur à décharge de surface a donc besoin de plus de puissance moyenne qu'un actionneur DBD pour produire une force équivalente. Toutefois, la décharge de surface n'étant pas limitée comme la DBD par des phénomènes de saturation ou de passage à l'arc, un actionneur à décharge de surface peut créer des forces plus importantes que son équivalent DBD.

L'utilisation à haute fréquence des décharges de surface peut toutefois endommager les matériaux.

Pour des études ultérieures, nous encourageons vivement l'utilisation de commutateurs solides pour s'affranchir du jitter inhérent aux éclateurs à gaz (qui doit être corrigé manuellement et ralentit d'autant la prise de mesure pour les diagnostics résolus en temps). D'autre part, les commutateurs solides sont plus compacts que les éclateurs à gaz (d'où un encombrement limité), et peuvent être utilisés à des fréquences plus élevées.

Nous nous sommes principalement intéressés à la phase d'arc de la décharge de surface : nous n'avons donc pas étudié en détail la phase de propagation ou le rôle du matériau diélectrique à la surface duquel se produit la décharge de surface. Ce matériau est d'ailleurs soumis à un important stress mécanique et thermique par la décharge, ce qui nous a forcé à le changer fréquemment après quelques centaines d'impulsions. Ceci constitue un problème qui doit être résolu avant de pouvoir déployer un actionneur à décharge de surface sur un engin volant.

Toutes les expériences sur la décharge de surface présentées ici ont été réalisées en absence d'écoulement, à pression ambiante. Des tests supplémentaires dans des conditions de vol plus réalistes sont donc nécessaires pour étudier le comportement de la décharge et des ondes de chocs créées. Notre modèle notamment prédit une impulsion indépendante de l'altitude, contrairement au sparkjet dont l'efficacité diminue avec l'altitude. D'autre part, certains travaux récents sur les DBD indiquent que les petites perturbations thermiques peuvent avoir un effet sur la couche limite, il serait donc opportun d'évaluer l'impact du canal de gaz chaud laissé par la décharge de surface sur un écoulement.

Contents

Abstract	xiii
Résumé	xv
1 Introduction	1
2 Overview of plasma actuation techniques	5
2.1 Plasma actuation	5
2.2 Pulsed Surface Discharge	12
3 Experimental setups and methods	17
3.1 Actuator principle	17
3.2 Electrical setup for discharge creation	18
3.3 Optical emission spectroscopy	21
3.4 Schlieren imaging	26
3.5 Impulse measurement	27
3.6 Conclusion	33
4 Development of an electric model for the arc phase	35
4.1 Electrical characterization of the discharge	36
4.2 Model of the arc phase	43
4.3 Comparison with experimental data	50
4.4 Conclusion	61
5 Optical and spectroscopic analysis of the pulsed surface discharge	63
5.1 Light intensity and discharge radius	63
5.2 Study of the broadening of the H_α line	69
5.3 Plasma characteristics	78
5.4 Conclusion	86
6 Mechanical effects of the surface discharge	89
6.1 Experimental study of the mechanical effects	90
6.2 Development a shock model	95

6.3	Comparison with experimental measures	101
6.4	Conclusion	109
7	Conclusion	113
7.1	Main results of this study	113
7.2	Comparison with other plasma actuators	115
7.3	Direction for further studies	116
A	Propagation of uncertainty	121
A.1	Principle	121
A.2	Examples of computation	122
B	The RLC circuit: general solutions	125
B.1	Governing equations for the RLC circuit	125
B.2	Over-damped circuit	126
B.3	Under-damped circuit	126
B.4	Complete circuit	127
C	Detailed calculations for the H_α multiplet	129
C.1	Average spectroscopic quantities	129
C.2	Computation of the resonant broadening	131
C.3	Computation of the van der Waals broadening	132
D	Self-similar theory for strong shocks and its extensions to low Mach numbers	135
D.1	Taylor-Sedov theory for strong shocks	135
D.2	Extension to weaker shocks	138
E	Computation of the linear impulse generated by the surface discharge	141
E.1	Computation method	141
E.2	Asymptotic approximation	142
E.3	First order approximation	144
	References	157

List of Tables

2.1	General actuator types and their characteristics.	12
4.1	Test cases series for measurements.	36
4.2	Joule efficiency χ_J for varying circuit capacitance at fixed discharge length $l = 95$ mm and circuit inductance $L = 0.8$ μ H. . .	39
4.3	Joule efficiency χ_J for varying discharge length at fixed circuit inductance $L = 0.8$ μ H and circuit capacitance $C = 5.8$ nF. . .	39
4.4	Joule efficiency χ_J for varying circuit inductance at fixed discharge length $l = 95$ mm and circuit capacitance $C = 5.8$ nF. . .	39
4.5	Propagation velocity parameters obtained from data fit and given by Toepler's law.	42
4.6	Expressions of R_0 and \tilde{A} and values for the m and n parameters for the different resistance models.	49
4.7	Mean values and standard deviation of the reconstruction error for the various resistance models in low inductance circuits. . .	54
4.8	Mean values and standard deviation of the reconstruction error for the various resistance models in high inductance circuits. . .	54
4.9	Mean value and standard deviation of the parameter A_0 for the various models.	55
4.10	Mean value and standard deviation of the parameter k for the various models and theoretical expectation.	55
5.1	Channel expansion velocity during the return stroke phase. . .	69
5.2	Components of the Balmer α ($3 \rightarrow 2$) transition multiplet and their spectroscopic properties.	73
5.3	Components of the Lyman α ($2 \rightarrow 1$) transition doublet and their spectroscopic properties.	73
5.4	Components of the Lyman β ($3 \rightarrow 1$) transition doublet and their spectroscopic properties.	73
6.1	Mechanical efficiency of the surface discharge for various setup configurations.	91
6.2	Air characteristics.	106
6.3	Joule energy fraction deposited per peak.	108

7.1	Comparison of three plasma actuator candidates.	117
C.1	Components of the Balmer α ($3 \rightarrow 2$) transition multiplet and their spectroscopic properties.	130

List of Figures

2.1.1 Corona actuator setup.	7
2.1.2 Single dielectric barrier discharge actuator.	7
2.1.3 Flow reattachment using an array of DBD actuators.	8
2.1.4 Sliding dielectric barrier discharge	8
2.1.5 Comparison of ionic wind profile for the DBD and SDBD actuators.	8
2.1.6 Circular dielectric barrier discharge.	9
2.1.7 Visualisation of various DBD actuators in operation.	9
2.1.8 Sparkjet actuation cycle.	10
2.1.9 Ramjet actuation cycle.	10
2.1.10 Visualization of the shock wave disturbance created by a surface direct current arc in a Mach 3 flow.	11
2.1.11 Setup of multiple LAFPA for azimuthal actuation on a jet.	11
2.1.12 Example of azimuthal instabilities generated in a jet.	12
2.2.1 Design of planar pulsed surface discharge.	13
2.2.2 Channel structure of the pulsed sliding discharge observed at different operating voltage and gas pressure.	13
2.2.3 Ridge structure on the dielectric layer to impose the location of plasma channels.	14
2.2.4 Setup used to create Lichtenberg figures.	14
2.2.5 Guiding of the pulsed surface discharge	15
3.1.1 Top and side view of the pulsed surface discharge electrodes configuration.	18
3.2.1 Actuator setup.	19
3.2.2 Complete electrical circuit.	20
3.2.3 Current and voltage measured on three different discharges for the same conditions.	20
3.3.1 Spectroscopy setup used for time-resolved measurements on the discharge.	21
3.3.2 Triggering sequence of the optical measurement setup.	22
3.3.3 Raw discharge spectra at various instants.	23
3.3.4 Intensity profile of the measured laser line.	24

3.3.5 Spectrum of the discharge before and after intensity correction and slit function deconvolution.	26
3.4.1 Schlieren setup used to visualize the shock wave along the discharge axis.	27
3.4.2 Shock wave visualization along the discharge axis.	28
3.4.3 Schlieren setup used to visualize the shock wave from the side of the discharge axis.	28
3.4.4 Schlieren setup for shock wave visualization.	29
3.4.5 Shock wave visualization across the discharge axis.	29
3.5.1 Impulse measurement setup.	30
3.5.2 Voltage oscillations of the torque balance.	31
3.5.3 Calibration of the torque balance.	32
4.1.1 Current and voltage measured on a pulsed surface discharge.	37
4.1.2 Energy deposited in the discharge as a function of the initial energy stored in the capacitors for various circuit configurations.	38
4.1.3 Definition of the characteristic times t_0 , t_{RS} and t_F	40
4.1.4 Total duration τ_D as a function of the energy stored in the capacitors.	40
4.1.5 Propagation duration τ_P and velocity v as a function of the initial energy and of the capacitors voltage.	41
4.1.6 Return stroke duration τ_{RS} as a function of of the initial energy and of the capacitors voltage, for a discharge of length 95 mm.	42
4.2.1 Equivalent circuit during the return stroke phase.	43
4.2.2 Normalized current measured in the plasma channel.	44
4.2.3 Current fit by damped sinusoidal waveform.	45
4.3.1 Measured current and reconstruction according to the various model in a low inductance circuit.	52
4.3.2 Measured current and reconstruction according to the various model in a high inductance circuit.	53
4.3.3 Resistance evolution predicted by the various models.	53
4.3.4 Resistance prefactor in the Rompe-Weizel model as a function of the linear energy.	56
4.3.5 Resistance prefactor in the Vlastós model as a function of the linear energy.	57
4.3.6 Resistance prefactor in the Toepler model as a function of the linear energy.	57
4.3.7 Resistance prefactor in the Braginskii model as a function of the linear energy.	58
4.3.8 Comparison of the plasma resistance computed from electrical data and predicted by the various models.	59
4.3.9 Plasma conductivity in the different models at the end of the return stroke.	60

5.1.1 Imaging of the light-emitting plasma channel.	64
5.1.2 Light intensity emitted by the discharge and corresponding power evolution in a low inductance circuit.	65
5.1.3 Light intensity emitted by the discharge in a low inductance circuit for increasing capacitance charging voltages.	65
5.1.4 Light intensity emitted by the discharge and corresponding power evolution in a high inductance circuit.	66
5.1.5 Intensity profile across the discharge at different times in a high inductance circuit.	67
5.1.6 Intensity profile across the discharge at different times in a low inductance circuit.	68
5.1.7 Channel radius evolution with time.	68
5.1.8 Channel radius evolution in a high inductance circuit.	69
5.1.9 Channel expansion velocity at the early stages as a function of the energy deposited during the corresponding power peak.	69
5.2.1 Time-integrated spectra of the discharges for varying voltage.	70
5.2.2 Time-integrated spectra of the discharges for varying length.	70
5.2.3 Time-integrated spectra of the discharges for varying capacitance.	71
5.2.4 Time-integrated spectra of the discharges for varying voltage and inductance.	71
5.2.5 Spectra of the pulsed surface discharge in a low inductance circuit at different times.	76
5.2.6 Spectra of the pulsed surface discharge in a high inductance circuit at different times.	77
5.3.1 Sensitivity analysis of the fit accuracy with respect to the Lorentz parameter.	79
5.3.2 Electron number density and corresponding linear power deposition in the discharge.	81
5.3.3 Channel resistance computed from spectroscopic and electrical measurements.	82
5.3.4 Examples of misfit reconstruction.	83
5.3.5 Electron number density profile across the plasma channel transverse dimension at different times.	84
5.3.6 Compared time evolution of the average and central electron densities.	85
5.3.7 Temperature and pressure estimates in the plasma.	85
5.3.8 Electron number density and corresponding linear power deposition.	86
6.1.1 Linear impulse delivered by the pulsed surface discharge as a function of the linear energy deposited in the discharge	90
6.1.2 Shock wave generated in a low inductance circuit.	92
6.1.3 Schlieren image of the shock wave with a pierced dielectric	92

6.1.4 Shock wave generated by the discharge and seen from the front in low and high inductance circuits.	93
6.1.5 Shock wave generated by the discharge and seen from the side in low and high inductance circuits.	93
6.1.6 Shock wave generated in a low inductance circuit for various charging voltages and discharge lengths.	94
6.1.7 Shock trajectory recorded for various conditions in low high inductance circuits.	95
6.1.8 Evolution of the remnant channel radius for various conditions in a high inductance circuit.	95
6.2.1 Shock trajectories for different energies ϵ_S	98
6.2.2 Contour used for the computation of the linear impulse.	99
6.2.3 Shock structure after a conventional or nuclear weapon detonation and after the return stroke phase of the surface discharge.	100
6.3.1 Evolution of the shock wave radius with time compared with predictions from the various models.	102
6.3.2 Evolution of the shock wave radius with time compared with predictions from the Lee model.	103
6.3.3 Computed overpressure as a function of distance from the source at different instants.	103
6.3.4 Measured and computed impulse for a low inductance circuit.	104
6.3.5 Total impulse generated by a sparkjet and by a pulsed surface discharge at sea level and at an altitude of 30000 feet.	105
6.3.6 Schlieren images and predicted structure of the shock waves generated by the pulsed surface discharge in a high inductance circuit.	107
6.3.7 Impulse measured and computed for a high inductance circuit.	108
6.3.8 Long term Schlieren images of the hot gas channel.	109
7.1.1 Engineering approach for a plasma actuator.	115
7.3.1 Shock front generated by multiple pulsed surface discharges.	118
B.1.1 Standard RLC circuit.	125
B.4.1 Equivalent circuit during the return stroke phase of the pulsed surface discharge.	128
C.2.1 Multiplet structure of L_α , L_β and B_α	131
D.1.1 Dimensionless functions for pressure, density and flow velocity behind the shock as functions of the nondimensional similarity variable.	137
E.2.1 Evolution of the integral and its approximate form.	143
E.3.1 Evolution of the integral, its asymptotic approximation and its linear approximation.	145

Chapter 1

Introduction

An aircraft is usually optimized for specific flight conditions, and may show degraded performances out of these, during take-off and landing for instance. Flow control then aims at improving the flight characteristics (lift, drag, ...) by manipulating the flow around the aircraft. This may also help for attitude control and steering of hypersonic vehicles. Indeed, for hypersonic flight, the standard steering techniques are no longer applicable, partly because of their high response time (on the order of a few tens of milliseconds). Considering a standard size vehicle (about 20-meter long) moving at Mach 6, steering would start to be noticeable after the vehicle has moved several times its own length: a faster way to act on the flow is needed.

Flow control is either active or passive. Passive flow control uses small surface obstacles (such as vortex generators or riblets) to modify locally the flow. In the case of active flow control, an actuator takes some energy input and transforms it into a mechanical or thermal action on the flow, to obtain a specific effect (such as transition delay or detachment delay). Various designs and actuation methods exist, including plasma actuators. These devices, devoid of any moving parts, can be installed on existing flight structures such as wings. A plasma actuator ionizes the gas in the flow in order to act upon it with electromagnetic fields. Ionization takes place either near a surface or in a small volume, with high voltages, microwaves or focalized laser for instance. The plasma thus created is then used to inject momentum or heat into the flow. Such a plasma actuator may achieve higher actuation frequency than its mechanical or fluidic counterparts. Various designs for plasma actuators have been proposed and may serve different purposes. Dielectric barrier discharge actuators, for instance, use an alternating current to create an ionic wind and add extra momentum to the flow: this enables a fine control of the boundary layer and its interactions with the main flow, and allows for instance flow reattachment (which increases the stall angle) or transition delay. However dielectric barrier discharge actuators cannot generate ionic wind in excess of a few meters per second: higher velocities require higher voltages; above

a threshold voltage, the discharge forms localized filaments that decrease the overall ionic wind efficiency. These filaments further risk turning into sparks, thus damaging the setup. For high speed flows, another example of plasma actuator is the sparkjet: a spark is created in a small cavity (using a pulse power supply), and rapidly heats up the gas contained in the cavity. The heated gas then generates a synthetic jet that can interact with the flow even at high speeds. The cavity recovery cycle (time needed to refill the cavity with gas from the outer flow) limits the sparkjet actuation frequency to a few kilohertz; the pulsed spark created in the cavity also erodes the electrodes.

The pulsed surface discharge that will be considered in this study is a new candidate for plasma actuation. Using a specific electrode configuration, it is possible to create in a pulsed manner a short-lived rectilinear plasma channel and to heat it up very quickly (several Joules in less than a microsecond) through Joule heating. This fast energy deposition causes the formation of shock waves that can then interact with the surrounding flow. In this study, we investigate the mechanical effects generated by the pulsed surface discharge and the efficiency of such an actuator. Our goal is to answer the following question: given a certain amount of electrical energy, how much impulse can the pulsed surface discharge deliver to the flow?

First of all, we study the pulsed surface discharge electrical behavior to assess the energy deposition in the plasma channel through Joule heating. To do so, we perform a parametric study on the circuit configuration and identify the main driving parameters of the discharge dynamics. The pulsed surface discharge occurs in two steps: a propagation phase during which the plasma channel is created between the electrodes; and an arc phase during which most of the energy is deposited in this channel. We develop an electrical model for the current measured in the pulsed surface discharge during the arc phase. Several resistance models for the discharge are implemented in a numerical description of the electrical circuit and their predictions in terms of current and energy deposition are compared with experimental measurements.

The various resistance models used in our electrical description of the pulsed surface discharge are based on different assumptions on the plasma properties. These properties, such as the channel radius or the electron temperature and number density can be accessed optically. We then focus on the plasma channel itself, and perform fast imaging of the discharge and optical emission spectroscopy. The measured spectra in different circuit configurations give access to plasma properties such as the electron number density. Fast imaging also gives insight into the plasma channel radius evolution with time.

Having determined the energy deposition in the pulsed surface discharge, we turn to the mechanical effects of this fast energy deposition, in order to assess the mechanical efficiency of the pulsed surface discharge. The shock waves

generated by the pulsed surface discharge in different circuit configurations are visualized through Schlieren imaging. These shock waves generate an impulse that we relate to the energy deposited in the discharge. We develop a shock model to describe the shock trajectory and to compute the impulse imparted by the pulsed surface discharge as a function of the energy deposited in the discharge.

We conclude this study by comparing the proposed pulsed surface discharge actuator to other common designs and offer some directions for future studies.

Chapter 2

Overview of plasma actuation techniques

*There are more things in heaven and earth, Horatio,
Than are dreamt of in your philosophy.*

William Shakespeare, Hamlet, Act I, Scene 5

In this chapter, we will briefly recall the principles of flow actuation and survey some of the main plasma actuators under investigation today. We will then briefly describe the pulsed surface discharge that will be studied further to look for its potential as a plasma actuator

2.1 Plasma actuation

2.1.1 General principle of flow actuation

Flow actuation aims to modify the characteristics of an airflow, whether external (around a flying body) or internal (inside a jet engine for instance), for various purposes. On an aircraft, for instance, flaps are extended during take-off and landing phases to increase the wing lift, whereas spoilers serve to increase drag for emergency braking. Ailerons on another hand are used to steer the aircraft. In a jet engine, flow control can be used to tackle noise generation or increase the fuel mixing, hence the engine efficiency. Flow control can be achieved through two strategies ([Cattafesta III and Sheplak \(2011\)](#)): one can either try to change the flow straightforwardly (in a sort of brute forcing the flow), or take advantage of the flow structure itself and interact with instabilities or transitions (in a kind of resonant forcing).

Flow control can further be distinguished between passive and active ([Cattafesta III and Sheplak \(2011\)](#); [Caruana \(2010\)](#)). In passive flow control, no energy or momentum input is added into the flow: it only changes because of the physical presence of fixed material structures such as vortex generators or winglets.

Active flow control, on the contrary, uses controllable mechanical structures (Cattafesta III and Sheplak (2011)) or performs localized energy or momentum deposition in the flow (Moreau (2007); Bletzinger et al. (2005)). Thus an actuator can be described as a device that converts an input energy (electrical, chemical or mechanical) into mechanical (as a force per unit volume \mathbf{F} in equation (2.1.1a)) or thermal energy (as a heat source per unit volume Q in equation (2.1.1b)) in the flow:

$$\frac{\partial}{\partial t}(\rho\mathbf{u}) + \nabla(\rho\mathbf{u}\mathbf{u}) = \mu\nabla^2\mathbf{u} - \nabla P + \mathbf{F}, \quad (2.1.1a)$$

$$\frac{\partial}{\partial t}(\rho\epsilon) + \nabla(\rho\epsilon\mathbf{u}) = -\nabla q - \mathcal{P}\nabla\mathbf{u} + Q. \quad (2.1.1b)$$

Among the various types of actuators (Cattafesta III and Sheplak (2011)), plasma actuators are devices that locally ionize the gas in order to act on the flow with the use of electromagnetic fields (Shang (2001); Fomin et al. (2004); Braun et al. (2009)). Plasma actuators can be non-intrusive when not operating, as they add no extra obstacle to the flow. Moreover, they can be used in a continuous or pulsed mode up to high frequencies and can have a very fast response time. This response time is of particular interest for high velocity (supersonic or even hypersonic) applications (Shang et al. (2005); Wang et al. (2012)).

We will now briefly describe some of the main plasma actuators that have been studied worldwide.

2.1.2 Corona and glow discharges

The simplest possible actuator is the direct current (DC) corona discharge. The discharge is created between two electrodes placed on a dielectric surface and separated by an air gap of several centimeter (see figure 2.1.1). A high voltage (in the order of a few kV) is applied between the electrodes, which causes the formation of a weakly ionized plasma that drifts between the electrodes. This setup thus produces an ionic wind (in the order of a few m/s) along the dielectric surface (Moreau and Touchard (2008); Mestiri et al. (2010); Colas et al. (2010)). Given the rather low velocity of the ionic wind, the corona discharge actuator is of interest for momentum injection in low speed applications. Investigations at ONERA with a different setup (Elias et al. (2008)) show that the corona discharge can also be used for acoustic forcing of the boundary layer to stabilize bow shocks.

The glow discharge has also been investigated for faster (even supersonic) flow. In such cases, the glow discharge behaves as a heat source which modifies the oblique shock waves present in the flow (Parisse et al. (2009); Parisse and Lago (2013)). The glow discharge has also been considered at ONERA for bow shock modification (Elias et al. (2007)) in order to reduce drag. Energy deposition in the discharge effectively turns into a possible airspike that can change the

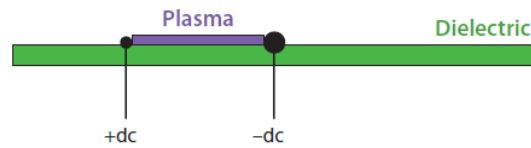


Figure 2.1.1: Corona actuator setup [figure 9a from (Cattafesta III and Sheplak (2011))].

flight characteristics of a blunt body (lift, drag, ...) (Anderson and Knight (2011); Erofeev et al. (2012); Soloviev et al. (2003)).

2.1.3 Dielectric Barrier Discharge

The dielectric barrier discharge (DBD) actuator is also based on momentum injection (Roth (2003); Corke et al. (2010); Seraudie et al. (2006); Thomas et al. (2009)). In the standard design (known as single dielectric barrier discharge and depicted in figure 2.1.2), one of the two electrodes is placed above the dielectric layer, and the other under the dielectric layer.

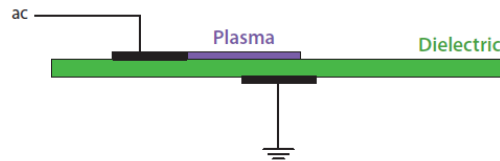


Figure 2.1.2: Single dielectric barrier discharge actuator [figure 9b from (Cattafesta III and Sheplak (2011))].

Most of the DBD actuators create a tangential ionic wind of low velocity (about 10 m/s). DBD actuators can be very useful to affect the boundary layer. A streamwise actuator will induce artificial vorticity (see figure 2.1.7), and can then be used as a controllable vortex generator, *e.g.* to suppress wingtip vortices that generate additional drag (Belson et al. (2012); Caruana (2010)). A streamlong actuator can modify the boundary layer transition from laminar to turbulent (in a resonant forcing on Tollmien-Schlichting waves (Duchmann et al. (2012))) and cause flow reattachment (Post and Corke (2004); Caruana (2010)) (see figure 2.1.3): this results in a net increase of the stall angle (Post and Corke (2004)) and has been considered for instance to improve the efficiency of wind turbines (Greenblatt et al. (2012)). DBD actuators have already been tested in flight (Duchmann et al. (2014)).

One could think that increasing the DBD driving voltage would increase the ionic wind: unfortunately, the actuator faces a problem of saturation (Durscher et al. (2012)), as too high a voltage leads to the formation of distinct current channels that might turn into arcs, which can be extremely damaging to the dielectric material. It is however possible to increase the ionic wind with the



Figure 2.1.3: Flow reattachment using an array of DBD actuators [figure 9c from (Caruana (2010))].

use of an alternate design (sliding DBD) (Louste et al. (2005); Moreau et al. (2008); Moreau et al. (2008); Sosa et al. (2008); Song et al. (2011),) in which a third electrode is added to create a DC bias (as shown in figure 2.1.4). This extends the plasma sheet further than achievable with a single DBD (as can be seen in figure 2.1.7) and increases the ionic wind (Moreau et al. (2008)) (see figure 2.1.5).

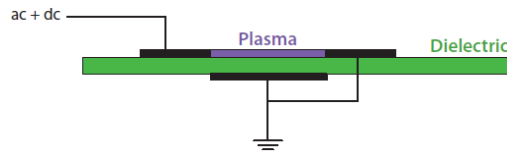


Figure 2.1.4: Sliding dielectric barrier discharge [figure 9 from (Cattafesta III and Sheplak (2011))].

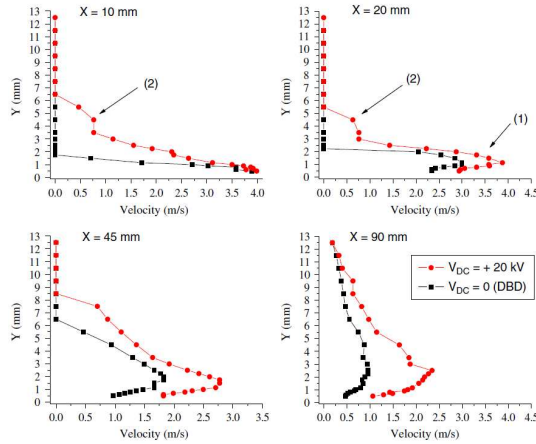


Figure 2.1.5: Comparison of ionic wind profile for the DBD and SDBD actuators. X is the distance from the ac HV electrode. In this experiment, the third electrode was placed 40 mm away from the ac HV electrode [figure 14 from (Moreau et al. (2008))].

More exotic designs can also be used to control the momentum injection direction, such as circular electrodes (Bénard et al. (2008)): instead of a tangential

ionic wind, one then gets a jet normal to the surface (see figures 2.1.6 and 2.1.7).

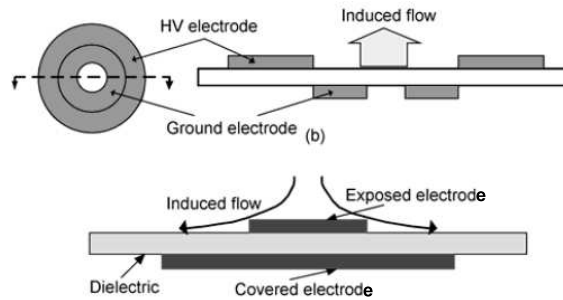


Figure 2.1.6: Circular dielectric barrier discharge [figure 12 from (Wang et al. (2012))].

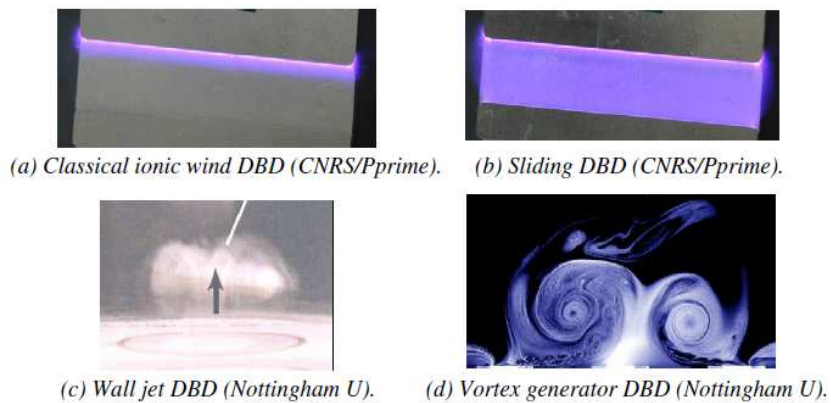


Figure 2.1.7: Visualisation of various DBD actuators in operation [figure 5 from (Caruana (2010))].

2.1.4 Nanosecond Dielectric Barrier Discharge

Another variation on the DBD actuator is the nanosecond DBD (nsDBD) (Starikovskii et al. (2008); Roupassov et al. (2009)), that is based on energy deposition. In this setup, a high voltage nanosecond pulse is used in place of the alternating current that drives the standard DBD actuator. This high voltage pulse rapidly heats up the gas, which causes the formation of shock waves. Several parameters of the duty cycle can be controlled to achieve the best performance. The nsDBD can be used either for flow control (through shock wave interaction) or for assisted combustion (through fast heating and creation of active species).

2.1.5 Sparkjet

The sparkjet (Bletzinger et al. (2005); Anderson and Knight (2012a); Anderson and Knight (2012b); Belinger et al. (2011); Belinger et al. (2011)) is a plasma actuator based on energy deposition that can be related to fluidic actuators. Two electrodes are placed within a small cavity in contact with the flow. A high voltage pulse between the two electrodes creates a spark which rapidly heats up the gas in the cavity. The heated gas then exhausts from the cavity in a high velocity (about 250 m/s) jet. This plasma synthetic jet can go through the boundary layer and have a net influence on the main flow, even at high velocity (Narayanaswamy et al. (2010); Reedy et al. (2012); Popkin et al. (2013)). However, once the jet has exited the cavity, fresh air must refill the cavity (recovery step) before another cycle (depicted in figure 2.1.8) can start.

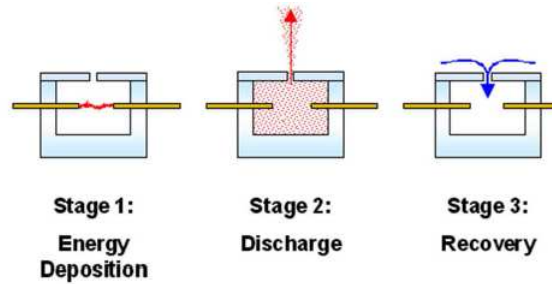


Figure 2.1.8: Sparkjet actuation cycle [figure 1 from (Popkin et al. (2013))].

To tackle this recovery issue (that limits the actuation frequency to a maximum of 5 kHz), an alternate ramjet design has been proposed (Wang et al. (2012)), in which an additional intake slit is added upstream of the cavity (see figure 2.1.9). This results in a faster refill of the cavity and allows to use some of the free stream energy to create a faster exhaust jet.

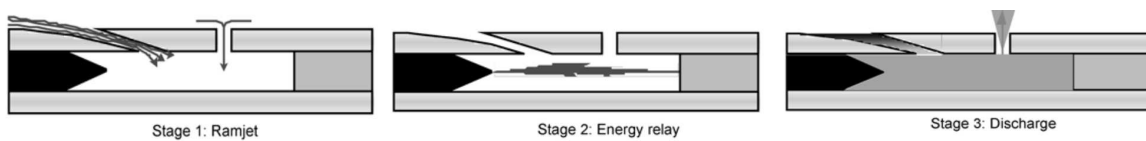


Figure 2.1.9: Ramjet actuation cycle [figure 16 from (Wang et al. (2012))].

2.1.6 Surface direct current arc

In a surface direct current arc (Leonov and Yarantsev (2008); Gnemmi et al. (2008)), two electrodes are placed on a dielectric material and separated by a small (about 1 cm) air gap. A discharge is then created between the two electrodes. The glow discharge rapidly turns into an arc (sustaining a current

of a few A), which heats the air locally. This actuator is another example of energy deposition, with the creation of shock waves that can interact with the flow (see figure 2.1.10) even at supersonic velocity (Gnemmi and Rey (2009); Gnemmi et al. (2013); Li et al. (2010)).

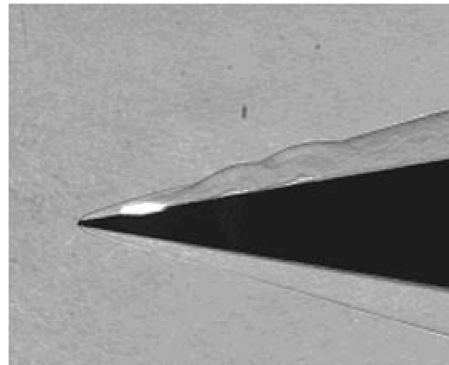


Figure 2.1.10: Visualization of the shock wave disturbance created by a surface direct current arc in a Mach 3 flow [figure 2 from (Gnemmi and Rey (2009))].

It is also possible to use several surface arcs for applications to high speed jets such as generated by jet engine nozzles. The use of multiple arcs (see figure 2.1.11) can create azimuthal instabilities (see figure 2.1.12) in the jet that may enhance mixing or affect noise generation (Samimy et al. (2007); Kim et al. (2010); Hahn et al. (2011); Speth and Gaitonde (2012)).

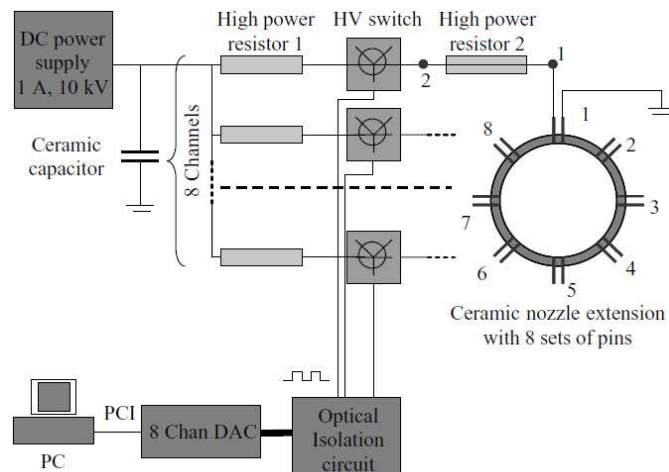


Figure 2.1.11: Setup of multiple LAFPA for azimuthal actuation on a jet [figure 1 from (Samimy et al. (2007))].

The various plasma actuators can be described very briefly as per table 2.1.

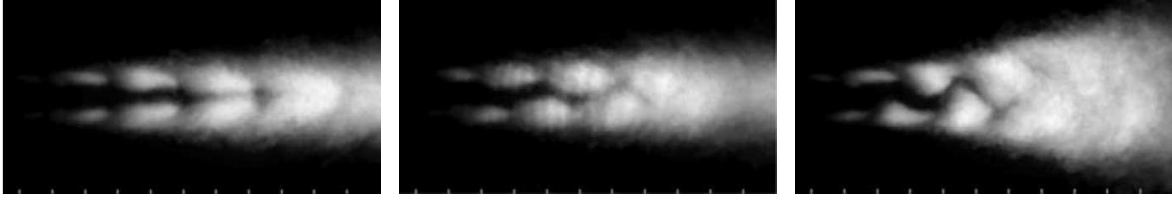


Figure 2.1.12: Example of azimuthal instabilities generated in a jet with an array of 8 LAFPA as installed in figure 2.1.11 [figure 9 from (Samimy et al. (2007))].

Table 2.1: General actuator types and their characteristics.

Actuation mechanism	Momentum addition	Energy deposition
Geometry	Flush	Point source
Actuation region	Diffuse along the wall	Point source
Compatible flow speed	Subsonic	Up to supersonic
Operation mode	Continuous	Pulsed

Both actuator types have some advantages and drawbacks, would it be possible to combine these types to obtain a new kind of flush actuator based on energy deposition? The pulsed surface discharge is a good candidate to do so. We will now describe the pulsed surface discharge and sum up the investigations that have taken place about it.

2.2 Pulsed Surface Discharge

The pulsed surface discharge (also called sliding gas discharge in the literature) was first investigated in rare gases as a light source for high power laser applications (Krasiuk et al. (1976); Andreev et al. (1975); Andreev et al. (1976); Andreev et al. (1978); Andreev et al. (1980); Baranov et al. (1981); Baranov et al. (1984); Beverly III et al. (1977); Lagarkov and Rutkevich (1994); Tuema et al. (2000)). The design considered most of the time is that of a plane (as depicted on figure 2.2.1).

The pulsed surface discharge has some similarities with the DBD in terms of electrodes geometry: the two electrodes are placed on opposite sides of a dielectric material. However, the ground electrode emerges atop of the dielectric some distance away (about 10 cm) from the high voltage (HV) electrode. The pulsed surface discharge always starts with a propagation phase: a plasma sheet is created on top of the dielectric material by the local electric field (that exceeds the breakdown threshold of the gas) near the high voltage electrode. If the initial voltage of the HV electrode is high enough, the plasma sheet can eventually bridge the gap between the HV electrode and the ground electrode: a conducting sheet now connects the two electrode so that current can flow in

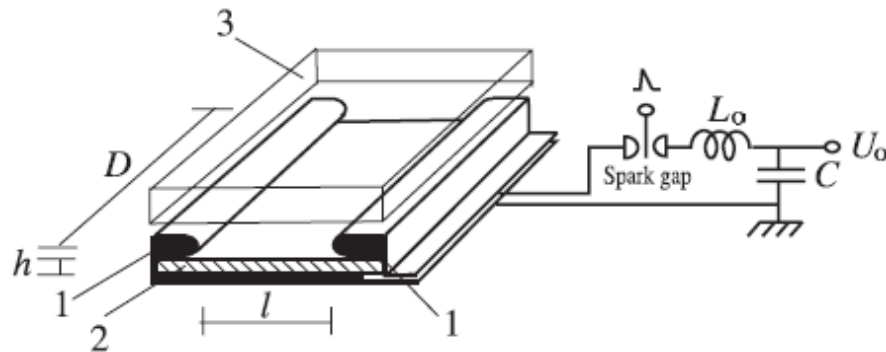


Figure 2.2.1: Design of planar pulsed surface discharge [figure 1 from (Trusov (2007))].

the circuit (Andreev et al. (1980); Bordage and Hartmann (1982); Beverly III (1986); Lagarkov and Rutkevich (1994); Trusov (1994); Trusov (2009)).

Provided there is an energy bank in the circuit, such as a peaking capacitor, it is possible to achieve fast energy deposition in the plasma sheet. The pulsed sliding discharge can then be used to generate shock waves (Arad et al. (1987)), which makes it a possible candidate for flow actuation. However, upon careful examination, the plasma sheet created by the planar pulsed surface discharge is found to consist of multiple small channels that appear at random (Trusov (2006); Trusov (2007)), depending on the conditions such as voltage or pressure (see figure 2.2.2).

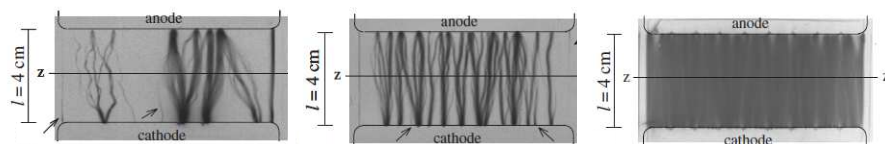


Figure 2.2.2: Channel structure of the pulsed sliding discharge observed at different operating voltage and gas pressure [images taken from figure 8, 9 and 10 from (Trusov (2007))].

The system of shock waves generated by such a discharge may be impeded by the existence of multiple channel sources. A solution (Znamenskaya et al. (2007); Znamenskaya et al. (2007)) was proposed to add a ridge structure to the dielectric layer (depicted on figure 2.2.3) so that the plasma channels generated between the electrodes remain parallel.

The pulsed surface discharge has been investigated at ONERA (Larigaldie et al. (1981); Larigaldie (1987b); Larigaldie (1987a); Larigaldie et al. (1992)) as a model of lightning stroke. The propagation phase (though taking place on a surface) is similar to the streamer-leader phase of a lightning bolt (which occurs in a volume between clouds and ground), whereas the ensuing arc phase

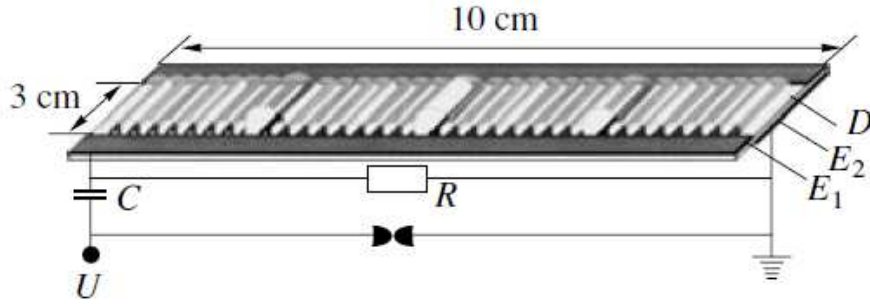


Figure 2.2.3: Ridge structure on the dielectric layer to impose the location of plasma channels [figure 2 from (Znamenskaya et al. (2007))].

(when the electrodes are connected by the plasma channel) can be related to the return stroke phase. In the course of this work, we will use this terminology of return stroke phase or arc phase indifferently. The electrode configuration in the ONERA setup is closer to that used for creating Lichtenberg figures (see figure 2.2.4).

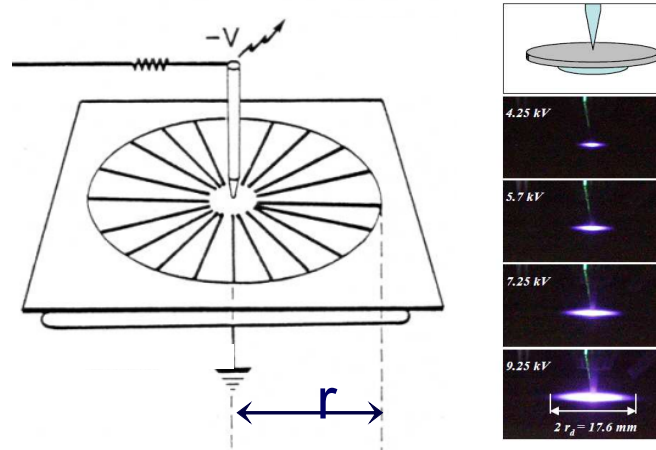


Figure 2.2.4: Setup used to create Lichtenberg figures. The circular discharge radius depends on the electrode voltage, according to Toepler's laws (Toepler (1906); Toepler (1921)).

In such a setup, multiple discharges branch from the high voltage electrode and form a circular pattern whose radius r_d is related to the applied voltage V according to Toepler's laws (Toepler (1906); Toepler (1921)) given in air by:

$$\frac{V}{r_d} = 5.5 \text{ kV/cm for } V > 0 \text{ (positive discharge),} \quad (2.2.1)$$

$$\frac{V}{r_d} = -11.5 \text{ kV/cm for } V < 0 \text{ (negative discharge).} \quad (2.2.2)$$

If the voltage exceeds a certain threshold, the circular pattern breaks down and individual filaments start to propagate on the dielectric (see figure 2.2.5a). Reducing the back electrode to a very narrow strip (just a few mm-wide) prevents branching from the HV electrode: the pulsed surface discharge generated is then essentially a single plasma channel, as visible in figure 2.2.5b.

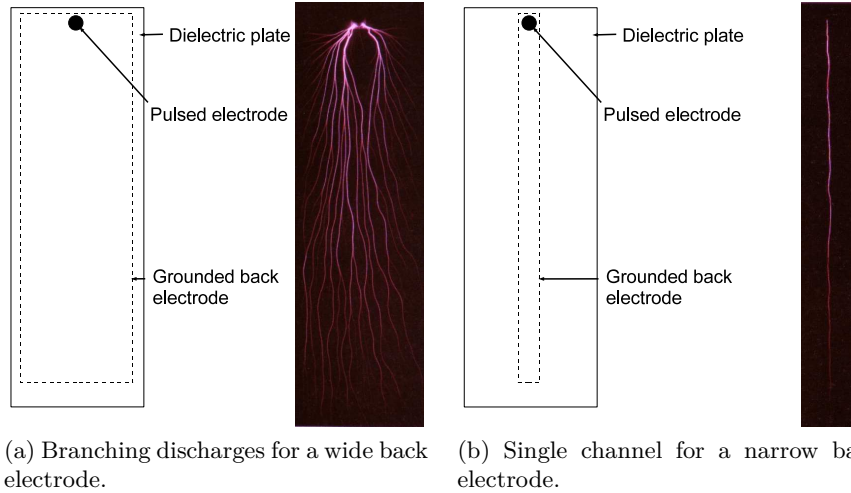


Figure 2.2.5: Using a narrower back electrode allows for guiding of the pulsed surface discharge: no more branching is observed, a single channel is created.

The discharge propagates in a specific way that depends on its polarity (Larigaldie et al. (1981); Larigaldie (1987b); Larigaldie (1987a)): for a negative discharge, its propagation speed is found to be proportional to the applied voltage. Spectroscopic measurements (Bordage and Hartmann (1982); Larigaldie et al. (1992)) indicate that the discharge is highly ionized, with electron number density in excess of 10^{18}cm^{-3} , with temperatures reaching above 10000 K. If the setup allows for connection and there is an additional energy supply (peaking capacitor (Larigaldie et al. (1992))), a return stroke phase can occur in which energy is deposited very quickly in the channel. This causes the creation of cylindrical shock waves that may be of interest for various applications, from combustion assistance to flow control.

Chapter 3

Experimental setups and methods

*Oh God, I could be bounded in a nutshell
And count myself a king of infinite space.*

William Shakespeare, Hamlet, Acte II, Scène 2

In this chapter, we will describe the various setups and measurements performed on the pulsed surface discharge. These include :

- electrical measurements to assess the circuit influence on the energy deposition in the discharge;
- emission spectroscopy on the discharge to evaluate some of its key properties, such as the electron number density;
- Schlieren imaging to image the shock waves created by the pulsed sliding discharge and follow their trajectory;
- impulse measurements, which are used together with electrical measurements to assess the pulsed sliding discharge efficiency and its interest as a possible flow actuator.

We start by briefly describing the actuator principle.

3.1 Actuator principle

The pulsed surface discharge under consideration in this study is created on the surface of a dielectric material with a high voltage pulse. The discharge requires only moderately high voltages (on the order of 20 kV) to bridge air gaps of several centimeters. This is possible because of the special geometry of the electrodes (depicted on figure 3.1.1):

- one of the electrodes, later called the high voltage (HV) electrode, is a single tip made of stainless steel and placed on the dielectric layer;

- the other electrode (later called the ground electrode) is placed below a dielectric layer and extends over several centimeter away from the HV electrode. It is held in place by conducting screw and bolt that get through the dielectric layer, thus exposing the ground potential above the dielectric layer.

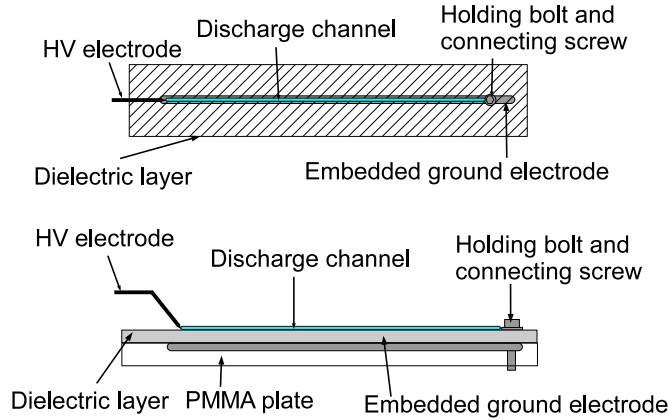


Figure 3.1.1: Top and side view of the pulsed surface discharge electrodes configuration. The HV electrode sits on top of the dielectric layer. The ground electrode is embedded below the dielectric layer.

When the tip electrode switches to negative high voltages, the electric field in its vicinity is high enough to ionize air, thanks to the presence of the grounded electrode below the dielectric layer. A plasma channel is formed gradually that closes the gap between the HV electrode and the grounded electrode. High current then starts flowing through the channel, which heats up the gas further and causes the formation of shock waves. We set up various diagnostic techniques to study the plasma channel evolution and behavior, and its possible use as an actuator.

3.2 Electrical setup for discharge creation

3.2.1 Setup overview

The actuator plate consists of a $10 \times 15 \text{ cm}^2$ dielectric sheet, of thickness 0.1 mm made of cellulose acetate, with a relative permittivity of $\epsilon_r \approx 3$. The stainless steel HV electrode is placed in contact with the dielectric. The counter-electrode is a $6 \times 140 \text{ mm}^2$ aluminum strip; it is placed directly below the dielectric sheet. Its edges are rounded to avoid local electric field intensification. The whole setup (see photograph in figure 3.2.1) is held by a $10 \times 15 \text{ cm}^2$, 1-cm thick PMMA plate. Since the discharge always connects both electrodes, the discharge length can be controlled by changing the distance

between the grounded brass electrode and the HV electrode.

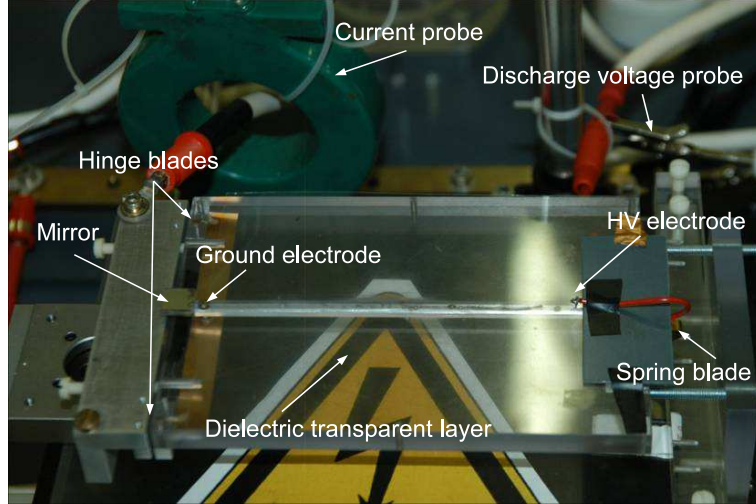


Figure 3.2.1: Actuator setup. The mirror, spring blade and hinge blades are used in torque measurements (see section 3.5.1).

3.2.2 Circuit description

Energy is supplied by a capacitor bank (on the order of a few nF) charged through a ballast resistance ($R_b = 1.7 \text{ k}\Omega$). The capacitor bank is connected to the discharge setup via a triggered spark gap (EG&G GP-12B) which is switched with a -30 kV pulse. The circuit is shown in figure 3.2.2. Before triggering the spark gap, the capacitors are charged to positive voltage U_C (usually between 18 and 27 kV). When the spark gap is triggered, the HV electrode voltage drops to $-U_C$ in a few nanoseconds. Streamers propagate from the HV electrode up to the ground electrode and bridge the gap. Once both electrodes are connected via the plasma channel, current starts flowing through it until all the energy initially stored in the capacitors has been dissipated.

3.2.3 Electrical diagnostics

The voltage on the HV electrode is monitored using a high voltage probe (PPE20kV Lecroy), with a 100MHz bandwidth. The current flowing in the plasma channel is measured with a Pearson coil (Pearson 110A), whose sensitivity is 0.1 VA^{-1} . The high voltage probe is located close to the HV electrode contact point with the dielectric sheet. The measurements are recorded with a 200 MHz TDS2024B Tektronix oscilloscope.

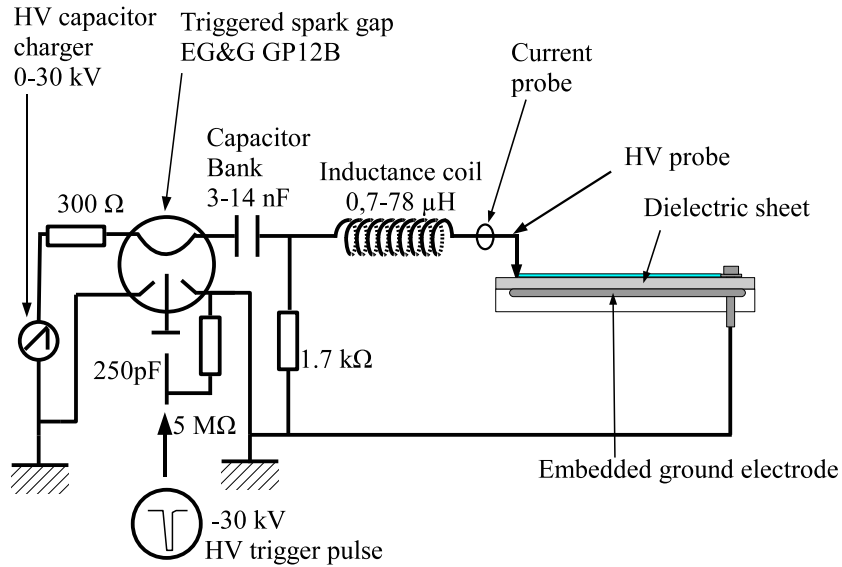


Figure 3.2.2: Complete electrical circuit. During the return stroke phase, the spark gap is modeled by a resistor $R_{sg} = 0.79 \Omega$ connecting the capacitor bank to the ground.

3.2.4 Shot-to-shot repeatability

For a given configuration, the measurements are repeated several times to check the shot-to-shot repeatability of the measured current. The repeatability is excellent, to a point where shot-to-shot changes in the measured current are barely noticeable, as demonstrated on figure 3.2.3. In the following analysis, only one sample current trace is considered for each condition.

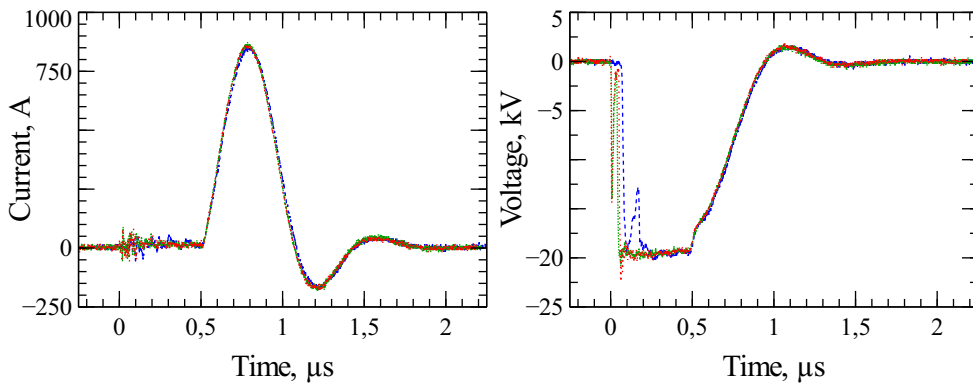


Figure 3.2.3: Current and voltage measured on three different discharges for the same conditions ($U = 20 \text{ kV}$, $C = 14.5 \text{ nF}$, $l = 85 \text{ mm}$, $L = 78 \text{ μH}$).

3.3 Optical emission spectroscopy

3.3.0.1 Measurement setup

Spectroscopic measurements are performed on the discharge using an Acton SP750 spectrometer, with a PIMAX2 gated ICCD camera, controlled via a STG133 unit. An achromatic lens of focal length 400 mm is used to image the discharge on the entrance slit of the spectrometer. Using the 0-th order of the spectrometer enables fast imaging of the discharge. Scale is determined by imaging an object of known height: a pixel on the camera then represents 20 μm in the setup. The achromatic lens cuts off all radiation below 350 nm. The whole setup, depicted on figure 3.3.1, is aligned with the discharge thanks to a HeNe laser.

- the gate corresponds to the working period of the camera and can be as low as 2 ns; it is set at different values depending on the measurement;
- the gain is the light intensification that takes place within the camera, it is set at different values depending on the measurement;
- a delay can be imposed on the camera, for time-resolved measurements, either via the STG133 control unit or the delay generator used to trigger the discharge itself; it is set at different values depending on the measurement.

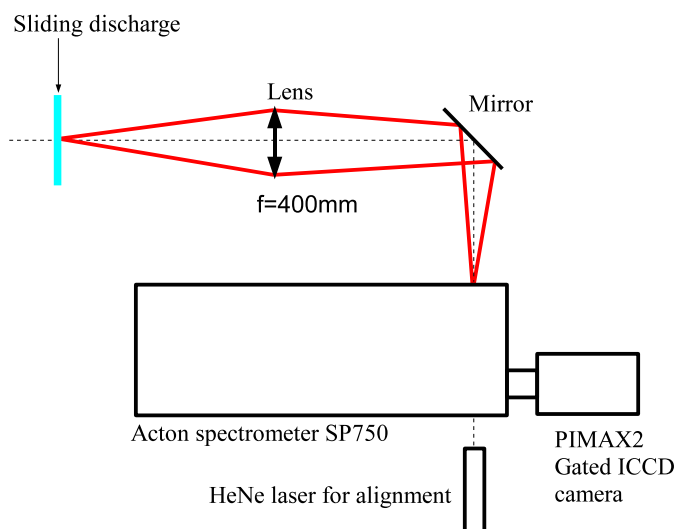


Figure 3.3.1: Spectroscopy setup used for time-resolved measurements on the discharge.

The camera records a full image of 512×512 pixels, with the spectral dispersion along the horizontal axis and the vertical position along the vertical axis of the discharge channel. Each horizontal line then represents a spectrum from a given point, integrated on the line of sight through the plasma channel. In our

analysis, we first present a spectrum averaged over the channel width, obtained by binning all the lines, and then we obtain some space-resolved images, with 16-lines binning of equivalent width $320 \mu\text{m}$.

Several gratings (300 grooves/mm, 1800 grooves/mm, 2400 grooves/mm) are installed on the spectrometer and can be used for spectroscopic measurements. Each grating offers a limited investigation range, from about 52 nm for the 300 grooves/mm, down to about 4 nm for the 2400 grooves/mm. Initial measurements on the discharge after proper wavelength calibration show that the H_α line exhibits large broadening (up to several nm), which leads us to use the 300 grooves/mm.

3.3.1 Setup synchronization

To perform time-resolved measurements, we need to synchronize the whole setup. This is done by measuring the propagation delay along the various cables and the internal delay of the PIMAX2 camera and STG133 control unit assembly. The camera opens 51 ns after the triggering signal has been sent to the STG133. However, the camera being some four meters away from the discharge, the light signal it receives is 14 ns-old, so the camera actually records the discharge light emitted 37 ns after emission of the triggering signal from the STG133. The discharge initiation exhibits a jitter of approximately 250 ns that must be accounted for. The discharge current and voltage are recorded on an oscilloscope onto which a signal is emitted to mark the starting point of image recording t_{IR} . The discharge initiation t_{D} is identified on the oscilloscope as the voltage drop below -2 kV , when the sparkgap switches, as depicted on figure 3.3.2.

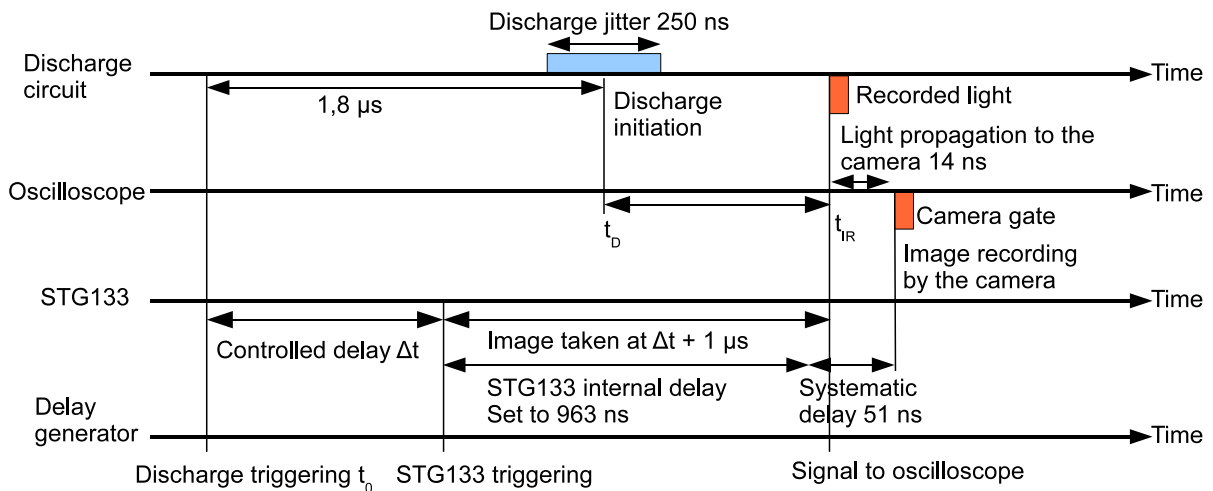


Figure 3.3.2: Triggering sequence of the optical measurement setup. The camera gate is marked by the orange rectangle.

The precise synchronization and triggering sequence of the whole setup allow us to perform time-resolved measurements with an accuracy down to 5 ns. As evidenced on figure 3.3.3, the spectrum structure varies in terms of peaks, hence the need for an automated peak detection.

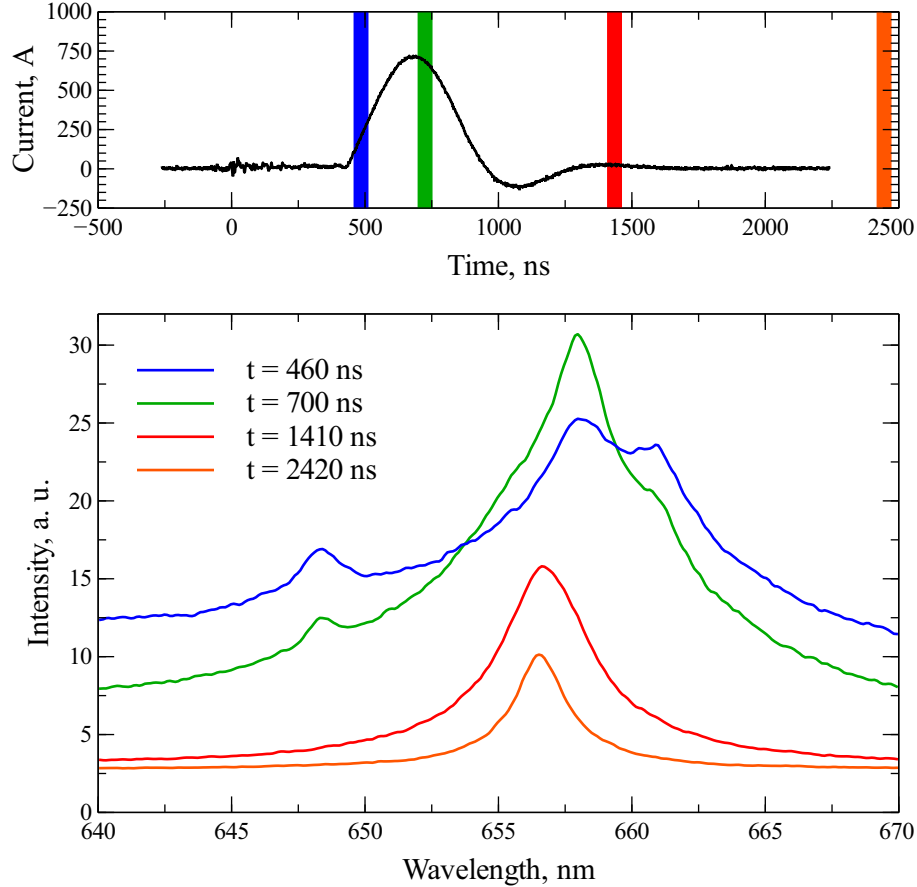


Figure 3.3.3: Raw discharge spectra (binned over the whole camera height) at various instants. The time stamp t given for each spectrum corresponds to the time difference $t_{IR} - t_D$ indicated on figure 3.3.2.

3.3.2 Intensity calibration and slit function deconvolution

When analysing the spectra, one has to take into account the slit function that limits the maximum resolution of the setup and the spectral response of the detector. The measured spectrum $M(\lambda, t)$ at instant t is

$$M(\lambda, t) = C(\lambda) (s(\lambda) * S(\lambda, t)), \quad (3.3.1)$$

where $S(\lambda, t)$ is the real spectrum emitted by the discharge at instant t , $s(\lambda)$ is the spectrometer slit function and $C(\lambda)$ the detector spectral response. $*$ is

the convolution, defined for two functions f and g by:

$$f * g(x) = \int_{-\infty}^{+\infty} f(y)g(x - y)dy.$$

We must then correct for the detector spectral response $C(\lambda)$ and the spectrometer slit function $s(\lambda)$ to obtain the real spectrum $S(\lambda, t)$ out of our measured spectrum. The detector spectral response $C(\lambda)$ is calibrated using a calibrated tungsten-halogen light source from Ocean Optics. This lamp spectral intensity is known *a priori*. Dividing the theoretical value by its measured value, we get an intensity correction function $C(\lambda)$.

The slit function is measured using a HeNe laser line. This very narrow line should appear on the spectrometer as a near-Dirac distribution, with a single peak centered at 632.8 nm. For the sake of sensitivity, we opened the entrance slit of spectrometer up to 100 μm , in order to have enough light to record a time resolved spectrum. Since the real spectrum emitted by the HeNe laser has a full width at middle height of 0.002 nm, the measured spectrum (depicted on figure 3.3.4) can be used directly as the slit function $s(\lambda)$. Deconvolution of the measured discharge spectrum is performed using Fourier transform, so the real spectrum $S(\lambda, t)$ is obtained as:

$$S(\lambda, t) = \mathcal{F}^{-1} \left(\frac{\mathcal{F} \left(\frac{M(\lambda, t)}{C(\lambda)} \right)}{\mathcal{F}(s(\lambda))} \right), \quad (3.3.2)$$

where \mathcal{F} is the Fourier transform and \mathcal{F}^{-1} is the inverse Fourier transform.

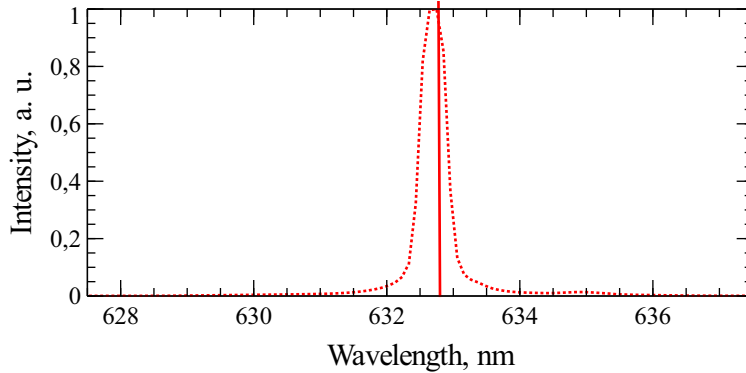


Figure 3.3.4: Intensity profile of the measured laser line at 632.8 nm. The various imperfections in the spectrometer measurement chain results in a line deformation (dotted line) that gives the slit function of the setup.

3.3.3 Spectrum reconstruction

In our analysis, we will focus on the H_{α} line, of wavelength $\lambda_0 = 656.279$ nm to access some of the plasma properties, such as the electron number density.

To do so, we will need to identify the H_α line in the corrected spectrum. The emission from a single atomic line (such as H_α) is described with the centered Voigt profile $V(x, \sigma, \gamma)$. This profile is the convolution of a centered Gaussian profile $G(x, \sigma)$ and of a centered Lorentzian profile $L(x, \gamma)$:

$$V(x, \sigma, \gamma) = G(x, \sigma) * L(x, \gamma) = \int_{-\infty}^{+\infty} \frac{e^{-\frac{x'^2}{2\sigma^2}}}{\sigma\sqrt{2\pi}} \frac{\gamma}{\pi(x-x')^2 + \gamma^2} dx',$$

where x is the deviation from the line central wavelength λ_c . To fit such a profile to experimental data, one will then need four parameters:

- λ_c the central wavelength
- A the line amplitude
- σ the Gaussian standard deviation
- γ the Lorentzian scale parameter

For computation, one can use an alternative definition of the Voigt profile (Schreier (1992); Janssen et al. (2013); Armstrong (1967))

$$V(x, \sigma, \gamma) = \frac{\Re(w(z))}{\sigma\sqrt{2\pi}}, \quad z = \frac{x + i\gamma}{\sigma\sqrt{2}}, \quad (3.3.3)$$

where $w(z)$ is the Faddeeva function:

$$w(z) = e^{-z^2} \left(1 + \frac{2i}{\sqrt{\pi}} \int_0^z e^{t^2} dt \right).$$

This gives direct access to the Gaussian and Lorentzian contributions (σ, γ) of the Voigt profile full width at half maximum, from which meaningful physical data can be extracted.

We measure the discharge spectrum $S(\lambda, t)$ at instant t and try to fit it with a sum of Voigt profiles:

$$\Sigma(\lambda) = a + b\lambda + \sum_i A_i V(\lambda - \lambda_i^{(c)}, \sigma_i, \gamma_i), \quad (3.3.4)$$

where a and b are some baseline parameters and $(A_i, \lambda_i^{(c)}, \sigma_i, \gamma_i)$ are the Voigt profile parameters for peak i . Before fitting the experimental spectrum $S(\lambda, t)$, it is then necessary to determine the peaks present in the spectrum in order to construct the theoretical profile $\Sigma(\lambda)$. This is done with a peak detection algorithm based on wavelet transform (Yang et al. (2009); Du et al. (2006)). To constrain the theoretical profile $\Sigma(\lambda)$ and fasten the convergence, we build $\Sigma(\lambda)$ so that it is strictly equal to the experimental profile for each of the isolated peaks $\lambda_j^{(p)}$, that is:

$$\forall \lambda_j^{(p)}, \Sigma(\lambda_j^{(p)}) = S(\lambda_j^{(p)}). \quad (3.3.5)$$

Equation (3.3.4) can be vectored on all the peaks $\lambda_j^{(p)}$ and inverted so as to get the amplitudes A_i that will guarantee the equality (3.3.5):

$$A_i = \sum_j \left(\Sigma \left(\lambda_j^{(p)} \right) - \left(a + b \lambda_j^{(p)} \right) \right) V_{j,i}^{-1}, \quad (3.3.6)$$

where $V_{j,i}$ is a tensor representing the pure Voigt profile amplitude of reconstructed peak $\lambda_i^{(c)}$ at observed peak position $\lambda_j^{(p)}$:

$$V_{j,i} = V \left(\lambda_j^{(p)} - \lambda_i^{(c)}, \sigma_i, \gamma_i \right) \quad (3.3.7)$$

Figure 3.3.5 shows the measured spectrum, the deconvolved spectrum and the peak detection rendering.

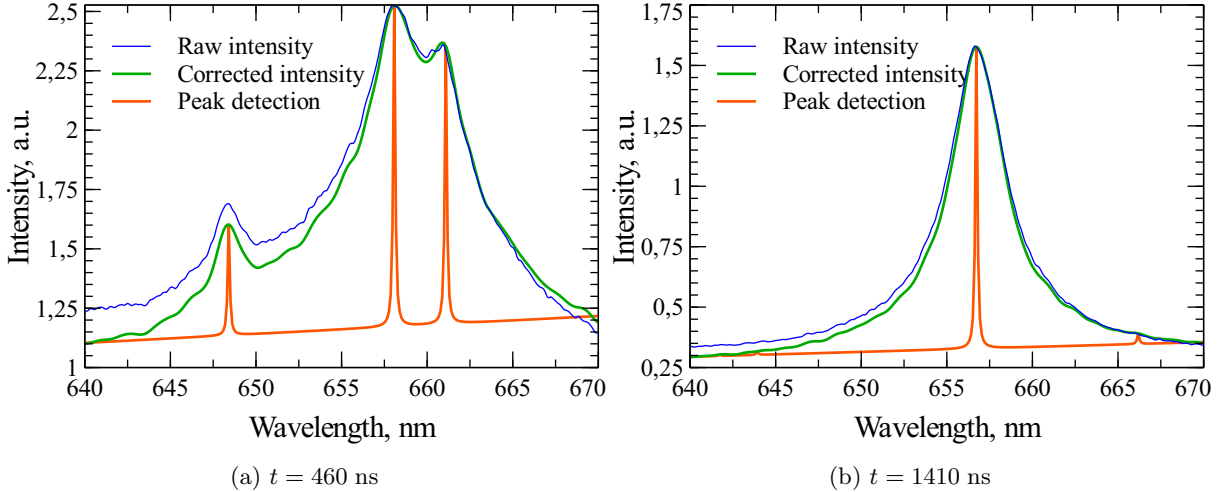


Figure 3.3.5: Spectrum of the discharge ($U = 20$ kV, $C = 11.6$ nF, $L = 0.7$ μ H, $l = 85$ mm) before and after intensity correction and slit function deconvolution.

3.4 Schlieren imaging

To study the shock wave generated by the surface discharge, our experiment is placed within the imaging field of a Schlieren setup. We use a CAVILUX[®] Smart laser diode light source to create a 100 ns pulse of wavelength 690 nm, stopped down with a pinhole of diameter 0.5 mm. This point-like source is placed at the focal point of a 1500 mm achromatic lens (L1) that generates the imaging field of parallel light rays. A knife edge is placed at the focal plate of a second 500 mm achromatic lens (L2). The final image is created on the detector with a 60 mm lens (L3) placed behind a filter at 690 nm that

limits stray light emitted by the discharge from reaching the detector. We use a GigE uEye CP industrial camera as our detector. The trigger pulse for the camera (duration $10 \mu\text{s}$) is emitted $50 \mu\text{s}$ before the light pulse, so as to let the camera shutter open. The whole setup is depicted on figure 3.4.1. We perform phase-locked measurements, granted the discharge phenomenon exhibits a good shot-to-shot repeatability.

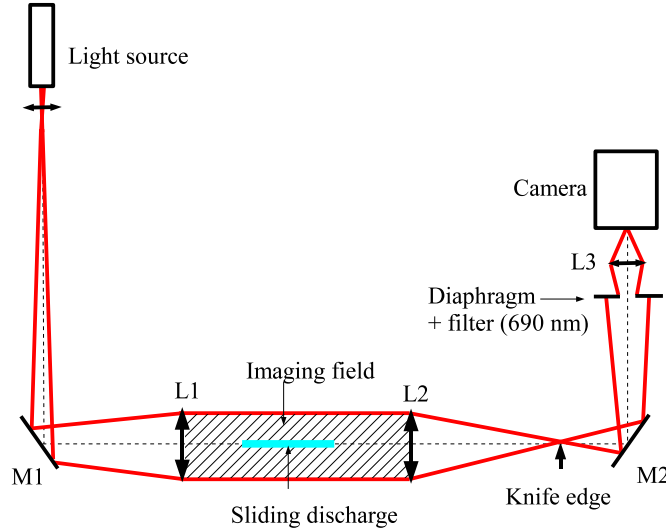


Figure 3.4.1: Schlieren setup used to visualize the shock wave generated by the sliding discharge along the discharge axis. L1: $f_1 = 1500 \text{ mm}$. L2: $f_2 = 500 \text{ mm}$. L3: $f_3 = 60 \text{ mm}$. M1 and M2 are plane mirrors.

Due to the setup configuration (bolt connecting the ground electrode on top of the dielectric layer), the first instants of the discharge cannot be accessed with this front view configuration. Furthermore, some stray light emitted by the discharge managed to reach the camera creating a sort of halo as shown in figure 3.4.2. We modified the discharge orientation to record the shock wave trajectory as seen from the side of the discharge (see figures 3.4.3 and 3.4.4). In addition, the knife edge was diaphragmed to prevent light emitted by the discharge from blinding the sensor. This allows for finer measurements of the early expansion of the discharge and its shock wave as depicted on figure 3.4.5. In addition, this side imaging confirms our assumption of the 2D geometry of the discharge.

The shock waves can be seen with these setups and their radius is measured in chapter 6.

3.5 Impulse measurement

During the return stroke phase, the energy initially stored in the capacitors is quickly released in the plasma channel, heating up the gas and causing

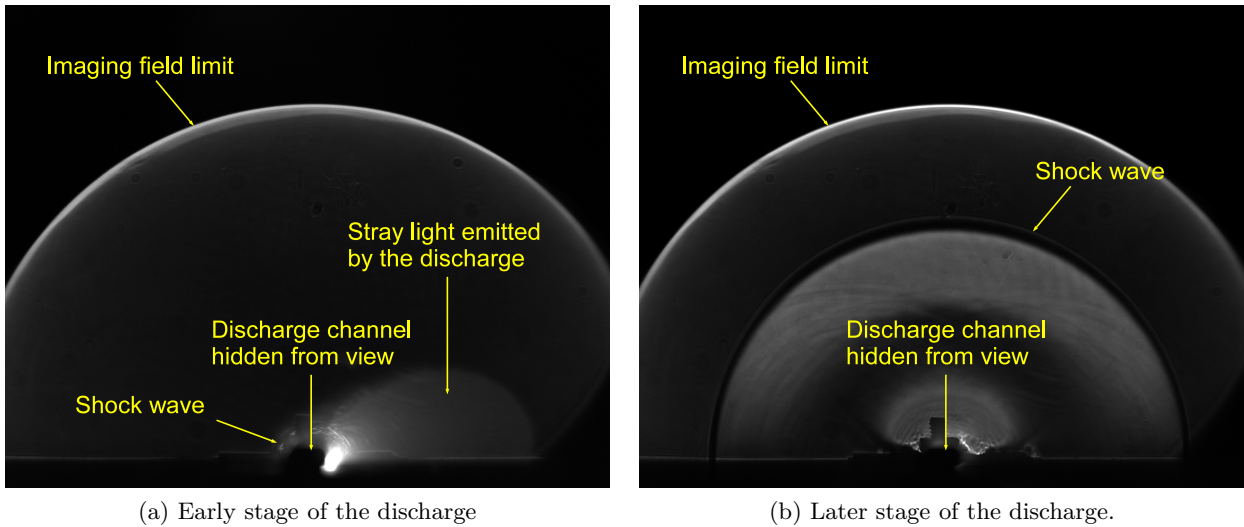


Figure 3.4.2: Shock wave visualization along the discharge axis. The imaging scale for this setup is $49 \mu\text{m}/\text{pixel}$.

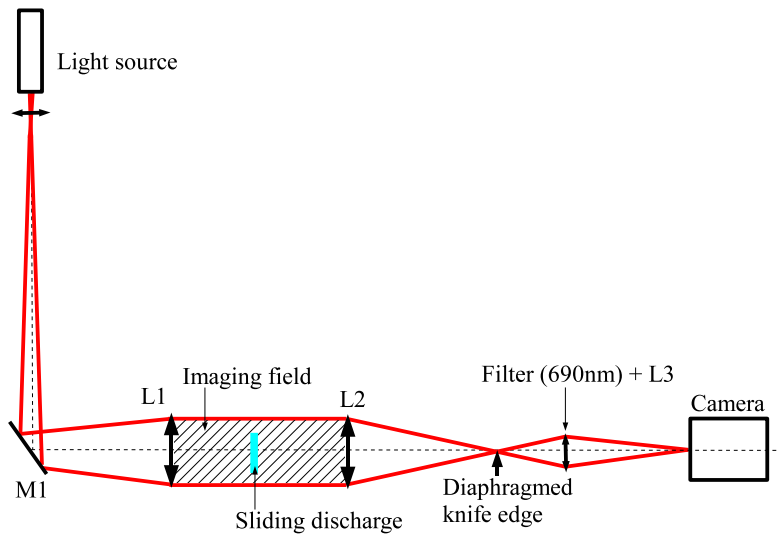


Figure 3.4.3: Schlieren setup used to visualize the shock wave generated by the sliding discharge from the side of the discharge axis.

the formation of shock waves. Overpressure behind the shock imparts a net force on the actuator plate, resulting in an impulse that we measure with a torque balance (Elias and Castera (2013)). The discharge actuator is placed on a hinge, of which the angular position is monitored optically. When the discharge is created on the actuator, the actuator starts to oscillate because of the shock overpressure. These oscillations can be related to the momentum, hence the impulse, imparted by the discharge.

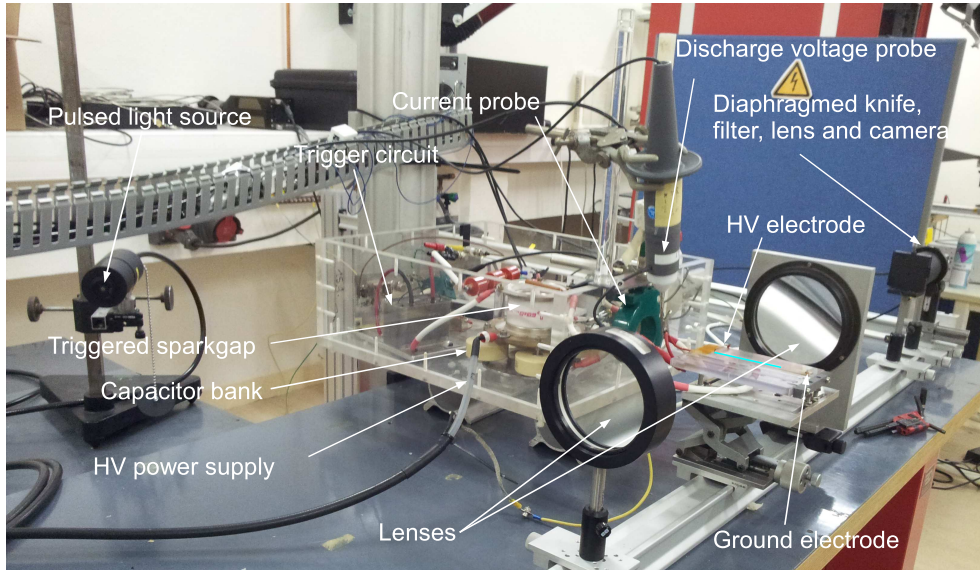


Figure 3.4.4: Schlieren setup for shock wave visualization. The electrical diagnostics and discharge circuit are also shown, with the blue line indicating the discharge position.

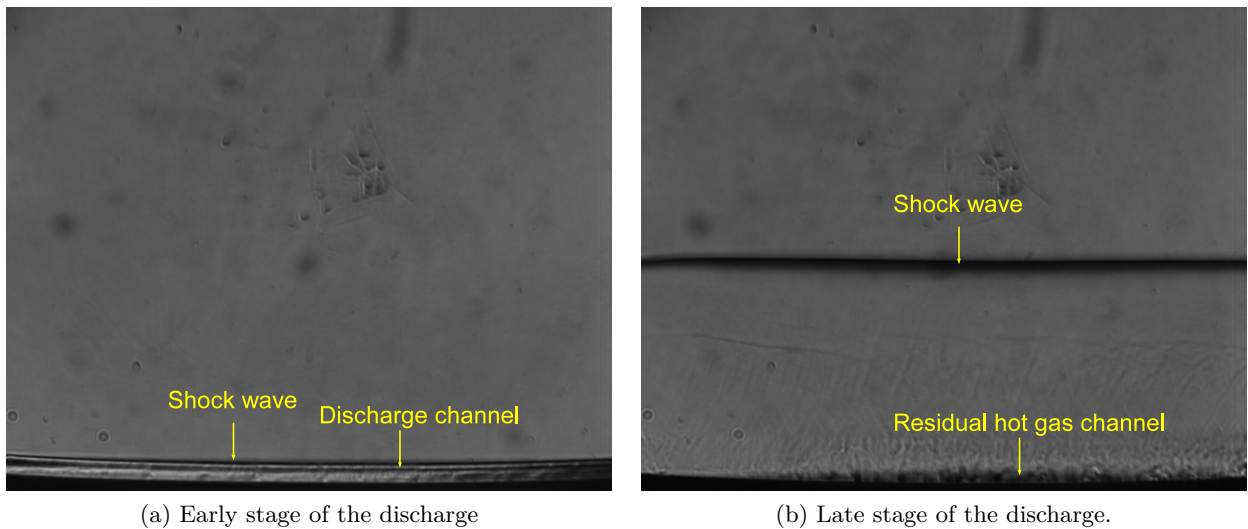


Figure 3.4.5: Shock wave visualization across the discharge axis. The imaging scale for this setup is $46.2 \mu\text{m}/\text{pixel}$.

3.5.1 General principle

Two thin (0.1 mm thick, 2.5 mm wide, 1 mm long) copper blades act as a hinge on one side of the plate. On the other side, a similar curved blade, of greater length (30 mm) acts as a spring. These copper blades are also used to

connect the actuator plate electrode to the HV circuit, to avoid stiffening the oscillator with additional wiring. A mirror is placed on the actuator on top of the hinge axis, on which a laser beam is reflected onto a linear optical detector Newport OBP-A-9L. For small enough oscillations, the beam displacement ds recorded on the detector can be linearised and is found to be proportional to the angular displacement θ :

$$ds = 2L \sin(\theta) \approx 2L\theta \quad (3.5.1)$$

The setup is depicted on figure 3.5.1.

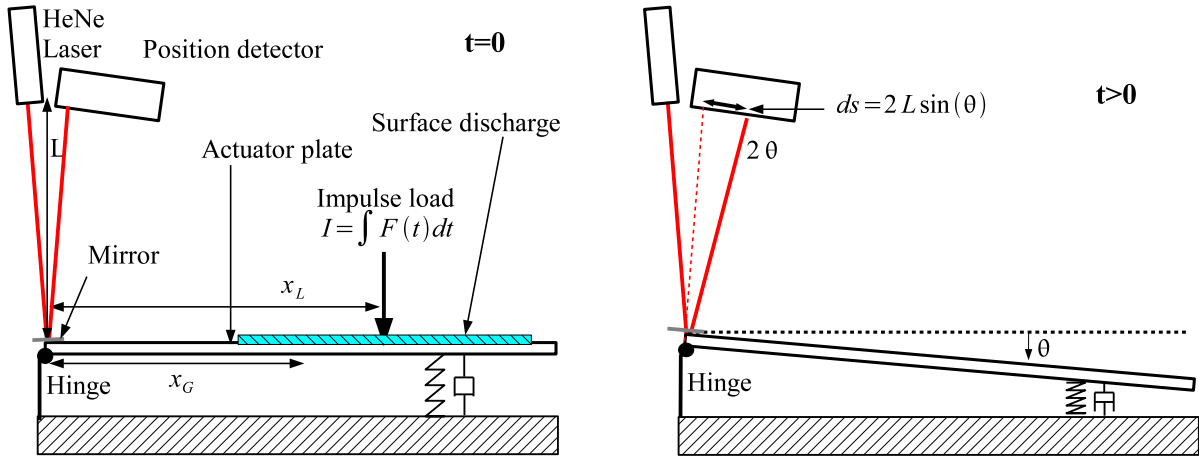


Figure 3.5.1: Impulse measurement setup.

The angular displacement θ is given by the standard formula for an under-damped oscillator:

$$\theta = \Theta \sin(\sqrt{\omega_0^2 - \alpha^2}t) e^{-\alpha t}. \quad (3.5.2)$$

Assuming an impulse p is applied normally on the actuator at time $t = 0$ at distance x_L of the tilting axis, the amplitude Θ is given by:

$$\Theta = \frac{x_L p}{I \sqrt{\omega_0^2 - \alpha^2}},$$

with ω_0 and α functions of mechanical parameters and I the actuator moment of inertia with respect to the hinge. We do not need to determine these factors precisely to measure the impulse delivered by the discharge. Indeed, the optical detector returns a voltage u proportional to the deflection angle θ , so the peak-to-peak voltage u_{pp} is proportional to the angular momentum applied to the plate:

$$u_{pp} = K x_L I, \quad (3.5.3)$$

where K is the dampening between two consecutive peaks, which is a function of these parameters (ω_0, α, I). This coefficient is determined experimentally through careful calibration of the torque balance, as detailed next.

3.5.2 Calibration

To determine the coefficient K , we calibrate the torque balance by dropping a steel ball of known mass $m = 879$ mg from a height $h = 1.5$ cm at varying distance x from the balance axis. If we neglect air friction, on reaching the plate, the marble has a downward impulse p_z given by:

$$p_z = m\sqrt{2gh}, \quad (3.5.4)$$

with $g = 9.81$ m/s² the local Earth gravity acceleration. Assuming a perfect rebound, the marble goes back up with an impulse $p'_z = -p_z$. The plate, steady before impact, now has an impulse:

$$\Delta p_z = p_z - p'_z = -2m\sqrt{2gh},$$

and starts to oscillate according to equation (3.5.2) with an amplitude proportional to this initial impulse Δp_z . These oscillations are recorded by the optical detector, as can be seen on figure 3.5.2.

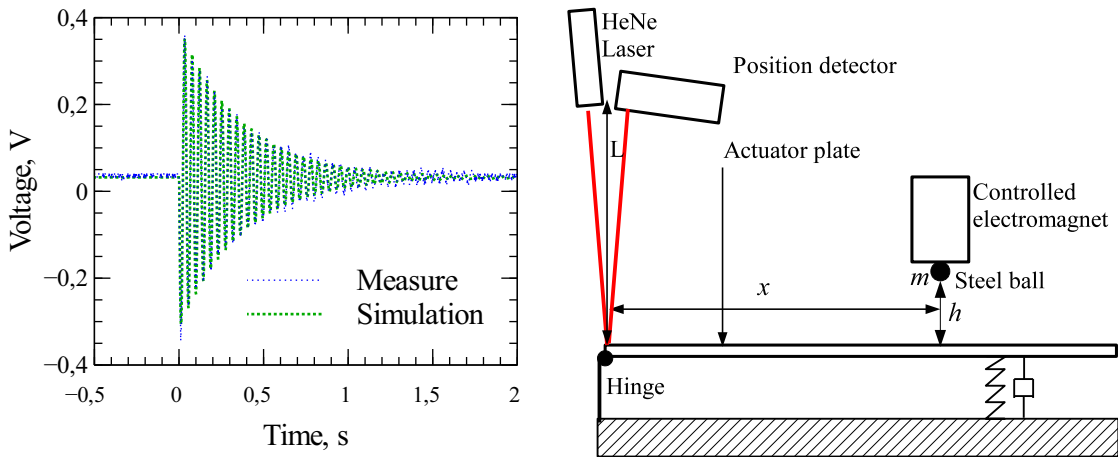


Figure 3.5.2: Voltage oscillations following a marble rebound and setup for controlled release. The measured data (in blue) can be fitted accurately with a standard damped sinusoid (in green).

In order to have a good shot-to-shot repeatability during our calibration, the ball is released by a controlled electromagnet. The electromagnet must be switched off for long enough to let the ball reach the plate and bounce back up without being pulled by the magnetic field. For a release height $h = 1.5$ cm, one gets a minimum switch off duration $t = 55$ ms. We set the switch off duration to 60 ms. The resulting calibration curve is shown in figure 3.5.3. The balance behaves linearly as expected and we get the coefficient K by regression.

It has been assumed so far that the ball rebound on the plate was perfect, which guarantees that $p'_z = -p_z$. However this may not be the case, and we

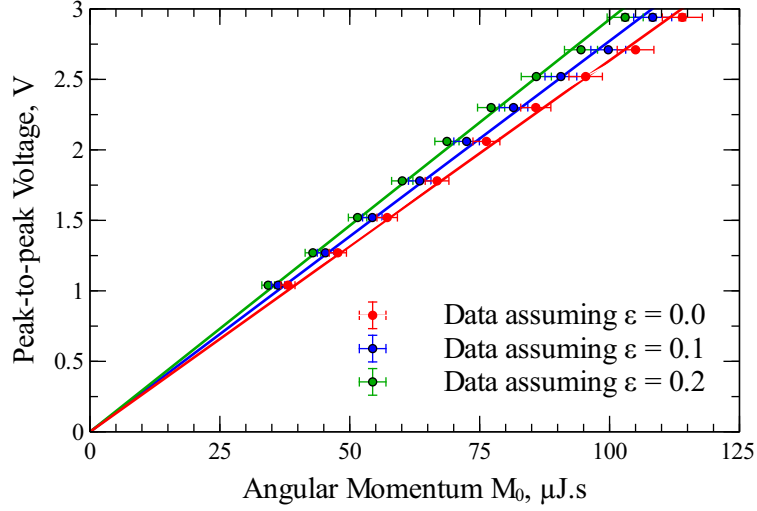


Figure 3.5.3: Calibration of the torque balance: each point is sampled 15 times to account for statistical dispersion. The lines are linear fit for the various data sets.

may have $p'_z = -(1 - \epsilon)p_z$. This leads to a plate impulse:

$$\Delta p_z = p_z - p'_z = -(2 - \epsilon)m\sqrt{2gh},$$

which results in a systematic error in our estimation of K :

- for $\epsilon = 0.0$, $K = 26309 \pm 906$ V/Js;
- for $\epsilon = 0.1$, $K = 27692 \pm 953$ V/Js;
- for $\epsilon = 0.2$, $K = 29231 \pm 1006$ V/Js.

The statistical and systematic errors are computed according to a variance formula (see appendix A for more details). For our impulse measurements, given that the ball bounces back up to about 80% of its original height (this a gross visual estimation), we will use the value corresponding to $\epsilon = 0.1$:

$$K = 27692 \pm 953 \text{ V/Js.} \quad (3.5.5)$$

3.5.3 Impulse measurement on the discharge

The measured momentum M_0 delivered by the sliding discharge is obtained by integration over the discharge length l of elementary momenta:

$$M_0 = \int_l dM = \int_l \Pi(x) x dx, \quad (3.5.6)$$

with $\Pi(x)$ the linear impulse. Assuming Π to be constant along the discharge length, we get the linear impulse generated by the discharge as a function of the measured peak-to-peak voltage:

$$\Pi = \frac{u_{pp}}{x_L K l}, \quad (3.5.7)$$

with x_L the center position of the discharge.

3.6 Conclusion

We have set up a range of diagnostics to study the behavior of the plasma channel and its time evolution. Electrical probes enable measurements of voltage and current in the plasma channel, which gives access to the energy deposition dynamics. We can then determine how much energy initially put in the electrical circuit is coupled into the discharge. The physical properties of the discharge channel are studied via optical and spectroscopic measurements. The whole setup has been carefully synchronized to perform time-resolved measurements, with an accuracy of 5 ns. Shock waves generated by the discharge are visualized using a Schlieren setup and the impulse imparted by these shock waves is measured with a calibrated torque balance.

Chapter 4

Development of an electric model for the arc phase

*With four parameters I can fit an elephant, and
with five I can make him wiggle his trunk.*

John von Neumann

The pulsed surface discharge takes place in two steps: a propagation phase, during which a plasma channel is created between the electrodes; and a return stroke phase, during which a high current flows into the newly formed conductive channel. This current causes a fast Joule heating of gas, which in turn creates shock waves that exert an impulse on the actuator and the surrounding gas. To assess the efficiency of the pulsed surface discharge for flow control, we need to know how much energy is deposited in the discharge itself during the return stroke phase. The propagation phase is not considered here, as most of the energy is deposited in the discharge during this high current phase only. The discharge is generated with a circuit that includes several components that can influence the energy deposition in the plasma. To understand the influence of the circuit on the discharge behavior, we measure the voltage and current in various configurations. These measurements are used to:

- conduct a parametric study to identify the governing circuit characteristics and their influence on the energy deposition dynamics;
- develop a simple model to describe the current pulse in the high current phase, hence the energy deposition in the discharge;
- compare this model to experimental results.

4.1 Electrical characterization of the discharge

4.1.1 Parametric study

We want to determine the main parameters that affect the discharge energy deposition. To do so, we measure the discharge current and voltage for different discharge configurations, where we vary the discharge length l , the total capacitance in the capacitor bank C , the initial charging voltage U_C or the total circuit inductance L . The discharge length, total capacitance and circuit inductance all modify the oscillatory behavior. In this work, only positive charging voltages are considered. Therefore, due to the circuit configuration, the voltage pulse applied to the HV electrode is always negative (see the circuit description in section 3.2, chapter 3). The different test cases are described in table 4.1.

Table 4.1: Test cases series for measurements.

Test series	l (cm)	C (nF)	L (μ H)	U_C (kV)
A	9.5	14.5	0.8	18, 19, 20, 21, 22, 23, 24, 25
B	9.5	11.6	0.8	19, 20, 21, 22, 23, 24, 25
C	9.5	8.9	0.8	19, 20, 21, 22, 23, 24, 25
D	9.5	5.8	0.8	19, 20, 21, 22, 23, 24, 25
E	9.5	5.8	78.2	19, 20, 21, 22, 23, 24, 25
F	5	11.6	0.8	19, 20, 21, 22, 23, 24, 25
G	6.5	11.6	0.8	19, 20, 21, 22, 23

4.1.2 Characteristic current and voltage curves

Typical current and voltage curves are depicted in figure 4.1.1. We clearly see on the voltage curve for the low inductance circuit (figure 4.1.1a) the existence of two distinct phases in the surface discharge (Trusov (2006); Andreev et al. (1980); Bordage and Hartmann (1982); Beverly III (1986); Larigaldie et al. (1981); Larigaldie (1987b); Larigaldie (1987a); Larigaldie et al. (1992); Lagarkov and Rutkevich (1994)):

- a propagation phase in the first 300 ns: this corresponds to the creation of a conductive plasma channel on the surface of the dielectric after the spark-gap switching;
- a return stroke phase, between 300 ns and 1 μ s, during which the capacitors release their energy and the current oscillates while the voltage returns to 0.

In the high inductance circuit (figure 4.1.1b), the high current phase lasts much longer, up to 15 μ s). The fast heating of the gas and the generation of shock waves takes place during the high current phase. We will then focus on this phase to understand the energy deposition in the discharge through Joule heat-

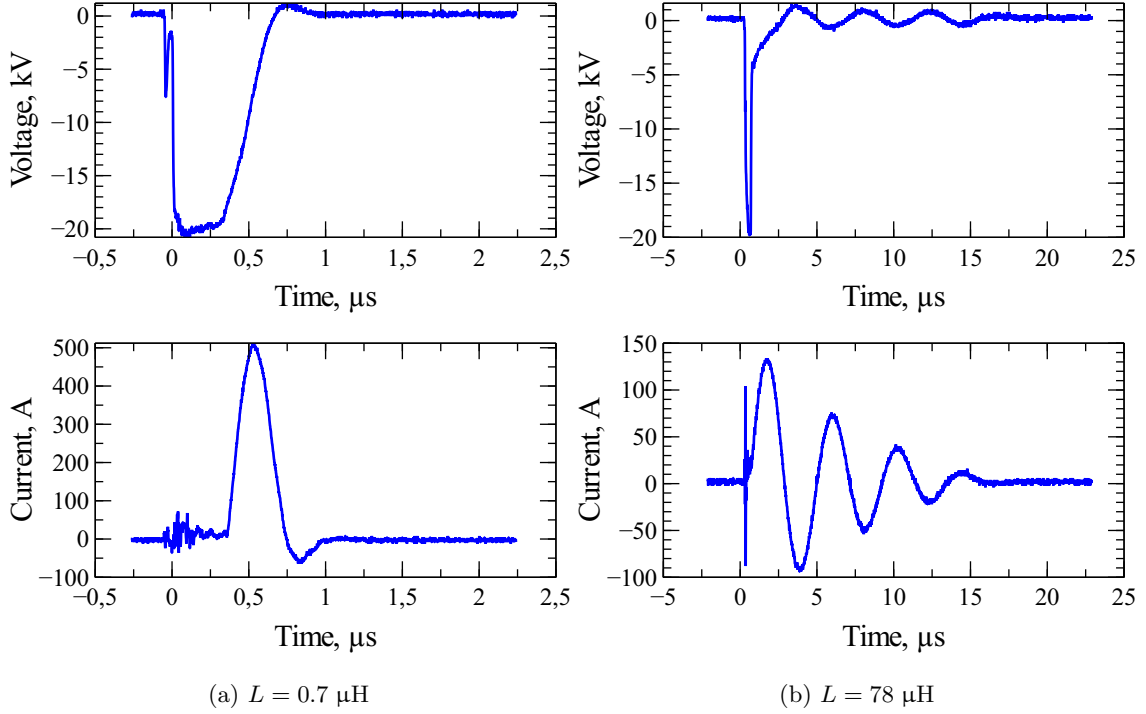


Figure 4.1.1: Current and voltage measured on a discharge of length $l = 95$ mm, with charging voltage $U_C = 22$ kV and total capacitance $C = 5.8$ nF.

ing.

4.1.3 Energy deposition efficiency

In a first analysis, we study the evolution of the energy E_J^∞ deposited in the discharge through Joule heating with the various parameters of table 4.1. The deposited energy is determined by integrating the product of voltage and current over time:

$$E_J^\infty = - \int_0^{+\infty} U_p i_p dt,$$

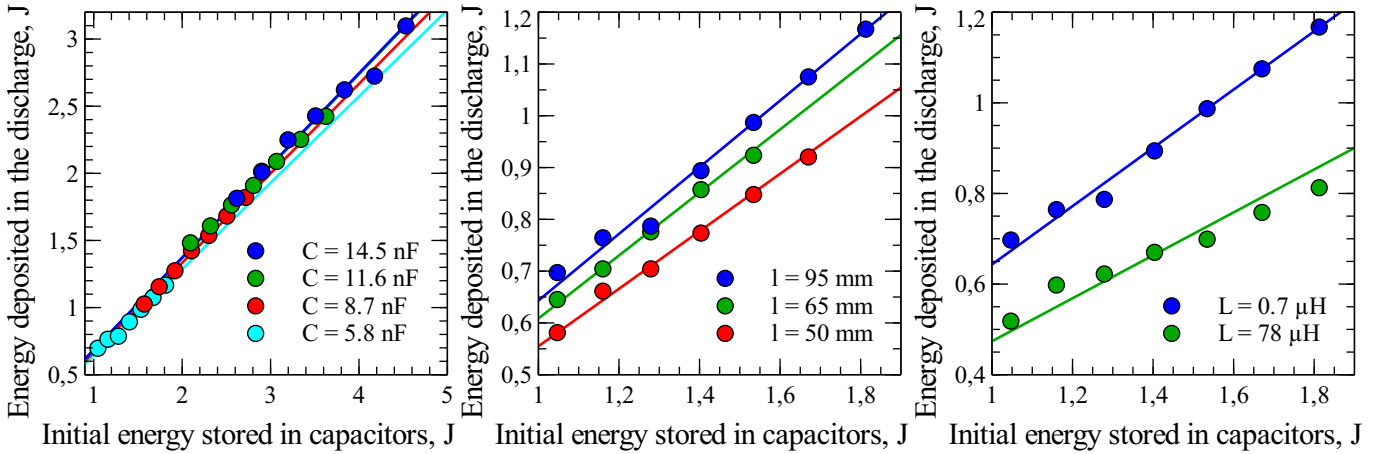
where the minus sign accounts for the circuit orientation. The measured voltage U_p is the sum of the resistive voltage across the discharge $R_p i_p$, and of the inductive voltage $L_p \frac{di_p}{dt}$ (L_p is a stray inductance related to the plasma channel and the wiring in the circuit of the voltage probe, see figure 4.2.1). The inductive component cancels out eventually:

$$E_J^\infty = R_p \int_0^{+\infty} i_p^2 dt + \int_0^{+\infty} L_p \frac{di_p}{dt} i_p dt = \int_0^{+\infty} R_p i_p^2 dt + [L_p i_p^2]_0^{+\infty},$$

given that the current tends to zero before and after the discharge. We can therefore determine the energy deposited in the discharge and the circuit coupling efficiency χ_J defined as the ratio of the energy deposited in the discharge through Joule effect to the total energy stored in the capacitors:

$$\chi_J = \frac{E_J^\infty}{E_C} = \frac{-\int_0^{+\infty} U_p i_p dt}{\frac{CU_C^2}{2}}. \quad (4.1.1)$$

The energy deposited is plotted for various configurations in figure 4.1.2.



(a) Varying capacitance (cases A, B, C and (b) Varying discharge length (cases D, F (c) Varying circuit inductance (cases D and D), $l = 95$ mm, $L = 0.8$ μ H and G), $C = 5.8$ nF, $L = 0.8$ μ H E), $C = 5.8$ nF, $l = 95$ mm

Figure 4.1.2: Energy deposited in the discharge as a function of the initial energy stored in the capacitors for various circuit configurations.

Increasing the circuit capacitance has little impact on the coupling efficiency: the energy deposited in the discharge always accounts for about 70% of the initial energy stored in the capacitors. However, shortening or lengthening the discharge does affect this coupling: the longer the discharge, the more energy is coupled into it. Assuming a given linear resistance for the discharge, increasing the discharge length will increase its total resistance R_p , but will also affect the current i_p . The circuit can be driven into a more or less oscillating mode, which will cause more current to flow in the discharge or in the ballast resistor. The importance of this oscillatory behavior of the circuit is further evidenced when varying the inductance of the circuit: a high inductance circuit exhibits a lower efficiency, with less than 50% of the initial energy effectively deposited in the discharge. The Joule efficiency χ_J is reported for the various circuit configurations in tables 4.2, 4.3, 4.4.

Table 4.2: Joule efficiency χ_J for varying circuit capacitance at fixed discharge length $l = 95$ mm and circuit inductance $L = 0.8$ μH .

Capacitance C , nF	14.5	11.6	8.7	5.8
χ_J	0.69 ± 0.1	0.68 ± 0.1	0.67 ± 0.1	0.64 ± 0.1

Table 4.3: Joule efficiency χ_J for varying discharge length at fixed circuit inductance $L = 0.8$ μH and circuit capacitance $C = 5.8$ nF.

Length l , mm	50	65	95
χ_J	0.55 ± 0.1	0.60 ± 0.1	0.64 ± 0.1

Table 4.4: Joule efficiency χ_J for varying circuit inductance at fixed discharge length $l = 95$ mm and circuit capacitance $C = 5.8$ nF.

Inductance L , μH	0.8	78.2
χ_J	0.64 ± 0.1	0.47 ± 0.1

4.1.4 Energy deposition duration

The circuit characteristics also affect the duration of the energy deposition in the plasma channel. Using voltage and current data (see for instance figure 4.1.3), we compute the Joule energy $E_J(t)$ deposited at time t in the discharge and define some characteristic times:

- t_0 is the discharge initiation time, corresponding to the breakdown of the sparkgap. t_0 is identified on the voltage curve when the discharge voltage U drops below 15 kV;
- t_{RS} marks the transition from the propagation phase to the return stroke phase. t_{RS} is identified on the current curve when the current oscillations start;
- t_F is the discharge finishing time. t_F is identified on the energy curve when the energy $E_J(t)$ reaches (for the first time, as there may be some oscillations as explained in section 4.1.3) 98% of its final value $E_J(t \rightarrow +\infty)$.

These various time marks are then used to define several characteristic durations:

- $\tau_D = t_F - t_0$ is the total duration of the discharge;
- $\tau_P = t_{RS} - t_0$ is the propagation phase duration;
- $\tau_{RS} = t_F - t_{RS}$ is the return stroke phase duration.

These characteristic times can then be plotted as functions of the capacitors initial energy or charging voltage. As can be seen in figure 4.1.4, the total duration of the discharge depends on the initial energy stored in the capacitors. For a given capacitance, increasing the charging voltage hence the initial energy decreases the total duration of the discharge. On the other hand, at a

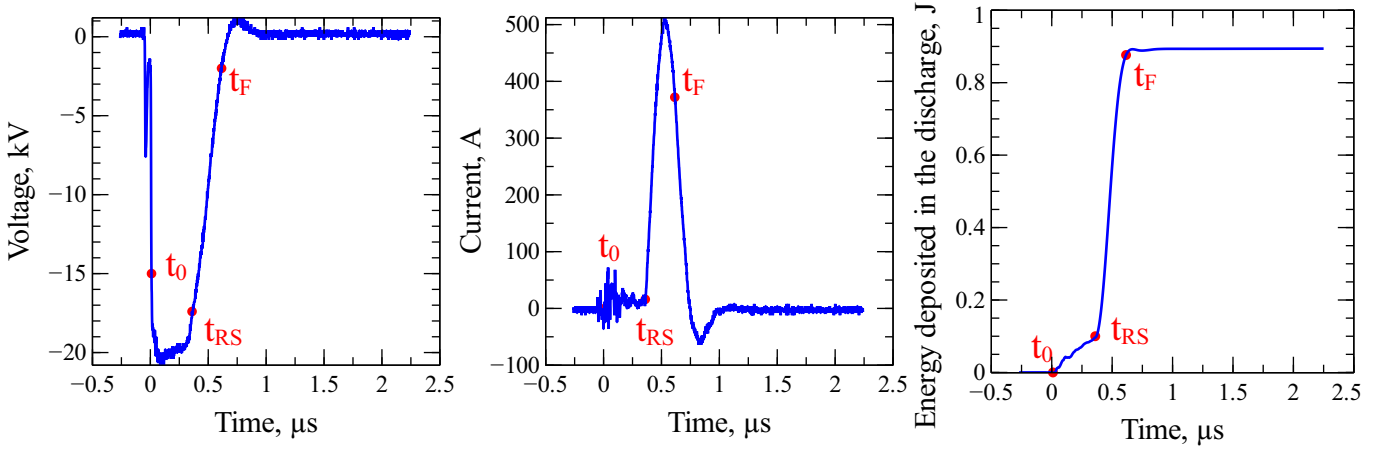


Figure 4.1.3: Definition of the characteristic times t_0 , t_{RS} and t_F .

given voltage, increasing the capacitance hence the initial energy increases the total duration of the discharge. To try and distinguish these influences more precisely, we focus separately on the two phases of the discharge.

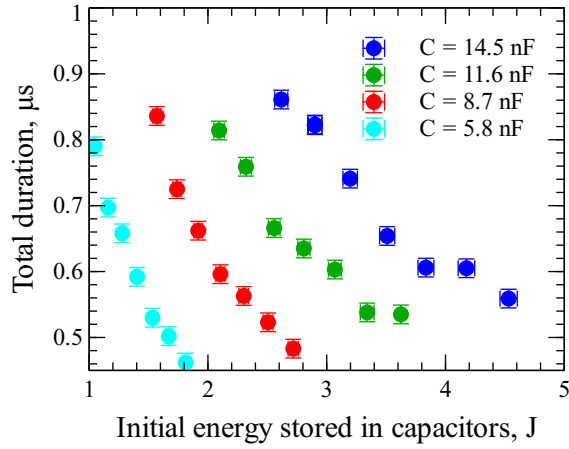


Figure 4.1.4: Total duration τ_D as a function of the energy stored in the capacitors.

4.1.4.1 Propagation phase duration

As can be seen in figure 4.1.5, the propagation phase duration is driven by the initial charging voltage of the capacitors. This is in agreement with the general understanding of the propagation phase of the pulsed surface discharge (Baranov et al. (1984); Andreev et al. (1980); Trusov (2006); Toepler (1921); Andreev et al. (1978); Bordage and Hartmann (1982); Beverly III (1986); Larigaldie et al. (1981); Larigaldie (1987b); Larigaldie (1987a); Larigaldie et al.

(1992); Lagarkov and Rutkevich (1994)): the plasma channel is created in a streamer-like mechanism. When the spark-gap commutes, the tip electrode is negatively biased, just above the surface of a dielectric under which runs the grounded counter-electrode. The local electric field near the high voltage electrode then exceeds the breakdown threshold of air, which leads to the formation of a negative streamer that propagates above the grounded electrode. The whole process of propagation and channel formation is only governed by the initial applied voltage (if the voltage is too low, the propagation can stop within the gap).

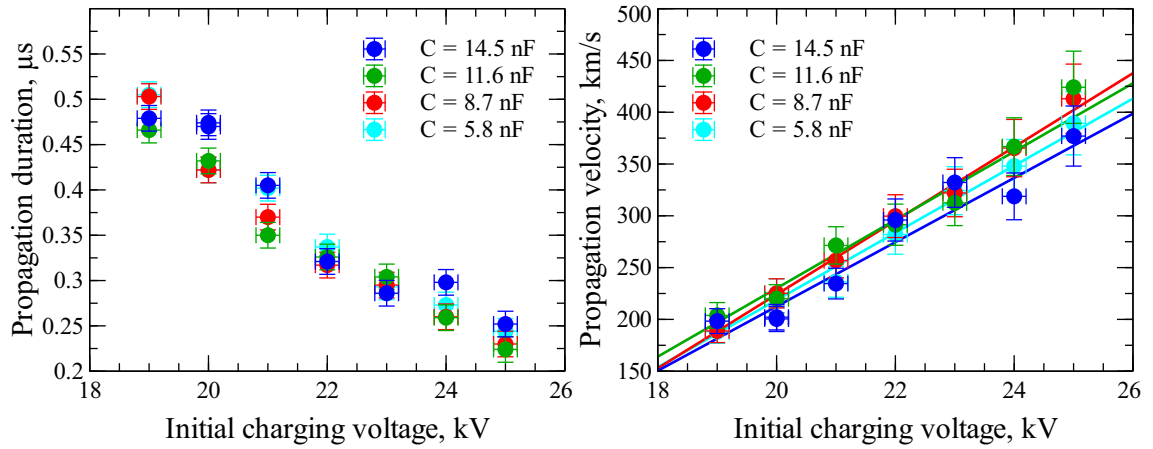


Figure 4.1.5: Propagation duration τ_P and velocity v as a function of the initial energy and of the capacitors voltage, for a discharge of length 95 mm.

The channel propagation velocity v reaches values ranging from 2×10^5 m/s to 4×10^5 m/s and is found to be proportional to the charging voltage U_C according to Toepler's law (Larigaldie et al. (1981); Larigaldie (1987b)):

$$v = \alpha (U_C - V_S), \quad (4.1.2)$$

where α is a constant and V_S a threshold voltage depending on the dielectric material properties (dielectric constant and thickness). The values expected for these parameters are reported in table 4.5.

4.1.4.2 Arc phase duration

The energy and voltage dependence of the arc phase duration (depicted in figure 4.1.6) is more complex to understand.

Increasing the capacitance at a given voltage does increase this duration. This behavior is understandable when considering the equivalent electrical circuit of figure 4.2.1: changing the capacitance in an RLC circuit will affect its parameters (α , ω_0) (see appendix B for details). However, increasing the voltage

Table 4.5: Propagation velocity parameters obtained from data fit and given by Toepler's law.

Constants	α , m/s/V	V_S , kV
Case A	31.0 ± 3.5	13.2 ± 0.9
Case B	33.0 ± 3.9	13.0 ± 0.9
Case C	35.6 ± 3.8	13.7 ± 0.8
Case D	32.4 ± 3.6	13.3 ± 0.9
Toepler	35.0	12.4

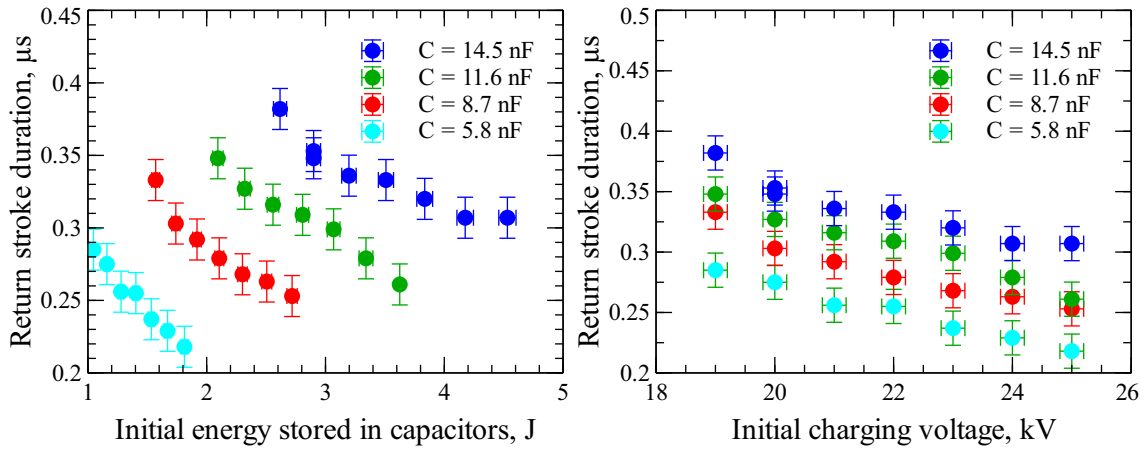


Figure 4.1.6: Return stroke duration τ_{RS} as a function of of the initial energy and of the capacitors voltage, for a discharge of length 95 mm.

at a given capacitance does decreases the return stroke duration. This observation is not compatible with the behavior of a simple RLC circuit (in which the plasma channel behaves as a constant resistance R_p). For a standard RLC circuit, the total Joule energy E_J^∞ deposited in the discharge is given by

$$E_J^\infty = R_p \int_0^{+\infty} i_p^2 dt = \frac{R_p U_0^2}{4\alpha L^2 \omega_0^2}, \quad (4.1.3)$$

where α and ω_0 are circuit parameters (see appendix B for more details). The energy $E_J(t)$ deposited at time t through Joule effect in a constant resistance R_p can therefore be expressed as a fraction f_{E_J} of the total Joule energy:

$$E_J(t) = f_{E_J}(\alpha, \omega_0, t) E_J^\infty, \quad (4.1.4)$$

where the fraction $f_{E_J}(\alpha, \omega_0, t)$ is a function of the RLC circuit parameters α and ω_0 (see equation B.3.6 in appendix B). The time needed to reach a given fraction f_{E_J} should not depend on the circuit charging voltage. This points to some non standard behavior for the plasma channel (variable resistance) that needs to be investigated further.

4.2 Model of the arc phase

4.2.1 Need for a time-varying resistance

The current and voltage curves exhibit oscillations similar to those of a standard RLC circuit. Assuming at first that the discharge behaves (during the return stroke phase) like a constant resistor in series with an inductance, the equivalent circuit is depicted on figure 4.2.1. L is the complete inductance of

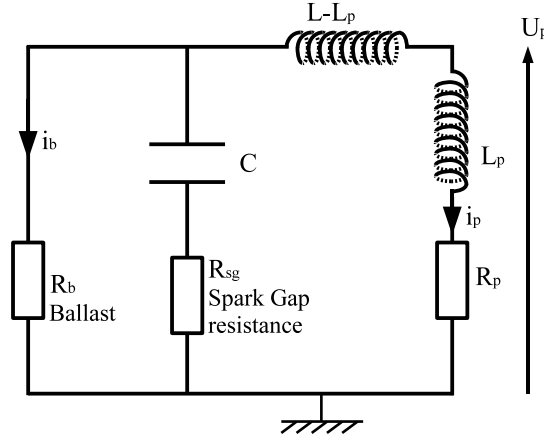


Figure 4.2.1: Equivalent circuit during the return stroke phase. R_{sg} models the wires and sparkgap resistance, the plasma channel is modeled by a resistance $R_p(t)$ and an inductance L_p .

the current loop comprising the discharge, whereas L_p is a stray inductance related to the plasma channel and the wiring between the connection points of the voltage probe.

The current i_p flowing in the discharge is driven by the following equation:

$$\partial_{tt}i_p + 2\alpha\partial_t i_p + \omega_0^2 i_p = 0.$$

We can solve this differential equation with initial conditions at $t = 0$:

$$\begin{aligned} i(t = 0) &= 0, \\ \partial_t i(t = 0) &= \frac{U_0}{L}, \end{aligned}$$

which leads to the standard oscillating solution (see appendix B for more details):

$$i(t) = \frac{U_0}{L\sqrt{\omega_0^2 - \alpha^2}} \sin\left(\sqrt{\omega_0^2 - \alpha^2}t\right) e^{-\alpha t} \quad (4.2.1)$$

with U_0 the capacitors voltage at the beginning of the return stroke phase. ω_0 and α are the frequency and dampening parameters for this circuit:

$$\alpha = \frac{R_p}{2L} + \frac{R_{sg}R_b}{2(R_{sg} + R_b)L} + \frac{1}{2(R_{sg} + R_b)C}, \quad \omega_0^2 = \frac{R_p + R_b}{R_{sg} + R_b} \frac{1}{LC}.$$

To determine the energy deposited by Joule heating in the discharge (see equation (4.1.3)), we must know the parameters α and ω_0 that are functions of the plasma channel resistance R_p and the wires and sparkgap resistance R_{sg} . If the plasma were indeed a constant resistor, for a given circuit configuration (with fixed value of inductance L , resistances R_{sg} and R_b and total capacitance C), the normalized currents measured at different voltages should collapse to the same damped sinusoidal waveform given by equation (4.2.1). However, as evidenced on figure 4.2.2, the current waveform clearly depends on the initial charging voltage (or initial energy stored in the capacitors): the higher this initial energy, the shorter the pseudo-period and the higher the oscillation amplitude. This leads us to assume a voltage (or energy) dependence for the plasma resistance $R_p(U)$.

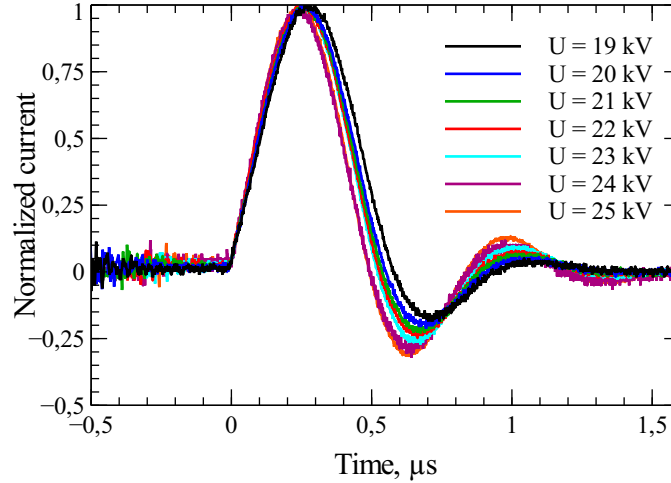


Figure 4.2.2: Current measured in the plasma channel and normalized by its maximum value, for different charging voltages and a fixed circuit configuration ($R_{sg} = 0.79 \Omega$, $L = 0.8 \mu\text{H}$, $C = 14.5 \text{ nF}$, $R_b = 1.7 \text{ k}\Omega$).

We tried to fit the measured current with the solution given by equation (4.2.1). If the fit is rather good for high inductance circuits, the reconstruction is not as good for the low inductance cases, where the first half oscillation cannot be fitted with the same parameters as the second half, as can be seen on figure 4.2.3. This further points to a time dependence of the plasma channel resistance $R_p(t)$

We must resort to a finer model of the circuit 4.2.1 with a time-varying resistance $R_p(t)$ for the plasma channel. During the return stroke phase, the electric charge Q carried by the capacitors and the current i_p flowing through the surface discharge are governed by a system of coupled differential equations:

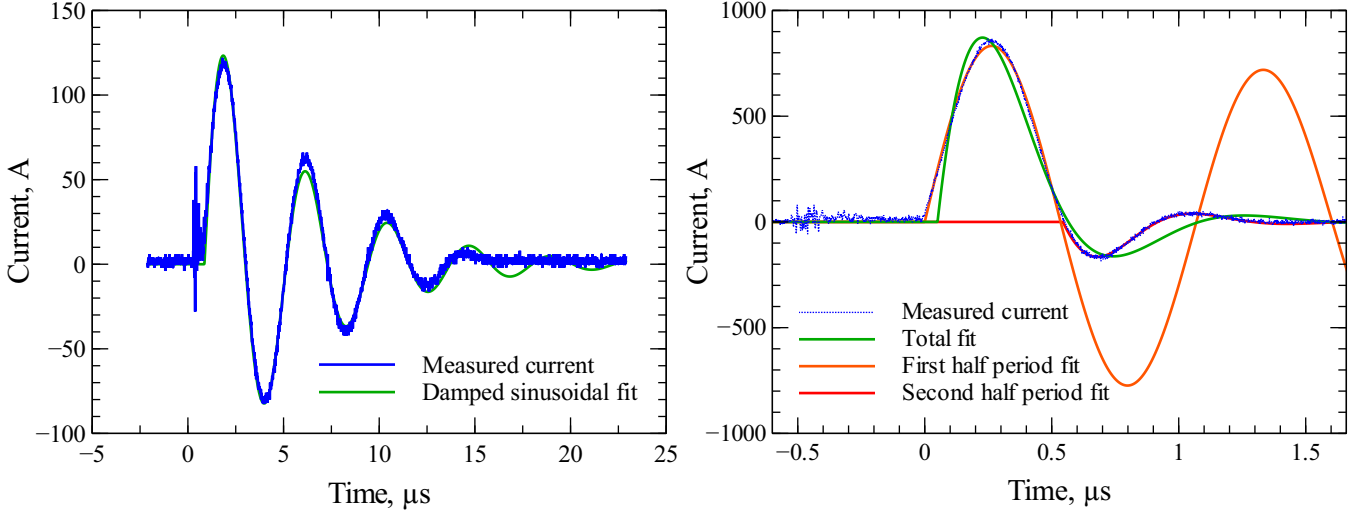
(a) $L = 78 \mu\text{H}$, $C = 5.8 \text{ nF}$ (b) $L = 0.7 \mu\text{H}$, $C = 14.5 \text{ nF}$

Figure 4.2.3: Current fit by a damped sinusoidal waveform in a high inductance circuit and in a low inductance circuit. In both cases, the discharge is 9.5 cm-long, and the capacitors were charged up to 20 kV. The discrepancies observed in the fit attempts for a low inductance circuit point to a time dependent resistor $R_p(t)$.

$$\frac{Q}{C} + R_{sg} \frac{dQ}{dt} = - \left(R_p(t) i_p + L \frac{di_p}{dt} \right), \quad (4.2.2a)$$

$$\frac{Q}{C} + R_{sg} \frac{dQ}{dt} = -R_b i_b = -R_b \left(\frac{dQ}{dt} - i_p \right). \quad (4.2.2b)$$

Note that the spark-gap is still modeled as a constant resistor R_{sg} , and not as a time-varying resistor. In fact, when the spark-gap is triggered, first the discharge propagates on the dielectric surface towards the grounded electrode. The propagation phase duration is linked to the streamer velocity, typically $10^5 - 10^6 \text{ m/s}$ (Larigaldie (1987a)). Therefore the propagation phase lasts a few hundreds of nanoseconds, during which a capacitive current flows through the spark-gap to propagate the leader toward the grounded electrode. Hence, at the beginning of the return stroke phase, the spark-gap, whose voltage fall time (during which the spark-gap resistance varies) is in the range of 5 – 10 ns has reached a steady resistance value. Since this analysis is restricted to the the return stroke phase, the spark-gap is therefore modeled as a simple constant resistor $R_{sg} = 0.79 \Omega$ (value obtained through fit).

We can write system (4.2.2) as two first order differential equations:

$$\partial_t Q = -\frac{Q}{(R_{sg} + R_b)C} + \frac{R_b i_p}{(R_{sg} + R_b)}, \quad (4.2.3a)$$

$$\partial_t i_p = -\left(\frac{R_b Q}{(R_{sg} + R_b)LC} + \left(\frac{R_{sg} R_b}{(R_{sg} + R_b)} + R_p(t)\right)\frac{i_p}{L}\right), \quad (4.2.3b)$$

that can be solved numerically. However, to do so, we first need to choose a model for the time-varying resistance $R_p(t)$.

In all that follows, we consider a cylindrical channel of length l with axial invariance, that is its properties do not depend on the position along the axis. The channel resistance $R_p(t)$ at time t is given by:

$$R_p(t) = \frac{l}{\int_{S(t)} \sigma(r, t) dS}, \quad (4.2.4)$$

where the channel conductivity $\sigma(r, t)$ is integrated over the channel section $S(t)$. Several resistance models for sparks have been proposed and analyzed in the literature (Engel et al. (1989); Montaño et al. (2006)). The oscillatory behavior of the measured current limits the possible choices to the Rompe-Weizel (Rompe and Weizel (1944); Weizel and Rompe (1947)), Vlastós (Vlastós (1972)), Braginskii (Braginskii (1958)) and Toepler (Toepler (1906); Toepler (1921)) models as other models would exhibit singularities and inconsistent values. The Toepler model lacks theoretical justification and is based solely on experimental results. The Rompe-Weizel, Vlastós and Braginskii resistance models are derived from energy considerations for a plasma channel of length l homogeneous on its cylindrical section.

4.2.2 Rompe-Weizel model

The Rompe-Weizel model (Rompe and Weizel (1944); Weizel and Rompe (1947)) assumes that the energy deposited in the plasma is channeled to the electron gas through ionization only. In other words, the power deposited in the channel is used to produce new electron-ion pairs, while the electron temperature remains unchanged and other loss terms (conductivity, radiation, elastic collisions) are neglected. With these assumptions, the rate of change of the electron energy u is directly related to the Joule heating:

$$\frac{du}{dt} = \frac{j^2}{\sigma} \quad (4.2.5)$$

where we have assumed the local Ohm's law $\mathbf{j} = \sigma \mathbf{E}$, with σ the channel conductivity and \mathbf{E} the driving electric field. The channel conductivity is:

$$\sigma = n_e \mu_e e, \quad (4.2.6)$$

with n_e and μ_e the electron number density and mobility, and the electron energy is (Rompe and Weizel (1944); Weizel and Rompe (1947)):

$$u = n_e \left(\frac{3}{2} k_B T_e + e\phi_I \right). \quad (4.2.7)$$

Here $e\phi_I$ is the ionization cost, that may be greater than the simple ionization energy of nitrogen or oxygen. For a simple numerical evaluation, we consider this cost to be at least equal to Stoletov's constant (Raizer (1997)) which gives the optimal ionization cost in an avalanche process in air. Replacing (4.2.6) and (4.2.7) in (4.2.5), the conductivity is obtained as:

$$\sigma^{\text{RW}} = \left(\frac{2\mu_e e \int j^2(t) dt}{\frac{3}{2} k_B T_e + e\phi_I} \right)^{\frac{1}{2}}. \quad (4.2.8)$$

We have assumed constant properties across the channel section, therefore the current density $j(t)$ is simply equal to the current divided by the channel section $j(t) = \frac{i_p(t)}{S(t)}$. Integrating across the channel section, all geometric dependence cancels out and we get eventually:

$$R_p^{\text{RW}}(t) = \frac{k^{\text{RW}} l}{\left(\int_{-\infty}^t i_p^2(t) dt \right)^{\frac{1}{2}}}, \quad k^{\text{RW}} = \left(\frac{\frac{3}{2} k_B T_e + e\phi_I}{2\mu_e e} \right)^{\frac{1}{2}}. \quad (4.2.9)$$

4.2.3 Vlastós model

The Vlastós model (Vlastós (1972)) considers a fully or quasi-fully ionized plasma (single ionization, $n_e = n_i = n$), where Coulomb collisions drive the plasma properties. The plasma internal energy at local thermal equilibrium ($T_e = T_i = T$) is:

$$u = \frac{3}{2} n_e k_B T_e + \frac{3}{2} n_i k_B T_i, \quad (4.2.10)$$

the first term corresponding to the electrons energy, and the second term to the ions energy. Using Spitzer formula for the plasma conductivity (Vlastós (1972)):

$$\sigma = 0.153 \frac{T^{\frac{3}{2}}}{\ln \Lambda}, \quad (4.2.11)$$

with $\ln \Lambda$ the Coulomb logarithm, where $\ln \Lambda \approx 12-15$ (Goldston and Rutherford (1995)). Note that in (4.2.11) the plasma conductivity is independent of the number density. By integration of (4.2.5) over the channel section and length, substituting σ for T from (4.2.11) in (4.2.10) yields:

$$R_p^{\text{V}}(t) = \frac{k^{\text{V}} l}{\left(\int_{-\infty}^t i_p^2(t) dt \right)^{\frac{3}{5}}}, \quad k^{\text{V}} = \frac{\left(r_0^2 \ln^2 \Lambda n^3 \right)^{\frac{1}{5}}}{6.97 \times 10^{12}}, \quad (4.2.12)$$

where r_0 is the plasma channel radius (assumed to be constant).

4.2.4 Braginskii model

The Braginskii model (Braginskii (1958); Oreshkin and Lavrinovich (2014)) assumes that the channel conductivity is constant over time and that the variation of resistance is due solely to the channel hydrodynamic expansion. Starting from a narrow current-carrying filament, energy deposition through Joule effects heats the channel, raising its pressure, temperature and ionization. Braginskii then considers that the channel behaves as a piston, generating a shock where ionization occurs. Behind the shock determined by the channel radius $a(t)$, the various channel properties are assumed to be constant. The channel squared radius $a^2(t)$ is determined through conservation of energy, taking into account the channel hydrodynamic expansion, which leads to:

$$a^2(t) = \left(\frac{4}{\pi^2 \rho_0 \xi \sigma} \right)^{\frac{2}{3}} \int_{-\infty}^t i_p(t)^{\frac{2}{3}} dt, \quad (4.2.13)$$

with σ and ρ_0 the gas conductivity and its density (outside of the channel radius), assumed to be constant. ξ is an additional constant that depends on the gas properties. Plugging this expression for the channel radius in the resistance formula 4.2.4, we get:

$$R_p^B(t) = \frac{k^B l}{\int_{-\infty}^t i_p(t)^{\frac{2}{3}} dt}, \quad k^B = \left(\frac{\xi \rho_0}{4\pi \sigma^2} \right)^{\frac{1}{3}} \quad (4.2.14)$$

4.2.5 Toepler model

The Toepler model (Toepler (1921)) is purely empirical, and the corresponding arc resistance is given by:

$$R_p^T(t) = \frac{k^T l}{\int_{-\infty}^t i_p(t) dt} \quad (4.2.15)$$

with k^T a constant.

4.2.6 Nondimensionalization and numerical resolution

The goal of our modeling is to describe the discharge current pulse during the return stroke phase, using equations (4.2.3a) and (4.2.3b) and the various models mentioned above. The propagation phase is not described here, but its effect of leaving an ionized channel that bridges the electrodes is accounted for by the initial channel resistance $R_p(0)$. If $t = 0$ is the beginning of the return stroke phase, the channel resistance, in the Rompe-Weizel model, is written as:

$$R_p^{RW}(t) = \frac{k^{RW} l}{\left(A_0 + \int_0^t i_p^2(t) dt \right)^{\frac{1}{2}}}, \quad t \geq 0 \quad (4.2.16)$$

where $A_0 = \int_{-\infty}^0 i_p^2(t) dt$.

An optimization process is used to fit the experimental current curves. We define the dimensionless variables:

$$\tilde{Q} = \frac{Q}{CU_0}, \quad \tilde{i} = \frac{i_p}{I}, \quad \tilde{t} = \frac{t}{\delta t} \quad (4.2.17)$$

with δt the reference timescale and I the reference current. For the Rompe-Weizel model, using the same formalism as equation (4.2.16), the time-varying-resistance can be rewritten as:

$$R_p^{\text{RW}}(t) = \frac{R_0^{\text{RW}}}{\tilde{A}^{\frac{1}{2}}}, \quad R_0^{\text{RW}} = \frac{k^{\text{RW}} l}{(I^2 \delta t)^{\frac{1}{2}}}, \quad \tilde{A} = \frac{A_0 + \int_0^t i_p^2 dt}{I^2 \delta t}. \quad (4.2.18)$$

Setting $\delta t = (R_b + R_{sg})C$, $I = U_0/R_b$, $\tau_C = R_b C$, $\tau_L = L/R_b$ the system of integro-differential equations can be transformed in:

$$\frac{d\tilde{Q}}{d\tilde{t}} = -\tilde{Q} + \tilde{i}, \quad (4.2.19a)$$

$$\frac{d\tilde{i}}{d\tilde{t}} = -\frac{\tau_C}{\tau_L} \left(\tilde{Q} + \frac{R_{sg}}{R_b} \tilde{i} \right) - \frac{\delta t R_0}{\tau_L R_b} \frac{\tilde{i}}{\tilde{A}^m}, \quad (4.2.19b)$$

$$\frac{d\tilde{A}}{d\tilde{t}} = \tilde{i}^n. \quad (4.2.19c)$$

m and n are dimensionless numbers relative to the resistance model, given in table 4.6 with the relevant expression of R_0 and \tilde{A} .

Table 4.6: Expressions of R_0 and \tilde{A} and values for the m and n parameters for the different resistance models.

Resistance model	R_0	\tilde{A}	m	n
Rompe-Weizel	$\frac{k^{\text{RW}} l}{(I^2 \delta t)^{\frac{1}{2}}}$	$\frac{A_0 + \int_0^t i_p^2 dt}{I^2 \delta t}$	$\frac{1}{2}$	2
Vlastós	$\frac{k^{\text{V}} l}{(I^2 \delta t)^{\frac{3}{5}}}$	$\frac{A_0 + \int_0^t i_p^2 dt}{I^2 \delta t}$	$\frac{3}{5}$	2
Braginskii	$\frac{k^{\text{T}} l}{I^{\frac{2}{3}} \delta t}$	$\frac{A_0 + \int_0^t i_p^{\frac{2}{3}} dt}{I^{\frac{2}{3}} \delta t}$	1	$\frac{2}{3}$
Toepler	$\frac{k^{\text{T}} l}{I \delta t}$	$\frac{A_0 + \int_0^t i_p dt}{I \delta t}$	1	1

The initial conditions for the integration are:

$$\tilde{Q}(0) = 1, \quad \tilde{i}(0) = 0, \quad \tilde{A}(0) = \tilde{A}_0 \quad (4.2.20)$$

The electrical circuit parameters (R_{sg}, R_b, L, C) are known experimentally, and the initial voltage U_0 is measured after the streamer phase that bridges the gap. The behavior of the non-dimensional current is driven by the choice of the

two parameters (R_0, \tilde{A}_0) . For a given set of parameters, the non-dimensional system (4.2.19) is solved using a 4-th order Runge-Kutta method. Hence, using an initial guess $(R_0, \tilde{A}_0)(0)$, these parameters (R_0, \tilde{A}_0) are iteratively optimized using a least square method to minimize the fit error e . The time evolution described by (4.2.19) is computed for each iteration.

For the three models under consideration here, the same initial guess and the same optimization process are retained. The optimization stops when one of the two following termination criteria is met:

$$\int (\tilde{i}^{\text{exp}} - \tilde{i}^{\text{fit}})^2 d\tilde{t} < 1.5 \times 10^{-8}. \quad (4.2.21)$$

or, at iteration n :

$$\sqrt{\left(\frac{R_0^{(n)} - R_0^{(n-1)}}{R_0^{(n)}}\right)^2 + \left(\frac{\tilde{A}_0^{(n)} - \tilde{A}_0^{(n-1)}}{\tilde{A}_0^{(n)}}\right)^2} < 1.5 \times 10^{-8}. \quad (4.2.22)$$

After the optimization procedure, the discharge resistance is given by:

$$R_p(t) = \frac{R_0}{\tilde{A}(t)^m}, \quad (4.2.23)$$

and the initial channel resistance, at the beginning of the return stroke phase, is $R_p(0) = R_0/\tilde{A}_0^m$.

4.3 Comparison with experimental data

4.3.1 Fit initialization with theoretical values

Initial values for the parameters (k, A_0) are needed to start the optimization process. We estimate a theoretical value of k for the various models, under the following assumptions:

- Rompe-Weizel model (4.2.9): to our knowledge, the electron temperature has not been measured in the return stroke phase of surface discharges in air. However, estimates of the electron temperature during the propagation phase have been obtained $T_e \approx 5 - 9$ eV based on spectroscopic measurement (Bordage and Hartmann (1982)). We assume that the plasma keeps this range of electron temperature afterwards, during the return stroke phase. The ionization cost can be taken equal to the ionization energy of O_2 , that is $e\phi_I = 12.2$ eV which leads to $k^{\text{RW}} = 12.9 \text{ V} \cdot \text{s}^{1/2} \cdot \text{m}^{-1}$. However, this completely overlooks other inelastic processes, such as ionization of N_2 , dissociation of both molecules and ionization of the corresponding atoms. Instead, we use the Stolev's constant, that gives the optimal (minimum) ionization cost in an avalanche process $e\phi_I = 66.0$ eV (Raizer (1997)) in air. For air at

atmospheric pressure (Raizer (1997)), the electron mobility is taken as $\mu_e \approx 0.059 \text{ m}^2\text{V}^{-1}\text{s}^{-1}$. These assumptions lead to a theoretical value of $k^{\text{RW}} = 25.0 \text{ V} \cdot \text{s}^{1/2} \cdot \text{m}^{-1}$.

- Vlastós model (4.2.12): an estimate of the arc channel radius is required. A time integrated imaging of the arc channel gives such an estimate $r_0 = 0.5 \text{ mm}$. The Coulomb logarithm is supposed to be constant $\ln^2 \Lambda \approx 12 - 15$ (Vlastós (1972)) and assuming full ionization of the gas initially in the arc channel volume, we get a plasma number density $n = 2.6 \times 10^{25} \text{ m}^{-3}$ (Vlastós (1972)). This leads to a theoretical value of $k^{\text{V}} = 41 \text{ V} \cdot \text{A}^{1/5} \cdot \text{s}^{3/5} \text{m}^{-1}$.
- Braginskii model (4.2.14): with a conductivity $\sigma = 200 \text{ } \Omega/\text{cm}$ and $\xi = 4.5$ (Braginskii (1958); Oreshkin and Lavrinovich (2014)) in air $\rho_0 = 1.29 \times 10^{-3} \text{ kg/m}^3$, the theoretical value for the resistance prefactor is $k^{\text{B}} = 2.4 \times 10^{-3} \text{ V} \cdot \text{A}^{-1/3} \cdot \text{s} \cdot \text{m}^{-1}$.

The Toepler model does not provide any formula for the prefactor k , but a generally used value (Toepler (1926); Toepler (1927); Vlastós (1969); Osmokrović et al. (1992)) is $k^{\text{T}} = 1.5 \times 10^{-2} \text{ V} \cdot \text{sm}^{-1}$.

We also need an initial value for the parameter A_0 (to avoid a division by zero in the resistance). This parameter gives the plasma channel resistance (see table 4.6 after its formation during the propagation phase. Since we focus our analysis on the return stroke phase, we lack any model for this value. We will simply assume an initial linear resistance of $1000 \text{ } \Omega/\text{m}$ and compute the A_0 parameter accordingly with the initial values of k mentioned previously.

4.3.2 Analysis in terms of reconstruction accuracy

As a first step, the result of the fitting procedure is analyzed for two cases. Figure 4.3.1 and 4.3.2 give the reconstructed current waveform and the error, for a measurement in a low inductance circuit and a high inductance circuit respectively. For the low inductance configuration, the best fit is obtained with the Rompe-Weizel model. The Vlastós, Toepler and Braginskii models capture the oscillations but deviate further from experimental values, especially in the first half-oscillation. As seen in section 4.1.4, most of the energy is coupled in the discharge in the early stage of the discharge.

For the high inductance configuration (figure 4.3.2), the Rompe-Weizel, Vlastós and Toepler models behave similarly and fit rather closely the experimental current. The Braginskii model however is not as successful, particularly in the later stage of the discharge (after about $8 \text{ } \mu\text{s}$). The discrepancy observed after $15 \text{ } \mu\text{s}$ for all models is probably due to the spark-gap extinction: setting $R_{sg} = \infty$ in system (4.2.3), the current i_p decreases down to zero.

As can be seen in figure 4.3.3, the channel resistance predicted by the various models falls down in the first microsecond down to an almost constant value, whether in a high or low inductance circuit. In a high inductance circuit, the resistance can be taken as constant, since the current oscillations last much

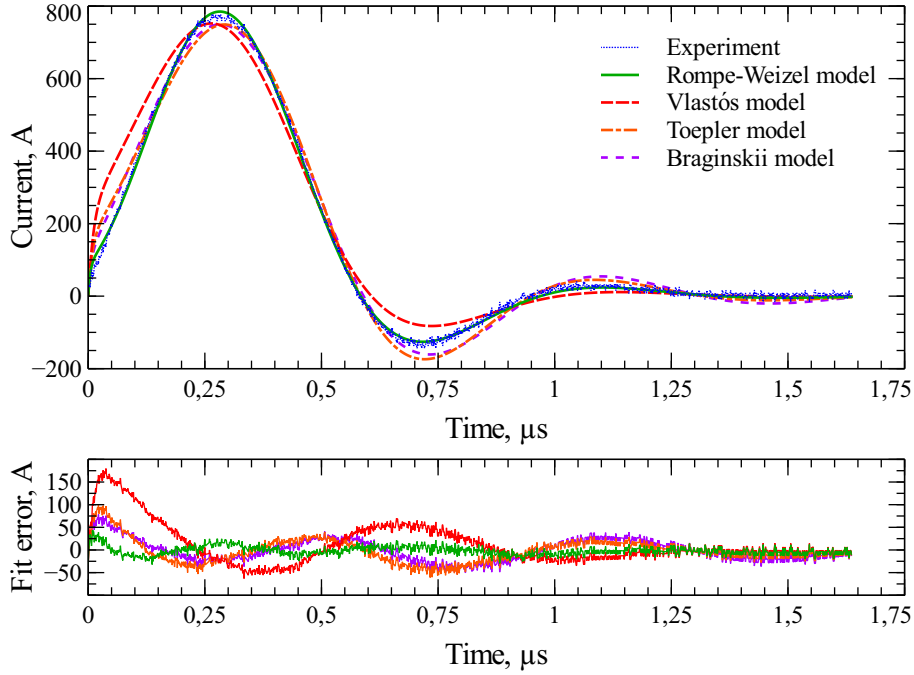


Figure 4.3.1: Current measured in the plasma channel during the return stroke phase and its reconstructions according to the various models ($L = 0.8 \mu\text{H}$, $l = 95 \text{ mm}$, $C = 14.5 \text{ nF}$, $U_C = 19 \text{ kV}$).

longer than the resistance evolution (see figures 4.3.2 and 4.3.3b). Thus, a high-inductance circuit can be described with a simple dampened oscillator, as evidenced in figure 4.2.3a. For a low inductance circuit however, the variable resistance must be taken into account to describe the early rise of the current, as seen in figure 4.2.3.

The various resistance models are compared by computing the reconstruction error between the (non-dimensional) measured current and its non-dimensional value predicted according to the various models in the return stroke phase:

$$e^M = \sqrt{\int (\tilde{i}^{\text{exp}} - \tilde{i}^M)^2 d\tilde{t}}. \quad (4.3.1)$$

with \tilde{i}^{exp} the non-dimensional experimental current, \tilde{i}^M the non-dimensional current computed according to model M, and \tilde{t} the non-dimensional time.

For all the low inductance configurations, the Rompe-Weizel gives the best current reconstruction accuracy, as indicated in table 4.7. The Vlastós model is also in rather good agreement, though not as good as the Rompe-Weizel model. A finer analysis shows that the two models differ mainly during the initial current rise of the return stroke, while they merge later during the discharge. This result is in agreement with the resistance expression for both

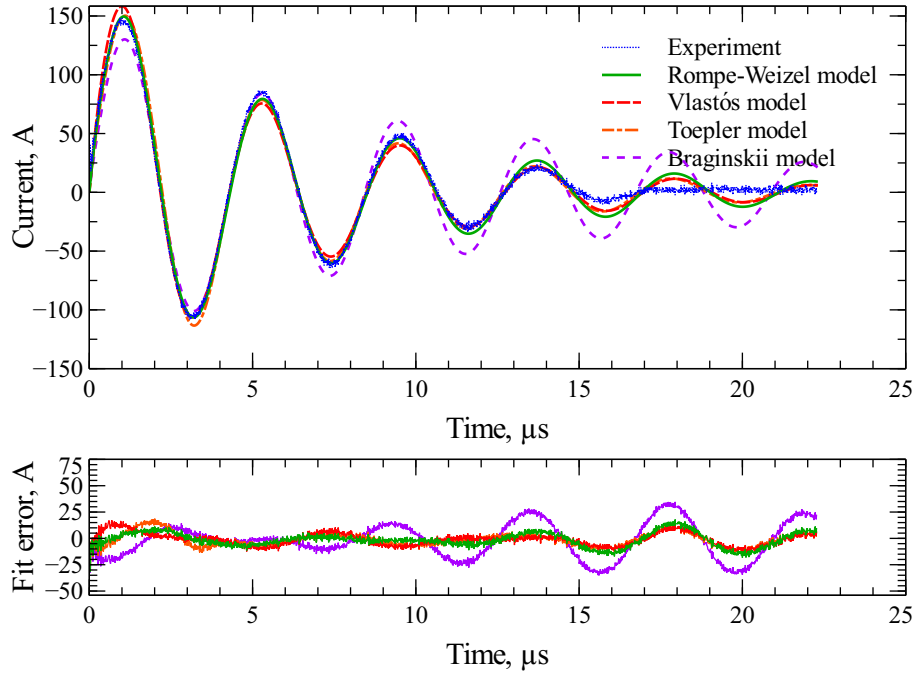
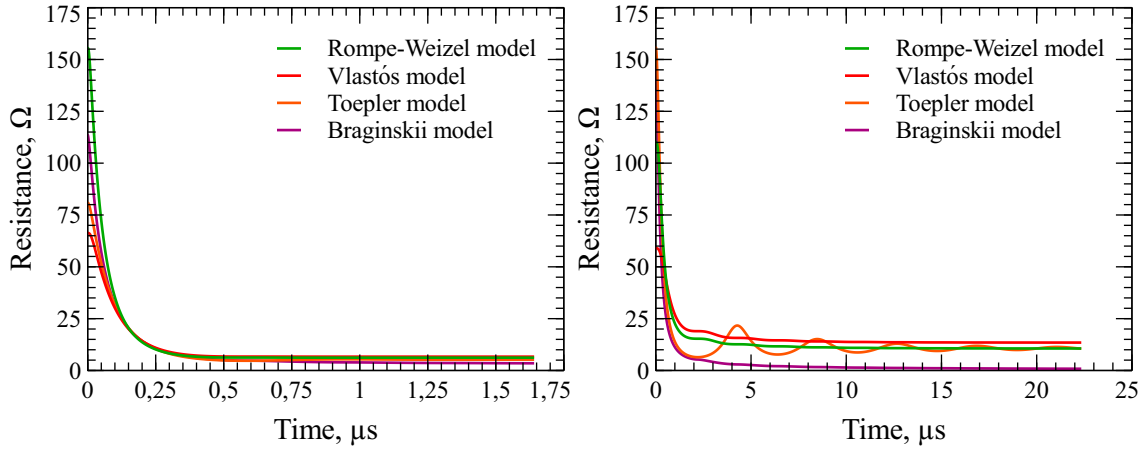


Figure 4.3.2: Current measured in the plasma channel during the return stroke phase and its reconstructions according to the various models ($L = 78.2 \mu\text{H}$, $l = 95 \text{ mm}$, $C = 5.8 \text{ nF}$, $U_C = 24 \text{ kV}$).



(a) $L = 0.7 \mu\text{H}$, $C = 14.5 \text{ nF}$, $U_C = 19 \text{ kV}$.

(b) $L = 78 \mu\text{H}$, $C = 5.8 \text{ nF}$, $U_C = 24 \text{ kV}$

Figure 4.3.3: Resistance evolution predicted by the various models for a discharge of length $l = 95 \text{ mm}$.

models, which is proportional to some power of the inverse action integral. The transient behavior of the channel resistance is blurred after a few hundreds ns,

as can be noticed on figure 4.3.8 for instance. Our optimization procedure will then fit the resistance parameters so that the asymptotic steady value allows the best current reconstruction. The Toepler and Braginskii models lead to both greater error and dispersion.

Table 4.7: Mean values and standard deviation of the reconstruction error e^M given by equation (4.3.2) for the various resistance models in low inductance circuits. The Rompe-Weizel gives the best fit for all test cases, whereas the Toepler and Braginski models deviate farther from experimental data. The Vlastós model is in good overall agreement with measurements, though careful examination shows a stronger deviation in the early stage of the return stroke phase.

Model	Rompe-Weizel	Vlastós	Toepler	Braginski
Case A	0.42 ± 0.07	0.69 ± 0.17	0.80 ± 0.07	0.81 ± 0.10
Case B	0.41 ± 0.05	0.79 ± 0.39	0.80 ± 0.06	0.77 ± 0.07
Case C	0.41 ± 0.07	0.59 ± 0.05	0.74 ± 0.04	0.73 ± 0.08
Case D	0.44 ± 0.05	0.58 ± 0.05	0.73 ± 0.04	0.68 ± 0.06
Case F	0.68 ± 0.24	0.79 ± 0.20	0.71 ± 0.09	1.01 ± 0.12
Case G	0.46 ± 0.08	0.69 ± 0.16	0.71 ± 0.03	0.81 ± 0.05

For the high inductance configuration, the reconstruction error given in table 4.8 is computed with equation (4.3.2) by integration up to times that may exceed the spark-gap extinction (15 μ s for instance in the case depicted in figure 4.3.2). The Braginskii model deviates the farthest from experiment, whereas the Rompe-Weizel, Vlastós and Toepler models exhibit similar accuracy.

Table 4.8: Mean values and standard deviation of the reconstruction error e^M given by equation (4.3.2) for the various resistance models in high inductance circuits.

Model	Rompe-Weizel	Vlastós	Toepler	Braginski
Case E	0.68 ± 0.06	0.71 ± 0.11	0.92 ± 0.23	2.78 ± 0.63

4.3.3 Evolution of the parameters k and A_0

The fitting procedure yields the two optimal parameters (R_0 and \tilde{A}_0) from which we compute back the dimensional parameters k and A_0 . In all cases, we obtain $\tilde{A}_0 \ll \tilde{A}$, where \tilde{A} is the total action integral during the return stroke phase. The parameter A_0 corresponds to the initial resistance of the discharge channel, as shown in (4.2.23), which in turn depends on the propagation phase that occurs before the return stroke. This phase is not modeled here, hence the lack of theoretically expected values for A_0 in the various models. The parametric experiments do not show a clear trend for this parameter. In fact,

the fit error is not very sensitive to the value of this parameter, since $A_0 \ll A(t)$. A change of 20% of the optimal value of \tilde{A}_0 leads to nearly identical value for the fit error e .

Table 4.9: Mean value and standard deviation of the parameter A_0 for the various models.

Model	Rompe-Weizel (SI)	Vlastós (SI)	Toepler (SI)	Braginski (SI)
Case A	$2.67 \pm 0.71 \times 10^{-4}$	$2.93 \pm 1.06 \times 10^{-3}$	$1.72 \pm 0.24 \times 10^{-5}$	$1.60 \pm 0.30 \times 10^{-6}$
Case B	$3.29 \pm 0.45 \times 10^{-4}$	$4.32 \pm 4.79 \times 10^{-3}$	$1.53 \pm 0.21 \times 10^{-5}$	$1.66 \pm 0.12 \times 10^{-6}$
Case C	$2.32 \pm 1.05 \times 10^{-4}$	$1.05 \pm 0.41 \times 10^{-3}$	$1.18 \pm 0.21 \times 10^{-5}$	$1.23 \pm 0.27 \times 10^{-6}$
Case D	$3.29 \pm 1.05 \times 10^{-4}$	$1.71 \pm 0.53 \times 10^{-3}$	$1.54 \pm 0.22 \times 10^{-5}$	$1.64 \pm 0.28 \times 10^{-6}$
Case F	$2.16 \pm 1.53 \times 10^{-4}$	$1.91 \pm 0.91 \times 10^{-3}$	$1.06 \pm 0.20 \times 10^{-5}$	$1.75 \pm 0.61 \times 10^{-6}$
Case G	$2.13 \pm 0.87 \times 10^{-4}$	$1.40 \pm 0.54 \times 10^{-3}$	$1.06 \pm 0.16 \times 10^{-5}$	$1.34 \pm 0.22 \times 10^{-6}$

On the contrary, the fitting procedure is sensitive to the parameter R_0 , since it drives the resistance prefactor k and thus the channel resistance. As an example, a change of 20% on k leads to a 5-times increase of the fit error. The optimum value of the parameter k for the various models and its theoretical value (see model details in sections 4.2.2, 4.2.3, 4.2.4, 4.2.5 and 4.3.1) in the different circuit configurations are given in table 4.10. The parameter k for the Rompe-Weizel and Toepler models shows a good agreement with its theoretical (initial for the Toepler model) value. The Braginskii model parameter k is about two thirds of its theoretical value, whereas the Vlastós model parameter k is only half of its value. When the discharge length decreases, the optimal parameter k for all models drifts away from its theoretical value; this is probably due to boundary effects.

Table 4.10: Mean value and standard deviation of the parameter k for the various models and theoretical expectation. The Rompe-Weizel, Toepler and Braginskii models are in good agreement with theoretical predictions.

Model	Rompe-Weizel (SI)	Vlastós (SI)	Toepler (SI)	Braginski (SI)
Case A	26.05 ± 0.63	22.24 ± 1.77	$1.36 \pm 0.06 \times 10^{-2}$	$1.65 \pm 0.09 \times 10^{-3}$
Case B	26.62 ± 0.40	23.61 ± 5.55	$1.30 \pm 0.05 \times 10^{-2}$	$1.70 \pm 0.08 \times 10^{-3}$
Case C	25.89 ± 1.00	18.23 ± 1.50	$1.26 \pm 0.06 \times 10^{-2}$	$1.70 \pm 0.04 \times 10^{-3}$
Case D	26.42 ± 0.64	19.89 ± 1.13	$1.33 \pm 0.02 \times 10^{-2}$	$1.73 \pm 0.07 \times 10^{-3}$
Case F	32.04 ± 3.06	26.73 ± 1.96	$1.35 \pm 0.06 \times 10^{-2}$	$2.07 \pm 0.13 \times 10^{-3}$
Case G	30.08 ± 1.74	22.90 ± 1.73	$1.32 \pm 0.04 \times 10^{-2}$	$1.89 \pm 0.06 \times 10^{-3}$
Theory	25	41	1.5×10^{-2}	2.4×10^{-3}

Previous experiments (Larigaldie (1987a)) reported a large discrepancy between theoretical and experimental values (an order of magnitude) for the resistance prefactor k^{RW} , but were based on other assumptions for the ionization cost. The theoretical evaluation of the resistance prefactor k^{RW} using the

Stoletov's constant (as discussed in section 4.3.1) is remarkably close to the experimental values. For the longer discharge, the mean value of the prefactor is $\langle k^{\text{RW}} \rangle = 26 \text{ V} \cdot \text{s}^{1/2} \cdot \text{m}^{-1}$, which is 8% above the theoretical value when taking the Stoletov's constant for ionization cost. For shorter discharges, the error is larger, around 25%. This is still a good agreement, the deviation probably originates from the lower aspect ratio of the discharge channel. Other experiments in Xenon (Trusov (1994)) obtained a best fit for $k^{\text{RW}} = 36 \text{ V} \cdot \text{s}^{1/2} \cdot \text{m}^{-1}$. A theoretical estimate of this coefficient, using the Stoletov's constant in Xenon $e\phi_I = 36 \text{ eV}$ (Raizer (1997)) and $\mu_e = 0.017 \text{ m}^2 \cdot \text{V}^{-1} \cdot \text{s}^{-1}$ (Raju (2005)), gives $k^{\text{RW}} = 34 \text{ V} \cdot \text{s}^{1/2} \cdot \text{m}^{-1}$. Thus, even though the assumptions of the Rompe-Weizel model are quite crude, it can give a fair description of the discharge channel resistance.

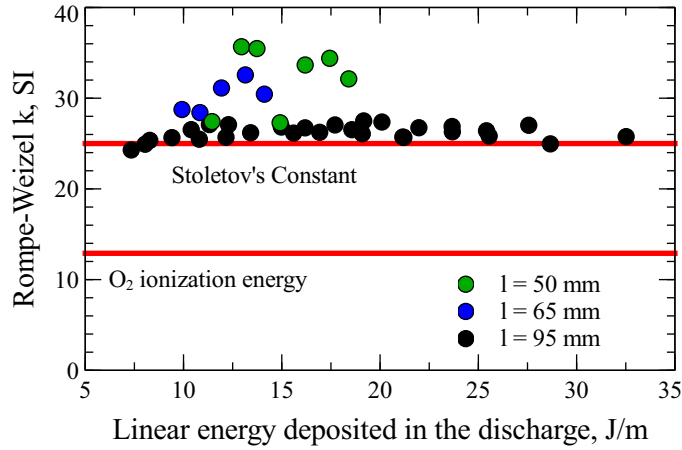


Figure 4.3.4: Resistance prefactor k^{RW} used in (4.2.9), as a function of the linear energy. The lines give the theoretical value of k^{RW} when considering an ionization cost corresponding solely to that of O_2 ($e\phi_I = 12.2 \text{ eV}$) or using the Stoletov's constant ($e\phi = 66.0 \text{ eV}$).

The resistance prefactor k^{V} obtained for the Vlastós model by our optimization procedure is approximately constant but lower than its theoretical value when a 100% ionization is assumed, as shown in figure 4.3.5. Better agreement can be reached with a lower ionization ratio of 30%.

The resistance prefactors obtained for the Toepler and Braginskii models are respectively 13% and 30% below their expected values, as evidenced in figures 4.3.6 and 4.3.7.

4.3.4 Evolution of the resistance

For the low inductance cases, the discharge channel resistance as given by the various models can be compared to the experiments. As a first approximation,

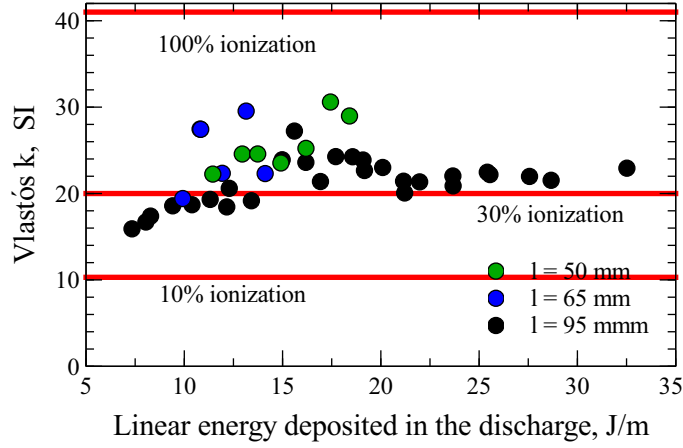


Figure 4.3.5: Resistance prefactor k^V used in (4.2.12), as a function of the linear energy. The upper and lower lines give the theoretical values when a 100% or 10% ionization is assumed, respectively.

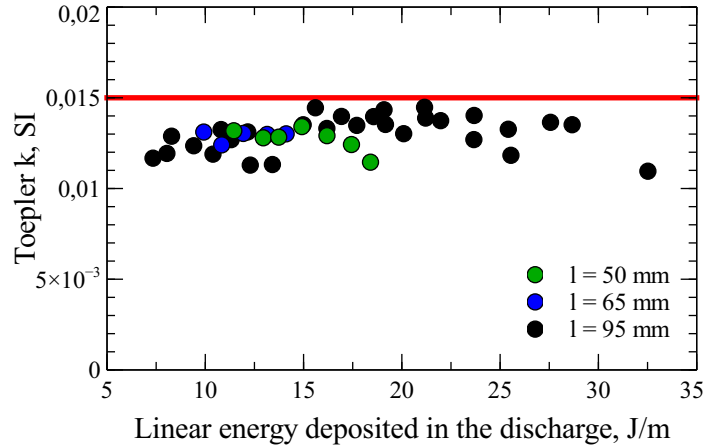


Figure 4.3.6: Resistance prefactor k^T used in (4.2.15), as a function of the linear energy. The line gives the initial value taken from the literature.

the channel resistance can be computed from experimental data as :

$$R_p(t) = -\frac{U_p(t)}{i_p(t)}, \quad (4.3.2)$$

where the $-$ sign accounts for the circuit orientation. This simple approach leads to singularities in the resistance value when the current crosses the $i_p = 0$ line. The zero crossing is due to the fact that the circuit is a damped pseudo-RLC oscillator. In the experiments, the HV probe measures the plasma voltage plus an inductive voltage drop, due to the stray inductance of the circuit loop, as shown in figure 4.2.1. Therefore, the voltage and current are slightly out

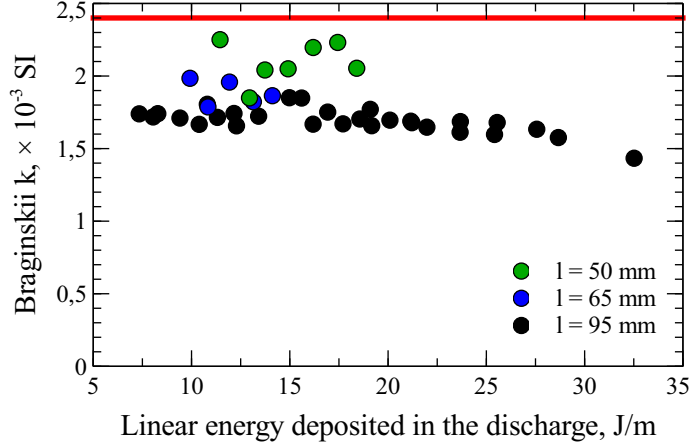


Figure 4.3.7: Resistance prefactor k^B used in (4.2.14), as a function of the linear energy. The line gives the theoretical value.

of phase and the measured voltage is not zero when the current crosses the zero line. To account for this, we subtract the inductive part to the measured voltage, before dividing by the current:

$$R'_p(t) = -\frac{U_p(t) - L_p \frac{di_p(t)}{dt}}{i_p(t)} \quad (4.3.3)$$

For L_p , based on the experimental setup, the measurement loop (including the plasma channel) is approximately a single turn wire loop of radius 10 cm and wire diameter 1 mm. In this condition, $L_p \approx 0.6 \mu\text{H}$. Thus the plasma channel accounts for most of the total inductance $L = 0.8 \mu\text{H}$, which is logical given that the circuit is arranged geometrically so as to minimize the inductance.

Figure 4.3.8 shows the plasma resistance computed using (4.3.2) and (4.3.3), with the resistances computed from (4.2.23) obtained by the reconstruction procedure. Overall, a fair agreement between the various models and the experiment is reached, though the Rompe-Weizel is the closest to the measured resistance value, particularly in the initial stage of the discharge in the first 100 ns. The resistance decays in the first 300 ns, before reaching a steady value. The use of (4.3.3) to correct for the stray inductance avoids the large divergence when the current crosses zero. A localized divergence is still observed around 590 ns when the current crosses 0, due to the measurement noise close to zero. In figure 4.3.8, the channel resistance value R_p computed from the experimental current and voltage values after 450 ns is too noisy to be meaningful, because the current becomes too small. Eventually, the resistance for all models reaches a steady value.

The various models agree fairly well on the final value of the discharge linear resistance, as shown in figure 4.3.9. This is not surprising for the Rompe-Weizel

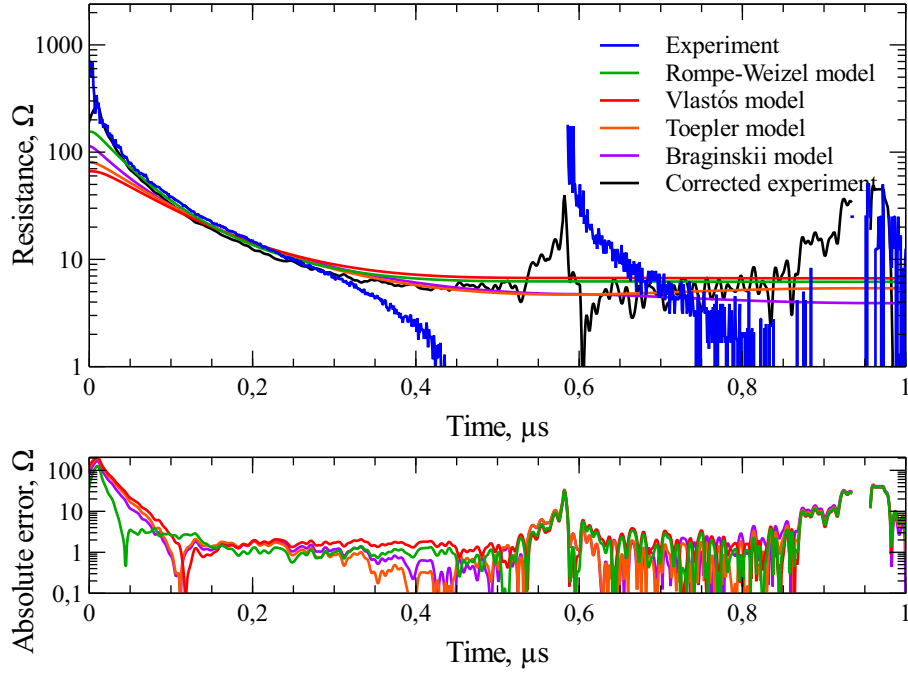


Figure 4.3.8: Comparison of the plasma resistance R_p during the return stroke phase as computed from experimental data ((4.3.2) and (4.3.3)) and predicted by the various models. The resistance decreases sharply during the first 150 ns, then reaches a steady value around 6 Ω ($L = 0.8 \mu\text{H}$, $l = 95 \text{ mm}$, $C = 14.5 \text{ nF}$, $U_C = 19 \text{ kV}$).

and Vlastós model since the two functional forms (4.2.9) and (4.2.12) are very similar. The final resistances R_{pf} of all low inductance cases can be used to compute the plasma conductivity averaged over the channel section as:

$$\langle \sigma S \rangle = \frac{l}{R_{pf}} \quad (4.3.4)$$

It appears also in figure 4.3.9 that this conductivity $\langle \sigma S \rangle$ increases linearly with the linear energy dissipated in the discharge, in agreement with the various models energy considerations. Following the Rompe-Weizel model, this is so because a higher input energy leads to a higher ionization fraction. In the Vlastós model, this means that the plasma reaches a higher temperature when the energy increases. In the Braginskii model, this is due to higher radial expansion of the channel when the energy increases. The physical truth most probably lies somewhere in between these various assumptions. Given its good reconstruction accuracy and agreement on the prefactor k^{RW} , plot 4.3.9a corresponding to the Rompe-Weizel model may be used to compute or extrapolate the channel resistance after the transient phase (approximately 400 ns after the return stroke phase begins).

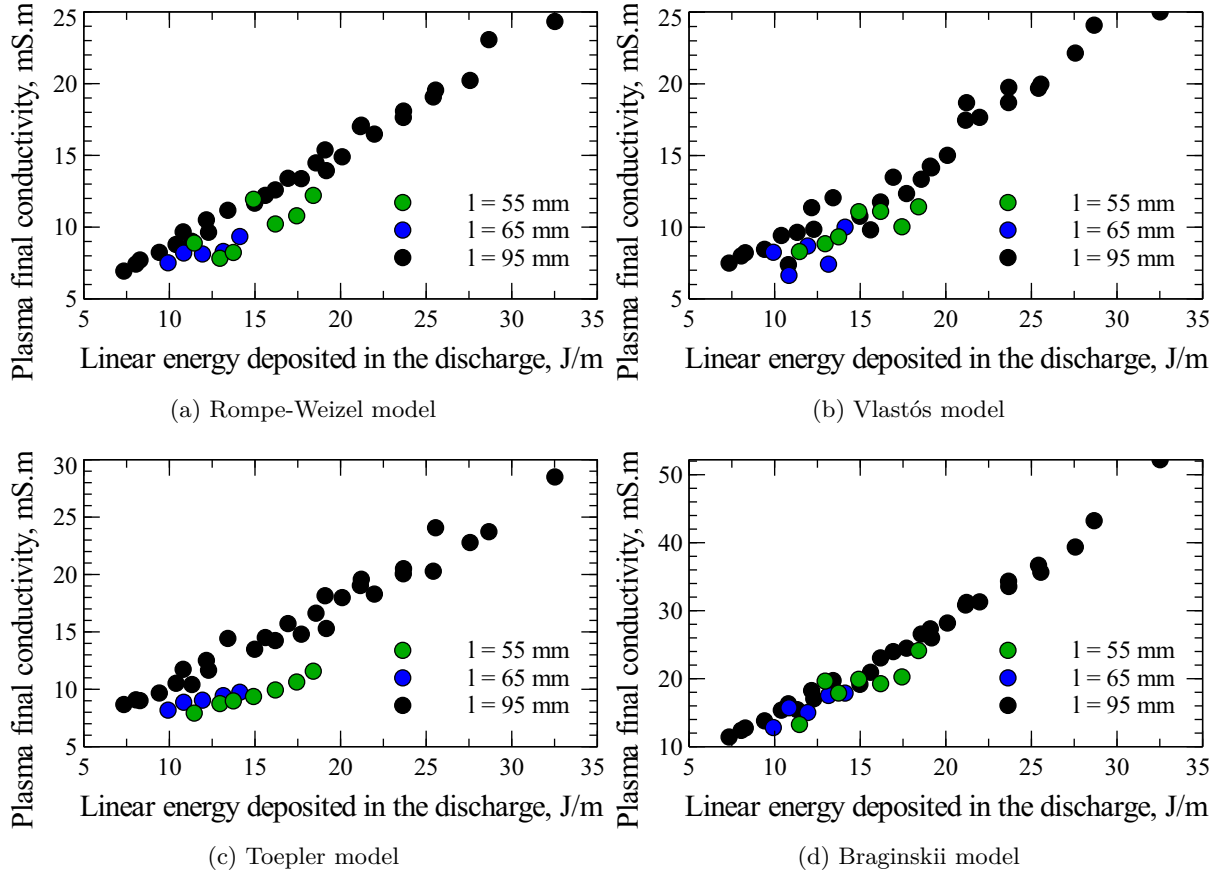


Figure 4.3.9: Plasma conductivity $\langle \sigma S \rangle$ in the different models at the end of the retun stroke.

4.3.5 Channel resistance, assumptions and plasma properties

The Rompe-Weizel, Vlastós and Braginskii resistance models are based on different assumptions for the plasma properties that can be summarized as:

- Rompe-Weizel: fixed electron temperature and mobility, no hypothesis on heavy particles temperature, the electron number density increases as the energy deposited in the discharge increases;
- Vlastós: fully ionized plasma, fixed electron and ion number density; the plasma temperature increases as the energy deposited in the discharge increases.
- Braginskii: plasma of fixed conductivity σ , the resistance evolution is driven by the channel radial expansion following energy deposition in the discharge.

The channel resistance $R_p^M(t)$ gives access to the variable plasma property for a given model M as a function of conductivity and the channel section:

$$R_p^M(t) = \frac{l}{\int_{S(t)} \sigma^M(t) dS},$$

where $S(t)$ is the channel section at a given instant. Based on the previous computations, it would therefore be possible to estimate several plasma parameters such as its electron number density n_e (for the Rompe-Weizel model), its temperature T (for the Vlastós model) or its radius r (for the Braginskii model). Such predictions can then be compared with experimental measurements of said quantities provided they can be measured, *e.g.* through optical emission spectroscopy (see chapter 5).

4.4 Conclusion

We studied the electrical behavior of the pulsed surface discharge for a range of circuit configurations, changing the capacitance, the initial charging voltage, the inductance or the discharge length (Castera and Elias (2014)). In low inductance configurations, the two phases of the pulsed surface discharge, namely the propagation phase (corresponding to the plasma channel formation) and the return stroke phase (corresponding to the energy deposition in the channel) were clearly visible on the current and voltage curves. Using these measurements, we assessed the discharge energy efficiency (how much of the energy initially stored in the capacitor bank is actually deposited in the discharge) and its duration. The total discharge duration was found to depend on the circuit configuration and on the initial energy stored in the capacitors. In a more detailed analysis, the propagation phase duration was found to be only voltage dependent according to Toepler's law (with a propagation velocity proportional to the charging voltage).

Given that most of the energy is deposited during the return stroke phase, we developed an electrical model to describe the current pulse and energy deposition in this phase. The measured current exhibits oscillations similar to that of a RLC circuit. Although a standard under-damped oscillator model provided a good match with the measurements for the high inductance case, the circuit could not be described so simply in the low inductance cases. We implemented several time-varying resistance models (Rompe-Weizel, Vlastós, Toepler and Braginskii) for the plasma channel and fitted them to experimental data. All these models predict a decreasing resistance that is inversely proportional to some integral power of the current flowing through the plasma channel. A set of coupled equations was solved numerically to compute this current in the return stroke phase. The solution is a function of two model dependent parameters: a prefactor k for which all save the Toepler model give a theoretical value, and

an initial value A_0 . This second parameter is related to the plasma channel formation during the propagation phase that was not investigated here.

The various models capture the oscillatory behavior of the circuit, but the Rompe-Weizel model was found to be in best agreement with our measurements in terms of current reconstruction, particularly in the early stage of the discharge. In addition, the prefactor k^{RW} determined experimentally is very close to the value predicted theoretically when using Stoletov's constant. The Vlastós model deviates more from experimental data and the associated prefactor k^{V} is about only half of the value expected by the model. In computing this theoretical value, we assumed a fixed channel radius and a fully ionized plasma, both hypotheses that are probably too stringent and explain this discrepancy. The Braginskii and Toepler model deviate even further from measurements, with prefactors below their theoretical (or initial in the case of the Toepler model) value.

All models show a resistance that falls rapidly within the first 500 ns before reaching a steady value, in accordance with the measured behavior. The high inductance configurations also exhibit this resistance transient behavior though it happens on a shorter time scale and is not visible in our setup. The RLC oscillation period is about ten times larger than the duration of this resistance transient: it would be interesting to study the case of fast-oscillating circuits with RLC oscillations shorter than the transient duration, to see whether this would influence the resistance evolution or not. In the low inductance configurations, the Rompe-Weizel, Vlastós and Toepler model gave similar values for the asymptotic channel conductivity, whereas the Braginskii model failed to do so. This asymptotic conductivity is proportional to the energy released in the discharge, which is coherent with the energy-based formalism of the Rompe-Weizel, Vlastós and Braginskii models.

The Rompe-Weizel, Vlastós and Braginskii time-varying resistance models are based on different (and even sometimes contradictory) assumptions on the plasma's physical and chemical characteristics, such as its electron number density, temperature or radius. The channel resistance computed with these various models can give estimates of these quantities that can be compared to experimental measurements obtained with optical emission spectroscopy. This will be the object of the following chapter.

Chapter 5

Optical and spectroscopic analysis of the pulsed surface discharge

Cerré los ojos, los abrí. Entonces, vi el Aleph.

Jorge Luis Borges, El Aleph

The plasma channel can be described in terms of energy consumption as a time-varying resistance, as evidenced in chapter 4. Several models can explain this behavior, each one making some assumptions on the plasma properties such as the electron number density, temperature or the channel radius. We would like to use optical emission spectroscopy to measure these various properties. To do so, we will:

- measure the total light intensity (over all wavelengths) emitted by the discharge over time and use this to assess the plasma channel radius;
- measure emission spectra of the discharge and in particular the temporal evolution of the H_α line;
- reconstruct the plasma physical properties (electron number density, ...) through analysis of our spectroscopic data.

5.1 Measurement of light intensity and estimation of the discharge radius

We start our analysis using the 0-th order of the spectrometer to do some fast imaging of the discharge. The spectrometer entrance slit is open to 2 mm. The ICCD camera records the light emitted by the discharge over a certain duration (gate τ) and integrated over all wavelengths. Each pixel of the ICCD returns a signal depending on the light intensity that falls onto it, so the final

output from the ICCD camera is a 512×512 pixel image as depicted on figure 5.1.1. We first investigate the time evolution of the light signal.

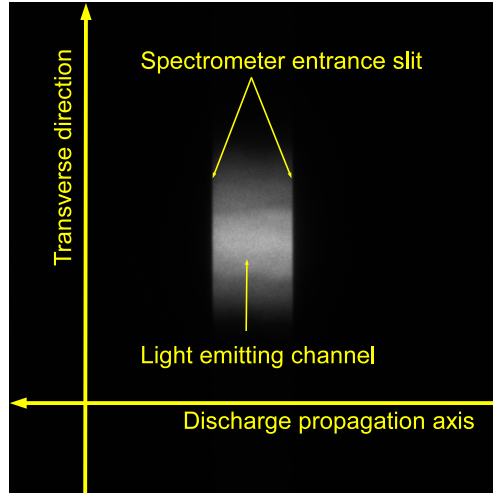


Figure 5.1.1: Imaging of the plasma channel as a light emitting channel in the field of view of the spectrometer used as a fast imager. X is the discharge axis and Y the discharge transverse direction.

5.1.1 Light intensity measurement

During the measurements, attention must be paid to the maximum light intensity falling onto the ICCD detector to avoid damaging it. We must then carefully control the camera gain and its gating, so that the system is sensitive enough to record a meaningful signal even at a high temporal resolution. The camera gain is set to a fixed value, and only the gate τ is changed for the measurements. The light emission is recorded in an intensity array of 512×512 pixels. For our temporal analysis, we simply sum up the whole array and get a value (in arbitrary unit) for the light intensity.

Figure 5.1.2 shows the light intensity recorded for a surface discharge in a low inductance circuit. We plot two data sets taken in the same conditions to illustrate the very good shot-to-shot repeatability of the surface discharge. This is a critical assumption for all of our time-resolved analyses.

The light intensity profile exhibits a very clear peak occurring about 100 ns after the main power peak during the return stroke phase of the surface discharge (there is no clear signal in the propagation phase). The first power peak is due to the energy consumption in the propagation phase to create the conducting channel between the electrodes. This light intensity profile is seen in all low inductance ($L = 0.7 \mu\text{H}$) cases surveyed, as can be seen on figure 5.1.3. When comparing the light signals with the power recordings for low inductance cases, the 100 ns delay appears to be constant.

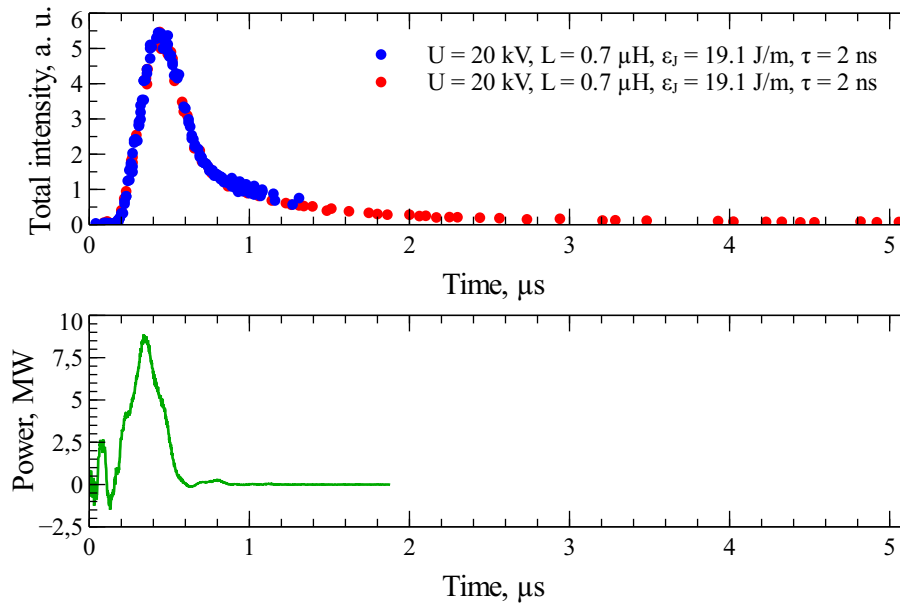


Figure 5.1.2: Light intensity emitted by the discharge and corresponding power evolution in a low inductance circuit.

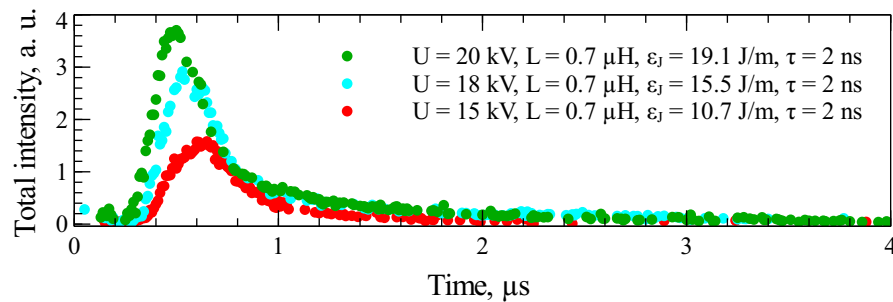


Figure 5.1.3: Light intensity emitted by the discharge in a low inductance circuit for increasing capacitance charging voltages.

As evidenced on figure 5.1.3, light emission by the discharge starts earlier and reaches higher values when the Joule energy deposited in the discharge increases. The light signal vanishes after a few microseconds.

With the high inductance circuit ($L = 78 \mu\text{H}$ in our configuration), light emission by the discharge is much less intense. To obtain a detectable signal, we have to increase the ICCD gate τ from 2 ns to 50 ns. Light emission lasts much longer than in a low inductance circuit, with a signal still clearly visible 25 μs after the discharge initiation. In addition, the light intensity signal shows strong oscillations as can be seen on figure 5.1.4. These oscillations are due to the multiple power peaks that cause reillumination in the channel.

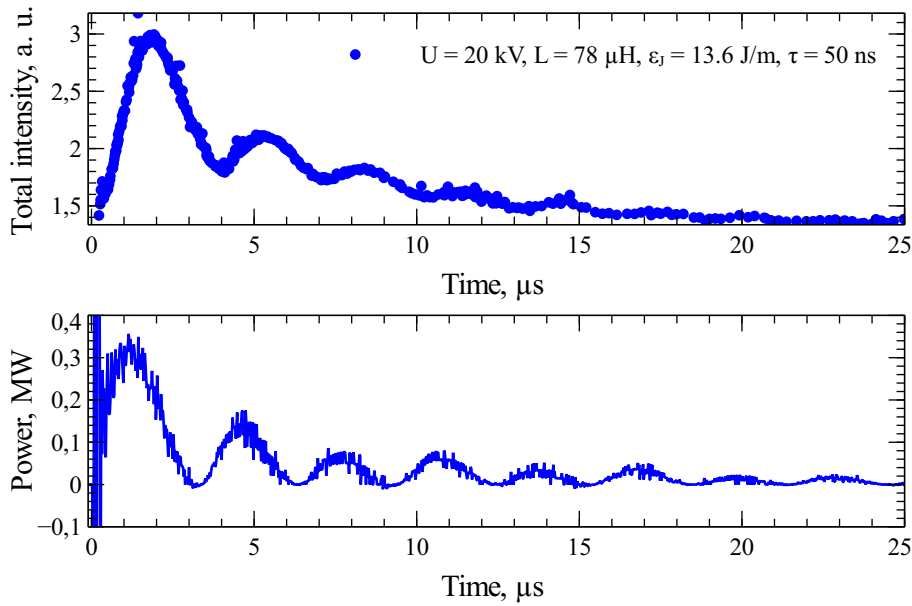


Figure 5.1.4: Light intensity emitted by the discharge and corresponding power evolution in a high inductance circuit.

5.1.2 Radius estimation of the plasma channel

Using the ICCD camera, it is possible to estimate the plasma channel radius during the return stroke phase (the light signal is not sufficient to study the propagation phase). To do so, we assume that the light emitting region encompasses the plasma channel. We measure the light intensity and sum up the signal along the discharge axis X (see figure 5.1.1). We then obtain an intensity profile along the discharge transverse direction Y . This intensity profile is then fitted with a Gaussian curve, whose half width at half-maximum is taken as the light-emitting radius. Figure 5.1.5 shows that the Gaussian fit is in very good agreement with our measurements for the high inductance configuration.

For low inductance configurations however (see figure 5.1.6), the intensity profile is not as neat and deviates from a simple Gaussian profile after a few microseconds. We will still use the Gaussian fit approach, for it gives a proper determination of the half width at half maximum.

Figure 5.1.7 shows the light emission channel radius as estimated with the Gaussian fit for several test conditions. Several regimes can be identified:

- in the first hundreds of nanoseconds (few microseconds for the high inductance case), the channel expands during the power peak while energy is deposited in the discharge. The channel expansion increases with increasing energy;
- when using a low inductance circuit, after the energy deposition has

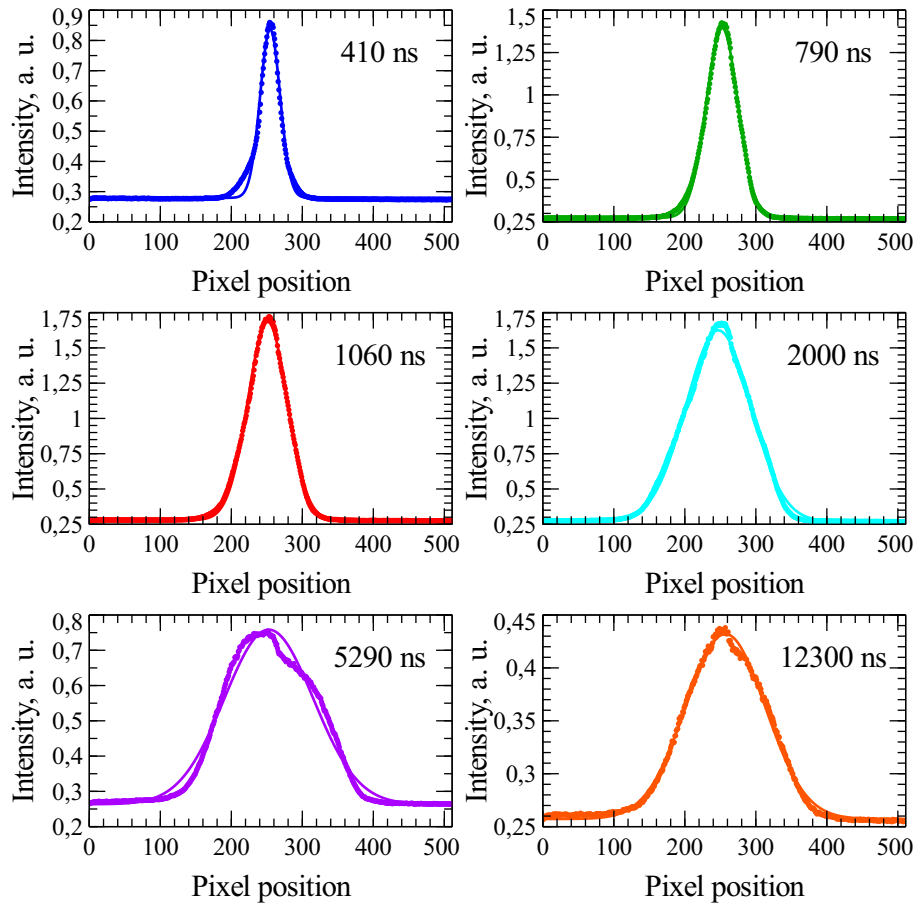


Figure 5.1.5: Intensity profile across the discharge at different times. Discharge conditions: $U = 20$ kV, $L = 78$ μ H, $\epsilon_J = 13.6$ J/m, $\tau = 50$ ns.

ended, the channel keeps expanding but at a slower rate that does not seem to depend on the deposited energy;

- when using a high inductance circuit, the radius starts oscillating after a few microseconds, as further evidenced by figure 5.1.8.

The channel under consideration here is actually the light emission channel, which may not encompass the whole of the discharge channel. In fact as seen with the light intensity measurements, for an oscillating circuit, the presence of power peaks leads to successive reilluminations of the channel. When the power starts to drop, the outer part of the channel starts to cool down, so the outer layer stops emitting light. Thus the channel appears to contract before a new power peak starts and the outer layer heats back up. The multiple power peaks cause multiple reilluminations of the channel, hence the light emission radius oscillations.

The channel expansion velocity during the return stroke phase is plotted as

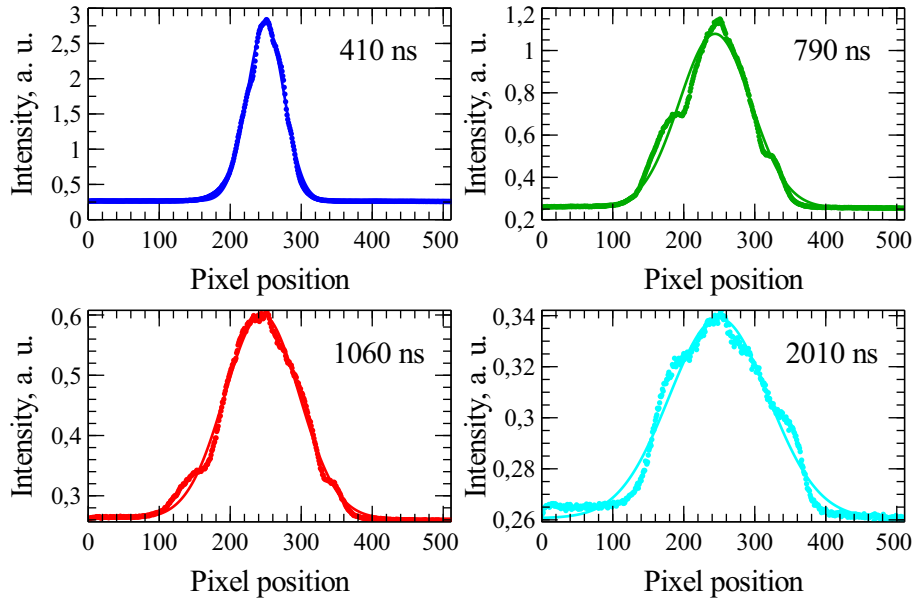


Figure 5.1.6: Intensity profile across the discharge at different times. Discharge conditions: $U = 18$ kV, $L = 0.7$ μ H, $\epsilon_J = 15.5$ J/m, $\tau = 2$ ns.

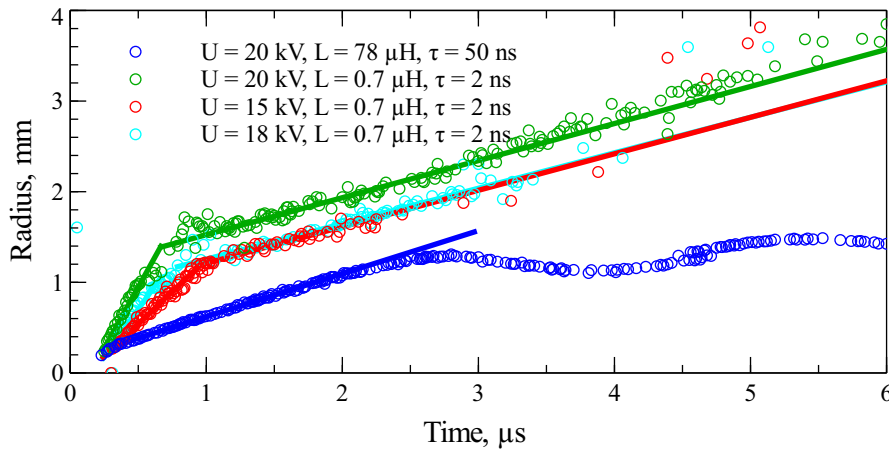


Figure 5.1.7: Channel radius evolution with time. The straight lines are linear fits through data points.

a function of the Joule energy deposited in the discharge in figure 5.1.9. The expansion velocity depends linearly on the Joule energy for the low inductance cases. This can be verified in the high inductance case too, if we assume that 37% of the total Joule energy E_J drives this radius expansion. This fraction of 0.37 corresponds to the energy fraction in the first power peak for a circuit where the plasma channel behaves as a constant resistance $R_p = 9$ Ω , see appendix B for more details. Table 5.1 summarizes these measurements.

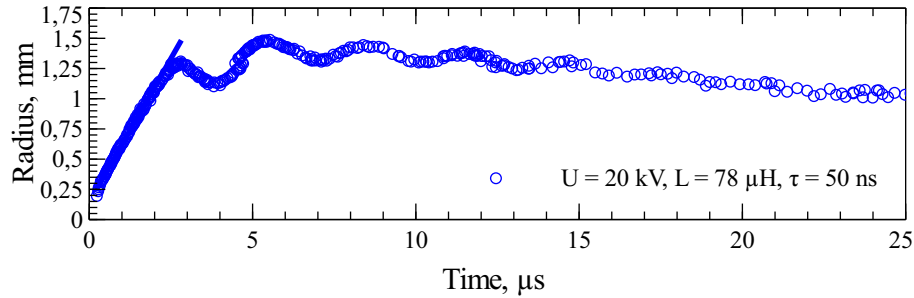


Figure 5.1.8: Channel radius evolution in a high inductance circuit. The channel first expands linearly before oscillating after the first power peak.

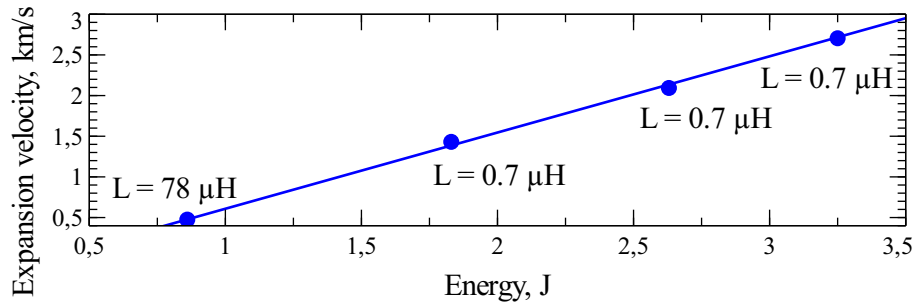


Figure 5.1.9: Channel expansion velocity at the early stages as a function of the energy deposited during the corresponding power peak.

Table 5.1: Channel expansion velocity during the return stroke phase.

L (μH)	78	0.7		
E_J (J)	0.86	1.83	2.63	3.25
Expansion velocity (m/s)	474.7	1430.8	2093.5	2704.7

The channel radius we studied here corresponds to the light-emitting region of the discharge. It may differ from the conducting radius that we can estimate with electron number density measurements. To do so, we use time-resolved optical emission spectroscopy of the discharge.

5.2 Study of the broadening of the H_α line

5.2.1 General spectrum features

We first investigate the general structure of the complete spectrum, integrated over the discharge duration. For this, we use an AvaSpec USB spectrometer. This spectrometer cannot provide time-resolved measurements and therefore the spectra shown in figures 5.2.4, 5.2.2, 5.2.1 and 5.2.1 are simply given as

illustrations of the discharge spectrum dependence on the various circuit parameters. Note that the spectra are corrected for the relative spectral response of the spectrometer.

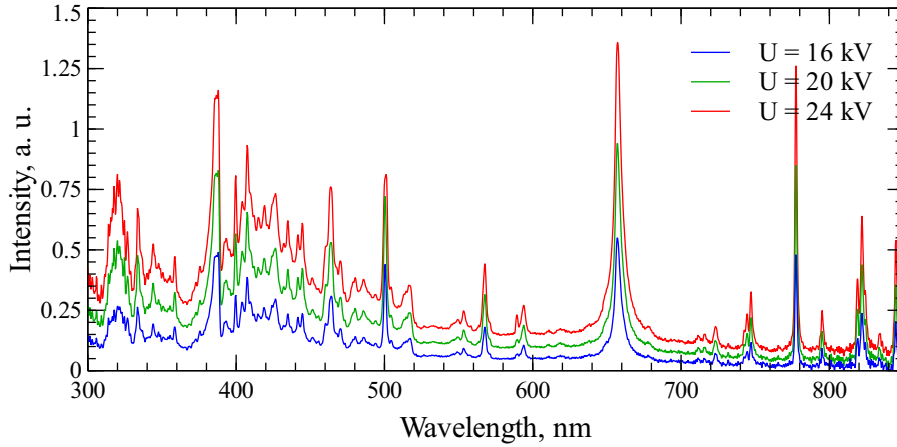


Figure 5.2.1: Time-integrated spectra of the discharges, with $L = 0.7 \mu\text{H}$, $l = 85 \text{ mm}$ and $C = 11.6 \text{ nF}$.

As can be seen in figures 5.2.1, 5.2.2 and 5.2.3, the spectrum intensity increases with the energy deposited in the discharge. Emission is quite strong at the lower wavelengths, which corroborates previous studies of the pulsed surface discharge as a UV source for laser pumping (Krasiuk et al. (1976); Baranov et al. (1981); Tuema et al. (2000)). Above 500 nm, isolated lines are visible, among which the H_α line which can be used to access some properties of the plasma channel.

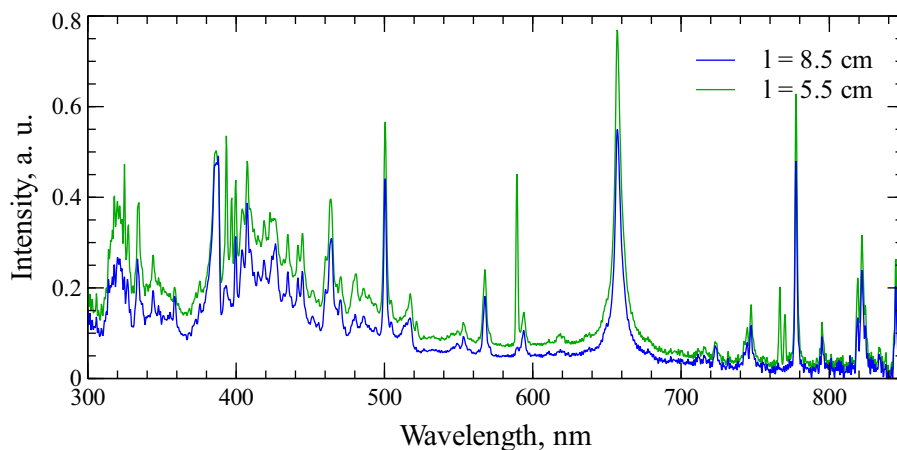


Figure 5.2.2: Time-integrated spectra of the discharges, with $L = 0.7 \mu\text{H}$, $C = 11.6 \text{ nF}$ and $U = 20 \text{ kV}$.

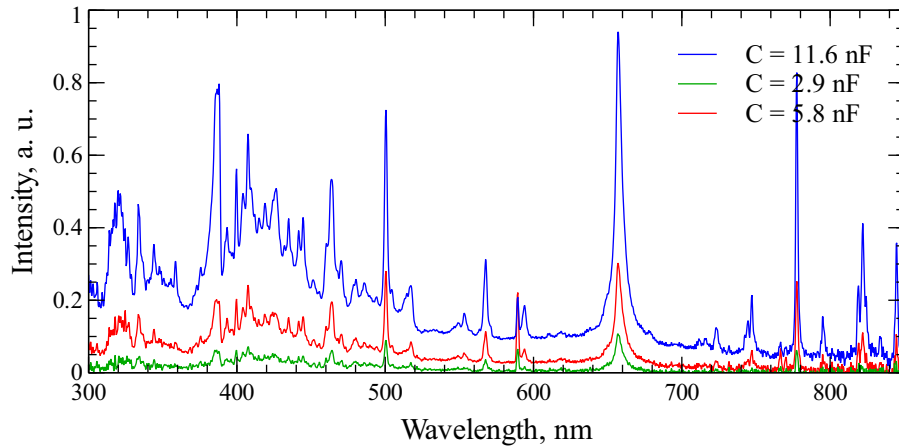


Figure 5.2.3: Time-integrated spectra of the discharges, with $L = 0.7 \mu\text{H}$, $l = 85 \text{ mm}$ and $U = 20 \text{ kV}$.

Figure 5.2.4 further proves that the discharge behavior depends not only on the energy deposited but also on the rate at which this deposition takes place. Adding inductance to the circuit "slows down" the discharge, as the current oscillates for much longer. The spectrum generated in such conditions is now less intense in the lower wavelengths region, but it still exhibits separated lines above 500 nm, including the H_α line.

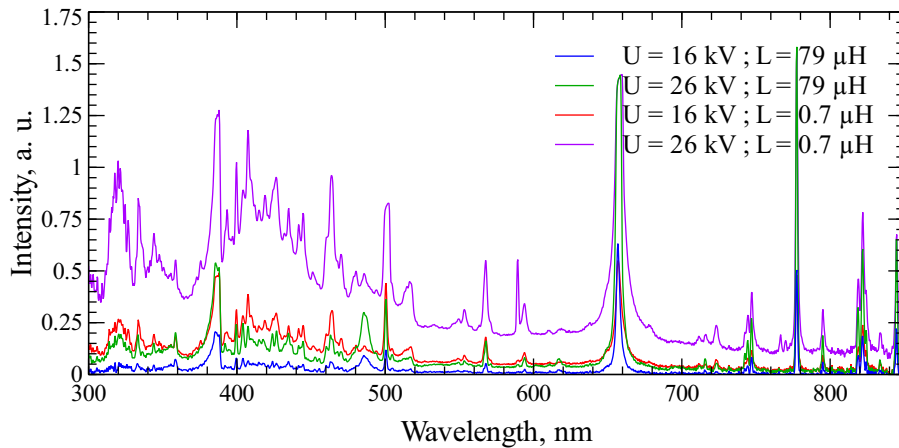


Figure 5.2.4: Time-integrated spectrum of the discharge, with $l = 85 \text{ mm}$ and $C = 11.6 \text{ nF}$.

In what follows, we will study the properties of pulsed surface discharges of length $l = 85 \text{ mm}$ generated with a capacitance $C = 11.6 \text{ nF}$ and a charging voltage $U = 20 \text{ kV}$.

5.2.2 Line profile and origin of the various broadenings and shifts

Spectra of the pulsed surface discharge are recorded using a grating with 300 grooves/mm. To get enough signal, the spectra are recorded with an integration window of 50 ns and a spectrometer entrance slit opened at 100 μm . They are then deconvoluted and corrected for the spectral response of the setup. Details on the spectroscopic setup and calibration are given in section 3.3. The corrected spectra are then fitted as explained in chapter 3. The H $_{\alpha}$ line is modeled with a Voigt profile $V(x, \sigma, \gamma)$. Fitting this profile to the measured spectrum $S(\lambda, t)$ gives the temporal evolution of the parameters $(\sigma(t), \gamma(t))$ that give access to some of the plasma properties. The Voigt parameters σ and γ give the Gauss and Lorentz full width at half maximum $\Delta\lambda_G$ and $\Delta\lambda_L$, which are related to various broadening mechanisms:

$$\Delta\lambda_G = 2\sigma\sqrt{2\ln 2} = \Delta\lambda_D, \quad (5.2.1)$$

$$\Delta\lambda_L = 2\gamma = \Delta\lambda_N + \Delta\lambda_R + \Delta\lambda_{vdW} + \Delta\lambda_S, \quad (5.2.2)$$

with $\Delta\lambda_D$ the Doppler broadening, $\Delta\lambda_N$ the natural broadening, $\Delta\lambda_R$ the resonant broadening, $\Delta\lambda_{vdW}$ the van der Waals broadening, and $\Delta\lambda_S$ the Stark broadening. All these are related to various physical phenomena that affect the emission for a given transition between energy levels. They are then specific for a given atomic line (Griem (1964); Janssen et al. (2013); Djurović and Konjević (2009); van der Horst et al. (2012)). We will focus on the H $_{\alpha}$ line of hydrogen Balmer series. The broadening and shifts of H $_{\alpha}$ have been extensively reviewed by Sainct (2014). The following section summarizes his recommendations.

5.2.2.1 Natural broadening

Natural broadening is related to quantum mechanics effects (finite lifetime of the excited level), and is modeled with a Lorentzian distribution with a full width at half-maximum $\Delta\lambda_N$:

$$\Delta\lambda_N = \frac{\lambda_{ul}^2}{2\pi c} \left(\sum_{n < u} A_{un} + \sum_{m < l} A_{lm} \right), \quad (5.2.3)$$

where λ_{ul} is the wavelength of the transition under consideration between upper and lower levels, A_{un} is the Einstein coefficient for the transition between the upper level u of the transition and a lower level n , A_{lm} is the Einstein coefficient for the transition between the lower level l of the transition and a lower level n . The H $_{\alpha}$ line corresponds to a transition between $u = 3$ and $l = 2$ and is in fact a multiplet of 7 lines (due to fine structure effects on the two levels, Kramida et al. (2014)). The ground level $n = 1$ must be considered, and is also degenerated. The various transitions to be taken into account are then the Balmer α ($u = 3 \rightarrow l = 2$), Lyman α ($l = 2 \rightarrow n = 1$) and Lyman β

($u = 3 \rightarrow n = 1$) lines. We use averaged values for these transitions in terms of wavelengths, Einstein coefficients and absorption oscillator strengths (see appendix C.1 for detailed calculations). The corresponding values are given in tables 5.2, 5.3 and 5.4.

Table 5.2: Components of the Balmer α ($3 \rightarrow 2$) transition multiplet and their spectroscopic properties.

Wavelength in air (nm)	A_{32} (s^{-1})	f_{23}	S_{23} (a. u.)	Upper level configuration	Lower level configuration	g_3	g_2
656.271	5.3877×10^7	0.69614	3.0089×10^1	3d $^2D_{3/2}$	2p $^2P_{1/2}^0$	4	2
656.272	2.2448×10^7	0.29005	1.2537×10^1	3p $^2P_{3/2}^0$	2s $^2S_{1/2}$	4	2
656.275	2.1046×10^6	0.013597	5.8769×10^{-1}	3s $^2S_{1/2}$	2p $^2P_{1/2}^0$	2	2
656.277	2.2449×10^7	0.14503	6.2688	3p $^2P_{1/2}^0$	2s $^2S_{1/2}$	2	2
656.285	6.4651×10^7	0.62654	5.4162×10^1	3d $^2D_{5/2}$	2p $^2P_{3/2}^0$	6	4
656.287	1.0775×10^7	0.069616	6.0181	3d $^2D_{3/2}$	2p $^2P_{3/2}^0$	4	4
656.291	4.2097×10^6	0.013599	1.1756	3s $^2S_{1/2}$	2p $^2P_{3/2}^0$	2	2
656.280	4.4102×10^7	0.64108	1.1084×10^2	3	2	18	8

Table 5.3: Components of the Lyman α ($2 \rightarrow 1$) transition doublet and their spectroscopic properties.

Wavelength in air (nm)	A_{21} (s^{-1})	f_{12}	S_{12}	Upper level configuration	Lower level configuration	g_2	g_1
121.567	6.2648×10^8	0.2776	2.2220	2p $^2P_{3/2}^0$	1s $^2S_{1/2}$	4	2
121.567	6.2649×10^8	0.13881	1.1110	2p $^2P_{1/2}^0$	1s $^2S_{1/2}$	2	2
121.567	4.6986×10^8	0.41641	3.3330	2	1	8	2

Table 5.4: Components of the Lyman β ($3 \rightarrow 1$) transition doublet and their spectroscopic properties.

Wavelength in air (nm)	A_{31} (s^{-1})	f_{13}	S_{13}	Upper level configuration	Lower level configuration	g_3	g_1
102.572	1.6725×10^8	0.052761	3.5633×10^{-1}	3p $^2P_{3/2}^0$	1s $^2S_{1/2}$	4	2
102.572	1.6725×10^8	0.026381	1.7817×10^{-1}	3p $^2P_{1/2}^0$	1s $^2S_{1/2}$	2	2
102.572	5.5750×10^7	0.079142	5.3450×10^{-1}	3	1	18	2

For the H_α line ($3 \rightarrow 2$) of central wavelength 656.280 nm, we get for the natural broadening:

$$\Delta\lambda_N = 1.30 \times 10^{-4} \text{ nm.} \quad (5.2.4)$$

This is three order of magnitude below our resolution of 0.104 nm and can be neglected afterwards.

5.2.2.2 Doppler broadening

Doppler broadening $\Delta\lambda_D$ is due to thermal motion of the radiation emitters. The spectral density is modeled by a Gaussian distribution, of which the full width at half-maximum $\Delta\lambda_D$ is a function of the temperature T , of the emitter mass M and of the central wavelength $\lambda^{(0)}$ for the given transition:

$$\Delta\lambda_D = 7.162 \times 10^{-7} \lambda^{(0)} \sqrt{\frac{T}{M}}. \quad (5.2.5)$$

$\Delta\lambda_D$ and $\lambda^{(0)}$ are given in nm, T is expressed in K, and M is given in atomic mass units. For the H α line ($M = 1$, $\lambda^{(0)} = 656.280$ nm as per table 5.2), we have:

$$\Delta\lambda_D = 4.700 \times 10^{-4} \sqrt{T}, \quad (5.2.6)$$

with $\Delta\lambda_D$ in nm and T in K. For temperatures in the range of a few eV (between 10000 and 40000 K), the Doppler broadening is on the order of 5×10^{-2} nm.

5.2.2.3 Resonant broadening

Resonant broadening is caused by collisions between radiation emitters and similar particles in another energy level that is connected via a permitted transition to either the lower or upper states (denoted l and u respectively) of the transition under consideration. It is generally sufficient to consider only the ground state, and the resonant broadening then has a full width at half maximum $\Delta\lambda_R$ given by (Djurović and Konjević (2009)):

$$\Delta\lambda_R = 8.60 \times 10^{-27} \lambda^2 \lambda_R f_R \sqrt{\frac{g_1}{g_R}}, \quad (5.2.7)$$

with $\Delta\lambda_R$ in nm, λ the wavelength of the transition under scrutiny in nm, λ_R the resonance wavelength in nm, f_R the resonance oscillator strength, g_1 the degeneracy of the ground level of the resonance transition and g_R the degeneracy of the resonant level (either upper or lower level of the main transition under examination). For the H α multiplet, one must take into account the ground level $1s^2S_{1/2}$ and the various levels $2p$ or $3p$ connected via Lyman transitions. All the components of the multiplet contribute to resonance broadening (see appendix C.2 for detailed calculations), so we get eventually:

$$\Delta\lambda_R = 4.30 \times 10^{-3} x_H \frac{P}{T}, \quad (5.2.8)$$

with $\Delta\lambda_R$ in nm, x_H the mole fraction of atomic hydrogen, P the pressure in Pa and T the temperature in K.

5.2.2.4 Stark broadening and shift

Stark broadening is caused by the presence of free charge carriers in the medium under consideration. The electric field generated by these charge carriers (namely electrons) modifies the line width. The spectral intensity is then described by a Lorentzian distribution with full width at half-maximum $\Delta\lambda_S$ (for the H_α line):

$$\Delta\lambda_S = 3.866 \times 10^{-12} n_e^{\frac{2}{3}}, \quad (5.2.9)$$

with $\Delta\lambda_S$ in nm and n_e in cm^{-3} .

Moreover, the presence of free charge carriers can also shift the central wavelength for the measured emission $\lambda^{(c)}$ with respect to the vacuum reference wavelength $\lambda^{(0)}$ for the same transition. This Stark redshift (the measured wavelength $\lambda^{(c)}$ is greater than the reference wavelength $\lambda^{(0)}$) can be directly related to Stark broadening. Using data from the literature, Sainct obtained:

$$s_S = 0.056 \cdot \Delta\lambda_S^{\frac{3}{2}} = 4.257 \times 10^{-19} n_e. \quad (5.2.10)$$

5.2.2.5 Van der Waals broadening and shift

Van der Waals broadening is due to collisions between the radiation emitters and other neutral particles in the medium. Its expression then depends on the chemical composition of the radiating medium under consideration (Djurović and Konjević (2009); Konjević et al. (2012); van der Horst et al. (2012); Yubero et al. (2013); Muñoz et al. (2009); Yubero et al. (2007)). It can be formally written as:

$$\Delta\lambda_{vdW} = 5.925 \times 10^{-2} K_1 \sum_j K_j \frac{P}{T^{0.7}}, \quad (5.2.11)$$

with $\Delta\lambda_{vdW}$ in nm, P in Pa and T in K. K_1 is a coefficient that depends on the transition under consideration. K_j are the contributions of the different neutral species in the medium. Determination of the sum $\sum_j K_j$ then requires some prior knowledge of the plasma chemical composition. However, we do not need it in a first analysis. It suffices to know that van der Waals broadening also is accompanied by a van der Waals shift, given by (Djurović and Konjević (2009)):

$$s_{vdW} = \frac{\Delta\lambda_{vdW}}{3}. \quad (5.2.12)$$

5.2.3 Spectrum reconstruction

As detailed in section 3.3.3, we reconstruct the discharge spectrum $S(\lambda)$ (after intensity correction and slit function deconvolution) with a synthetic profile $\Sigma(\lambda)$ that is a sum of multiple Voigt peaks and a linear baseline :

$$\Sigma(\lambda) = a + b\lambda + \sum_i A_i V\left(\lambda - \lambda_i^{(c)}, \sigma_i, \gamma_i\right), \quad (5.2.13)$$

where $\lambda_i^{(c)}$, σ_i , γ_i are the central wavelength, the Gauss and the Lorentz parameters respectively for peak i . The corresponding peak amplitude A_i for peak i is a function (see section 3.3.3 for detailed calculations) of all the peaks j parameters and of the linear baseline :

$$A_i = A_i \left(a, b, \left(\lambda_j^{(c)}, \sigma_j, \gamma_j \right) \right),$$

so that for n peaks in the measured spectrum $S(\lambda)$, the synthetic spectrum $\Sigma(\lambda)$ is built with $3n + 2$ parameters. We then fit the synthetic spectrum $\Sigma(\lambda)$ to the measured spectrum $S(\lambda)$. This yields a set of optimum parameters $\left(a^{(O)}, b^{(O)}, \left(\lambda_i^{(O)}, \sigma_i^{(O)}, \gamma_i^{(O)} \right) \right)$. Figures 5.2.5 and 5.2.6 shows several spectra and their reconstruction with the synthetic profile.

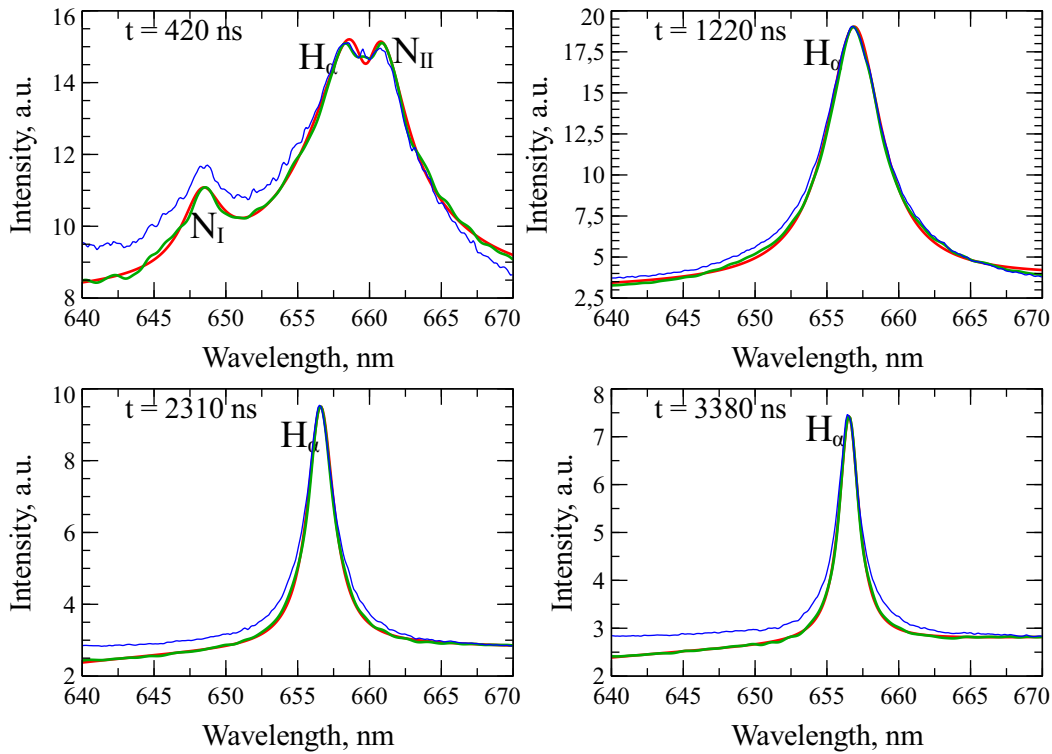


Figure 5.2.5: Spectra of the pulsed surface discharge ($L = 0.7 \mu\text{H}$) at different times. The blue spectra are raw measurements, the green ones correspond to deconvolution and intensity correction (see section 3.3.3 for more details) and the red ones are the reconstructed fits defined by equation (5.2.13).

As can be seen in figures 5.2.5 and 5.2.6, several other lines are present in the vicinity of the H $_{\alpha}$ line. These atomic nitrogen lines fade away after 2750 ns in the high inductance configuration. In the low inductance configuration, these nitrogen lines disappear after 750 ns: however, they may still be present but blended in the broadened H $_{\alpha}$ line. This line blending makes reconstruction in

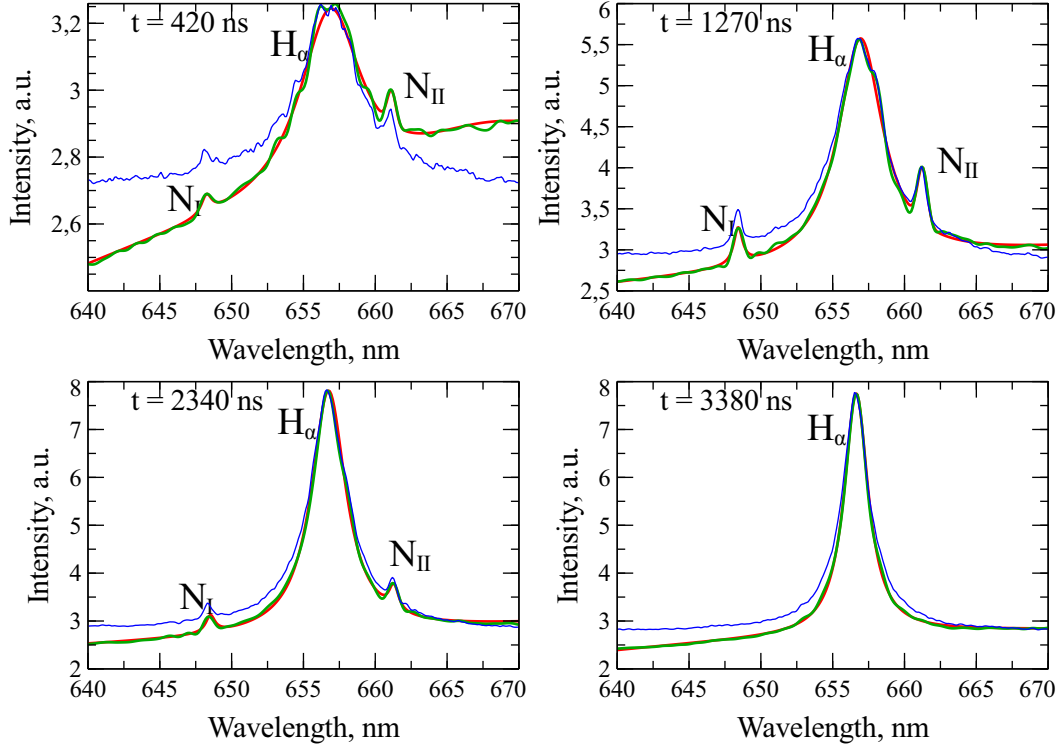


Figure 5.2.6: Spectra of the pulsed surface discharge ($L = 78 \mu\text{H}$) at different times. The blue spectra are raw measurements, the green ones correspond to deconvolution and intensity correction (see section 3.3.3 for more details) and the red ones are the reconstructed fits defined by equation (5.2.13).

the early phase of the discharge more difficult, as the optimizer may lock on a local minimum.

5.2.4 Separation of broadening contributions

Isolating the H_α line, we get the temporal evolution of the Lorentz broadening and of the wavelength shift, from which we can then separate van der Waals and Stark contributions:

$$\Delta\lambda_{L,H_\alpha} = 2\gamma_{H_\alpha} = \Delta\lambda_{vdW} + \Delta\lambda_S + \Delta\lambda_R + \Delta\lambda_N, \quad (5.2.14a)$$

$$s_{H_\alpha} = \lambda_{H_\alpha}^{(c)} - \lambda_{H_\alpha}^{(0)} = \frac{\Delta\lambda_{vdW}}{3} + 0.056\Delta\lambda_S^{\frac{3}{2}}. \quad (5.2.14b)$$

We can neglect here the natural broadening $\Delta\lambda_N$ and the resonant broadening with respect to van der Waals broadening: indeed, even assuming a fraction of hydrogen of 0.1%, if the numerical factors of the van der Waals and resonance broadening are on the same order of magnitude, the temperature dependences

of both van der Waals and resonant broadening imply that:

$$\frac{\Delta\lambda_R}{\Delta\lambda_{vdW}} = O\left(\frac{0.1}{T^{0.3}}\right), \quad (5.2.15)$$

which falls below 2% as soon as T exceeds room temperature $T = 300$ K.

We now have the separate temporal evolution of the van der Waals and Stark broadening contributions. As mentioned previously, these quantities can be related to plasma channel characteristics. We turn to the determination of such quantities such as the electron number density, gas temperature and pressure in the discharge.

5.3 Plasma characteristics

5.3.1 Electron number density and plasma channel resistance

The electron number density n_e is easily obtained from the Stark broadening $\Delta\lambda_S$ using equation 5.2.9. To compute the corresponding error bars σ_{n_e} , we apply a variance formula (see appendix A for detailed calculations):

$$\sigma_{n_e} = 1.973 \times 10^{17} \Delta\lambda_S^{\frac{1}{2}} \sigma_S. \quad (5.3.1)$$

To obtain the uncertainty on the Stark broadening σ_S , we use once again the variance formalism on the system of equations (5.2.14) used to separate the van der Waals and Stark broadening contributions. This gives:

$$\begin{aligned} 4\sigma_\gamma^2 &= \sigma_{vdW}^2 + \sigma_S^2, \\ \sigma_s^2 &= \frac{\sigma_{vdW}^2}{9} + 0.070\Delta\lambda_S\sigma_S^2, \end{aligned}$$

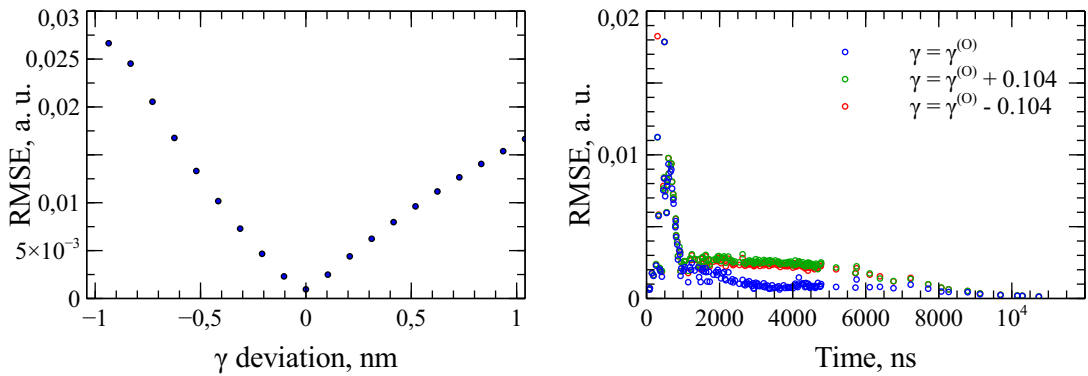
which can be rewritten as (see appendix A.2.2 for detailed calculations):

$$\sigma_S^2 = \frac{\sigma_s^2 + \frac{4}{9}\sigma_\gamma^2}{7.056 \times 10^{-3}\Delta\lambda_S + \frac{1}{9}}. \quad (5.3.2)$$

We now need an estimate for the shift uncertainty σ_s and the Lorentz parameter uncertainty σ_γ to conclude the computation. All wavelength measurements are ultimately limited by the finite size of the camera pixel, we then set $\sigma_s = 0.104$ nm (wavelength coverage for a single pixel in our setup). To assess the uncertainty on the Lorentz parameter, we perform a sensitivity analysis. Starting from the optimum value of γ , we define the root mean square error e between the measured spectrum $S(\lambda)$ and its synthetic reconstruction $\Sigma(\lambda)$:

$$e = \sqrt{\int (\tilde{\Sigma}(\tilde{\lambda}) - \tilde{S}(\tilde{\lambda}))^2 d\tilde{\lambda}}, \quad (5.3.3)$$

and we compute this error as a function of γ . It should be noted once again that all computations are performed on dimensionless quantities (as indicated by the $\tilde{\sim}$ symbol), the Voigt fit parameters parameters are then renormalized properly to their proper unit. As can be seen in figure 5.3.1, the error e increases up to an order of magnitude when γ deviates from its optimum value. Our measurement are limited by our resolution of 0.104 nm, which is a sufficient deviation to double the error value e . We then choose this minimum resolution for the Lorentz parameter uncertainty $\sigma_\gamma = 0.104$ nm.



(a) Evolution of the error as a function of the deviation from the optimum value $\gamma^{(0)}$ at $t = 2960$ ns. (b) Time evolution of the error for various deviations from the optimum value $\gamma^{(0)}$.

Figure 5.3.1: Sensitivity analysis of the fit accuracy (in terms of error defined by equation (5.3.3) with respect to the Lorentz parameter γ .

With these measurements of the electron number density and of the conducting radius, it is possible to get a "spectroscopic" estimate of the channel resistance:

$$R_p^S = \frac{2l}{n_e \mu_e e \pi r^2}, \quad (5.3.4)$$

with l the discharge length (in m), n_e the electron number density (in m^{-3}), $\mu_e = 0.059 \text{ m}^2 \text{V}^{-1} \text{s}^{-1}$ the electron mobility (in agreement with our analysis in chapter 4) and $e = 1.6 \times 10^{-19} \text{ C}$. We assume that the discharge channel is a half-cylinder of radius r (in m) in which the electron number density n_e is homogeneous.

5.3.2 Determination of pressure and temperature

From van der Waals broadening, we can in principle determine the evolution of temperature and pressure in the plasma channel. Van der Waals broadening is expressed as:

$$\Delta\lambda_{vdW} = 5.925 \times 10^{-2} K_1 \sum_j K_j \frac{P}{T^{0.7}},$$

with $\Delta\lambda_{vdW}$ in nm, P in Pa and T in K. K_1 is a transition specific coefficient that depends on the energy levels and their orbital number (see appendix C.3 for detailed calculations). As mentioned previously, the H_α line is in fact a multiplet of 7 lines, to which will correspond 7 values of this K_1 parameter. Following the method used by [Laux et al. \(2003\)](#), we compute the K_1 parameter for the various components and take a value averaged by the relative intensity of the different components. We get $K_1 = 2.78277 \times 10^6 \text{ nm}^2$. K_j is the contributions of the neutral perturber species j , and can be expressed for species j as:

$$K_j = \frac{x_j \alpha_j^{0.4}}{\mu_j^{0.3}}, \quad (5.3.5)$$

with x_j its mole fraction, α_j its polarizability in cm^{-3} , and μ_j its reduced mass in Da. To compute the van der Waals broadening, we need to determine the composition of the plasma. Assuming local thermodynamic equilibrium, there is a relation between temperature T , pressure P and chemical composition (x_j) of the plasma:

$$f(T, P, (x_j)) = 0. \quad (5.3.6)$$

We first determine the temperature and pressure such that the chemical composition (x_j) is compatible with the observed electron number density n_e :

$$T, P, (x_j) / f(T, P, (x_j)) = 0 \text{ and } \frac{Px_e}{k_B T} = n_e. \quad (5.3.7)$$

This gives us a set of possible states ($T, P, (x_j)$) for the plasma channel. We then explore this set of plausible temperature, pressure and chemical composition by computing the corresponding van der Waals broadening $\Delta\lambda_{vdW}$ and comparing it to the value obtained through equations (5.2.14).

The temperature and pressure obtained through this procedure will be subject to uncertainties that can be computed (see appendix A.2.2 for detailed calculations):

$$\sigma_P^2 = \frac{T^{1.4}}{1.49} \left(\frac{\sigma_{vdW}^2}{\left(5.925 \times 10^{-2} K_1 \sum_j K_j\right)^2} + 0.49 \frac{P^2 \sigma_e^2}{n_e^2 T^{1.4}} \right), \quad (5.3.8a)$$

$$\sigma_T^2 = \frac{T^{3.4}}{1.49 P^2} \left(\frac{\sigma_{vdW}^2}{\left(5.925 \times 10^{-2} K_1 \sum_j K_j\right)^2} + \frac{P^2 \sigma_e^2}{n_e^2 T^{1.4}} \right). \quad (5.3.8b)$$

5.3.3 Low inductance case

As can be seen on figure 5.3.2, the electron number density evolution can be separated in two phases related to power deposition in the discharge.

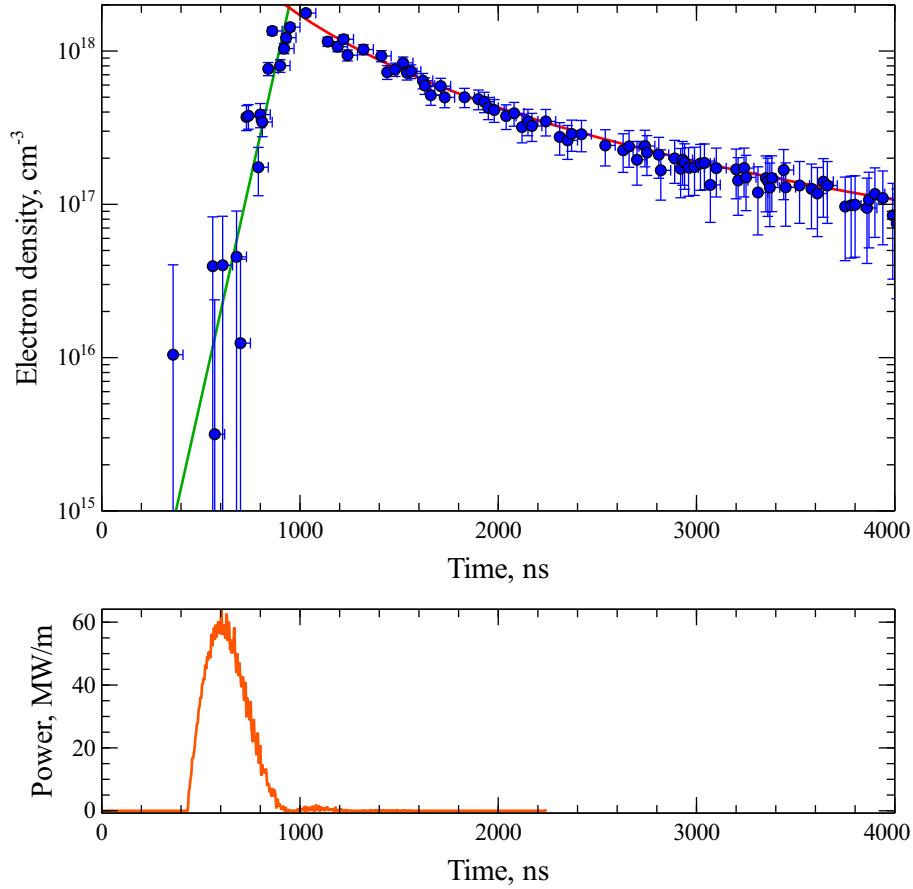


Figure 5.3.2: Electron number density and corresponding linear power deposition in the discharge. Two distinct phases are visible: an exponential growth up to a peak value $n_e = 2 \times 10^{18} \text{ cm}^{-3}$, followed by a decay in a power law of time. The spectroscopy analysis is done on a 85 mm-long discharge, though the electrical data correspond to a 95 mm-long discharge (no reliable electrical measurement for the 85 mm-long discharge).

During the Joule power peak (roughly between 400 ns and 900 ns), one can see an exponential increase of the electron number density:

$$n_e \propto e^{1.326 \times 10^{-2} t} \quad (5.3.9)$$

with t in ns and n_e in cm^{-3} . After about 1 μs , the electron number density decreases in a power law of time that can be obtained by fitting the data points between 1 μs and 4 μs :

$$n_e \propto t^{-2} \quad (5.3.10)$$

These electron number density trends are consistent with the Rompe-Weizel model of variable resistance detailed in chapter 4. As seen in section 5.1.2, the

channel radius increases linearly (at different velocities) during and after the power peak: $r \propto t$. Using these trends, we can compute the channel resistance:

$$R_p \propto \frac{1}{n_e r^2},$$

which gives:

- during the power peak, the resistance drops very quickly:

$$R_p \propto \frac{1}{t^2 e^{1.326 \times 10^{-2} t}};$$

- after the power peak, the resistance remains constant:

$$R_p \propto \frac{1}{t^2 t^{-2}} \propto 1.$$

This seems to corroborate our choice of the Rompe-Weizel model following our analysis of the pulsed surface discharge electrical behavior (see chapter 4): in this formalism, the input energy serves to ionize the gas, which causes a rapid fall of the resistance. We compute the "spectroscopic" resistance R_p^S (as defined in section 5.3.1) and compare it to our electrical measurement (4.3.3) and estimate according to the Rompe-Weizel model (4.2.9) on figure 5.3.3.

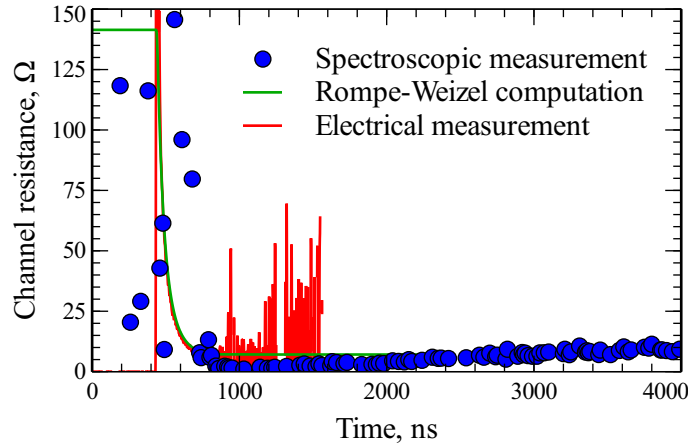


Figure 5.3.3: Channel resistance: comparison between spectroscopic emission and electrical measurements.

Although these various methods agree on an asymptotic value of the resistance of about 8Ω , our spectroscopic measurement is not accurate enough to determine the resistance in the first 700 ns (though the few available points seem to point to a decreasing resistance). In fact, we miss reliable data on the electron number density at early times. Upon looking more thoroughly into our fitting procedure, it appears there may be additional lines in the spectrum that are

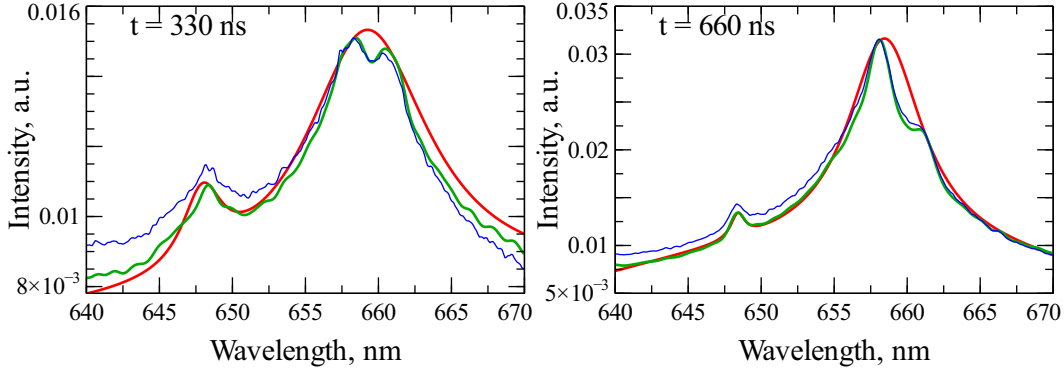


Figure 5.3.4: Examples of misfit reconstruction: optimization failed due to the presence of another line that is not properly taken into account. The blue spectra are raw measurements, the green ones correspond to deconvolution and intensity correction (see section 3.3.3 for more details) and the red ones are the reconstructed fits defined by equation (5.2.13).

not clearly identified and properly taken into account, as illustrated on figure 5.3.4.

Furthermore, given the power law decay of the electron number density after the power peak and the linear radius expansion, the total number of electron in the discharge remains constant, which leads us to expect rather high temperature (on the order of an eV) in the plasma, to prevent the recombination process.

The fitted spectrum was obtained by binning all the pixel lines of the camera over the the vertical axis (512 pixels along the Y axis of figure 5.1.1). Therefore the electron number density is averaged on the transverse dimension of discharge, and we do not take into account the hydrodynamic processes likely to take place as the discharge channel expands. To get a finer insight on the plasma, we decompose the CCD image in 15 bands of 30 pixels (each band covers 0.6 mm) and then apply our fit procedure and electron number density reconstruction to these transverse spectra. We obtain crude transverse electron number density profile $n_e(y)$, as depicted on figure 5.3.5.

The data is still a bit too noisy to perform an Abel transform and obtain the radial density profile $n_e(r)$. However, we can compare the average electron number density $\langle n_e \rangle_y$ plotted in figure 5.3.2 and the electron number density in the central band of this transverse decomposition $n_e(y = 0)$. As can be seen in figure 5.3.6, the central electron number density $n_e(y = 0)$ varies in a similar fashion, with an exponential increase at early times followed by power law decay.

Estimates of the temperature and pressure in the plasma through van der Waals broadening analysis are plotted in figure 5.3.7. The chemical composition was

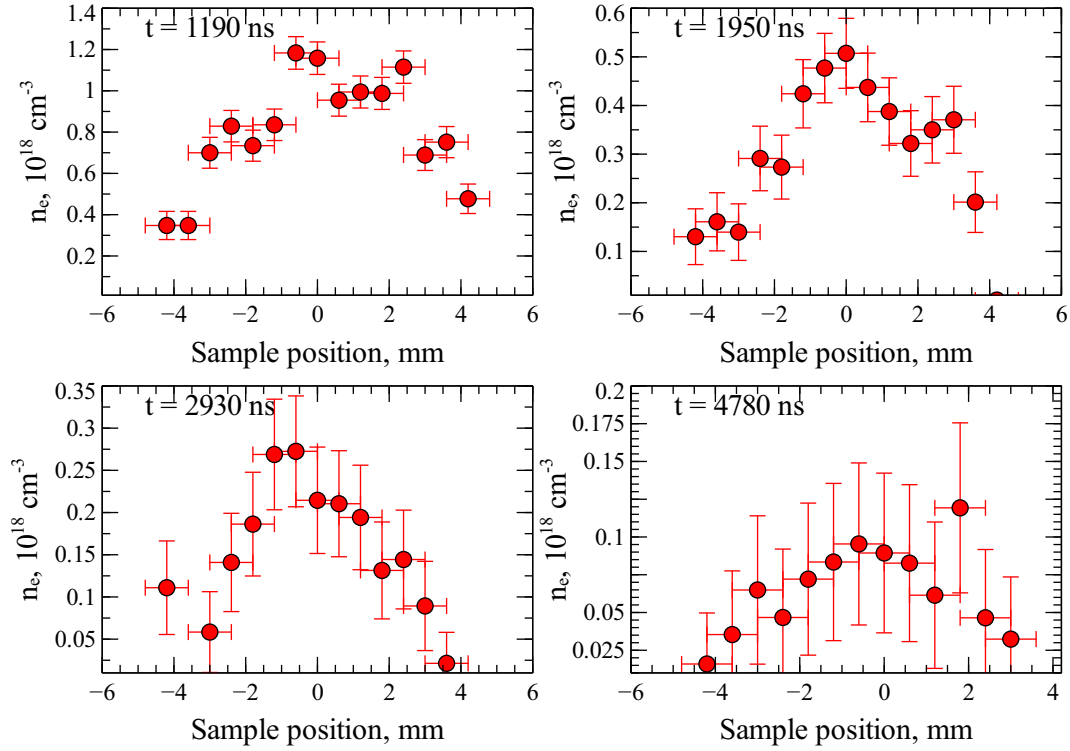


Figure 5.3.5: electron number density profile across the plasma channel transverse dimension $n_e(y)$ at different times.

obtained for air at equilibrium over a wide range of pressure and temperature with the use of the CEA code developed by NASA¹. The temperature values obtained with this method are reasonable (in the order of a few eV) and in agreement with prior studies (Bordage and Hartmann (1982); Beverly III (1986); Larigaldie et al. (1981); Larigaldie (1987b); Larigaldie (1987a); Larigaldie et al. (1992)). In addition, they are coherent with our observation of a plasma that stays too hot for recombination to occur. However, the pressure values are above 50 bar, which is not consistent with previous hydrodynamics simulation (Elias and Castera (2013)). Several reasons may explain this:

- We have assumed an equilibrium composition for the plasma during and after energy deposition. This may not be the case, which would change the factor $\sum_j K_j$ in the broadening calculation.
- In the first 1.5 μs , other lines may be present and get mixed with the H_α multiplet. For future studies, a finer grating (with more than 300 grooves/mm) should be used to distinguish the lines.
- The grating used in our measurements limits our resolution, as can be

¹Executable online at <http://www.grc.nasa.gov/WWW/CEAWeb/ceaHome.htm>

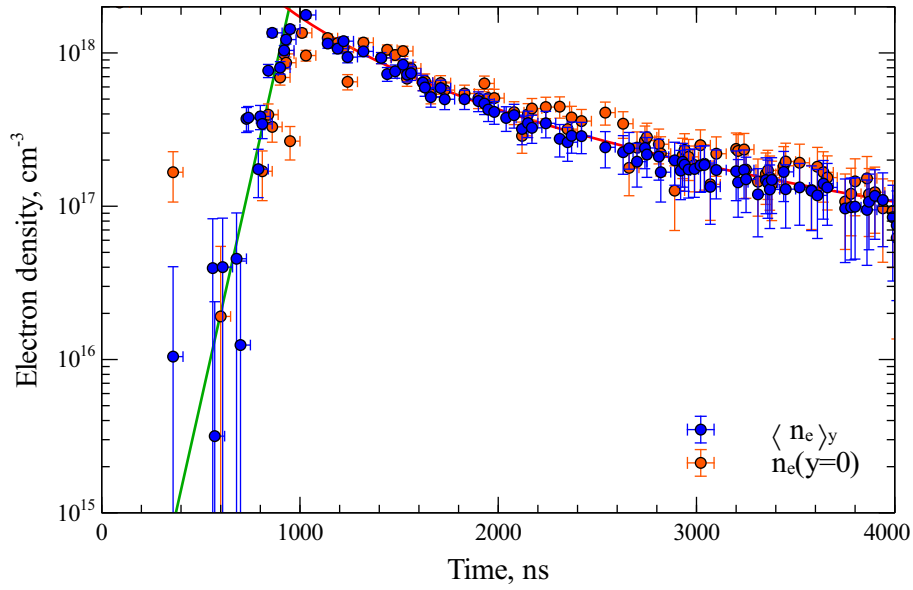


Figure 5.3.6: Compared time evolution of the average electron number density $\langle n_e \rangle_y$ and the central electron number density $n_e(y = 0)$. Both quantities follow the same trends.

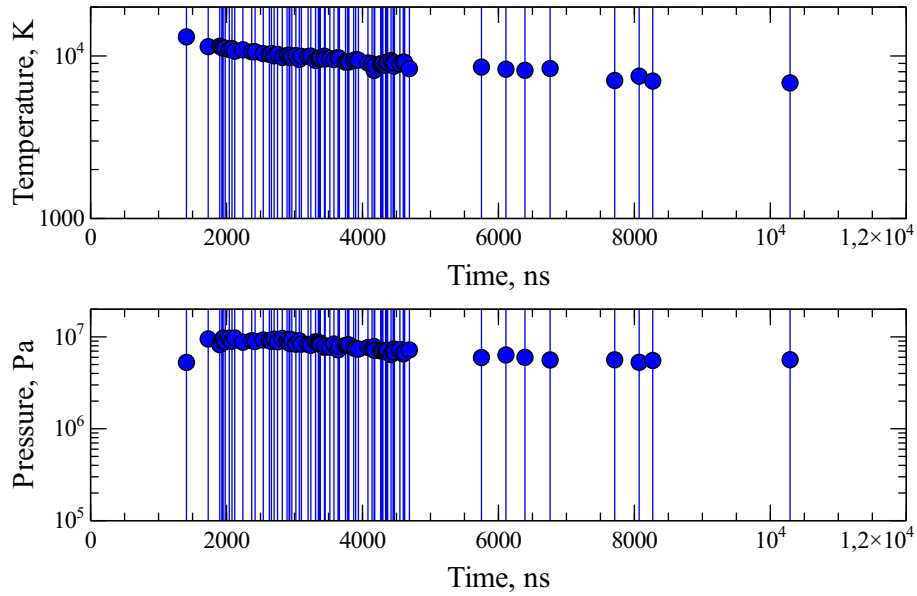


Figure 5.3.7: Evolution of temperature and pressure in the plasma. The very large error bars were computed using equation (5.3.8) and indicate the low accuracy of this method.

seen with our error bars. In fact, after a few microsecond, the Lorentz parameter γ and wavelength shift s (from which we extract the Stark and van der Waals broadening) become comparable to the pixel resolution of 0.104 nm. Here again, a finer grating (with 1200 groves/mm, for instance) would probably help improve our results.

5.3.4 High inductance case

For the high inductance case depicted in figure 5.3.8, the two phases can still be seen, with a transition around 2 μ s. During the exponential decay however, some surges can be seen around 4, 7, 10 and 13 μ s. These roughly correspond to the measured secondary Joule power peaks.

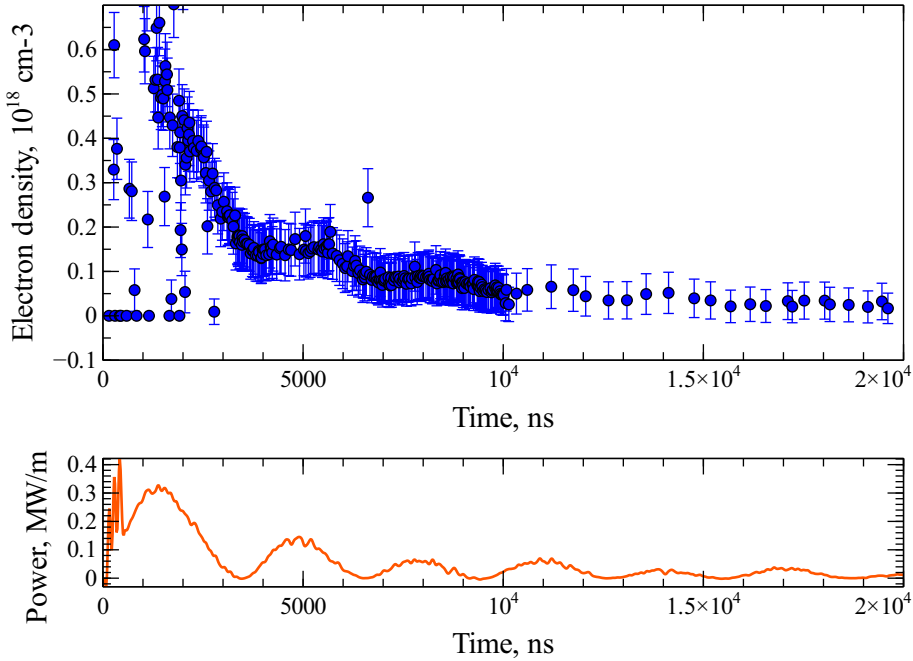


Figure 5.3.8: electron number density and corresponding linear power deposition in the discharge.

Here again, the data below 2 μ s is extremely noisy: an additional line is visible near H_{α} and gets mixed with it. This additional line corresponds to ionized carbon that most likely originates from the surface of the dielectric material that is ablated by the discharge.

5.4 Conclusion

We investigated the plasma channel evolution using fast-imaging and time-resolved spectroscopy. Light emission by the channel radius was found to be

correlated with the Joule power deposition in the discharge. Using a Gaussian fit on the recorded transverse light intensity, we estimated a light-emitting channel radius. For low inductance configurations, this radius evolves in two very clear steps: during the return stroke phase (Joule power peak), the channel expands very quickly, with a velocity that is proportional to the energy deposited in the discharge. This behavior is also observed for high inductance configurations, provided we assume the channel expansion is only driven by the energy deposited in the first power peak. Afterwards, for low inductance configurations, the channel expands at a slower rate that does not depend on the deposited energy. In the high inductance configuration, we observe some oscillations in the channel radius that coincide with the power peaks: at the end of a power peak, the channel cools down and stops emitting light from the outer layer, before later power peaks reignite the plasma.

We then performed time-resolved spectroscopy on the H_α line to access some of the plasma properties. By fitting the measured spectrum, we reconstructed the average electron number density on the transverse dimension of the discharge. At low inductance, the electron number density first increases exponentially during the return stroke phase up to values in the order of $2 \times 10^{18} \text{cm}^{-3}$: this in agreement with the Rompe-Weizel resistance model we used in our electrical analysis of the discharge in chapter 4. Using the channel radius determined previously, we computed a "spectroscopic"-based resistance for the plasma channel that we then compared to our electrical measurements. The spectrum reconstruction is difficult under 700 ns (possibly due to some line mixing or local minima encountered by the optimizer) but the quality of the data improves afterwards. Moreover, the data after 1 μs are in good agreement with the Rompe-Weizel model and yield the same asymptotic value of the channel resistance, about 8Ω . The electron number density decreases in a power law of time after the end of the power peak. This information should be useful to provide insight into the recombination mechanisms that take place in the channel. Our analysis was first performed on the average electron number density across the discharge transverse dimension. We also computed the electron number density profile across this transverse dimension: the electron number density still exhibits the two trends of an exponential increase followed by a power law decay. For high inductances, the electron number density exhibits some surges during the decrease that correspond to the secondary Joule power peaks: later energy deposition restarts ionization in the plasma channel, which further reinforces our choice of the Rompe-Weizel model for the channel resistance.

Using the van der Waals broadening measured on the spectra, we computed the gas temperature and the pressure inside the plasma channel. The temperature is in the range of a few electronvolts, in agreement with previous experiments but the pressure values are quite high. Further work is required to get more

accurate values of these quantities.

The spectroscopic analysis we performed corroborates our choice of the Rompe-Weizel model to describe the variable resistance of the plasma channel. Energy deposition leads to high electron number density values in the discharge and increases very quickly its temperature. This high temperature causes the formation of shock waves that we will study in chapter 6.

Chapter 6

Mechanical effects of the surface discharge

*We are such stuff
As dreams are made on, and our little life
Is rounded with a sleep.*

William Shakespeare, *The Tempest*, Act IV, Scene 1

The energy deposition in the plasma channel is fast compared to the hydrodynamic response time $\tau = \frac{R}{c_0}$, with R the channel radius and c_0 the speed of sound: for a channel of radius $R = 1$ mm, the hydrodynamic response time τ is on the order of a few tens of microseconds, whereas the energy deposition duration is on the order of a few hundred nanoseconds (as evidence in chapter 4). This causes the formation of shock waves that expand radially. These shock waves delimit a region where the pressure differs from ambient. This pressure difference imparts on the discharge actuator an instantaneous linear force $F(t)$ that results, when integrated over time, in a net impulse on the actuator. We would like to relate the energy deposition in the plasma channel to this impulse. To do so, we need to determine both the shock trajectory and the pressure behind the shock. We will then:

- measure the impulse imparted by the discharge on the actuator and the shock radius evolution with time for various configurations and outline its main characteristics;
- develop a model to compute the shock radius and the impulse generated by the surface discharge;
- compare the model predictions with our measurements.

6.1 Experimental study of the mechanical effects of the surface discharge

6.1.1 Measurement of the surface discharge impulse

We measure the impulse for a range of test cases at different capacitor charging voltages, inductances, and discharge lengths. We keep the same capacitance $C = 11.6$ nF for all measurements. The linear impulse as a function of the linear energy deposited in the discharge ϵ_J is shown in figure 6.1.1 for all cases surveyed in table 6.1.

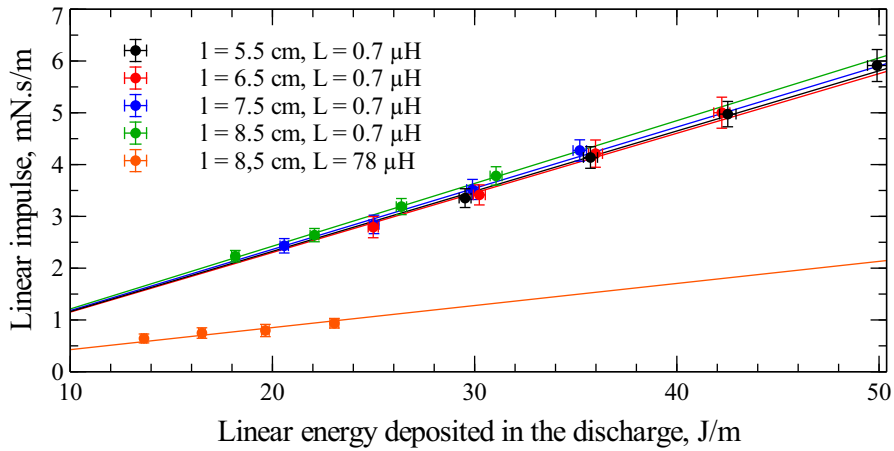


Figure 6.1.1: Linear impulse delivered by the pulsed surface discharge as a function of the linear energy deposited in the discharge: each point is averaged over 15 successful measurements (under the same conditions) to account for statistical dispersion.

Figure 6.1.1 shows that the impulse I delivered by the surface discharge scales linearly with the energy deposited in the discharge. The slope of these curves is η_J , the mechanical efficiency with respect to the linear energy deposited in the discharge:

$$\eta_J = \frac{I}{\epsilon_J}. \quad (6.1.1)$$

As we can see in table 6.1, within the tested range of linear energy, the mechanical efficiency η_J is independent of the discharge length. The efficiency does not depend either on the linear energy deposited in the discharge. We note that the system also exhibits two regimes depending on the inductance in the circuit. The high inductance ($L = 78.2$ μH) circuit is less efficient than the low inductance ($L = 0.7$ μH) circuit by a factor of 2.7. This points to a mechanical difference between the two configurations, even when taking into account the difference of electrical behavior. This difference also appears in the sparkjet

Table 6.1: Mechanical efficiency of the surface discharge for various setup configurations. For all low inductance cases, the average efficiency is $\eta_J = 118.2 \pm 3.3 \mu\text{N}\cdot\text{s}/\text{J}$.

l (cm)	L (μH)	ϵ_J (J/m)	η_J ($\mu\text{N}\cdot\text{s}/\text{J}$)
8.5	0.7	18.2, 22.1, 26.4, 31.1	121.2 ± 6.0
7.5	0.7	20.6, 25.0, 29.9, 35.2	118.4 ± 6.5
6.5	0.7	25.0, 30.2, 36.0, 42.2	116.1 ± 7.3
5.5	0.7	29.5, 35.8, 42.5, 49.9	116.9 ± 6.1
8.5	13.6	16.5, 19.7, 23.1, 26	42.4 ± 5.3

investigations by [Belinger et al. \(2011\)](#)). They studied the influence of the power supply on the sparkjet behavior in terms of discharge duration, energy deposition, and on the jet itself. Two generators were used for this analysis: a capacitive power supply (CPS) and an inductive power supply (IPS). As is the case with our setup, energy deposition was much slower using the IPS than with the CPS. For a similar amount of energy released, the discharges created by both systems behave differently. Belinger *et al* concluded that to achieve greater mechanical efficiency, energy should be delivered to the sparkjet setup as fast as possible (*e.g.* with the CPS in their analysis).

The impulse being generated by the over-pressure behind the shock wave, we expect to see two regimes in our Schlieren images.

6.1.2 Shock wave geometry and structure

First, we investigate the geometry of the shock wave generated by the discharge, by looking either across or along the discharge axis. We clearly see on our Schlieren images that the discharge generates a cylindrical shock wave, as evidenced in figures [6.1.2a](#) and [6.1.2b](#).

The shock-wave appears like a half cylinder, in accordance with our previous assumption. During one of the runs in the side Schlieren configuration, the discharge pierced the dielectric in the center of our field of view: we then observe very clearly (on figure [6.1.3](#)) that the shock wave is a half cylinder terminated by quarter-spheres.

Schlieren imaging of the discharge shock wave in both low and high inductance circuit exhibits different behaviors for the two circuit configurations: several nested shock waves are emitted with the oscillating (high inductance) circuit as shown in figure [6.1.4b](#) while only one shock wave is emitted with the low inductance circuit (see figure [6.1.4a](#)). This is visible either in front view (figure [6.1.4](#)) or side view Schlieren (figure [6.1.5](#)). In addition, the shock wave generated with a low inductance circuit (figures [6.1.4a](#)) travels further, at any given instant, than the outer one generated with a high inductance circuit (figure [6.1.4b](#)).

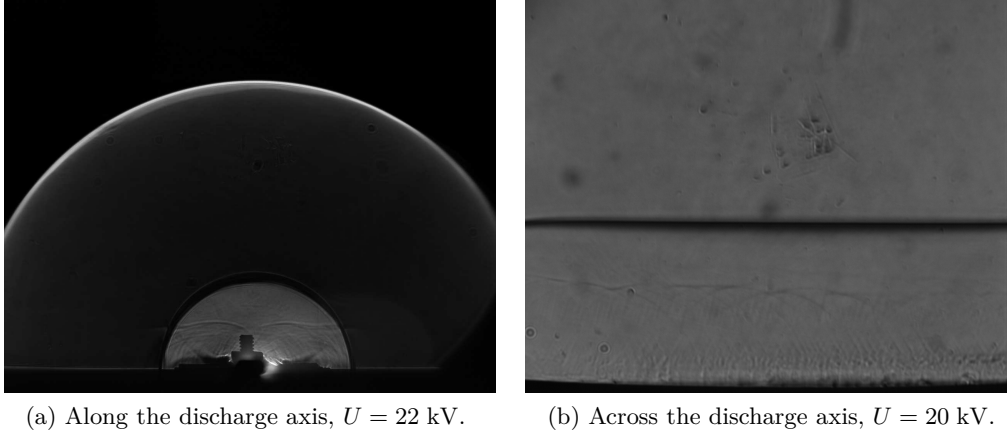


Figure 6.1.2: Shock wave generated by a 85 mm-long surface discharge for a low inductance circuit $L = 0.7 \mu\text{H}$.

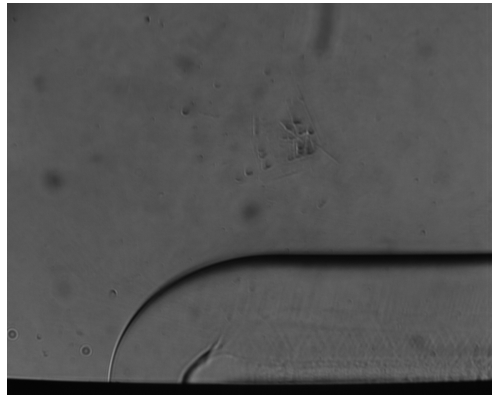


Figure 6.1.3: Schlieren image (from the side) of the shock wave generated by the discharge, with a pierced dielectric. The discharge effective length is reduced to 55 mm.

We can explain this behavior by considering the power deposition in the discharge: for a low inductance circuit, almost all of the energy is deposited in the discharge in a single high power pulse, whereas energy deposition occurs in multiple peaks in the high inductance circuit.

6.1.3 Shock wave trajectory

The phase-locked stroboscopy setup enables us to follow the shock wave trajectory as for a range of configurations (see figure 6.1.6). Having measured the scale in millimeter per pixel, we implemented an edge detection algorithm (based on peak identification in the image intensity gradient) to identify the outer pixel bounding the shock front.

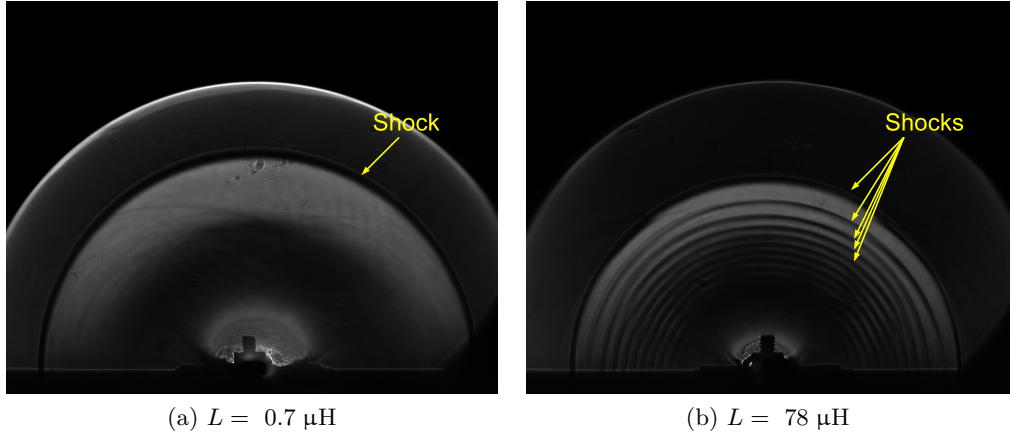


Figure 6.1.4: Shock wave generated by the surface discharge ($U_C = 22 \text{ kV}$), front images taken at the same instant after the discharge initiation.

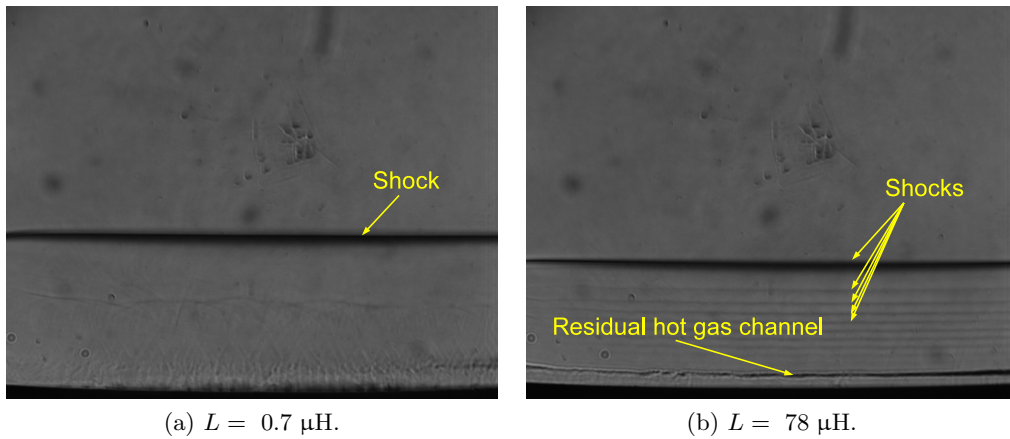


Figure 6.1.5: Shock wave generated by the surface discharge ($U_C = 20 \text{ kV}$), side images taken at $t = 35 \mu\text{s}$ after the discharge initiation.

We plot the shock trajectory for the various configurations in figure 6.1.7. We notice first that all the trajectories tend to the same asymptotic behavior. After approximately $15 \mu\text{s}$, the shock wave always propagates at a constant velocity, no matter what the initial energy stored in the discharge circuit or its inductance. Before $15 \mu\text{s}$, the shock wave expands in what appears to be a power law of time for the low inductance case. Moreover, we see that the higher the energy, the further the shock wave travels in these $15 \mu\text{s}$.

In addition, a density gradient stays visible close to the plate for a long time after the discharge initiation as can be seen in figure 6.1.5b for a high inductance circuit. This gradient delimits the low density high temperature channel

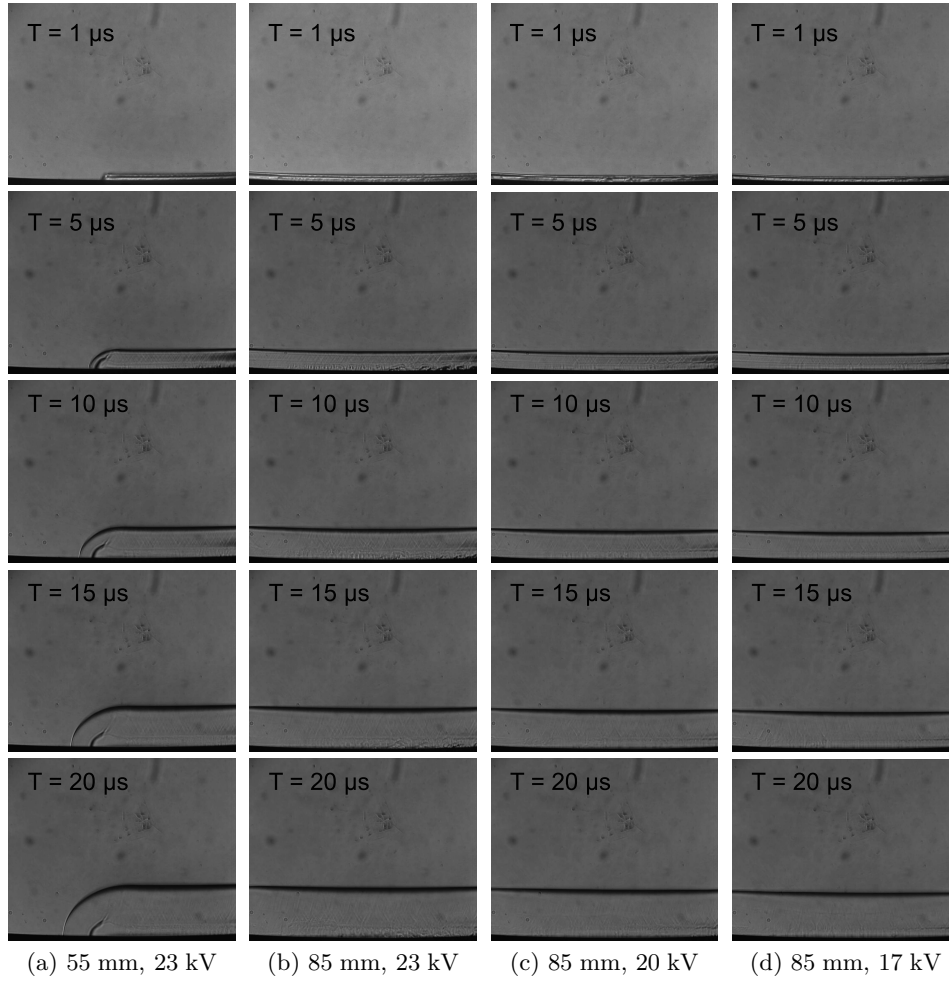


Figure 6.1.6: Shock wave generated in a low inductance ($L = 0.7 \mu\text{H}$) circuit for various charging voltages and discharge lengths.

that remains after the discharge. The measurements presented in figure 6.1.8 show that this radius quickly increases until it reaches an asymptotic value that depends on the input energy. This behavior is in agreement with the measurements of Xu et al. (2014) for nanosecond repetitive pulsed discharges. The residual channel radius evolution differs from that of the light emitting radius we measured previously (see chapter 5 section 5.1.2), for which we observed some oscillations. The residual hot gas channel does not contract as these previous measurements would have led to think, but its outer layer starts cooling and stops emitting light when the instantaneous power decreases. When another power peak starts, the extinguished region starts to emit light again, hence increasing the apparent light-emitting radius measured in section 5.1.2.

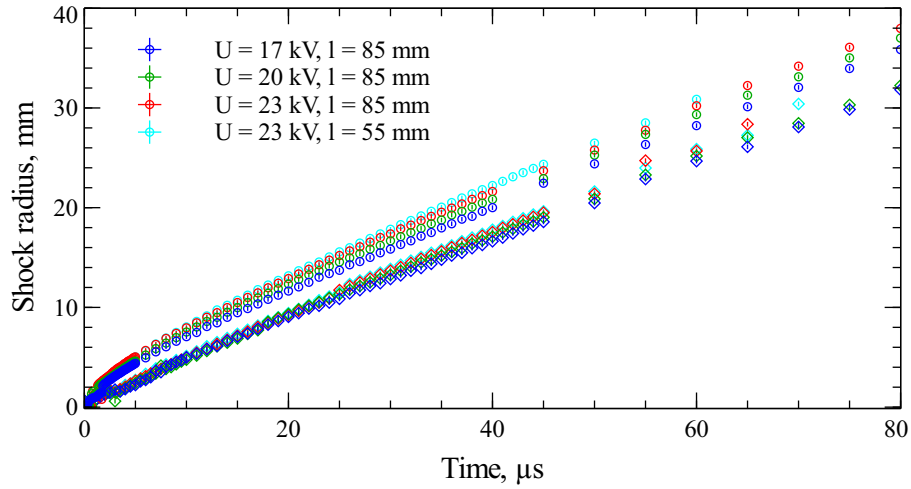


Figure 6.1.7: Shock trajectory recorded for various conditions in a low inductance circuit (circles) and a high inductance circuit (diamonds).

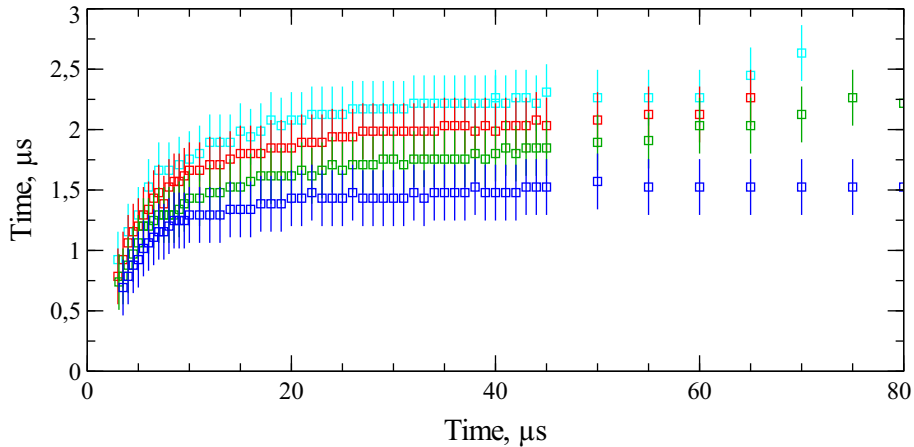


Figure 6.1.8: Evolution of the remnant channel radius for various conditions in a high inductance circuit. In the first few microseconds, the channel cannot be distinguished from the expanding shock wave.

6.2 Development a shock model

To compute the impulse generated by the discharge, we need a model for the shock structure that can give the pressure profile behind the shock and the shock radius as a function of time. We first investigate models to describe the shock trajectory, starting with the Taylor-Sedov model for strong shocks.

6.2.1 Taylor-Sedov theory for strong shocks

A well-known shock theory was developed in the 1950s by Sir Geoffrey Taylor (Taylor (1950a); Taylor (1950b)) and Leonid Sedov (Sedov (1946)). They studied the shock wave generated by the sudden release of energy in a point source, such as in nuclear weapons. Their reasoning for a spherically symmetrical system was adapted by Shao-Chin Lin (Lin (1954)) for the case of a cylindrically symmetrical system (see appendix D for more details on the calculations). Starting from conservation equations for the fluid behind the shock, if one neglects the gas initial energy (before the shock), the problem can be described in a self-similar fashion with functions of a single dimensionless variable $\xi = \frac{r}{R(t)}$, where $R(t)$ is the shock radius. This shock radius should be a function of the energy released in the shock per unit length ϵ_S , the gas density before the shock ρ_0 , some constant depending on the gas properties $S(\gamma)$ and time t . By dimensional analysis, $R(t)$ should be of the form:

$$R(t) = S(\gamma) \left(\frac{\epsilon_S}{\rho_0} \right)^{\frac{1}{4}} t^{\frac{1}{2}}.$$

Using the various conservation equations behind the shock eventually yields for the shock radius:

$$R(t) = 1.004 \left(\frac{2\epsilon_S}{\rho_0} \right)^{\frac{1}{4}} t^{\frac{1}{2}}. \quad (6.2.1)$$

We have taken into account the fact that the discharge occurs on the surface of a dielectric plate: similarly to the contact surface burst of a nuclear weapon (Glasstone and Dolan (1977)), the shock in a half-cylinder is equivalent to one generated by twice the amount of energy in a full cylinder. In addition, the Taylor-Sedov model also provides some profile functions for the various flow quantities behind the shock as functions of the similarity variable ξ and the shock radius (see figure D.1.1 in appendix D.1).

However, this theory is not applicable to the case of the shock waves generated by the surface discharge. The shock radius increases linearly after a certain time, so the time-dependence of the Taylor-Sedov radius is no longer accurate. This discrepancy is probably due to the strong shock assumption being invalid: the energy released in the shock ϵ_S is not high enough to neglect all counter-pressure effects. Some extensions to the Taylor-Sedov theory were proposed to describe this transition from a strong shock to a weak shock (see D.2) but did not yield better results in our case. We decided to try another model based on a snowplow assumption.

6.2.2 Vlases-Jones and Lee piston model

Vlases and Jones (Vlases and Jones (1966)) suggested to use a snowplow theory to describe the shock wave expansion. In a reasoning similar to the one used by Chernyi (Chernyi (1957)), they consider an instantaneous release of energy

ϵ_S at time $t = 0$ along an infinite line, and they assume that the shocked gas behind the shock wave is contained within a thin shell. They write the conservation of energy for this shocked shell:

$$\epsilon_S = \rho_0 \pi R^2 \left(F \dot{R}^2 - G c_0^2 \right), \quad (6.2.2)$$

with c the speed of sound, and F and G some functions of the ratio of specific heats γ . We integrate this equation with the initial condition $R_0 = R(t = 0)$ to get the shock radius:

$$R(t) = R_0 + \sqrt{\left(\sqrt{\frac{G}{F}} c_0 t + R_c \right)^2 - R_c^2}, \quad R_c = \sqrt{\frac{\epsilon_S}{\rho_0 \pi G c_0^2}}. \quad (6.2.3)$$

The radius R_c is a characteristic radius that depends on the energy released in the shock and that marks the transition from a strong shock to a weak shock. Vlases and Jones formula exhibits a correct behavior, with a shock radius proportional to the square root of time in the first instants and later proportional to time:

$$\begin{aligned} t \longrightarrow 0, R(t) &\propto t^{\frac{1}{2}}, \\ t \longrightarrow \infty, R(t) &\propto t. \end{aligned}$$

Lee (Lee (1966)) noted that Vlases and Jones used strong shock relations in writing the coefficients F and G in equation (6.2.2), and suggested to use for these quantities other formulas based on Rankine-Hugoniot relations:

$$\text{Vlases-Jones: } \begin{cases} F = \frac{1}{2} + \frac{2}{(\gamma+1)^2} \\ G = \frac{2(\gamma-1)}{\gamma(\gamma+1)^2} \end{cases} \implies \text{Lee: } \begin{cases} F = \frac{4}{(\gamma+1)^2} \\ G = \frac{2(3\gamma-1)}{\gamma(\gamma+1)^2} \end{cases} \quad (6.2.4)$$

We should then use these new coefficients in our own computations.

6.2.3 Adaptation of the shock model to the surface discharge configuration

In their description, Vlases and Jones assume a full cylindrical geometry over 2π . Due to our setup geometry, the shocked gas is contained in a half-cylinder shell only, so we write equation (6.2.2):

$$\epsilon_S = \rho_0 \frac{\pi}{2} (R - R_0)^2 \left(F \dot{R}^2 - G c_0^2 \right), \quad (6.2.5)$$

Integrating this equation yields the shock radius:

$$R(t) = R_0 + \sqrt{\left(\sqrt{\frac{G}{F}} c_0 t + R_c \right)^2 - R_c^2}, \quad R_c = \sqrt{\frac{2\epsilon_S}{\rho_0 \pi G c_0^2}}, \quad (6.2.6)$$

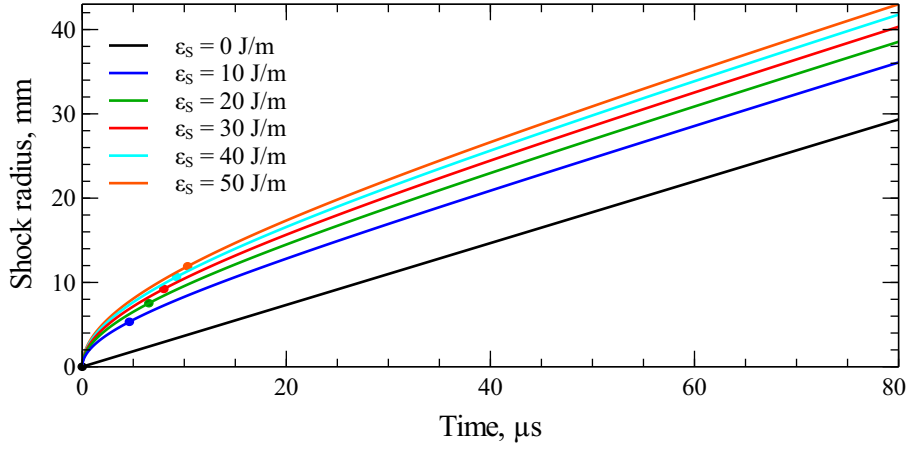


Figure 6.2.1: Shock trajectories for different energies ϵ_S . The dots indicate for each trajectory the characteristic radius R_c that marks the transition from a strong shock to a weak shock.

with $R_0 = R(t = 0)$ the initial shock radius corresponding to the plasma channel radius.

As seen in figure 6.2.1, the shock trajectory given by equation (6.2.6) comprises two phases. At the beginning, the shock expands in a strong shock fashion ($R(t) \propto t^{\frac{1}{2}}$), whereas after some time it simply expands linearly ($R(t) \propto t$) with an identical velocity for all shocks (approximately 350 m/s). The initial phase exhibits a dependence on the shock energy ϵ_S : the more input energy, the faster and farther the shock expands.

6.2.4 Impulse computation

The fast energy deposition in the plasma channel causes the formation of shock waves that expand radially. These shock waves delimit a region where the pressure differs from ambient. This pressure difference imparts on the discharge actuator an instantaneous linear force $\mathbf{F}(t)$ that can be computed:

$$\mathbf{F}(t) = \oint P(\mathbf{r}, t) d\mathbf{n}(\mathbf{r}),$$

where the closed integral is circulated on the actuator contour. $d\mathbf{n}(\mathbf{r})$ is the inward oriented length element at point \mathbf{r} on the contour (see figure 6.2.2). Assuming the setup is symmetrical with respect to the discharge axis, denoting $R(t)$ the shock wave radius at time t and $P_1(\mathbf{r}, t)$ the pressure inside the shocked region, the linear force applied on the actuator then sums up to:

$$\mathbf{F}(t) = 2 \int_0^{R(t)} (P_0 - P_1(r, t)) dr \mathbf{e}_z.$$

Through integration over time, we get from the previous equation the linear impulse generated by the surface discharge :

$$\mathbf{I}(t) = 2 \int_0^t \int_0^{R(\tau)} (P_0 - P_1(r, \tau)) dr d\tau \mathbf{e}_z. \quad (6.2.7)$$

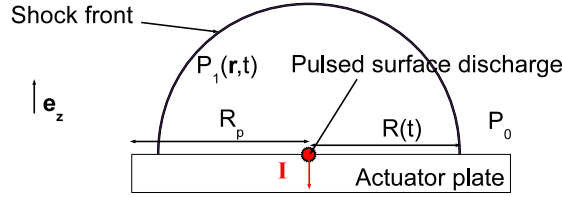


Figure 6.2.2: Contour used for the computation of the linear impulse imparted by the pulsed surface discharge.

The modified snowplow model gives the fluid quantities behind the shock thanks to the Rankine Hugoniot relations:

$$P_1 = \frac{2\rho_0 U^2}{\gamma + 1} - \frac{\gamma - 1}{\gamma + 1} P_0, \quad (6.2.8)$$

$$v_1 = \frac{\gamma - 1}{\gamma + 1} U + \frac{2}{\gamma + 1} \frac{c_0^2}{U}, \quad (6.2.9)$$

with $U = \dot{R}$ the shock front velocity. However, our model can not describe the flow field far behind the shock, so we still miss the pressure profile $P_1(r, t)$. The problem of a pressure profile behind a shock wave has been studied extensively for damage assessment on buildings following (spherical) blasts created by conventional or nuclear weapons. In the various analyses, the impulse imparted by the blast wave is computed at a fixed distance r from the source, with a surface $S(r)$ normal to the blast propagation, and integrated over time. Far enough from the source, the pressure can be approximated as homogeneous over the integration surface, so that the total impulse computation amounts to a sole integration over time, which requires the time history of pressure at position r :

$$I(t) = \int_0^t \int_{S(r)} \Delta P(r, t) dS dt \approx S(r) \int_0^t \Delta P(r, t) dt, \quad (6.2.10)$$

where $\Delta P(r, t) = P(r, t) - P_0$ is the overpressure behind the shock with respect to the ambient pressure P_0 . A standard profile for the pressure history is given by the modified Friedlander function (Goel et al. (2012); Larcher (2007); Larcher (2008); Lam et al. (2004); Sochet et al. (2011)):

$$P(r, t) = P_0 + P_S(r) \left(1 - \frac{t}{t_c}\right) e^{-b \frac{t}{t_c}}, \quad (6.2.11)$$

where $P_S(r) = P_1 - P_0$ is the overpressure when the shock arrives at position r at time $t = 0$. t_c and b are two parameters that have been tabulated, alongside P_S , as a function of a scaled distance to the source. Many formulas were proposed to compute these values as a function of the initial energy deposited in the shock by the source. However, equation (6.2.11) gives the time history of pressure at a given position after the shock has passed, whereas in the surface discharge we are interested in a space history of pressure at a given moment, as shown in figure 6.2.3.

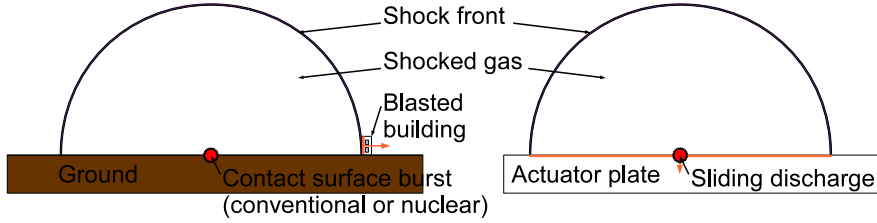


Figure 6.2.3: Shock structure after a conventional or nuclear weapon detonation (left) and after the return stroke phase of the surface discharge (right). The impulse of interest is depicted by the orange arrow for both cases.

By similarity with equation (6.2.11), we assume a pressure profile behind the shock:

$$P(r, t) = P_0 + P_S(R(t)) \left(1 - \frac{R(t) - r}{R_c}\right) e^{-b \frac{R(t) - r}{R_c}}, \quad (6.2.12)$$

with r the distance from the source, $R(t)$ the shock radius at time t and R_c and b two parameters to be determined. For R_c , we use the radius derived from our expression of the shock trajectory (6.2.6):

$$R_c = \sqrt{\frac{2\epsilon_S}{\rho_0 \pi G c_0^2}}. \quad (6.2.13)$$

As mentioned in section 6.2.2, this characteristic radius R_c marks the transition from a strong shock to a weak shock. Using this radius R_c is plausible under the assumption that it is the strong portion of the shock that exerts the push. The b parameter can be related to a characteristic thickness of the piston that pushes the shock.

The downward linear impulse generated by the discharge can be computed with this pressure profile (6.2.12) and a shock radius given by the Lee model (6.2.6):

$$I(t) = 2 \int_0^t \int_0^{R(\tau)} (P_1(r, \tau) - P_0) dr d\tau. \quad (6.2.14)$$

The impulse can be computed by a numerical double integration over space and time, which can be rather costly in terms of computational power. Through

a change of variable (see appendix E.1 for more details), we have transformed equation (6.2.14) into a single integration over a non-dimensional variable l :

$$I(L) = \frac{8\epsilon_S}{\pi(\gamma+1)c_0} \sqrt{\frac{F}{G}} \int_0^L \left(\frac{1}{l^2} + \left(\frac{1}{F} - \frac{1}{G} \right) \right) \frac{A(b,l)l}{\sqrt{l^2+1}} dl, \quad (6.2.15)$$

where A is a dimensionless function of the parameter b and L is a cut-off length (dimensionless parameter) for integration. It may still be helpful to have an approximate formula to outline the main dependencies of the impulse with the various physical parameters of the system. After some computation (see appendix E.2 for more details), the impulse can be approximated with the analytic expression:

$$\begin{aligned} I &= \frac{8\epsilon_S}{\pi(\gamma+1)bc_0} \sqrt{\frac{F}{G}} \left(1 + \log \left(\frac{2Lb}{\sqrt{L^2+1}+1} \right) + \left(\frac{1}{F} - \frac{1}{G} \right) (\sqrt{L^2+1} - 1) \right), \\ I &= \frac{0.993\epsilon_S}{bc_0} \left(1 + \log \left(\frac{2Lb}{\sqrt{L^2+1}+1} \right) + 0.180 (\sqrt{L^2+1} - 1) \right), \end{aligned} \quad (6.2.16)$$

with numerical coefficients given for air ($\gamma = 1.4$). b is the thickness parameter of the Friedlander-like formula (6.2.12). The overpressure on the plate can be neglected when the shock wave has reached $\frac{5R_c}{b}$ beyond the actuator plaque. Consequently, we set:

$$L = \frac{R_p}{R_c} + \frac{5}{b}. \quad (6.2.17)$$

We can then write the surface discharge mechanical efficiency η_J in air:

$$\eta_J = \frac{0.993}{bc_0} \frac{\epsilon_S}{\epsilon_J} \left(1 + \log \left(\frac{2Lb}{\sqrt{L^2+1}+1} \right) + 0.180 (\sqrt{L^2+1} - 1) \right). \quad (6.2.18)$$

The efficiency $\eta_J(c_0, \gamma, b, \frac{\epsilon_S}{\epsilon_J}, L)$ depends on the fluid properties (speed of sound c_0 and numerical coefficients), on the parameter b , on the fraction of energy used to heat the gas and create the shock, and on the integration cut-off L . The latter quantity is inversely proportional to the characteristic radius R_c that depends on the square root of the linear energy ϵ_S . Thus, the efficiency decreases with increasing linear energy.

6.3 Comparison with experimental measures

6.3.1 Low inductance circuit

The shock trajectory predicted with equation (6.2.6) is governed by the amount of linear energy ϵ_S released in the shock, which is a fraction of the linear energy ϵ_J deposited in the discharge by Joule heating. We determine this fraction by fitting **one** of our measurements with the predicted radius. Our shock wave prediction matches the shock radius evolution as can be seen on figure 6.3.1,

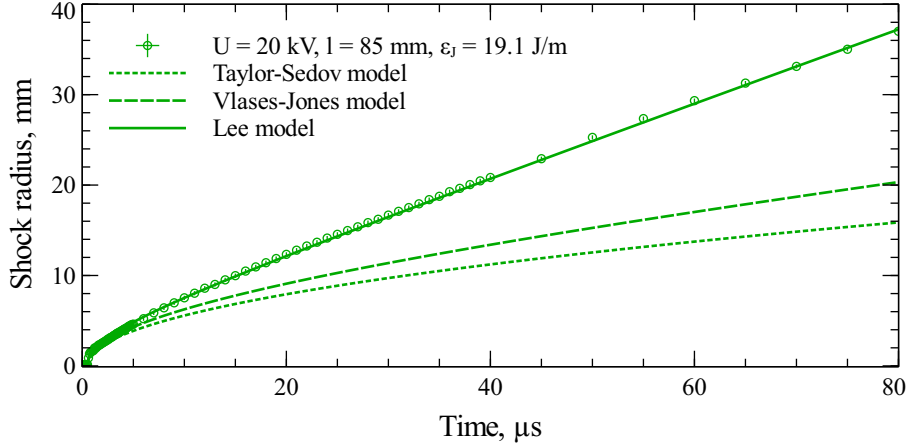


Figure 6.3.1: Evolution of the shock wave radius with time compared with predictions from the Taylor-Sedov model, the Vlasses-Jones model, and the Lee model. We have assumed in all models that 30% of the linear energy deposited in the discharge ϵ_J is used to generate the shock wave.

when we consider an initial radius equal to the discharge channel radius at the end of the Joule power peak, and that 30% of the linear energy ϵ_J deposited in the discharge by Joule heating is transferred to the shock-wave ($\epsilon_S = 0.3\epsilon_J$). This factor of 0.3 is consistent with shock wave calculations performed by Znamenskaya (Znamenskaya et al. (2007)) for similar discharges in CO_2 or by Xu (Xu (2013); Xu et al. (2014)) for nanosecond discharges in air. Xu *et al.* (Xu (2013); Xu et al. (2014)) studied the fast heating of small plasma columns in air, and found that using about 25% of the energy deposited in these discharges to launch the shock waves could explain his Schlieren images in air at room temperature. Thus the simplified shock model presented here is in good agreement with Xu's computations (even though the experimental configurations differ) and appears to be robust: using this same coefficient of 0.3 for other low inductance test cases yields radius predictions that fall within experimental error bars.

The shock model presented here seems to accurately predict the shock wave behavior in terms of radius. We now investigate the impulse computation with this model. As a first approximation, we assume that the parameter b of equation (6.2.12) is a constant that does not depend on time, space or energy released in the shock. This constant is determined empirically by fitting the measured impulse for **one** given configuration. To do so, one must determine a finite computation time t_F for the impulse numerical integration using equation 6.2.4. The impulse generated by the discharge is measured with a torque balance under the assumption that its characteristic time is negligible with respect to the balance oscillating frequency. In agreement with our theoretical estimate of the impulse in section 6.2.4, we set t_F such that the shock front has

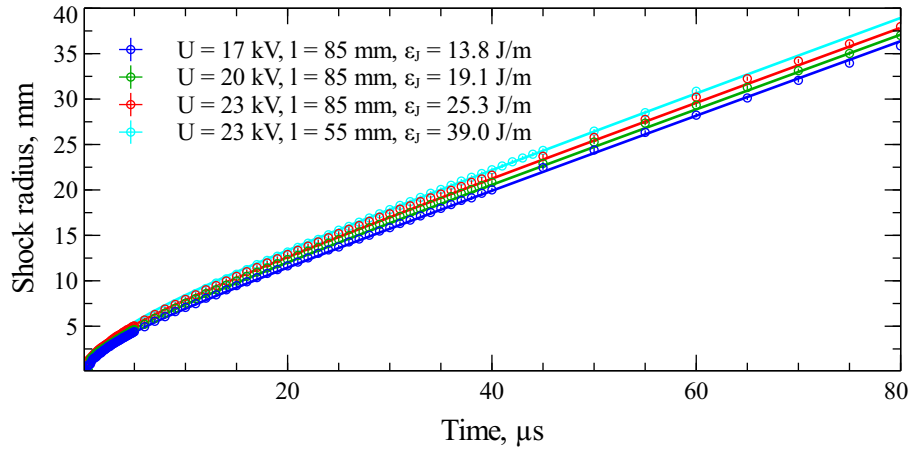


Figure 6.3.2: Evolution of the shock wave radius with time compared with predictions from the Lee model.

reached a distance of $5R_c$ beyond the plate boundary. After t_F , the shock wave has moved out of the actuator plate, and there is no more overpressure hence no more impulse. This is consistent with the piston model used to describe the shock radius: the overpressure is concentrated in a thin layer behind the shock as can be seen on figure 6.3.3.

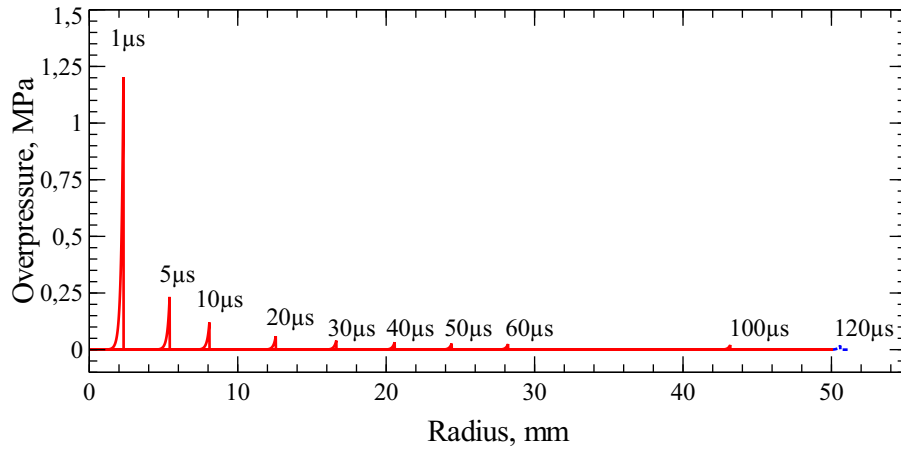


Figure 6.3.3: Computed overpressure as a function of distance from the source at different instants (the blue curve shows the overpressure out of the actuator). Discharge conditions: $l = 85$ mm, $U = 20$ kV, $\epsilon_J = 19.1$ J/m.

Figure 6.3.4 depicts the impulse computed with the pressure profile given by (6.2.12) for $b = 43$, for all the low inductance cases. Our analytic expression 6.2.16 falls within 10% above the numerical integration, despite its apparent simplicity: one should note once again that the parameter b was obtained

through fitting a **single** measurement point and that the optimum value was then used for all cases. The impulse overestimation with formula (6.2.16) is due to our asymptotic approximation. Using a finer expression (see appendix E.3 for more details), the analytic impulse computation falls within 3% of the numerical integration.

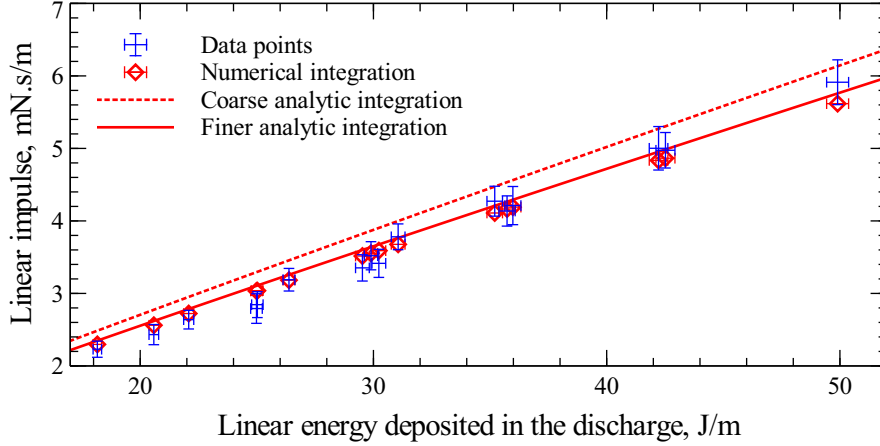


Figure 6.3.4: Measured and computed impulse for a low inductance circuit.

We use equation (6.2.18) to compute the surface discharge mechanical efficiency. The computed efficiency ranges from $137.6 \mu\text{N.s/J}$ to $123.4 \mu\text{N.s/J}$, which is higher than the experimental value of $118.2 \pm 3.3 \mu\text{N.s/J}$ as expected due to the overestimation of the impulse with formula (6.2.16). However, doubling the amount of energy for a fixed value of the parameter b only reduces the mechanical efficiency by 10%. Over the range of energies tested in our experiments, the surface discharge thus seems to have a constant efficiency. This is in agreement with the form of equation (6.2.18): the last term that depends on the pseudo-length L is dampened by the numerical coefficient. In contrast, changing the parameter b by 10% results in an equivalent modification of the efficiency, as b appears in the prefactor of equation (6.2.18). Thus, for a fixed value of b , the linear impulse can be considered to be simply proportional to the linear energy deposited in the discharge, the proportionality constant depending mainly on the gas properties (γ, c_0) and the parameter b .

We want to compare the surface discharge to another plasma actuator to assess its interest. As we have focused on the impulse generated by the surface discharge, we consider another actuator for which a similar analysis has been performed: the sparkjet. The impulse delivered by the surface discharge scales linearly with the energy deposited in the shock, whereas the sparkjet produces an impulse that increases as the square root of the energy, as shown by Anderson and Knight (2012b); Anderson and Knight (2012a). The sparkjet configuration is that of a point source, so to compare properly the two systems,

we have to consider a surface discharge of a given length. Assuming the linear impulse to be constant over the discharge length, the total impulse I generated for an input energy Q can be expressed as:

$$\text{surface discharge: } I \propto \frac{Q}{c_0}, \quad (6.3.1a)$$

$$\text{sparkjet: } I \propto \sqrt{\rho_0 V Q}, \quad (6.3.1b)$$

where V is the sparkjet cavity volume. In the surface discharge, we have found experimentally that Q is about 30% of the total energy deposited in the discharge, which is in good agreement with the results of [Anderson and Knight \(2012b\)](#); [Anderson and Knight \(2012a\)](#) who consider that Q is about 25% of the energy deposited in the sparkjet cavity. At sea level, a 10-cm long surface discharge appears to be more efficient than a sparkjet actuator, since it delivers more impulse for the same input energy (see figure 6.3.5).

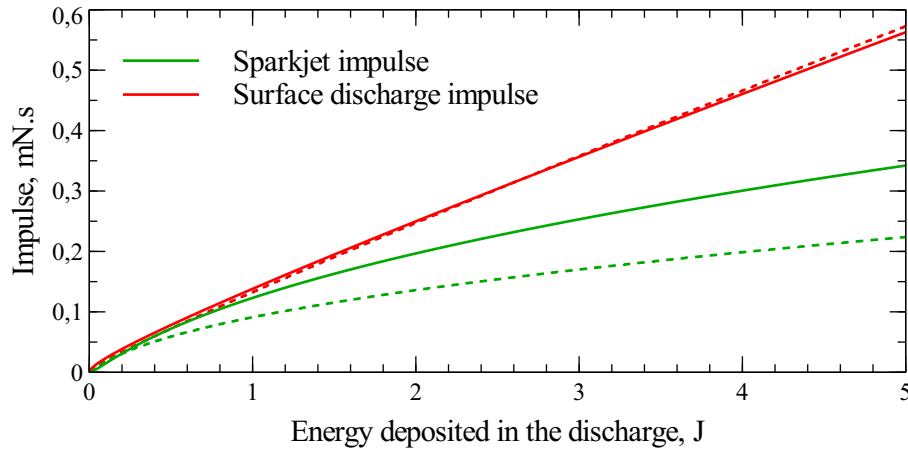


Figure 6.3.5: Total impulse generated by a sparkjet and by a 10 cm-long surface discharge for an input energy varying between 10 mJ and 5 J, at sea level (plain lines) and at an altitude of 30000 feet (dotted lines).

Moreover, the surface discharge impulse varies as the inverse of the speed of sound, whereas the sparkjet impulse scales as the square root of the density at rest: the surface discharge might then be also more efficient at higher altitude (where c_0 and ρ_0 are lower) than the sparkjet, assuming our model and hypotheses hold. We plot on figure 6.3.5 the impulse generated by the two actuators at sea level and at an altitude of 30000 feet (see table 6.2 for the values of the relevant quantities). Although the sparkjet-generated impulse decreases with altitude as expected, the surface discharge-generated impulse appears to be almost altitude-independent. In our analysis of the compared efficiency of both actuators (6.3.1), we simply considered the main driving prefactor: the other terms must also be taken into account and explain this apparent inconsistency. Experimental studies should be conducted to verify this behavior.

Table 6.2: Air characteristics.

Altitude (ft)	P_0 (Pa)	T_0 (K)	ρ_0 (kg/m ³)	c_0 (m/s)
0	101325	293	1.2	343
30000	30000	229	0.45	303

It should also be noted that the actuator geometry influences the impulse generated by both systems. Further studies will be needed to assess the optimal parameters.

6.3.2 High inductance circuit

The snowplow model can be used to compute the radius of the single shock wave of a low inductance circuit ($L = 0.7 \mu\text{H}$). We use it in the oscillating circuit ($L = 78 \mu\text{H}$) where multiple shock waves are observed. For such a circuit, the current flowing in the plasma channel can be accurately described with a standard under-damped oscillator solution:

$$i_p(t) = K(\omega_0, \alpha) \sin(\sqrt{\omega_0^2 - \alpha^2}t)e^{-\alpha t}, \quad (6.3.2)$$

where α and ω_0 are defined for the circuit of figure 4.2.1 in chapter 4:

$$\alpha = \frac{R_p}{2L} + \frac{R_{sg}R_b}{2(R_{sg} + R_b)L} + \frac{1}{2(R_{sg} + R_b)C}, \quad (6.3.3)$$

$$\omega_0 = \sqrt{\frac{R_p + R_b}{R_{sg} + R_b} \frac{1}{LC}}. \quad (6.3.4)$$

Here we have assumed a constant resistance $R_p = 8 \Omega$ for the plasma channel. This is consistent with our previous analysis of the plasma channel transient resistance in chapter 4. We can then compute the energy $\epsilon_{J,k}$ released in the k -th peak power as a fraction of the total energy ϵ_J released by Joule heating in the discharge:

$$\frac{\epsilon_{J,k}}{\epsilon_J} = \left(1 - e^{-\frac{2\pi\alpha}{\sqrt{\omega_0^2 - \alpha^2}}}\right) e^{-\frac{2\pi\alpha(k-1)}{\sqrt{\omega_0^2 - \alpha^2}}}. \quad (6.3.5)$$

The radius for the k -th shock wave is then computed starting from time t_k (end of the k -th power pulse) with an energy $\epsilon_{S,k}$ equal to 30% of the corresponding Joule energy $\epsilon_{J,k}$. With this model we are then able to predict the multiple shock structure, as can be seen on figure 6.3.6, and we confirm our hypothesis that this structure is due to the Joule heating of the plasma channel.

Our snowplow model can describe accurately the shock front in both the single shock and multiple shock regimes. We now want to use it to compute the impulse imparted by the discharge to the actuator.

Given the success of our Friedlander-like approach in a low inductance circuit, we try to compute the impulse generated in a high inductance circuit. We keep

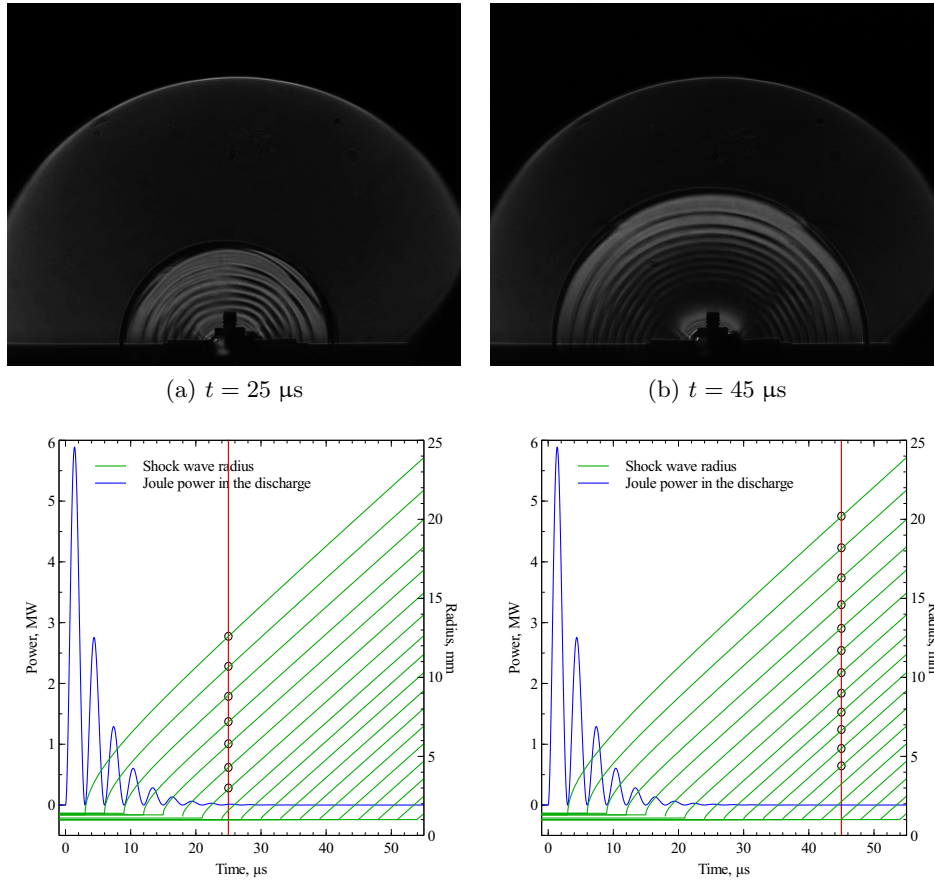


Figure 6.3.6: Schlieren images (upper row) and predicted structure (lower row) of the shock waves generated by the pulse surface discharge ($U_C = 22$ kV) in a high inductance circuit ($L = 78$ μ H) at various instants. The model enables a proper prediction of the shock structure in terms of visible shock waves (circles). No attempt was made to measure these nested shock waves radius.

the same value for b and assume that 30% of the Joule energy (equal to 50% of the initial capacitor energy in a high inductance circuit) is used in the shock. Multiple nested shocks are generated by the discharge in an oscillating circuit. In a first attempt, each shock is assumed to push on the plate. To determine these elementary impulse, one needs to know the amount of energy released in each shock. Following the reasoning for shock radius, we use equation (6.3.2) to get the energy fraction in each peak:

Considering that the ten first peaks all push with a pressure profile given by the Friedlander-like formula (6.2.12) with $b = 43$ and R_c given for each peak by equation (6.2.4), the computed impulse is equal to more than twice the measured value. However, in the snowplow model, most of the shocked gas is

Table 6.3: Joule energy fraction deposited per peak.

Peak number	1	2	3	4	5	6	7	8	9	10
Energy fraction (%)	37.3	23.4	14.7	9.2	5.8	3.6	2.3	1.4	0.9	0.6

supposed to be contained in a thin layer behind the shock front. Assuming then that only the first peak can push on the plate, the computed impulse falls within 30% of the measured value, as seen on figure 6.3.7. The remaining deviation is probably due to the simplicity of our pressure profile model which may not be accurate enough in the case of a nested shocks configuration. We have again assumed here a constant value of the b parameter, set to $b = 43$: allowing this parameter to vary, it is possible to find better agreement between experiments and the one peak model for $b = 55$.

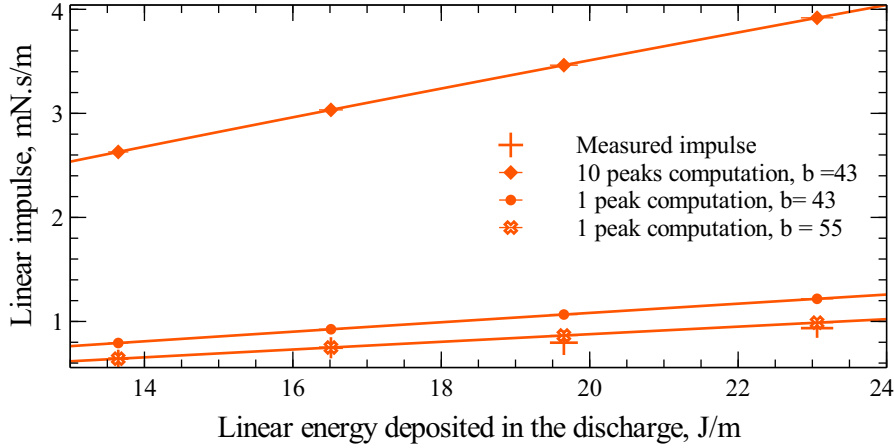


Figure 6.3.7: Impulse measured and computed for a high inductance circuit.

The behavior observed in this high inductance configuration points to a limit in the actuation regime achievable by the surface discharge. Indeed, one of the main interests of plasma actuators is their fast response timescale and the possibility of pulsed actuation (of particular interest to couple with aerodynamic instabilities for instance). A first limit to this actuation frequency f_a is imposed by the energy deposition mechanism in the discharge. As studied in chapter 4, the whole discharge setup behaves like a pseudo-RLC circuit, of which the oscillations can be tuned by properly setting the circuit characteristics. Reducing the inductance to a minimum, the circuit can be overdamped, with all the energy initially stored in the capacitors transferred to the discharge in a single power peak of duration t_e . This leads to a first maximum actuation frequency $f_e = \frac{1}{t_e}$ due to the sole electrical behavior of the actuator. However, our impulse measurements and computation with a high inductance circuit indicate that there exists another limiting frequency f_s related to the shock structure. Indeed, we observe a clear non-linearity of the impulse with

the input energy:

$$I \left(\sum_{\text{peak}} E_{\text{peak}} \right) < \sum_{\text{peak}} I(E_{\text{peak}}) \quad (6.3.6)$$

In our snowplow formalism, the first power peak observed with an oscillating circuit pushes most of the gas behind the shock front. Following shocks due to the later power peaks take place in a hot gas channel (visible on our Schlieren images) and thus lack the gas density to impart a meaningful impulse. Therefore, efficient pulsed actuation can only be achieved if the successive power pulses are separated enough for the gas to recover after the shock, that is if the actuation frequency f_a is lower than a recovery frequency f_r . If the discharge occurs in still air, the gas recovery can be either achieved through convection of the the hot gas channel: as shown in figure 6.3.8, this convection process takes up to a few milliseconds, which gives a recovery frequency f_r in the order of a few hundred Hertz.

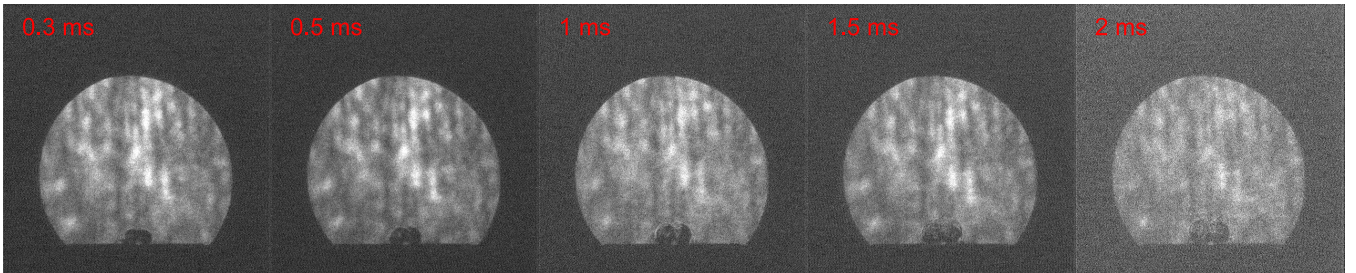


Figure 6.3.8: Long term Schlieren images: the residual hot gas channel left by the discharge has started to convect (mushroom cloud pattern) but is still close to the dielectric layer.

If however the discharge takes place across the leading edge of a flying aircraft, the hot gas channel (of characteristic radius 1.5 mm) will be swept away by the airflow (of typical velocity 300 m/s) in about 10 μs , which gives a recovery frequency of 100 kHz. This conclusion is based solely on impulse measurements with an oscillating circuit in still air and should be verified in an airflow with separated power peaks, which would require additional experiments with a controllable pulsed power supply.

6.4 Conclusion

Using a calibrated torque balance, we measured the linear impulse delivered by the surface discharge in various configurations. This linear impulse was found to be proportional to the linear energy deposited in the discharge. Varying the discharge length increased the linear energy deposited in the discharge without any other significant effect. However, changing the inductance of the circuit, hence its oscillatory behavior did change dramatically the linear impulse: the

high inductance configuration was found to be almost three times less efficient than the low inductance one, even when taking into account the difference in Joule efficiency. This was attributed to the shock wave structure, which is different in the low and high inductance cases (Castera et al. (2014)).

Schlieren imaging first proved that the shock wave exhibits a half cylinder structure (terminated by quarter-sphere). This means that the energy deposition is uniform along the discharge axis, thus confirming our hypothesis of translational invariance. The low inductance and high inductance circuits exhibit a different shock structure: although a single shock wave is visible in the low inductance circuit, multiple nested shock waves are generated in the high inductance one. This was assumed to be related to the energy deposition in the discharge: in a low inductance circuit, almost all of the Joule energy is deposited in a single peak, whereas multiple peaks occur in a high inductance circuit. The shock trajectory was recorded and found to be in a transition between the strong shock regime (in the first few microseconds) and a weak shock regime that tends to a sonic expansion. We adapted a snowplow model that predicts properly the shock radius, when considering that 30% of the Joule energy deposited in the discharge is used to heat the gas. This result is in good agreement with other observations of shock waves generated by different type of discharges. When considering the high inductance circuit, the model was able to describe properly the shock structure due to multiple Joule peaks.

To compute the linear impulse generated by the discharge, we made the hypothesis that the pressure behind the shock follows a Friedlander-like profile. This profile normally includes two parameters, one of which was chosen from the piston model. The other parameter was obtained from fitting a single measured impulse. These values were then used to compute the impulse for all low inductance configurations and were found to be in good agreement, within 2% of the measured impulse. In the case of a high inductance circuit, we assumed that only the first shock wave pushed on the plate, in accordance with the snowplow formalism. The computed impulse was still about 25% higher than measurements. The model however does agree with the linear behavior observed for the impulse generated by the surface discharge as a function of the input energy.

The surface discharge seems to be an interesting actuator when compared to the sparkjet: for the same amount of energy, the discharge generates more impulse. Furthermore, being an open-flow design, the surface discharge actuation frequency is not constrained by a cavity recovery cycle as in a sparkjet, though the pulsed discharge mechanism itself imposes a limit on the maximum achievable actuation frequency. Two phenomena should be accounted for in order to estimate this maximum actuation frequency: the electric circuit duty cycle on the one hand, and the shock structure on the other hand. All the experiments

on the surface discharge were performed at sea level, additional tests should be done in more realistic flight-like condition. Further study would also require the comparison of electrodes erosion between the two systems, and to take into account the dielectric aging in a surface discharge.

Chapter 7

Conclusion

Hin ist alle meine kraft.

Joseph Haydn, Der Greis

7.1 Main results of this study

We have investigated the electrical behavior of the pulsed surface discharge in a range of circuit configurations, changing the capacitance, the initial charging voltage, the inductance or the discharge length. The propagation phase (corresponding to the plasma channel formation) and the arc phase (corresponding to the energy deposition in the channel) are clearly visible on the current and voltage curves. As presented in the literature, the propagation phase is governed by Toepler's laws, with a propagation velocity proportional to the charging voltage. Most of the energy initially stored in the capacitor bank is deposited into the channel during the arc phase. This energy deposition takes place over a duration that depends on the circuit configuration and on the initial energy stored in the capacitors. To understand this energy deposition, we have developed an electrical model for the current pulse measured in the plasma channel. Although the current exhibits some RLC-like oscillations, low inductance circuits cannot be described with the standard under-damped oscillator. Based on previous studies, we have implemented non-linear time-varying resistance models for the plasma channel resistance. The various models (Rompe-Weizel, Vlastós, Toepler and Braginskii) have been fitted to experimental data. All of these models save Toepler are based on theoretical derivations and offer a value for a given parameter that we have compared with our fits. These models all describe a resistance that decays very quickly before reaching a constant value. The Rompe-Weizel model shows the best agreement with our experimental data, especially during the first 300 ns of the return stroke phase. Moreover, the parameter value given by our fits is in good agreement with its theoretical prediction.

The Rompe-Weizel model assumes that the electron number density increases during the arc phase. We therefore performed time-resolved spectroscopy on the discharge to study the electron number density in the discharge. Using a synthetic Voigt profile, we fitted the H_α line whose broadenings and shifts have been extensively investigated in the literature. We have obtained the temporal evolution of the electron number density in the discharge channel. In a low inductance circuit, the electron number density increases exponentially up to values on the order of $2 \times 10^{18} \text{ cm}^{-3}$ during the power peak of the arc phase; the exponential growth of the electron number density is in accordance with the Rompe-Weizel model assumption that the deposited energy is used to ionize the gas. Once the energy has been deposited, the electron number density decreases in an inverse square law of time. We obtained electron number density profiles across the transverse direction of the discharge that show the same trends (initial exponential increase followed by an inverse square law decrease). We also measured the channel radius through fast imaging of the discharge: the radius is found to increase linearly during the power peak and even after energy deposition has ended (though at a slower rate). Using these observations and the measured electron number densities, we inferred a "spectroscopic"-based resistance for the plasma channel that roughly agrees with our electrical measurements and with the Rompe-Weizel model, further justifying our choice of this model to describe the discharge channel behavior in an electrical circuit. In a high inductance circuit, our spectroscopic measurements show that the electron number density presents oscillations that coincide with the energy deposition in the discharge: in such an oscillating circuit, there are several successive Joule power peaks that heat the discharge. The electron number density increases (up to about $6 \times 10^{17} \text{ cm}^{-3}$) during the first power peak before decreasing. The following power peak then restarts the ionization process, which cause a small increase in the electron number density. Oscillations can also be seen in the discharge radius evolution.

The fast heating of the plasma channel causes the formation of shock waves that generate an impulse. Using a calibrated torque balance, we measured the impulse generated by the pulsed surface discharge. This impulse is proportional to the energy deposited in the discharge in a low inductance circuit. In high inductance circuits however, the impulse is much weaker and corresponds only to the first power peak. To understand this difference in efficiency, we studied the shock waves generated by the pulsed surface discharge with Schlieren imaging. In low inductance circuits, a single cylindrical shock wave is emitted, whereas multiple nested shocks are emitted in high inductance circuits. We recorded the shock trajectory for both configurations and found it to be in a transition between a strong shock (at the beginning) and a weak shock. At later stages, the shock wave travels with the same velocity no matter the energy deposited in the discharge. Adding more energy only changes the initial stage of the discharge, when its propagation can be explained by the Taylor-Sedov model.

To describe the transition between the two regimes, we used a snowplow model that gives the shock trajectory as a function of time, the gas conditions and the initial energy deposited in the discharge. Our model accurately predicts the shock trajectory for low inductance circuits when we consider that 30% of the energy deposited in the discharge is used to create the shock wave. This result agrees with other experiments on various discharge configurations.

To compute the impulse generated by the discharge, we assumed a Friedlander-like profile for the pressure behind the shock wave and derived an analytic formula that gives the impulse of the discharge as a function of the energy deposited in the discharge and the gas physical conditions. The values predicted with this formula are within 2% of our measured values for a low inductance circuit. For a high inductance circuit however, the computed impulse (created by the first power peak) is larger than our experimental measurements.

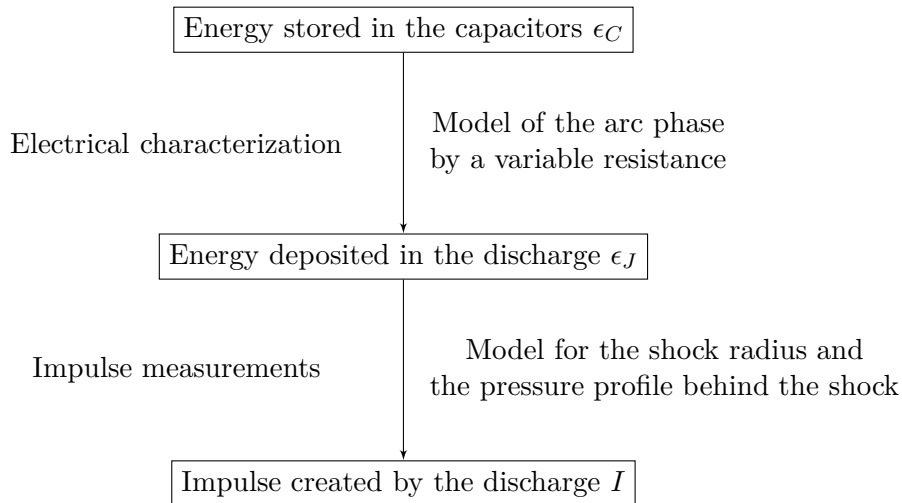


Figure 7.1.1: Engineering approach for a plasma actuator.

We now have a set of models to describe the energy deposition in the pulsed surface discharge and to compute the impulse created by the surface discharge for a given amount of energy. The impulse increases linearly with the input energy, and we have determined experimentally and theoretically the mechanical efficiency of the pulsed surface discharge which is 0.12 mNs/J in our configuration. We can now compare the pulsed surface discharge with other plasma actuators.

7.2 Comparison with other plasma actuators

Since our surface discharge is a pulsed system, we first compare it with another pulsed actuator, the spark jet. Whereas the spark jet generates an impulse

proportional to the square root of the deposited energy (Anderson and Knight (2012b); Anderson and Knight (2012a)), the pulsed surface discharge generates an impulse that is directly proportional to the deposited energy. The spark jet actuation frequency is limited to a few kHz by the recovery cycle of the cavity. Because there is no cavity in the pulsed surface discharge hence no cavity recovery cycle limit, the circuit design and the power supply can be adjusted to reach higher actuation frequency. However, the nested shocks observed in the high inductance circuit limit the efficiency of the pulsed surface discharge. This is most likely due to the hot gas channel that remains above the dielectric after the initial energy deposition. In quiescent air, this limits the actuation frequency to a few hundred Hz. However, if the pulsed surface discharge is placed in a transonic or supersonic flow (about 300 m/s), the hot gas channel is quickly swept away after energy deposition, and the pulsed surface discharge may be used up to frequencies on the order of 100 kHz. This could be a significant advantage for pulsed surface discharges.

When the pulsed surface discharge operates in a repetitive mode, it creates an impulse I at frequency f . The average force $F = fI$ can be compared to the thrust created by dielectric barrier discharge actuators. First, it should be noted that most DBD actuators generate tangential force, whereas the pulsed surface discharge force is normal to the dielectric. We measured the mechanical efficiency of the pulsed surface discharge, which is equal to 0.12 mN/W. For the DBD actuator, the mechanical efficiency can vary depending on the electrodes geometry and duty cycle: values ranging from 0.1 to 0.6 mN/W have been reported in the literature (Durscher and Roy (2010); Benard and Moreau (2014)). On average, the pulsed surface discharge needs more power than DBD actuator to generate an equivalent force. However, since the pulsed surface discharge is not limited by thrust saturation or arc transition like a DBD, greater forces can be obtained with a pulsed surface discharge actuator than with a DBD. However, high frequency burst modes with high energy may damage the dielectric layer. Further study is needed to determine a suitable dielectric able to withstand the heat load in burst mode.

The main comparison points between the three actuator candidates presented above are summarized in table 7.1

7.3 Direction for further studies

For further studies, we strongly advocate for the use of solid state switches to operate the pulsed surface discharge in order to avoid the jitter inherent to a spark gap (which has to be corrected manually and slows down the data acquisition in time-resolved diagnostics). In addition, solid state switches are more compact and reliable than spark gaps and can be used at higher frequencies for burst operation of the pulsed surface discharge.

Table 7.1: Comparison of three plasma actuator candidates: the dielectric barrier discharge (DBD), the sparkjet and the pulsed surface discharge (PSD).

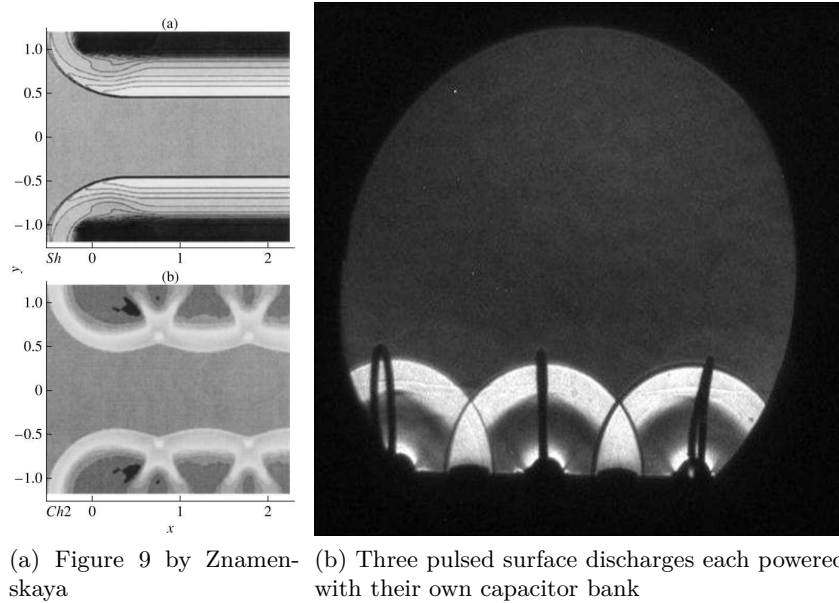
Actuator	DBD	sparkjet	PSD
Mode of operation	continuous	burst	burst
Force dependence on power and frequency	$F \propto P$	$F \propto \sqrt{fP}$	$F \propto P$
Maximum actuation frequency	10 kHz	2 – 5 kHz	Tested at 300 Hz, potential for higher frequency 100 kHz?
Physical limitations	thrust saturation at high voltage, risk of arc transition	electrodes erosion	dielectric layer erosion
Mechanical efficiency (mN/W)	0.10-0.60 (Durscher and Roy (2010); Benard and Moreau (2014))	0.16 (Anderson and Knight (2012b))	0.12 [this work]

In our experiments, we did not investigate the role of the dielectric material, which may be very important in the propagation phase (due to Toepler’s law dependence on the dielectric properties). Moreover, we did not model in depth the propagation phase: it is simply taken into account as an initial condition for our model. The dielectric material on which the pulsed surface discharge occurs is also subjected to some severe stress by the arc phase of the pulsed surface discharge: in our experiments, we have frequently had to change the dielectric, after a few hundreds pulses. This is a serious limitation that has to be overcome before the pulsed surface discharge can be used as a plasma actuator aboard a flying body. Various ceramic materials could be investigated such as alumina or mica.

In the oscillating circuit configurations used in this study, the RLC oscillation period is about ten times longer than the duration of the resistance transient: it would be interesting to study the case of fast-oscillating circuits with RLC oscillations shorter than the transient duration, to see how this would influence the resistance evolution. Moreover, it would be interesting to use a pulsed power supply to study the mechanical effects of the pulsed surface discharge in bursts. Znamenskaya et al. (2007) has studied the shock wave system created

by multiple pulsed surface discharges powered by a single energy supply. If energy is distributed evenly over all the discharge channels (upper left panel), the cylindrical shocks merge to form a plane shock. If all the channels are powered by a single capacitor bank however, there may be some inhomogeneities in the energy deposition (lower left level), which will cause some shocks to be more intense. The merged front will not be as plane, as can be seen in figure 7.3.1.

This issue may be overcome with our setup for the pulsed surface discharge if each channel has its own energy supply.



(a) Figure 9 by Znamenskaya (2007) (b) Three pulsed surface discharges each powered with their own capacitor bank

Figure 7.3.1: Shock front wave generated by multiple surface discharge. The left panel presents computation by Znamenskaya et al. (2007) of the shock front created by multiple pulsed surface discharges sharing a single common energy supply. Our Schlieren images (on the right) were obtained with three separate pulsed surface discharges each with their own capacitor bank and triggered simultaneously.

All the experiments on the surface discharge were performed at sea level in quiescent air. Additional tests should be done in more realistic flight conditions, to study the pulsed surface discharge dependence on the gas conditions such as pressure and temperature and to see how the shock waves generated by the discharge interact with an external flow. In particular, the analytic model we have developed for impulse computation indicates that the pulsed surface discharge mechanical efficiency does not depend on the altitude, contrary to the sparkjet whose efficiency decreases with altitude.

Furthermore, recent work by Leonov et al. (2014) points to some interesting coupling between the boundary layer and the stochastic perturbations caused by the rapid heating in nsDBD actuators near the electrodes. In the case of the pulsed surface discharge, we have observed an homogeneous energy deposition along the whole discharge length and not only at the electrodes. A hot gas channel remains visible for a long time after the discharge initiation in the oscillating circuit configuration, whereas turbulence is seen in the dampened circuit configuration. Coupling may then appear between these stochastic

perturbations and the boundary layer when the actuator is placed in a flow, which may result in performance enhancement for the pulsed surface discharge actuator.

Appendix A

Propagation of uncertainty

A.1 Principle

In the various measurements we performed, we have to take into account the uncertainties of our experiments. They can be:

- statistical uncertainties, due to the shot-to-shot variability of the experiments; these are purely random and can be reduced by increasing the size of our measurement sample;
- systematic uncertainties, due to the experiment configuration; these are biases that can affect the measurement accuracy, no matter the size of our measurement sample.

It is necessary to account for these uncertainties. To do so, we use the propagation of error: let f be a function describing a physical phenomenon of interest. f is computed with a set of parameters $\mathbf{p} = (p_i)$ and a set of measurements $\mathbf{m} = (m_i)$:

$$f = f(\mathbf{p}, \mathbf{m}).$$

The errors are computed using a variance formula for f (Ku (1966)), where the different variables are supposed to be independent (the correlation terms thus vanish). One can separate the statistical and systematic uncertainties:

$$\sigma_{f,\text{stat}}^2 = \sum_i \left(\frac{\partial f}{\partial m_i} \right)^2 (\sigma_{m_i})^2, \quad (\text{A.1.1a})$$

$$\sigma_{f,\text{sys}}^2 = \sum_i \left(\frac{\partial f}{\partial p_i} \right)^2 (\sigma_{p_i})^2, \quad (\text{A.1.1b})$$

where (σ_{m_i}) are the statistical uncertainties on the measurements and (σ_{p_i}) are the systematic uncertainties on the parameters. In our analysis, we will use a global error σ that encompasses both statistical and systematic errors:

$$\sigma_f = \sqrt{\sigma_{f,\text{stat}}^2 + \sigma_{f,\text{sys}}^2} \quad (\text{A.1.2})$$

A.2 Examples of computation

A.2.1 Torque balance calibration

In the case of the torque balance described in chapter 3, the calibration constant K (see section 3.5.2) is obtained through linear regression without intercept using the formula:

$$K = \frac{\sum_i U_i L_i}{\sum_j L_j^2},$$

where U_i is the mean voltage averaged over 15 measurements for an input momentum L_i . Applying equations (A.1.1), we obtain the total uncertainty:

$$\sigma_K = \sqrt{\sum_i \left(\frac{L_i}{\sum_j L_j^2} \right)^2 \sigma_{U_i}^2 + \left(\frac{1}{\sum_j L_j^2} \right)^2 \sum_i \left(U_i - \frac{2L_i \left(\sum_j L_j^2 \right)}{\sum_j L_j^2} \right)^2 \sigma_{L_i}^2}.$$

Here, (σ_{U_i}) is the statistical uncertainty on the measurement U_i , taken equal to the standard deviation of the measurement sample for U_i . (σ_{L_i}) is the systematic uncertainty associated with the input momentum L_i .

A.2.2 Spectroscopic measurements

In our spectroscopic analysis (see section 5.2), we reconstruct the plasma properties such as electron number density, pressure and temperature out of spectra measurements. To compute the corresponding errorbars, we apply the variance formula to the expression of the electron number density (expressed as a function of the Stark broadening):

$$\sigma_{n_e} = 1.973 \times 10^{17} \Delta \lambda_S^{\frac{1}{2}} \sigma_S, \quad (\text{A.2.1})$$

and to the van der Waals broadening:

$$\sigma_{vdW}^2 = \left(5.925 \times 10^{-2} K_1 \sum_j K_j \right)^2 \left(\frac{\sigma_P^2}{T^{1.4}} + 0.49 \frac{P^2 \sigma_T^2}{T^{3.4}} \right). \quad (\text{A.2.2})$$

A third equation is needed to relate, temperature T , pressure P and electron number density n_e . We assume local thermal equilibrium and use the ideal gas law:

$$P = n k_B T = \frac{n_e}{x_e} k_B T.$$

Applying the variance formula gives:

$$\sigma_P^2 = \left(\frac{k}{x_e}\right)^2 (n_e^2 \sigma_T^2 + T^2 \sigma_e^2). \quad (\text{A.2.3})$$

Here we have assumed that the mole fraction of electron is known perfectly. Solving this set of equations requires to know the Stark broadening σ_S uncertainty and the van der Waals broadening uncertainty σ_{vdW} . These two quantities are coupled in a set of equations obtained through the variance formula:

$$\begin{aligned} 4\sigma_\gamma^2 &= \sigma_{vdW}^2 + \sigma_S^2, \\ \sigma_s^2 &= \frac{\sigma_{vdW}^2}{9} + 0.070\Delta\lambda_S\sigma_S^2, \end{aligned}$$

with σ_s^2 and σ_γ^2 the uncertainties on the shift and Lorentz broadening. To solve this system, we only add the uncertainties, as they cannot compensate, which brings:

$$\sigma_S^2 = \frac{\sigma_s^2 + \frac{4}{9}\sigma_\gamma^2}{7.056 \times 10^{-3}\Delta\lambda_S + \frac{1}{9}}, \quad (\text{A.2.4a})$$

$$\sigma_{vdW}^2 = \frac{\sigma_s^2 + 2.822 \times 10^{-2}\Delta\lambda_S\sigma_\gamma^2}{7.056 \times 10^{-3}\Delta\lambda_S + \frac{1}{9}}. \quad (\text{A.2.4b})$$

This leads eventually to the temperature and pressure uncertainties:

$$\sigma_P^2 = \frac{T^{1.4}}{1.49} \left(\frac{\sigma_{vdW}^2}{\left(5.925 \times 10^{-2} K_1 \sum_j K_j\right)^2} + 0.49 \frac{P^2 \sigma_e^2}{n_e^2 T^{1.4}} \right), \quad (\text{A.2.5a})$$

$$\sigma_T^2 = \frac{T^{3.4}}{1.49P^2} \left(\frac{\sigma_{vdW}^2}{\left(5.925 \times 10^{-2} K_1 \sum_j K_j\right)^2} + \frac{P^2 \sigma_e^2}{n_e^2 T^{1.4}} \right). \quad (\text{A.2.5b})$$

Appendix B

The RLC circuit: general solutions

B.1 Governing equations for the RLC circuit

Let us consider a RLC circuit during the discharge phase:

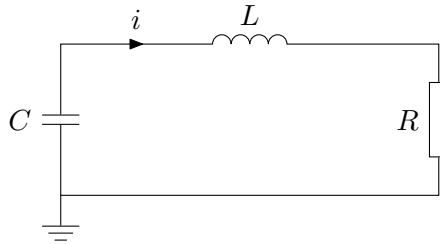


Figure B.1.1: Standard RLC circuit.

We find very easily the governing equation for the current $i(t)$:

$$\partial_{tt}i + \frac{R}{L}\partial_t i + \frac{i}{LC} = 0,$$

that can be written:

$$\left(\partial_{tt} + 2\alpha\partial_t + \omega_0^2\right) i = 0, \quad (\text{B.1.1})$$

with the parameters:

$$\alpha = \frac{R}{2L},$$
$$\omega_0^2 = \frac{1}{LC}.$$

Changing anyone of the three circuit characteristics (R, L, C) can flip the circuit from an over-damped condition (the double-exponential where $\alpha^2 > \omega_0^2$) to an under-damped condition (the damped oscillator where $\alpha^2 < \omega_0^2$).

B.2 Over-damped circuit

For an over-damped circuit where:

$$\alpha^2 > \omega_0^2, \quad (\text{B.2.1})$$

the generic solution for the current is:

$$\begin{aligned} i(t) &= \left(I_1 e^{-\sqrt{\alpha^2 - \omega_0^2} t} + I_2 e^{\sqrt{\alpha^2 - \omega_0^2} t} \right) e^{-\alpha t}, \\ i(t) &= \left(I'_1 \cosh \left(\sqrt{\alpha^2 - \omega_0^2} t \right) + I'_2 \sinh \left(\sqrt{\alpha^2 - \omega_0^2} t \right) \right) e^{-\alpha t}. \end{aligned}$$

Considering the discharge phase of the circuit, with the capacitors initially charged at U_0 , the boundary conditions at $t = 0$ for the current $i(t)$ are:

$$\begin{aligned} i(t = 0) &= 0 = I'_1, \\ \partial_t i(t = 0) &= \frac{U_0}{L} = I'_2 \sqrt{\alpha^2 - \omega_0^2} - \alpha I'_1, \end{aligned}$$

hence the solution :

$$i(t) = \frac{U_0}{L \sqrt{\alpha^2 - \omega_0^2}} \sinh \left(\sqrt{\alpha^2 - \omega_0^2} t \right) e^{-\alpha t}. \quad (\text{B.2.2})$$

The current exhibits a double exponential behavior, and reaches its maximum i_M at instant t_M such that:

$$\partial_t i(t_M) = 0 = \frac{U_0 e^{-\alpha t_M}}{L \sqrt{\alpha^2 - \omega_0^2}} \left(-\alpha \sinh \left(\sqrt{\alpha^2 - \omega_0^2} t_M \right) + \sqrt{\alpha^2 - \omega_0^2} \cosh \left(\sqrt{\alpha^2 - \omega_0^2} t_M \right) \right),$$

that is:

$$t_M = \frac{1}{\sqrt{\alpha^2 - \omega_0^2}} \operatorname{arctanh} \left(\frac{\omega_0}{\alpha} \right), \quad (\text{B.2.3})$$

$$i_M = \frac{U_0}{L \sqrt{\alpha^2 - \omega_0^2}} \sinh \left(\operatorname{arctanh} \left(\frac{\omega_0}{\alpha} \right) \right) e^{-\frac{\alpha}{\sqrt{\alpha^2 - \omega_0^2}} \operatorname{arctanh} \left(\frac{\omega_0}{\alpha} \right)}. \quad (\text{B.2.4})$$

B.3 Under-damped circuit

For an under-damped circuit where:

$$\alpha^2 < \omega_0^2, \quad (\text{B.3.1})$$

the generic solution for the current is:

$$\begin{aligned} i(t) &= \left(I_1 e^{-\sqrt{\omega_0^2 - \alpha^2} t} + I_2 e^{\sqrt{\omega_0^2 - \alpha^2} t} \right) e^{-\alpha t}, \\ i(t) &= \left(I'_1 \cos \left(\sqrt{\omega_0^2 - \alpha^2} t \right) + I'_2 \sin \left(\sqrt{\omega_0^2 - \alpha^2} t \right) \right) e^{-\alpha t}. \end{aligned}$$

Considering the discharge phase of the circuit, with the capacitors initially charged at U_0 , the boundary conditions at $t = 0$ for the current $i(t)$ are:

$$\begin{aligned} i(t=0) &= 0 = I'_1, \\ \partial_t i(t=0) &= \frac{U_0}{L} = I'_2 \sqrt{\omega_0^2 - \alpha^2} - \alpha I'_1, \end{aligned}$$

hence the solution:

$$i(t) = \frac{U_0}{L\sqrt{\omega_0^2 - \alpha^2}} \sin\left(\sqrt{\omega_0^2 - \alpha^2}t\right) e^{-\alpha t} \quad (\text{B.3.2})$$

The current exhibits a damped harmonic oscillator behavior, and reaches its maximum i_M at instant t_M such that:

$$\partial_t i(t_M) = 0 = \frac{U_0 e^{-\alpha t_M}}{L\sqrt{\omega_0^2 - \alpha^2}} \left(-\alpha \sin\left(\sqrt{\omega_0^2 - \alpha^2}t_M\right) + \sqrt{\omega_0^2 - \alpha^2} \cos\left(\sqrt{\omega_0^2 - \alpha^2}t_M\right) \right),$$

that is:

$$t_M = \frac{1}{\sqrt{\omega_0^2 - \alpha^2}} \arctan\left(\frac{\omega_0}{\alpha}\right), \quad (\text{B.3.3})$$

$$i_M = \frac{U_0}{L\sqrt{\omega_0^2 - \alpha^2}} \sin\left(\arctan\left(\frac{\omega_0}{\alpha}\right)\right) e^{-\frac{\alpha}{\sqrt{\omega_0^2 - \alpha^2}} \arctan\left(\frac{\omega_0}{\alpha}\right)}. \quad (\text{B.3.4})$$

For such an oscillating circuit, the current goes through 0 at instant $t_{i=0}$ whenever the sin term in equation (B.3.2) is zero, that is for:

$$t_{i=0} \equiv 0 \pmod{\frac{\pi}{\sqrt{\omega_0^2 - \alpha^2}}} \quad (\text{B.3.5})$$

Each power peak in an oscillating circuit thus lasts a duration of $\frac{\pi}{\sqrt{\omega_0^2 - \alpha^2}}$. It is also possible to derive how much energy is contained in the k^{th} peak:

$$\frac{E_{J,k}}{E_J} = \frac{\int_{t_{k-1}}^{t_k} Ri^2 dt}{\int_0^{+\infty} Ri^2 dt} = \left(1 - e^{-\frac{2\pi\alpha}{\sqrt{\omega_0^2 - \alpha^2}}}\right) e^{-\frac{2\pi\alpha(k-1)}{\sqrt{\omega_0^2 - \alpha^2}}}. \quad (\text{B.3.6})$$

B.4 Complete circuit

The complete circuit of the discharge setup includes a ballast resistance and R_b and a sparkgap that is modeled by a constant resistance R_{sg} , as depicted in figure B.4.1.

If the plasma channel resistance R_p can be taken as constant, the current i_p flowing through the discharge is governed by the following equation :

$$\partial_{tt} i_p + \left(\frac{R_p}{L} + \frac{R_{sg} R_b}{(R_{sg} + R_b)L} + \frac{1}{(R_{sg} + R_b)C} \right) \partial_t i_p + \frac{R_p + R_b}{R_{sg} + R_b} \frac{1}{LC} i_p = 0, \quad (\text{B.4.1})$$

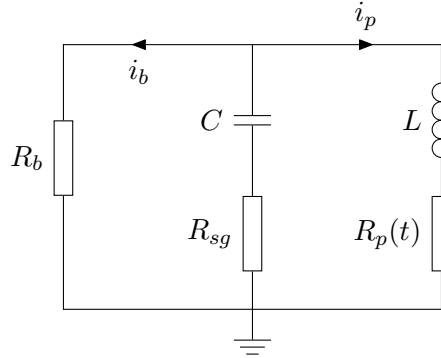


Figure B.4.1: Equivalent circuit during the return stroke phase of the pulsed surface discharge. The resistance R_{sg} takes into account the wires and spark-gap, the plasma channel is described by the resistance R_p .

which corresponds to equation (B.1.1) with the parameters:

$$\alpha = \frac{R_p}{2L} + \frac{R_{sg}R_b}{2(R_{sg} + R_b)L} + \frac{1}{2(R_{sg} + R_b)C},$$

$$\omega_0^2 = \frac{R_p + R_b}{R_{sg} + R_b} \frac{1}{LC}.$$

These parameters can be simplified when we neglect the resistance R_{sg} and assume a very high ballast resistance R_b (open circuit):

$$\left| \begin{array}{l} R_{sg} \rightarrow 0 \\ R_b \rightarrow \infty \end{array} \right| \implies \left| \begin{array}{l} \alpha = \frac{R_p}{2L} \\ \omega_0^2 = \frac{1}{LC} \end{array} \right| \quad (\text{B.4.2})$$

Appendix C

Detailed calculations for the H_α multiplet

C.1 Average spectroscopic quantities

The H_α line studied in chapter 5 is in fact a multiplet of 7 lines, due to fine structure effects on the upper and lower levels. To compute the various broadenings of the multiplet, we have to average the spectroscopic quantities of the different allowed transitions. To do so, we use the procedure described by [Wiese and Fuhr \(2009\)](#).

The total intensity of the multiplet $\overline{S_{ik}}$ is equal to the sum of intensity from all components $S_{ik,j}$:

$$\overline{S_{ik}} = \sum_j S_{ik,j}. \quad (\text{C.1.1})$$

The average wavelength for the multiplet can be obtained from the various components energy levels,

$$\overline{\lambda_{ik,\text{vac}}} = \frac{hc}{\overline{\Delta E_{ik}}}, \quad (\text{C.1.2})$$

$$\overline{\Delta E_{ik}} = \frac{\sum_j g_{k,j} E_{k,j}}{\sum_j g_{k,j}} - \frac{\sum_l g_{i,l} E_{i,l}}{\sum_l g_{i,l}}, \quad (\text{C.1.3})$$

where $g_{k,j}$ is the degeneracy of the j^{th} orbital term of level k . This computation gives the multiplet wavelength in vacuum $\overline{\lambda_{ik,\text{vac}}}$. Since our measurements are performed in air, we need to divide this wavelength by the corresponding

refractive index of air as given by [Ciddor \(1996\)](#):

$$\overline{\lambda_{ik}} = \frac{\overline{\lambda_{ik,\text{vac}}}}{n_{\text{air}}(\overline{\lambda_{ik,\text{vac}}})}, \quad (\text{C.1.4})$$

$$n_{\text{air}}(\lambda) = 1 + \frac{0.05792105}{238.0185 - \lambda^{-2}} + \frac{0.00167917}{57.362 - \lambda^{-2}}. \quad (\text{C.1.5})$$

The average Einstein coefficient $\overline{A_{ki}}$ and absorption oscillator strength $\overline{f_{ik}}$ are computed from the component lines:

$$\overline{A_{ki}} = \frac{\sum_j g_{k,j} \lambda_{ik,j}^3 A_{ki,j}}{2n_k^2 \overline{\lambda_{ik}}^3} \approx \frac{\sum_j g_{k,j} A_{ki,j}}{2k^2}, \quad (\text{C.1.6})$$

$$\overline{f_{ik}} = \frac{\sum_j g_{i,j} \lambda_{ik,j} f_{ik,j}}{2n_i^2 \overline{\lambda_{ik}}} \approx \frac{\sum_j g_{i,j} f_{ik,j}}{2i^2}, \quad (\text{C.1.7})$$

with $g_{k,j}$ ($g_{i,j}$) the degeneracy of the j^{th} orbital term of level k (i) and $\lambda_{ik,j}$ the wavelength of the j^{th} component of the multiplet¹. In the case of hydrogen, the various wavelengths $\lambda_{ik,j}$ are very close to the average wavelength $\overline{\lambda_{ik}}$, so the wavelength terms can be simplified in the previous equations.

The various components of the H_α multiplet and its average values are given in table [C.1](#)

Table C.1: Components of the Balmer α ($3 \rightarrow 2$) transition multiplet and their spectroscopic properties.

Wavelength in air (nm)	A_{32} (s^{-1})	f_{23}	S_{23} (a. u.)	E_3 (cm^{-1})	E_2 (cm^{-1})	g_3	g_2	R^2
656.271	5.3877×10^7	0.69614	3.0089×10^1	97492.319	82258.919	4	2	96.00
656.272	2.2448×10^7	0.29005	1.2537×10^1	97492.320	82258.954	4	2	138.00
656.275	2.1046×10^6	0.013597	5.8769×10^{-1}	97492.222	82258.919	2	2	177.00
656.277	2.2449×10^7	0.14503	6.2688	97492.211	82258.9544	2	2	138.00
656.285	6.4651×10^7	0.62654	5.4162×10^1	97492.356	82259.285	6	4	96.00
656.287	1.0775×10^7	0.069616	6.0181	97492.320	82259.285	4	4	150.00
656.291	4.2097×10^6	0.013599	1.1756	97492.222	82259.285	4	2	150
656.280	4.4102×10^7	0.64108	1.1084×10^2	97492.309	82259.111	18	8	107.06

¹In the formulae given by [Wiese and Fuhr \(2009\)](#), the denominator is given as k^2 instead of $2k^2$, thus forgetting the spin degeneracy of the energy level. This contradicts the rest of the formalism presented in their paper and gives values that deviate from the accepted standards for averaged spectral quantities as per [Kramida et al. \(2014\)](#).

C.2 Computation of the resonant broadening

As described in section 5.2.2.3, resonant broadening is caused by collisions between radiation emitters and similar particles in the ground state connected via an allowed transition to the upper or lower level of the main transition:

$$\Delta\lambda_R = 8.60 \times 10^{-27} \lambda^2 \lambda_R f_R \sqrt{\frac{g_1}{g_R}}, \quad (\text{C.2.1})$$

with $\Delta\lambda_R$ in nm, λ the wavelength of the transition under scrutiny in nm, λ_R the resonance wavelength in nm, f_R the resonance oscillator strength, g_1 the degeneracy of the ground level of the resonance transition and g_R the degeneracy of the resonant level. For hydrogen, all the multiplet components will have a resonance broadening, as can be seen from the energy diagram C.2.1.

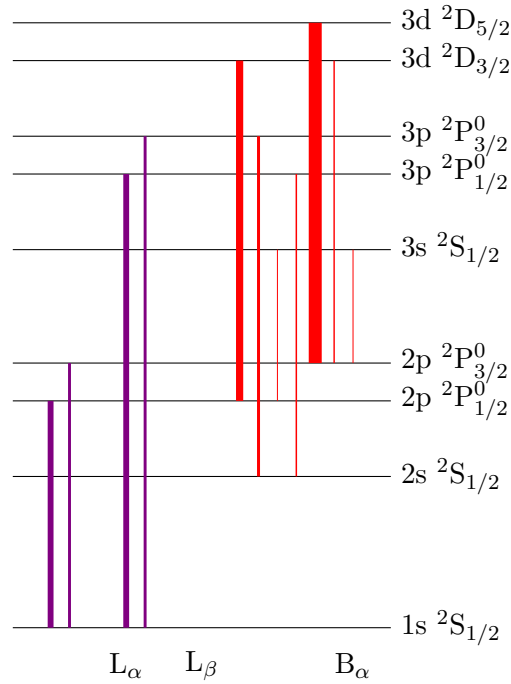


Figure C.2.1: Multiplet structure of L α , L β and B α . The line thickness is proportionnal to the relative strength of the component in a given multiplet. Red lines correspond to the main wavelength λ in equation (C.2.1) and violet lines are the resonant wavelength λ_R

We compute all these contributions and take an average value (following Laux

et al. (2003)) equal to:

$$\overline{\Delta\lambda_R} = \frac{\sum_j S_j \Delta\lambda_{R,j}}{\sum_j S_j}. \quad (\text{C.2.2})$$

We then express the hydrogen number density as a function of pressure P , temperature T and hydrogen mole fraction x_H , which gives eventually:

$$\Delta\lambda_R = 4.30 \times 10^{-2} x_H \frac{P}{T}. \quad (\text{C.2.3})$$

C.3 Computation of the van der Waals broadening

As described in sections 5.2.2.5 and 5.3.2, van der Waals broadening can be written as:

$$\Delta\lambda_{vdW} = 5.925 \times 10^{-2} K_1 \sum_n K_n \frac{P}{T^{0.7}}, \quad (\text{C.3.1})$$

with $\Delta\lambda_{vdW}$ in nm, P in Pa and T in K. K_n are the contributions of the different neutral species in the medium. K_1 is a coefficient that depends on the transition under consideration:

$$K_1 = \lambda^2 \langle R^2 \rangle^{0.4}, \quad (\text{C.3.2})$$

$$\langle R^2 \rangle = R_u^2 - R_l^2. \quad (\text{C.3.3})$$

with λ the transition wavelength (in nm) and $\langle R^2 \rangle$ the difference between the square radii of the emitting atom (hydrogen in our case) in the upper and lower level. R_k^2 is given for level k in the Coulomb approximation by:

$$R_k^2 = \frac{n_k^{*2}}{2} \left(5n_k^{*2} + 1 - 3l_k(l_k + 1) \right). \quad (\text{C.3.4})$$

l_k is the orbital quantum number and n_k^* an effective quantum number defined in the case of the H_α line by:

$$n_k^{*2} = \frac{E_H}{E_H - E_k} \quad (\text{C.3.5})$$

with $E_H = 109678.77174307 \text{ cm}^{-1}$ and E_k the energy of level k . We compute the $\langle R^2 \rangle$ for the different terms of the H_α multiplet and take an average value (following Laux et al. (2003)) equal to:

$$\overline{\langle R^2 \rangle^{0.4}} = \frac{\sum_j S_{ik,j} \langle R_j^2 \rangle^{0.4}}{\sum_j S_{ik,j}}. \quad (\text{C.3.6})$$

The numerical values are reported in table C.1. We then compute the average value $\overline{K_1}$ using the same averaging procedure:

$$\overline{K_1} = \frac{\sum_j S_{ik,j} \lambda_{ik,j}^2 \langle R_j^2 \rangle^{0.4}}{\sum_j S_{ik,j}} \approx \overline{\lambda_{ik}}^2 \overline{\langle R^2 \rangle^{0.4}}, \quad (\text{C.3.7})$$

where we have once again considered the small wavelength differences of the various terms of the multiplet to be negligible so as to replace the terms wavelengths by the average multiplet wavelength $\lambda_{ki,j} \approx \overline{\lambda_{ki}}$. We get eventually:

$$\overline{K_1} = 2.78277 \times 10^6 \text{ nm}^2 \quad (\text{C.3.8})$$

Appendix D

Self-similar theory for strong shocks and its extensions to low Mach numbers

D.1 Taylor-Sedov theory for strong shocks

Sir Geoffrey Taylor was the first to study strong shocks for the Manhattan project. The similarity formalism he developed (Taylor (1950a)) was found to be in excellent agreement with experimental measurements performed on the first nuclear test (Trinity test in Alamogordo) on July 16, 1945 (Taylor (1950b)). Leonid Sedov developed a similar model on the other side of the Iron Curtain (Sedov (1946)). Hereafter, we recall this similarity formalism for a strong cylindrical shock as described by Shao-Chin Lin (Lin (1954)).

We assume that an amount of energy per unit length ϵ is released instantaneously at $t = 0$, which causes the formation of a shock wave of radius $R(t)$. Conservation equations behind the shock are:

$$\partial_t \rho + u \partial_r \rho + \rho \partial_r u + \frac{\rho u}{r} = 0, \quad (\text{D.1.1})$$

$$\partial_t u + u \partial_r u + \frac{\partial_r p}{\rho} = 0, \quad (\text{D.1.2})$$

$$\partial_t e + u \partial_r e - \frac{p}{\rho^2} (\partial_t \rho + u \partial_r \rho) = 0, \quad (\text{D.1.3})$$

with ρ , u , p and e the density, velocity, pressure, and energy per unit mass behind the shock respectively. The equation of state for a perfect gas is:

$$(\partial_t + u \partial_r) (p \rho^{-\gamma}) = 0, \quad (\text{D.1.4})$$

with γ the specific heat ratio. We can then write a conservation equation for the pressure:

$$\partial_t p + u \partial_r p + \gamma p \partial_r u + \gamma \frac{p u}{r} = 0. \quad (\text{D.1.5})$$

Neglecting the pressure P_0 ahead of the shock, the pressure P , density ρ , and flow velocity u behind the shock can be expressed as functions of the shock position $R(t)$, the shock speed \dot{R} and of a dimensionless similarity variable $\xi = \frac{r}{R(t)}$:

$$\rho(r, t) = \rho_0 \psi(\xi), \quad (\text{D.1.6a})$$

$$u(r, t) = \frac{\phi_1(\xi)}{R}, \quad (\text{D.1.6b})$$

$$P(r, t) = \frac{P_0}{R^2} f_1(\xi), \quad (\text{D.1.6c})$$

We write the conservation equations of mass, momentum, and energy behind the shock in terms of the functions $f_1(\xi)$, $\phi_1(\xi)$, $\psi(\xi)$, taking into account the equation of state for a perfect gas. Introducing these dimensionless functions in the previous system, we get:

$$\begin{aligned} (\phi_1 + \xi \phi_1') \frac{\dot{R}}{R^2} - \frac{\phi_1 \phi_1'}{R^3} &= \frac{P_0}{\rho_0} \frac{f_1'}{\psi R^3}, \\ \xi \phi_1' \frac{\dot{R}}{R} - \frac{\phi_1 \psi'}{R^2} - \left(\phi_1' + \frac{\phi_1}{\xi} \right) \frac{\psi}{R^2} &= 0, \\ \left(\gamma \xi f_1 \frac{\psi'}{\psi} - \xi f_1' - 2f_1 \right) \frac{\dot{R}}{R^3} + \frac{\phi_1 f_1'}{R^4} - \frac{\gamma f_1 \phi_1 \psi'}{\psi R^4} &= 0, \end{aligned}$$

where $\dot{X} = \frac{dX}{dt}$ and $X' = \frac{dX}{d\xi}$. By separation of variables, we can rearrange these equations so as to have $R\dot{R}$ (a pure function of time) equal to pure functions of the dimensionless variable ξ . This is possible if and only if all those functions are equal to a common constant A , which gives us the shock radius as a function of time:

$$R\dot{R} = A \implies R(t) = \sqrt{2At}, \quad (\text{D.1.7})$$

with the initial condition $R(t=0) = 0$. We redefine the dimensionless functions for velocity and pressure in order to take this constant A into account:

$$\begin{aligned} u(r, t) &= \frac{\phi_1(\xi)}{R} = \dot{R} \phi(\xi), \\ P(r, t) &= \frac{P_0}{R^2} f_1(\xi) = P_0 \dot{R}^2 f(\xi). \end{aligned}$$

The new dimensionless functions (ψ , ϕ , f) are then obtained as solutions of a system of three coupled ordinary differential equations:

$$f' = \frac{2\xi(\xi - \phi) + \gamma\phi^2 \psi f}{f - \psi(\xi - \phi)^2} \frac{\psi f}{\xi}, \quad (\text{D.1.8a})$$

$$\phi' = \frac{\gamma\phi(\xi\psi(\phi - \xi) + f) - 2f}{\xi\gamma(\psi(\xi - \phi)^2 - f)}, \quad (\text{D.1.8b})$$

$$\psi' = \frac{\psi(\phi^3\psi\gamma - \xi(\phi^2\psi\gamma + 2f))}{\xi\gamma(\xi - \phi)(\psi(\xi - \phi)^2 - f)}, \quad (\text{D.1.8c})$$

The system is solved numerically for $\xi \in [0, 1]$ with boundary conditions given by the Rankine-Hugoniot relations for a strong shock which lead to:

$$f(1) = \frac{2\gamma}{\gamma + 1}, \quad (\text{D.1.9a})$$

$$\phi(1) = \frac{2}{\gamma + 1}, \quad (\text{D.1.9b})$$

$$\psi(1) = \frac{\gamma + 1}{\gamma - 1}. \quad (\text{D.1.9c})$$

The resulting profiles are depicted in figure D.1.1 for a perfect diatomic gas (with $\gamma = 1.4$). The constant A appearing in the shock radius formula is

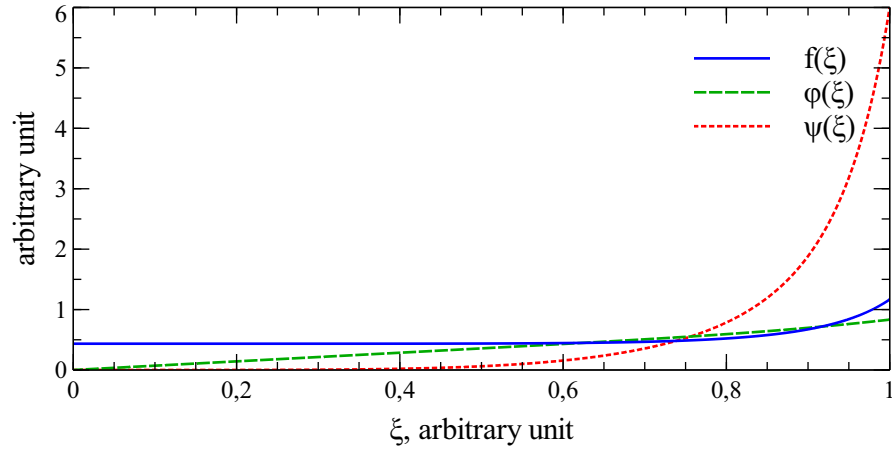


Figure D.1.1: Dimensionless functions for pressure (f), density (ϕ) and flow velocity (ψ) behind the shock as functions of the nondimensional similarity variable $\xi = \frac{r}{R(t)}$.

determined through conservation of energy behind the shock:

$$\epsilon = 2\pi \int_0^R \left(\frac{p}{\gamma + 1} + \frac{\rho u^2}{2} \right) r dr = 2\pi \rho_0 A^2 \int_0^1 \left(\frac{f}{\gamma(\gamma + 1)} + \frac{\psi \phi^2}{2} \right) \xi d\xi. \quad (\text{D.1.10})$$

We then obtain the standard formula for a strong cylindrical shock:

$$R^{\text{TS}} = 1.004 \left(\frac{\epsilon_S}{\rho_0} \right)^{\frac{1}{4}} t^{\frac{1}{2}}, \quad (\text{D.1.11})$$

where ρ_0 is the density ahead of the shock, and ϵ_S is the energy per unit meter released at time $t = 0$ that causes the shock wave formation. Though the solutions presented here are purely numerical, analytic formalisms were found independently for spherical strong shocks by John von Neumann (Bethe et al. (1947)) and J. L. Taylor (Taylor (1955)) and for cylindrical strong shocks by Chakraborti (Chakraborti (1962)).

D.2 Extension to weaker shocks

When dealing with a weak shock, one must take into account the counter-pressure ahead of the shock. The self-similar variable ξ is not sufficient to describe the flow, so we have to introduce another variable. A standard choice for such a dimensionless variable is:

$$\eta = \frac{c_0^2}{\dot{R}^2}, \quad (\text{D.2.1})$$

that is the inverse squared Mach number, c_0 being the speed of sound ahead of the shock and \dot{R} the shock celerity. If we express the various fluid quantities as functions of these dimensionless variables:

$$\begin{aligned} \rho(r, t) &= \rho_0 \psi(\xi, \eta), \\ u(r, t) &= \dot{R} \phi(\xi, \eta), \\ p(r, t) &= \rho_0 \dot{R}^2 f(\xi, \eta), \end{aligned}$$

we can rewrite equations (D.1.1), (D.1.2) and (D.1.5):

$$(\phi - \xi) \partial_\xi \psi + \psi \partial_\xi \phi + \frac{\phi \psi}{\xi} = 2\theta \eta \partial_\eta \psi \quad (\text{D.2.2a})$$

$$(\phi - \xi) \partial_\xi \phi + \theta \phi + \frac{\partial_\xi f}{\xi} = 2\theta \eta \partial_\eta \phi \quad (\text{D.2.2b})$$

$$(\phi - \xi) \partial_\xi f + \gamma f \left(\partial_\xi \phi + \frac{\phi}{\xi} \right) + 2\theta f = 2\theta \eta \partial_\eta f, \quad (\text{D.2.2c})$$

with

$$\theta = \frac{R\ddot{R}}{\dot{R}^2}. \quad (\text{D.2.3})$$

The Rankine-Hugoniot relations for a shock give us boundary conditions at the shock front:

$$\psi(1, \eta) = \frac{\gamma + 1}{\gamma - 1 + 2\eta}, \quad (\text{D.2.4a})$$

$$\phi(1, \eta) = \frac{2(1 - \eta)}{\gamma + 1}, \quad (\text{D.2.4b})$$

$$f(1, \eta) = \frac{2\gamma + \eta(1 - \gamma)}{\gamma + 1}. \quad (\text{D.2.4c})$$

D.2.1 Power series expansion

Sakurai (Sakurai (1953); Sakurai (1954)) and Mel'nikova (Kochina and Mel'nikova (1958); Kochina and Mel'nikova (1960)) proposed independently to solve this system using a power series expansion of the dimensionless functions:

$$\Omega^i = \Omega^{i(0)}(\xi) + \eta \Omega^{i(1)}(\xi) + \eta^2 \Omega^{i(2)}(\xi) + \dots, \quad (\text{D.2.5})$$

with $\Omega^1 = \psi$, $\Omega^2 = \phi$, $\Omega^3 = f$. The first order solution $(\psi^{(0)}, \phi^{(0)}, f^{(0)})$ matches the Taylor-Sedov theory for strong shocks. Through iterations, one can then solve for higher orders (see for instance [Freeman \(1968\)](#); [Plooster \(1971b\)](#); [Plooster \(1971a\)](#) or [Swigart \(1960\)](#) for a third order development). However, this perturbation method converges rather slowly, as more and more terms must be computed when the shock gets weaker.

D.2.2 Quasi-similarity solution

[Oshima \(1960\)](#) proposed instead a quasi-similar approach, based on the separation of the two dimensionless variables:

$$\Omega^i(\xi, \eta) = \Omega_1^i(\xi)\Omega_2^i(\eta), \quad (\text{D.2.6})$$

Separating the variables allows us to express the η derivative at any position behind the shock as a function of the boundary condition at the shock:

$$\left. \frac{\partial \Omega^i}{\partial \eta} = \frac{\partial \ln \Omega^i}{\partial \eta} \right|_{\xi=1} \Omega^i. \quad (\text{D.2.7})$$

We can then write the equations for the flow functions:

$$(\phi - \xi) \psi' + \psi \phi' = \left(\Lambda_1 - \frac{\phi}{\xi} \right) \psi, \quad (\text{D.2.8a})$$

$$(\phi - \xi) \phi' + \frac{f'}{\psi} = \Lambda_2 \phi, \quad (\text{D.2.8b})$$

$$(\phi - \xi) f' + \gamma f \phi' = \left(\Lambda_3 - \frac{\gamma \phi}{\xi} \right) f, \quad (\text{D.2.8c})$$

where the (Λ_i) are functions of the shock conditions:

$$\Lambda_1 = -\frac{4\theta\eta}{\gamma - 1 + 2\eta}, \quad (\text{D.2.9a})$$

$$\Lambda_2 = -\theta \left(\frac{2\eta}{1 - \eta} + 1 \right), \quad (\text{D.2.9b})$$

$$\Lambda_3 = -2\theta \left(\frac{(\gamma - 1)\eta}{2\gamma - \eta(\gamma - 1)} + 1 \right). \quad (\text{D.2.9c})$$

The system [\(D.2.8\)](#) can then be solved, provided the shock trajectory is known, in order to compute the (Λ_i) and the θ parameter. This is often done using an iterative scheme:

1. assume a value of θ
2. compute the related η and (Λ_i)
3. solve the system [\(D.2.8\)](#)
4. compute a new value of θ using the energy conservation behind the shock
5. iterate until a convergence criterion is met.

The quasi-similarity formalism can describe the shock trajectory rather accurately but does not conserve mass behind the shock, so the flow structure exhibits discrepancies for weak shocks. We must therefore look for another formalism to describe the transition from a strong shock to a weak shock such as the one observed in our experiments.

Appendix E

Computation of the linear impulse generated by the surface discharge

E.1 Computation method

The downward linear impulse generated by the surface discharge is obtained by a double integration of the overpressure behind the moving shock front:

$$I(t) = 2 \int_0^t \int_0^{R(\tau)} (P_1(r, \tau) - P_0) dr d\tau = 2 \int_0^t \partial_t I dt. \quad (\text{E.1.1})$$

The integrand can be expressed as:

$$\partial_t I = 2P_S(t) \int_0^{R(t)} \left(1 - \frac{R(t) - r}{R_c}\right) e^{-b \frac{R(t) - r}{R_c}} dr, \quad (\text{E.1.2})$$

with the overpressure P_S given by:

$$P_S = P_1 - P_0 = \frac{2\rho_0}{\gamma + 1} (U^2 - c_0^2). \quad (\text{E.1.3})$$

The Lee model gives the shock velocity U :

$$U^2 = \dot{R}^2 = \frac{2\epsilon_S}{\rho_0 \pi R^2} + \frac{G}{F} c_0^2 \quad (\text{E.1.4})$$

so the overpressure can be written as:

$$P_S = \frac{\alpha \epsilon_S}{R^2} + \beta, \quad \alpha = \frac{4}{\pi(\gamma + 1)}, \quad \beta = \frac{2\rho_0 c_0^2}{\gamma - 1} \left(\frac{G}{F} + 1\right) \quad (\text{E.1.5})$$

Using the change of variable:

$$\eta = \frac{R(t) - r}{R_c}, \quad d\eta = -\frac{dR}{R_c},$$

equation (E.1.2) becomes:

$$\partial_t I = 2 \left(\frac{\alpha \epsilon_S}{l^2} + \beta R_c^2 \right) \frac{A(b, l)}{R_c}, \quad A(b, l) = \int_0^l (1 - \eta) e^{-b\eta} d\eta. \quad (\text{E.1.6})$$

Differentiating the shock radius expression (6.2.6) (divided by R_c) with respect to time:

$$R^2 = (at + R_c)^2 - R_c, \quad a = \sqrt{\frac{G}{F}} c \implies l^2 = \left(\frac{a}{R_c} + 1 \right) - 1,$$

$$2l \partial_t l = 2 \frac{a}{R_c} \left(\frac{a}{R_c} t + 1 \right) = 2 \frac{a}{R_c} \sqrt{l^2 + 1}$$

we use the chain rule for derivation and write:

$$\partial_t I = \partial_l I \partial_t l \implies \partial_t I = \partial_t I \partial_t t$$

hence:

$$\partial_l I = 2 \left(\frac{\alpha \epsilon_S}{l^2} + \beta R_c^2 \right) \frac{A(b, l) l}{a \sqrt{l^2 + 1}}. \quad (\text{E.1.7})$$

This expression is then integrated up to a cut-off pseudo-length L (which is in fact a dimensionless value).

E.2 Asymptotic approximation

Though the impulse can be computed by integrating equation (E.1.7) numerically, it may be helpful to have an approximate formula to outline the main dependences of the impulse with the various physical parameters of the system. To do so, we need an approximate formula for the function A that simplifies the integration of equation (E.1.7). A is found to be equal to:

$$A(b, l) = \frac{e^{-bl}(b(l-1) + 1) + b - 1}{b^2},$$

which, for a high enough value of b , can be approximated by the linearised function A_{asympt} :

$$A_{\text{asympt}}(b, l) = \begin{cases} l & \text{when } l < \frac{b-1}{b^2} \\ \frac{b-1}{b^2} & \text{when } l > \frac{b-1}{b^2} \end{cases} \quad (\text{E.2.1})$$

Figure E.2.1 depicts the function $A(b, l)$ and its asymptotic approximation $A_{\text{asympt}}(b, l)$ for various values of the parameter b . The higher this parameter, the closer the asymptotic approximation matches the real function.

Assuming that $L \gg \frac{b-1}{b^2}$, the integral is split between the two domains for A_{asympt} :

$$I = \frac{2}{a} \left(\int_0^{\frac{b-1}{b^2}} \left(\frac{\alpha \epsilon_S}{l^2} + \beta R_c^2 \right) \frac{l^2 dl}{\sqrt{l^2 + 1}} + \frac{b-1}{b^2} \int_{\frac{b-1}{b^2}}^L \left(\frac{\alpha \epsilon_S}{l^2} + \beta R_c^2 \right) \frac{ldl}{\sqrt{l^2 + 1}} \right) = I_1 + I_2$$

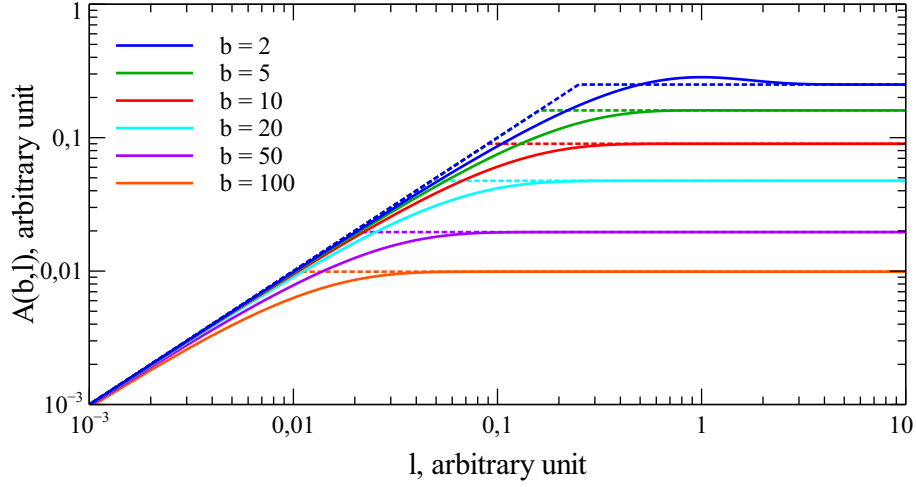


Figure E.2.1: Evolution of the integral A (plain line) and its approximate form A_{asympt} (dotted line) for different values of b .

The two integrals are obtained easily:

$$I_1 = \frac{2}{a} \left(\alpha \epsilon_S \operatorname{arcsinh} \left(\frac{b-1}{b^2} \right) + \beta R_c^2 \left(\frac{b-1}{b^2} \sqrt{\left(\frac{b-1}{b^2} \right)^2 + 1} - \operatorname{arcsinh} \left(\frac{b-1}{b^2} \right) \right) \right),$$

$$I_2 = \frac{2b-1}{a b^2} \left(\alpha \epsilon_S \log \left(\frac{b^2 L \left(\sqrt{\left(\frac{b-1}{b^2} \right)^2 + 1} + 1 \right)}{(b-1) \left(\sqrt{L^2 + 1} + 1 \right)} \right) + \beta R_c^2 \left(\sqrt{L^2 + 1} - \sqrt{\left(\frac{b-1}{b^2} \right)^2 + 1} \right) \right),$$

so the linear impulse is given by:

$$I = \frac{2}{a} \left(\alpha \epsilon_S \left(\operatorname{arcsinh} \left(\frac{b-1}{b^2} \right) + \frac{b-1}{b^2} \log \left(\frac{b^2 L \left(\sqrt{\left(\frac{b-1}{b^2} \right)^2 + 1} + 1 \right)}{(b-1) \left(\sqrt{L^2 + 1} + 1 \right)} \right) \right) \right. \\ \left. + \beta R_c^2 \left(\frac{b-1}{b^2} \left(\sqrt{L^2 + 1} - \frac{1}{2} \sqrt{\left(\frac{b-1}{b^2} \right)^2 + 1} \right) - \frac{\operatorname{arcsinh} \left(\frac{b-1}{b^2} \right)}{2} \right) \right). \quad (\text{E.2.2})$$

For $b \gg 1$, we can simplify this expression using Taylor expansions of the first

order:

$$\begin{aligned}
b \gg 1 &\implies \frac{b-1}{b^2} \sim \frac{1}{b}, \\
\operatorname{arcsinh}\left(\frac{b-1}{b^2}\right) &\sim \frac{1}{b}, \\
\log\left(\frac{b^2\left(\sqrt{\left(\frac{b-1}{b^2}\right)^2+1}+1\right)}{b-1}\right) &\sim \log(2b), \\
\sqrt{\left(\frac{b-1}{b^2}\right)^2+1}\frac{b-1}{b^2} &\sim \frac{1}{b},
\end{aligned}$$

so replacing the various parameters by their expression, we get eventually:

$$I = \frac{8\epsilon_S}{\pi(\gamma+1)bc_0} \sqrt{\frac{F}{G}} \left(1 + \log\left(\frac{2Lb}{\sqrt{L^2+1}+1}\right) + \left(\frac{1}{F} - \frac{1}{G}\right) (\sqrt{L^2+1} - 1)\right) \quad (\text{E.2.3})$$

E.3 First order approximation

Comparison between numerical integration performed for the various cases and this semi-analytic formula (E.2.3) indicates an overestimation by almost 10% of the linear impulse. This can be linked to the approximation of the function A by its asymptotic behavior A_{asympt} that leads to a large error around $l_0 = \frac{b-1}{b^2}$ (intersection of the two asymptotic behaviors). Greater accuracy can be obtained using a finer approximation for A with a first-order Taylor expansion around l_0 :

$$A_{\text{linear}}(b, l) = \begin{cases} l & \text{when } l < l_- \\ A(l_0) + (1-l_0)e^{-bl_0}(l-l_0) & \text{when } l_- < l < l_+ \\ l_0 = \frac{b-1}{b^2} & \text{when } l > l_+ \end{cases} \quad (\text{E.3.1})$$

l_- and l_+ are intersections points between the various parts of the curve described by A_{linear} :

$$l_- = \frac{A(l_0) - l_0(1-l_0)e^{-bl_0}}{1 - (1-l_0)e^{-bl_0}}, \quad (\text{E.3.2a})$$

$$l_+ = \frac{l_0\left(1 + (1-l_0)e^{-bl_0}\right) - A(l_0)}{(1-l_0)e^{-bl_0}}. \quad (\text{E.3.2b})$$

This new function A_{linear} matches more closely the real function A than its asymptotic form A_{asympt} , as can be seen on figure E.3.1

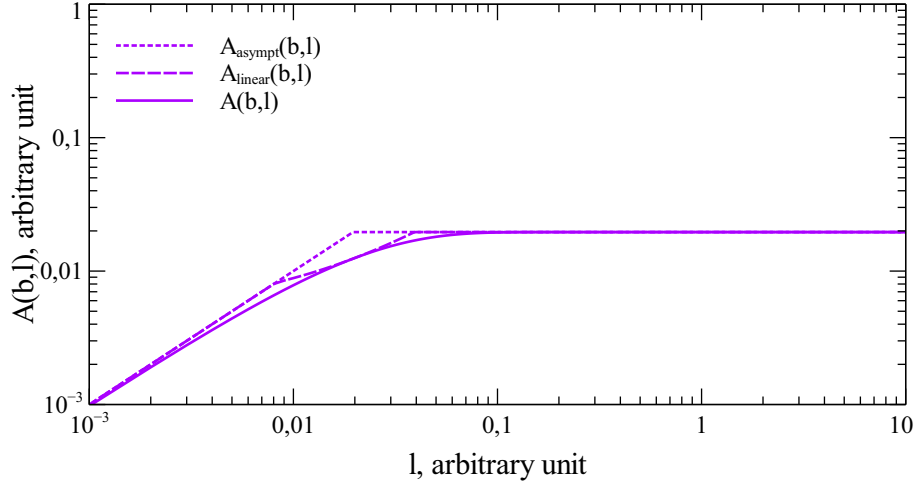


Figure E.3.1: Evolution of the integral A (plain line), its asymptotic approximation A_{asympt} (dotted line) and its linear approximation A_{linear} (dashed line), for $b = 50$.

Defining:

$$\begin{aligned} B_0 &= (1 - l_0)e^{-bl_0}, \\ C_0 &= A(l_0) - l_0(1 - l_0)e^{-bl_0}, \end{aligned}$$

the linear impulse created by the surface discharge is given by:

$$I = \frac{8\epsilon_S}{\pi(\gamma + 1)c_0} \sqrt{\frac{F}{G}} (J_1 + J_2 + J_3) \quad (\text{E.3.3})$$

with J_1, J_2, J_3 the integrals between the various boundaries:

$$\begin{aligned} J_1 &= \text{arcsinh}(l_-) + \left(\frac{1}{F} - \frac{1}{G}\right) \left(\frac{l_- \sqrt{l_-^2 + 1} - \text{arcsinh}(l_-)}{2}\right), \\ J_2 &= C_0 \log \left(\frac{l_+(\sqrt{l_-^2 + 1} + 1)}{l_-(\sqrt{l_+^2 + 1} + 1)}\right) + B_0(\text{arcsinh}(l_+) - \text{arcsinh}(l_-)) \\ &\quad + \left(\frac{1}{F} - \frac{1}{G}\right) C_0(\sqrt{l_+^2 + 1} - \sqrt{l_-^2 + 1}) \\ &\quad + \left(\frac{1}{F} - \frac{1}{G}\right) \frac{B_0}{2} \left(l_+ \sqrt{l_+^2 + 1} - l_- \sqrt{l_-^2 + 1} - (\text{arcsinh}(l_+) - \text{arcsinh}(l_-))\right) \\ J_3 &= l_0 \left(\log \left(\frac{L(\sqrt{l_+^2 + 1} + 1)}{l_+(\sqrt{L^2 + 1} + 1)}\right) + \left(\frac{1}{F} - \frac{1}{G}\right) \left(\sqrt{L^2 + 1} - \sqrt{l_+^2 + 1}\right)\right) \end{aligned}$$

References

- Anderson, K. V. and D. D. Knight (2011, February). Interaction of heated filaments with a blunt cylinder in supersonic flow. *Shock Waves* 21(2), 149–161. (p. 7)
- Anderson, K. V. and D. D. Knight (2012a). Characterization of Single Pulse of Plasma Jet. In *50th AIAA Aerospace Sciences Meeting including the New Horizons Forum and Aerospace Exposition*, pp. 0188. (p. 10, 104, 105, 116)
- Anderson, K. V. and D. D. Knight (2012b, September). Plasma Jet for Flight Control. *AIAA Journal* 50(9), 1855–1872. (p. 10, 104, 105, 116, 117)
- Andreev, S. I., I. M. Belousova, P. N. Dashuk, D. I. Zaroslov, E. A. Zobov, N. V. Karlov, G. P. Kuzmin, S. M. Nikiforov, A. M. Prokhorov, and A. N. Sidorov (1975). CO₂ laser initiated by a gliding discharge. *ZHETF Pis'ma v Redaktsiiu* 21, 424–426. (p. 12)
- Andreev, S. I., E. A. Zobov, and A. N. Sidorov (1976). Method of controlling the growth and formation of a system of parallel sliding spark channels in air at atmospheric pressure. *Journal of Applied Mechanics and Technical Physics* 17(3), 308–312. (p. 12)
- Andreev, S. I., E. A. Zobov, and A. N. Sidorov (1978). Investigation of Sliding Spark in Air. *Journal of Applied Mechanics and Technical Physics* 19(3), 309–314. (p. 12, 41)
- Andreev, S. I., E. A. Zobov, A. N. Sidorov, and V. D. Kostousov (1980). An investigation of a long sliding spark. *Journal of Applied Mechanics and Technical Physics* 21(1), 103–106. (p. 12, 13, 36, 41)
- Arad, B., Y. Gazit, and A. Ludmirsky (1987). A sliding discharge device for producing cylindrical shock waves. *Journal of Physics D: Applied Physics* 20, 360–367. (p. 13)
- Armstrong, B. H. (1967). Spectrum line profiles: The Voigt function. *Journal of Quantitative Spectroscopy and Radiative Transfer* 7(2), 61–88. (p. 25)
- Baranov, V. Y., V. M. Borisov, A. M. Davidovskii, and O. B. Khristoforov (1981). Use of a discharge over a dielectric surface for preionization in excimer lasers. *Soviet Journal of Quantum Electronics* 11(1), 42–45. (p. 12, 70)
- Baranov, V. Y., V. M. Borisov, F. I. Vysikailo, and O. B. Khristoforov (1984). Study of the conditions of formation of a uniform high-current

- sliding discharge. *High Temperature* 22(4), 528–533. (p. 12, 41)
- Belinger, A., P. Hardy, P. Barricau, J. P. Cambronne, and D. Caruana (2011, September). Influence of the energy dissipation rate in the discharge of a plasma synthetic jet actuator. *Journal of Physics D: Applied Physics* 44(36), 365201–01 – 365201–12. (p. 10, 91)
- Belinger, A., P. Hardy, N. Gherardi, N. Naudé, J. P. Cambronne, and D. Caruana (2011). Influence of the Spark Discharge Size on a Plasma Synthetic Jet Actuator. *IEEE Transactions on Plasma Science* 39(11), 2334–2335. (p. 10)
- Belson, B. A., K. Meidell, R. E. Hanson, D. Palmeiro, P. Lavoie, and C. W. Rowley (2012). Comparison of plasma actuators in simulations and experiments for control of bypass transition. In *50th AIAA Aerospace Sciences Meeting including the New Horizons Forum and Aerospace Exposition*, Number January, pp. 1–9. (p. 7)
- Bénard, N., J. Jolibois, E. Moreau, R. Sosa, G. Artana, and G. Touchard (2008, August). Aerodynamic plasma actuators: A directional micro-jet device. *Thin Solid Films* 516(19), 6660–6667. (p. 8)
- Benard, N. and E. Moreau (2014). Electrical and mechanical characteristics of surface AC dielectric barrier discharge plasma actuators applied to airflow control. *Experiments in Fluids* 55(11). (p. 116, 117)
- Bethe, H. A., K. Fuchs, J. O. Hirschfelder, J. L. Magee, R. E. Peierls, and J. von Neumann (1947). Blast wave. Technical report, Los Alamos National Laboratory. (p. 137)
- Beverly III, R. E. (1986). Electrical, gasdynamic, and radiative properties of planar surface discharges. *Journal of Applied Physics* 60(1), 104–124. (p. 13, 36, 41, 84)
- Beverly III, R. E., R. H. Barnes, C. E. Moeller, and M. C. Wong (1977, June). Ultraviolet spectral efficiencies of surface-spark discharges with emphasis on the iodine photodissociation laser pumpband. *Applied optics* 16(6), 1572–7. (p. 12)
- Bletzinger, P., B. N. Ganguly, D. M. van Wie, and A. Garscadden (2005, February). Plasmas in high speed aerodynamics. *Journal of Physics D: Applied Physics* 38(4), R33–R57. (p. 6, 10)
- Bordage, M. C. and G. Hartmann (1982). Spectroscopic measurements on discharges along a dielectric surface. *Journal of Applied Physics* 53(12), 8568–8576. (p. 13, 15, 36, 41, 50, 84)
- Braginskii, S. I. (1958). Theory of the development of a spark channel. *Soviet Physics Journal of Experimental and Theoretical Physics* 34(7), 1068–1074. (p. 46, 48, 51)
- Braun, E. M., F. K. Lu, and D. R. Wilson (2009, January). Experimental research in aerodynamic control with electric and electromagnetic fields. *Progress in Aerospace Sciences* 45(1-3), 30–49. (p. 6)
- Caruana, D. (2010, December). Plasmas for aerodynamic control. *Plasma Physics and Controlled Fusion* 52(12), 124045–01 – 124045–12. (p. 5, 7,

- 8, 9)
- Castera, P. and P.-Q. Elias (2014, jul). Resistance Models Applied to the Return Stroke Phase of Negative Pulsed Surface Discharges in Air. *IEEE Transactions on Plasma Science* 42(7), 1922–1931. (p. 61)
- Castera, P., P.-Q. Elias, and C. O. Laux (2014). Application of Linear Sliding Discharges for Flow Control: Study of the Energy Coupling Mechanisms. In *45th AIAA Plasmadynamics and Lasers Conference*, pp. 116–128. (p. 110)
- Cattafesta III, L. N. and M. Sheplak (2011, January). Actuators for Active Flow Control. *Annual Review of Fluid Mechanics* 43(1), 247–272. (p. 5, 6, 7, 8)
- Chakraborti, P. K. (1962). An exact analytic solution for a cylindrical blast wave propagation in still air. *Proceedings of the Indian National Science Academy* 28(5), 683–694. (p. 137)
- Chernyi, G. G. (1957). The problem of a point explosion. *Doklady Akademii Nauk SSSR* 112, 213–216. (p. 96)
- Ciddor, P. E. (1996, mar). Refractive index of air: new equations for the visible and near infrared. *Applied Optics* 35(9), 1566–73. (p. 130)
- Colas, D. F., A. Ferret, D. Z. Pai, D. A. Lacoste, and C. O. Laux (2010). Ionic wind generation by a wire-cylinder-plate corona discharge in air at atmospheric pressure. *Journal of Applied Physics* 108(10), 103306. (p. 6)
- Corke, T. C., C. Lon Enloe, and S. P. Wilkinson (2010, January). Dielectric Barrier Discharge Plasma Actuators for Flow Control. *Annual Review of Fluid Mechanics* 42(1), 505–529. (p. 7)
- Djurović, S. and N. Konjević (2009). On the use of non-hydrogenic spectral lines for low electron density and high pressure plasma diagnostics. *Plasma Sources Science and Technology* 18(3), 035011. (p. 72, 74, 75)
- Du, P., W. A. Kibbe, and S. M. Lin (2006, September). Improved peak detection in mass spectrum by incorporating continuous wavelet transform-based pattern matching. *Bioinformatics (Oxford, England)* 22(17), 2059–65. (p. 25)
- Duchmann, A., A. Kurz, A. Widmann, S. Grundmann, and C. Tropea (2012). Characterization of Tollmien-Schlichting Wave Damping by DBD Plasma Actuators Using. In *50th AIAA Aerospace Sciences Meeting including the New Horizons Forum and Aerospace Exposition*, Number January. (p. 7)
- Duchmann, A., B. Simon, C. Tropea, and S. Grundmann (2014). Dielectric Barrier Discharge Plasma Actuators for In-Flight Transition Delay. *AIAA Journal* 52(2), 358–367. (p. 7)
- Durscher, R. and S. Roy (2010). Novel Multi-Barrier Plasma Actuators for Increased Thrust. In *48th AIAA Aerospace Sciences Meeting including the New Horizons Forum and Aerospace Exposition*, Number January, Orlando, Florida, pp. 2010–965. (p. 116, 117)
- Durscher, R., S. Stanfield, and S. Roy (2012). Characterization and manip-

- ulation of the “saturation” effect by changing the surface temperature of a dielectric barrier discharge actuator. *Applied Physics Letters* 101(25), 252902. (p. 7)
- Elias, P.-Q. and P. Castera (2013, September). Measurement of the impulse produced by a pulsed surface discharge actuator in air. *Journal of Physics D: Applied Physics* 46(36), 365204. (p. 28, 84)
- Elias, P.-Q., B. Chanetz, S. Larigaldie, and D. Packan (2007, September). Study of the Effect of Glow Discharges Near a $M = 3$ Bow Shock. *AIAA Journal* 45(9), 2237–2245. (p. 6)
- Elias, P.-Q., B. Chanetz, S. Larigaldie, D. Packan, and C. O. Laux (2008, August). Mach 3 Shock Wave Unsteadiness Alleviation Using a Negative Corona Discharge. *AIAA Journal* 46(8), 2042–2049. (p. 6)
- Engel, T. G., A. L. Donaldson, and M. Kristiansen (1989, April). The Pulsed Discharge Arc Resistance and its Functional Behavior. *IEEE Transactions on Plasma Science* 17(2), 323–329. (p. 46)
- Erofeev, A. V., T. A. Lapushkina, S. A. Poniaev, R. O. Kurakin, and B. G. Zhukov (2012). Flow around different bodies at the pellet or plasma jet injection. In *50th AIAA Aerospace Sciences Meeting including the New Horizons Forum and Aerospace Exposition*, Number January, pp. 1–11. (p. 7)
- Fomin, V. M., P. K. Tretyakov, and J.-P. Taran (2004, July). Flow control using various plasma and aerodynamic approaches (Short review). *Aerospace Science and Technology* 8(5), 411–421. (p. 6)
- Freeman, R. A. (1968). Variable-energy blast waves. *Journal of Physics D: Applied Physics* 1, 1697–1710. (p. 139)
- Glasstone, S. and P. J. Dolan (Eds.) (1977). *The Effects of Nuclear Weapons* (Third Edition ed.). Washington D.C.: United States Department of Defense. (p. 96)
- Gnemmi, P., R. Charon, J.-P. Dup eroux, and A. George (2008, June). Feasibility Study for Steering a Supersonic Projectile by a Plasma Actuator. *AIAA Journal* 46(6), 1308–1317. (p. 10)
- Gnemmi, P. and C. Rey (2009, September). Plasma Actuation for the Control of a Supersonic Projectile. *Journal of Spacecraft and Rockets* 46(5), 989–998. (p. 11)
- Gnemmi, P., C. Rey, A. Eichhorn, M. Bastide, and J.-L. Striby (2013). Pressure, temperature and free-flight projectile-displacement measurements during a plasma discharge generated on a supersonic projectile. *International Journal of Aerodynamics* 3, 84–104. (p. 11)
- Goel, M. D., V. A. Matsagar, A. Gupta, and S. Marburg (2012, September). An Abridged Review of Blast Wave Parameters. *Defence Science Journal* 62(5), 300–306. (p. 99)
- Goldston, R. J. and P. H. Rutherford (1995). *Introduction to plasma physics*. IOP Publishing Ltd. (p. 47)
- Greenblatt, D., A. Ben-Harav, and M. Schulman (2012). Dynamic Stall Con-

- trol on a Vertical Axis Wind Turbine Using Plasma Actuators. In *50th AIAA Aerospace Sciences Meeting including the New Horizons Forum and Aerospace Exposition*, Number January. (p. 7)
- Griem, H. R. U. o. M. (1964). *Plasma spectroscopy*. New-York: McGraw-Hill. (p. 72)
- Hahn, C., M. Kearney-Fischer, and M. Samimy (2011, August). On factors influencing arc filament plasma actuator performance in control of high speed jets. *Experiments in Fluids* 51(6), 1591–1603. (p. 11)
- Hinton, T. J., Q. Jallerat, R. N. Palchesko, J. H. Park, M. S. Grodzicki, H.-J. Shue, M. H. Ramadan, A. R. Hudson, and A. W. Feinberg (2015, oct). Three-dimensional printing of complex biological structures by freeform reversible embedding of suspended hydrogels. *Science Advances* 1(9), e1500758–e1500758. (p. x)
- Janssen, J. F. J., M. Gnybida, J. L. G. Suijker, A. J. Rijke, and J. van Dijk (2013). On the atomic line profiles in high pressure plasmas. *Journal of Applied Physics* 114(18), 183301. (p. 25, 72)
- Kim, J.-H., M. Nishihara, I. V. Adamovich, M. Samimy, S. V. Gorbатов, and F. V. Pliavaka (2010, January). Development of localized arc filament RF plasma actuators for high-speed and high Reynolds number flow control. *Experiments in Fluids* 49(2), 497–511. (p. 11)
- Kochina, N. N. and N. S. Mel'nikova (1958). On the nonstationary motion of a gas, due to a piston, including the counter-pressure. *Doklady Akademii Nauk SSSR* 122(2). (p. 138)
- Kochina, N. N. and N. S. Mel'nikova (1960). On the motion of a piston in an ideal gas. *Prikladnaya Matematika i Mekhanika* 24(2), 213–218. (p. 138)
- Konjević, N., M. Ivković, and N. Sakan (2012, October). Hydrogen Balmer lines for low electron number density plasma diagnostics. *Spectrochimica Acta Part B: Atomic Spectroscopy* 76, 16–26. (p. 75)
- Kramida, A., Yu. Ralchenko, J. Reader, and NIST ASD Team (2014). NIST Atomic Spectra Database (ver. 5.2), [Online]. Available: <http://physics.nist.gov/asd> [2015, April 22]. National Institute of Standards and Technology, Gaithersburg, MD. (p. 72, 130)
- Krasiuk, I. K., N. I. Lipatov, and P. P. Pashinin (1976). Formation of an ultraviolet radiation pulse in a surface-discharge plasma by the front of an electromagnetic shock wave. *Soviet Journal of Quantum Electronics* 6(11), 1298–1302. (p. 12, 70)
- Ku, H. H. (1966). Notes on the Use of Propagation of Error Formulas. *Journal of Research of the National Bureau of Standards - C. Engineering and Instrumentation* 70C(4), 263–273. (p. 121)
- Lagarkov, A. N. and I. M. Rutkevich (1994). *Ionization Waves in Electrical Breakdown of Gases*. New York: Springer-Verlag. (p. 12, 13, 36, 41)
- Lam, N., P. Mendis, and T. Ngo (2004). Response Spectrum Solutions for Blast Loading. *Electronic Journal of Structural Engineering* 4, 28–44. (p. 99)

- Larcher, M. (2007). Simulation of the Effects of an Air Blast Wave. Technical report. (p. 99)
- Larcher, M. (2008). Pressure-Time Functions for the Description of Air Blast Waves. Technical report. (p. 99)
- Larigaldie, S. (1987a). Mechanisms of spark propagation in ambient air at the surface of a charged dielectric. II. Theoretical modeling. *Journal of Applied Physics* 61(1), 102–108. (p. 13, 15, 36, 41, 45, 55, 84)
- Larigaldie, S. (1987b). Spark propagation mechanisms in ambient air at the surface of a charged dielectric. I. Experimental: The main stages of the discharge. *Journal of Applied Physics* 61(1), 90–108. (p. 13, 15, 36, 41, 84)
- Larigaldie, S., G. Labaune, and J.-P. Moreau (1981). Lightning leader laboratory simulation by means of rectilinear surface discharges. *Journal of Applied Physics* 52(12), 7114–7120. (p. 13, 15, 36, 41, 84)
- Larigaldie, S., A. Roussaud, and B. Jecko (1992). Mechanisms of high-current pulses in lightning and long-spark stepped leaders. *Journal of Applied Physics* 72(5), 1729–1739. (p. 13, 15, 36, 41, 84)
- Laux, C. O., T. G. Spence, C. H. Kruger, and R. N. Zare (2003, May). Optical diagnostics of atmospheric pressure air plasmas. *Plasma Sources Science and Technology* 12(2), 125–138. (p. 80, 132)
- Lee, T. S. (1966). Comments on "Blast Waves from an Inverse Pinch Machine". *Physics of Fluids* 9(11), 2303. (p. 97)
- Leonov, S. B., V. Petrishchev, and I. V. Adamovich (2014). Dynamics of energy coupling and thermalization in barrier discharges over dielectric and weakly conducting surfaces on μs to ms time scales. *Journal of Physics D: Applied Physics* 47(46), 465201. (p. 118)
- Leonov, S. B. and D. A. Yarantsev (2008). Control of Separation Phenomena in a High-Speed Flow by Means of the Surface Electric Discharge. *Fluid Dynamics* 43(6), 945–953. (p. 10)
- Li, Y., J. Wang, C. Wang, Z. An, S. Hou, and F. Xing (2010, April). Properties of surface arc discharge in a supersonic airflow. *Plasma Sources Science and Technology* 19(2), 025016. (p. 11)
- Lin, S.-C. (1954). Cylindrical Shock Waves Produced by Instantaneous Energy Release. *Journal of Applied Physics* 25(1), 54. (p. 96, 135)
- Louste, C., G. Artana, E. Moreau, and G. Touchard (2005, June). Sliding discharge in air at atmospheric pressure: electrical properties. *Journal of Electrostatics* 63(6-10), 615–620. (p. 8)
- Mestiri, R., R. Hadaji, and S. Ben Nasrallah (2010). An experimental study of a plasma actuator in absence of free airflow: Ionic wind velocity profile. *Physics of Plasmas* 17(8), 083503. (p. 6)
- Montaño, R., M. Becerra, V. Cooray, M. Rahman, and P. Liyanage (2006). Resistance of Spark Channels. *IEEE Transactions on Plasma Science* 34(5), 1610–1619. (p. 46)
- Moreau, E. (2007, February). Airflow control by non-thermal plasma actua-

- tors. *Journal of Physics D: Applied Physics* 40(3), 605–636. (p. 6)
- Moreau, E., C. Louste, and G. Touchard (2008, January). Electric wind induced by sliding discharge in air at atmospheric pressure. *Journal of Electrostatics* 66(1-2), 107–114. (p. 8)
- Moreau, E., R. Sosa, and G. Artana (2008, June). Electric wind produced by surface plasma actuators: a new dielectric barrier discharge based on a three-electrode geometry. *Journal of Physics D: Applied Physics* 41(11), 115204. (p. 8)
- Moreau, E. and G. Touchard (2008, January). Enhancing the mechanical efficiency of electric wind in corona discharges. *Journal of Electrostatics* 66(1-2), 39–44. (p. 6)
- Muñoz, J., M. Dimitrijević, C. Yubero, and M. Calzada (2009, February). Using the van der Waals broadening of spectral atomic lines to measure the gas temperature of an argon–helium microwave plasma at atmospheric pressure. *Spectrochimica Acta Part B: Atomic Spectroscopy* 64(2), 167–172. (p. 75)
- Narayanaswamy, V., L. L. Raja, and N. T. Clemens (2010, February). Characterization of a High-Frequency Pulsed-Plasma Jet Actuator for Supersonic Flow Control. *AIAA Journal* 48(2), 297–305. (p. 10)
- Oreshkin, V. I. and I. V. Lavrinovich (2014, April). Energy loss in spark gap switches. *Physics of Plasmas* 21(4), 043513. (p. 48, 51)
- Oshima, K. (1960). Blast Waves Produced by Exploding Wires. Technical report, Aeronautical Research Institute. (p. 139)
- Osmokrović, P., S. Krstic, M. Ljevak, and D. Novakovic (1992). Parameters on the Topler Const ant. *IEEE Transactions on Electrical Insulation* 27(2), 214–220. (p. 51)
- Parisse, J.-D. and V. Lago (2013). Shock modification induced by a DC discharge : numerical and experimental study. *Int. J. Aerodynamics* 3, 105–121. (p. 6)
- Parisse, J. D., L. Léger, E. Depussay, V. Lago, and Y. Burtschell (2009). Comparison between Mach 2 rarefied airflow modification by an electrical discharge and numerical simulation of airflow modification by surface heating. *Physics of Fluids* 21(10), 106103. (p. 6)
- Plooster, M. N. (1971a). Numerical Model of the Return Stroke of the Lightning Discharge. *Physics of Fluids* 14(10), 2124–2133. (p. 139)
- Plooster, M. N. N. C. f. A. R. (1971b). Numerical Simulation of Spark Discharges in Air. *Physics of Fluids* 14(10), 2111–2123. (p. 139)
- Popkin, S. H., B. Z. Cybyk, H. B. Land III, T. M. Emerick II, C. H. Foster, and F. S. Alvi (2013). Recent Performance-Based Advances in Spark-Jet Actuator Design for Supersonic Flow Applications. In *51st AIAA Aerospace Sciences Meeting*, Number January, Grapevine, Texas, pp. AIAA 2013–0322. (p. 10)
- Post, M. L. and T. C. Corke (2004, November). Separation Control on High Angle of Attack Airfoil Using Plasma Actuators. *AIAA Journal* 42(11),

- 2177–2184. (p. 7)
- Raizer, Y. P. (1997). *Gas Discharge Physics* (1997 ed.). Berlin Heidelberg New York: Springer-Verlag. (p. 47, 50, 51, 56)
- Raju, G. G. (2005). *Gaseous Electronics : Theory and Practice*. CRC Press. (p. 56)
- Reedy, T. M., N. V. Kale, J. C. Dutton, and G. S. Elliott (2012). Experimental Characterization of a Pulsed Plasma Jet. In *50th AIAA Aerospace Sciences Meeting including the New Horizons Forum and Aerospace Exposition*, Number January, pp. 1–13. (p. 10)
- Rompe, R. and W. Weizel (1944). Über das Toeplersche Funkengesetz. *Zeitschrift für Physik A Hadrons and Nuclei* 122(9-12), 636–639. (p. 46, 47)
- Roth, J. R. (2003). Aerodynamic flow acceleration using paraelectric and peristaltic electrohydrodynamic effects of a One Atmosphere Uniform Glow Discharge Plasma. *Physics of Plasmas* 10(5), 2117. (p. 7)
- Roupassov, D. V., A. A. Nikipelov, M. M. Nudnova, and A. Y. Starikovskii (2009, January). Flow Separation Control by Plasma Actuator with Nanosecond Pulsed-Periodic Discharge. *AIAA Journal* 47(1), 168–185. (p. 9)
- Sainct, F. (2014, February). *Experimental study of nanosecond atmospheric pressure plasma discharges in water vapor*. Theses, Ecole Centrale Paris. (p. 72)
- Sakurai, A. (1953). On the propagation and structure of the blast wave I. *Journal of the Physical Society of Japan* 8(5), 662–669. (p. 138)
- Sakurai, A. (1954). On the propagation and structure of the blast wave II. *Journal of the Physical Society of Japan* 9(2), 256–266. (p. 138)
- Samimy, M., J.-H. Kim, J. Kastner, I. V. Adamovich, and Y. Utkin (2007, April). Active control of high-speed and high-Reynolds-number jets using plasma actuators. *Journal of Fluid Mechanics* 578, 305–330. (p. 11, 12)
- Schreier, F. (1992). The voigt and complex error function: a comparison of computational methods. *Journal of Quantitative Spectroscopy and Radiative Transfer* 48(5-6), 743–762. (p. 25)
- Sedov, L. I. (1946). Propagation of intense blast waves. *Prikladnaya Matematika i Mekhanika* 10, 241–250. (p. 96, 135)
- Seraudie, A., J. P. Cambonne, E. Aubert, and N. Naudé (2006). Effect of plasma actuators on a flat plate laminar boundary layer in subsonic conditions. In *3 rd AIAA Flow Control ...*, San Francisco, CA, USA. (p. 7)
- Shang, J. S. (2001). Recent research in magneto-aerodynamics. *Progress in Aerospace Sciences* 37(1), 1–20. (p. 6)
- Shang, J. S., S. T. Surzhikov, R. Kimmel, D. Gaitonde, J. Menart, and J. Hayes (2005, November). Mechanisms of plasma actuators for hypersonic flow control. *Progress in Aerospace Sciences* 41(8), 642–668. (p. 6)
- Sochet, I., D. Gardebas, S. Calderara, and B. Marchal, Y. Longuet (2011).

- Blast Wave Parameters for Spherical Explosives Detonation in Free Air. *Open Journal of Safety Science and Technology* 01(02), 31–42. (p. 99)
- Soloviev, V. R., V. M. Krivstov, A. M. Konchakov, and N. D. Malmuth (2003, December). Drag Reduction by Plasma Filaments over Supersonic Forebodies. *AIAA Journal* 41(12), 2403–2409. (p. 7)
- Song, H., Y. Li, Q. Zhang, J. Min, and Y. Wu (2011). Experimental Investigation on the Characteristics of Sliding Discharge Plasma Aerodynamic Actuation. *Plasma Science and Technology* 13(5), 608–611. (p. 8)
- Sosa, R., H. Kelly, D. Grondona, A. Márquez, V. Lago, and G. Artana (2008, February). Electrical and plasma characteristics of a quasi-steady sliding discharge. *Journal of Physics D: Applied Physics* 41(3), 035202. (p. 8)
- Speth, R. L. and D. V. Gaitonde (2012). Parametric Study of a Supersonic Jet Subjected to Plasma-based Flapping Mode Excitation. In *50th AIAA Aerospace Sciences Meeting including the New Horizons Forum and Aerospace Exposition*, Number January, pp. 1–24. (p. 11)
- Starikovskii, A. Y., N. B. Anikin, I. N. Kosarev, E. I. Mintoussov, M. M. Nudnova, A. Rakitin, D. V. Roupasov, S. M. Starikovskaia, and V. P. Zhukov (2008, November). Nanosecond-Pulsed Discharges for Plasma-Assisted Combustion and Aerodynamics. *Journal of Propulsion and Power* 24(6), 1182–1197. (p. 9)
- Sun, Y., Q. Jallerat, J. M. Szymanski, and A. W. Feinberg (2015, feb). Conformal nanopatterning of extracellular matrix proteins onto topographically complex surfaces. *Nature methods* 12(2), 134–6. (p. x)
- Swigart, R. J. (1960). Third-order blast wave theory and its application to hypersonic flow past blunt-nosed cylinders. *Journal of Fluid Mechanics* 9(4), 613–620. (p. 139)
- Taylor, G. I. (1950a). The formation of a blast wave by a very intense explosion. I. Theoretical discussion. *Proceedings of the Royal Society of London. Series A, Mathematical and Physical Sciences* 201(1065), 159–174. (p. 96, 135)
- Taylor, G. I. (1950b). The formation of a blast wave by a very intense explosion. II. The atomic explosion of 1945. *Proceedings of the Royal Society of London. Series A, Mathematical and Physical Sciences* 201(1065), 175–186. (p. 96, 135)
- Taylor, J. L. (1955). An exact solution of the spherical blast wave problem. *The London, Edinburgh, and Dublin Philosophical Magazine and Journal of Science: Series 7* 46(374), 317–320. (p. 137)
- Thomas, F. O., T. C. Corke, M. Iqbal, A. Kozlov, and D. Schatzman (2009, September). Optimization of Dielectric Barrier Discharge Plasma Actuators for Active Aerodynamic Flow Control. *AIAA Journal* 47(9), 2169–2178. (p. 7)
- Toepler, M. (1906). Zur Kenntnis der Gesetze der Gleitfunkenbildung. *Annalen der Physik* 326(12), 193–222. (p. 14, 46)
- Toepler, M. (1921). Über die physikalischen Grundgesetze der in der Iso-

- latorentchnik auftretenden elektrischen Gleiterscheinungen. *Archiv für Elektrotechnik* 10, 157–185. (p. 14, 41, 46, 48)
- Toepler, M. (1926). Neuer Weg zur Bestimmung der Funkenkonstanten , einzelne Spannungsstöße mit berechenbarem gesamten Spannungsverlaufe . *Archiv für Elektrotechnik* 17, 91–70. (p. 51)
- Toepler, M. (1927). Zusammenhang zwischen Funken, Büschellichtbogen und Bogen. *Archiv für Elektrotechnik* 18, 563–566. (p. 51)
- Trusov, K. K. (1994). Application of an high-voltage capacitance generator to transverse-discharge flashlamp excitation. *J. Phys. D : Applied Physics* 27, 1076–1081. (p. 13, 56)
- Trusov, K. K. (2006, January). A model of multichannel mode formation in a sliding electric gas discharge. *Journal of Physics D: Applied Physics* 39(2), 335–341. (p. 13, 36, 41)
- Trusov, K. K. (2007, February). Dynamics of multichannel and quasi-homogeneous sliding discharge formation in rare gases. *Journal of Physics D: Applied Physics* 40(3), 786–794. (p. 13)
- Trusov, K. K. (2009). Look at the Spark Cross Size Development in a Sliding Submicrosecond Discharge from the Theory of Ionization Wave Front Propagation. In *Progress In Electromagnetics Research Symposium Proceedings*, Number 1, pp. 1766–1770. (p. 13)
- Tuema, F. A., S. J. MacGregor, R. A. Fouracre, D. J. Fulker, F. A. J., and P. A. Winstanley (2000). Factors affecting the UV emission from pulsed surface discharges. *IEEE Transactions on Plasma Science* 28(5), 1588–1592. (p. 12, 70)
- van der Horst, R. M., T. Verreycken, E. M. van Veldhuizen, and P. J. Bruggeman (2012, August). Time-resolved optical emission spectroscopy of nanosecond pulsed discharges in atmospheric-pressure N₂ and N₂/H₂O mixtures. *Journal of Physics D: Applied Physics* 45(34), 345201. (p. 72, 75)
- Vlases, G. C. and D. L. Jones (1966). Blast Waves from an Inverse Pinch Machine. *Physics of Fluids* 9(3), 478. (p. 96)
- Vlastós, A. E. (1969). Restrike Channel Resistance of Thin Exploding Wires. *Journal of Applied Physics* 40(1969), 4752–4760. (p. 51)
- Vlastós, A. E. (1972). The Resistance of Sparks. *Journal of Applied Physics* 43(4), 1987–1989. (p. 46, 47, 51)
- Wang, L., Z. Luo, Z. Xia, B. Liu, and X. Deng (2012, May). Review of actuators for high speed active flow control. *Science China Technological Sciences* 55(8), 2225–2240. (p. 6, 9, 10)
- Weizel, W. and R. Rompe (1947). Theorie des elektrischen Funkens. *Annalen der Physik* 436(6), 285–300. (p. 46, 47)
- Wiese, W. L. and J. R. Fuhr (2009). Accurate Atomic Transition Probabilities for Hydrogen, Helium, and Lithium. *Journal of Physical and Chemical Reference Data* 38(3), 565. (p. 129, 130)
- Xu, D. A. (2013). *Thermal and Hydrodynamic Effects of Nanosecond Dis-*

- charges in Air and Application to Plasma-Assisted Combustion*. Ph. D. thesis, Ecole Centrale Paris. (p. 102)
- Xu, D. A., M. N. Shneider, D. A. Lacoste, and C. O. Laux (2014). Thermal and hydrodynamic effects of nanosecond discharges in atmospheric pressure air. *Journal of Physics D: Applied Physics* 47, 235202. (p. 94, 102)
- Yang, C., Z. He, and W. Yu (2009, January). Comparison of public peak detection algorithms for MALDI mass spectrometry data analysis. *BMC bioinformatics* 10(4), 1–13. (p. 25)
- Yubero, C., M. Dimitrijević, M. García, and M. Calzada (2007, February). Using the van der Waals broadening of the spectral atomic lines to measure the gas temperature of an argon microwave plasma at atmospheric pressure. *Spectrochimica Acta Part B: Atomic Spectroscopy* 62(2), 169–176. (p. 75)
- Yubero, C., M. García, M. Varo, and P. Martínez (2013, December). Gas temperature determination in microwave discharges at atmospheric pressure by using different Optical Emission Spectroscopy techniques. *Spectrochimica Acta Part B: Atomic Spectroscopy* 90, 61–67. (p. 75)
- Znamenskaya, I. A., D. F. Latfullin, A. E. Lutsky, I. V. Mursenkova, and N. N. Sysoev (2007, May). Development of gas-dynamic perturbations propagating from a distributed sliding surface discharge. *Technical Physics* 52(5), 546–554. (p. 13, 14, 102, 117, 118)
- Znamenskaya, I. A., I. V. Mursenkova, D. M. Orlov, and N. N. Sysoev (2007, July). Localization of pulsed energy deposition in a transverse surface discharge initiated in a gas flow with shock wave. *Technical Physics Letters* 33(7), 575–577. (p. 13)

